AFWL-TR-65-180

AFWL-TR
65-180

AD 630792

A STUDY OF THE PROPAGATION OF STRESS WAVES IN SAND

Robert L. McNeill

The Eric H. Wang Civil Engineering Research Facility
University of New Mexico
Albuquerque, New Mexico

Contract AF 29(601)-6002

TECHNICAL REPORT NO. AFWL-TR-65-180

March 1966

AIR FORCE WEAPONS LABORATORY
Research and Technology Division
Air Force Systems Command
Kirtland Air Force Base
New Mexico

CLEARINGHOUSE
FOR FEDERAL SCIENTIFIC AND
TECHNICAL INFORMATION
Hardcopy Microfiche
6.00 $ 1.25 238 as
ARCHIVE COPY

Code 1

AFWL-TR-65-180

Research and Technology Division
AIR FORCE WEAPONS LABORATORY
Air Force Systems Command
Kirtland Air Force Base
New Mexico

When U. S. Government drawings, specifications, or other data are used for any purpose other than a definitely related Government procurement operation, the Government thereby incurs no responsibility nor any obligation whatsoever, and the fact that the Government may have formulated, furnished, or in any way supplied the said drawings, specifications, or other data, is not to be regarded by implication or otherwise, as in any manner licensing the holder or any other person or corporation, or conveying any rights or permission to manufacture, use, or sell any patented invention that mev in any way be related thereto.

This report is made available for study with the understanding that proprietary interests in and relating thereto will not be impaired. In case of apparent conflict or any other questions between the Government's rights and those of others, notify the Judge Advocate, Air Force Systems Command, Andrews Air Force Base, Washington, D. C. 20331.

Distribution of this document is unlimited.

AFWL-TR-65-180

A STUDY OF THE PROPAGATION OF STRESS WAVES IN SAND

Robert L. McNeill

The Eric H. Wang Civil Engineering Research Facility
University of New Mexico
Albuquerque, New Mexico
Contract AF29(601)-6002

TECHNICAL REPORT NO. AFWL-TR-65-180

Distribution of this
report is unlimited.

BLANK PAGE

FOREWORD

This report was prepared by the Eric H. Wang Civil Engineering Research Facility, University of New Mexico, Albuquerque, New Mexico, under Contract AF29(601)-6002. The research was performed under Program Element 7.60.06.01.D, Project 5710, Subtask 13.144, and was funded by the Defense Atomic Support Agency (DASA).

Inclusive dates of research were January 1964 to May 1965. The report was submitted 21 February 1966 by the AFWL Project Officer, Lt Cornelius J. Higgins, (WLDC).

It is a pleasure to acknowledge the patient guidance offered by Dr. Eugene Zwoyer, Director of the Eric H. Wang Civil Engineering Research Facility where the work was performed. Dr. George E. Triandafilidis, Supervisor of Soil Dynamics Research at the facility, was of inestimable help in his review of the work, and his editing of the drafts. Messrs. W.J. Baker and F.M. Babcock, Research Engineers at the facility, assisted greatly in both the experimental and theoretical work. Messrs. Robert Fisher and Bert Wilkinson designed and assembled the experimental equipment, and performed many of the tests. The assistance of other personnel at the facility was invaluable and is gratefully acknowledged.

This report has been reviewed and is approved.

CORNELIUS J. HIGGINS
1Lt USAF
Project Officer

FREDRICK W. KORBITZ, JR.
Lt Colonel USAF
Chief, Civil Engineering Branch

JOHN W. KODIS
Colonel USAF
Chief, Development Division

ABSTRACT

The propagation of near-failure, soft-fronted stress waves in 5-foot-long, 1-inch-diameter, unconstrained rods of dry 20-30 Ottawa sand is studied. The input is created by a shock tube, modified to yield soft-fronted, long-duration, air-pressure loadings. Primary data are displacement-time histories from seven stations along the rod, read by light-sensing gages designed for negligible inertia and friction; secondary data are stress-time histories at the input and the rigidly held reaction ends. Static, dynamic, and additional static triaxial data are given. Variables are applied ambient stress and sand density. From findings that the material is strain-rate insensitive and follows Coulomb's failure law at subfailure stresses, the following observations of wave-propagation parameters for above-seismic stresses and a specific material condition have been made: (1) wave and particle velocities depend on the one-half power of ambient stress; (2) all energy densities depend on the first power of ambient stress; and (3) energy partitioning and reflection are independent of ambient stress. Effects of density on wave-propagation parameters for the sand and the variables studied are that (1) all increase with increasing density, (2) some are specifically linear on density, and all can be taken as such for engineering purposes, and (3) waveform parameters are much less sensitive to small errors in density than are static parameters. Also shown: (1) reflections of stress from rigid boundaries can be estimated for nonlinear materials; and (2) correlation between seismic velocity and triaxial strength exists, provided there is a power-function relationship between seismic velocity and ambient stress and the material follows Coulomb's law.

This page intentionally left blank.

CONTENTS

		Page
I.	Introduction	1
	Statement of Problem	1
	Scope of Study	1
II.	Review of Literature	3
	Wave-Propagation Laws	3
	Waves in Elastic Materials	10
	Waves in Plastic Materials	16
	Wave Propagation in Soil Masses	22
	Dynamic Properties of Sand	26
	Previous Unconstrained Wave-Propagation Experiments on Sands	29
III.	Extension of Theory of Plastic Waves for Strain-Rate-Insensitive Materials	38
	Basic Concepts	38
	Waveform Computations	39
IV.	Experimental Equipment	50
	General Description	50
	Specimen	51
	Specimen Containment	51
	Loading Device	53
	Displacement Measurements	56
	Force Measurements	65
	Fabrication and Placement of Specimen	67
	Remote-Recording System	71
	Triaxial Tests	71
V.	Experimental Results	76
	Vacuum Triaxial Tests	76
	Analysis by Subfailure Coulombic (SFC) Method	90
	Pilot Wave-Propagation Tests	95
	Static Long-Specimen Tests	97
	Wave-Propagation Tests	99
VI.	Analysis and Discussion	117
	Study of Dynamic and Static Tests	117
	Wave Propagation in Strain-Rate-Insensitive SFC Materials	127

CONTENTS (Cont'd)

		Page
	Effects of Ambient Stress on Wave-Propagation Parameters.....	152
	Effects of Density on Wave-Propagation Parameters.....	152
	Relationships Between Seismic Velocity and Triaxial Parameters	164
VII.	Conclusions and Recommendations.....	169
	Appendix A. Development of Experimental Equipment and Verification Tests.....	173
	B. Discussion of Static Long-Specimen Tests.....	193
	C. Example of Computations.....	210
	References.....	212
	Distribution.....	217

ILLUSTRATIONS

Figure		Page
1	General stress-strain curve for conditions of single loading, constitutive uniqueness, and strain-rate insensitivity.....	6
2	Reflection.....	13
3	Exact-phase velocities in an infinite elastic rod--longitudinal mode and infinite sinusoidal train (Fig. 1, p. 590, in Ref. 7).....	15
4	Donnell's simplification for wave-propagation phenomena (Ref. 8)	
	(a) Stress-strain curve.....	17
	(b) Wave-position plot.....	17
5	Constrained stress-strain curve.....	19
6	Input stress pulses	
	(a) Step-pulse input.....	21
	(b) Soft-pulse input.....	21
7	Near-zero parameters.....	21
8	Plastic loading-unloading curve.....	23
9	Strain-rate effect for dry sands	
	(a) Influence of rate of loading on stress-strain curve.....	28
	(b) Relationship between strain rate and strength.....	28
10	Wave velocities in dry 20-30 Ottawa sand (Ref. 49).....	31
11	Velocity-density relationships for dry 20-30 Ottawa sand at selected ambient stresses.....	32
12	Initial computation of basic wave quantities (no scale)	
	(a) Plastic stress, σ_p.....	40
	(b) Plastic modulus, E_p.....	40
	(c) Plastic wave velocity, c_p.....	40
	(d) Plastic particle velocity, v_p.....	40
	(e) Plastic energy densities.....	40
13	Computation of stress-dependent basic wave quantities (sketch, no scale)	
	(a) Stress-strain curve.....	42
	(b) Stress-wave velocity curve.....	42
14	Plastic waveforms (sketches, no scale)	
	(a) Stress-position plots at different times.....	43
	(b) Stress-time plots at different positions.....	43

ILLUSTRATIONS (Cont'd)

Figure		Page
15	Interpretation of position-time plot	45
16	Preparing experimental raw data	
	(a) Particle-displacement vs. time plots	46
	(b) Particle-velocity vs. time plots	46
	(c) Position vs. time plots	46
17	Compatibility fitting	48
18	Simple data analyses	
	(a) Reciprocal of wave-velocity vs. particle-velocity plot	49
	(b) Plastic-strain vs. particle-velocity plot	49
19	Grain-size distribution of 20-30 Ottawa sand	52
20	Typical sections of foam bed	
	(a) Normal section	54
	(b) Section showing one cutout at light station	54
21	Frame and cradle	55
22	Displacement flags	
	(a) Dimensions of displacement flags	57
	(b) Different-sized displacement flags	57
23	Light-sensitive crystal	58
24	Light source	
	(a) Details of light source	59
	(b) Photograph of light source	59
25	Photodiode and carrier	60
26	Displacement-measuring system	
	(a) Detailed drawing of displacement-measuring system	61
	(b) Photograph of displacement-measuring system	61
27	Output-displacement calibration device	
	(a) Detailed drawing of calibration device	63
	(b) Photograph of calibration system	63
28	Output-displacement calibration	
	(a) Photograph of output-displacement calibration	64
	(b) Drawing of output-displacement calibration	64
29	Preexperiment calibrations	
	(a) Direct CRO calibrate	66
	(b) Remote calibrate	66
30	Force-link calibrate with eccentricities	68

ILLUSTRATIONS (Cont'd)

Figure		Page
31	Lowering specimen into bed	70
32	Locations of displacement-measuring stations	72
33	Remote-record circuitry	73
34	Initial tests of membrane effects	75
35	Typical scatter in first-load tests on sand	79
36	Triaxial results: dense, high-ambient stress	81
37	Triaxial results: dense, middle-ambient stress	82
38	Triaxial results: dense, low-ambient stress	83
39	Triaxial results: medium-dense, high-ambient stress	84
40	Triaxial results: medium-dense, middle-ambient stress	85
41	Triaxial results: medium-dense, low-ambient stress	86
42	Triaxial results: loose, high-ambient stress	87
43	Triaxial results: loose, middle-ambient stress	88
44	Triaxial results: loose, low-ambient stress	89
45	Preparatory analysis of triaxial results	
	(a) Parametricizing on ambient stress	91
	(b) Smoothing stress-density curves	91
	(c) Semi-smooth stress-strain curves	91
46	SFC smoothing of triaxial results	93
47	SFC-smoothed stress-strain curves	94
48	Displacement gages: typical raw data	101
49	Displacement gages: typical full-event computer reduction	102
50	Displacement gages: typical expanded computer reduction	103
51	Front force link: typical raw data	103
52	Front force link: typical full-event computer reduction	104
53	Front force link: typical expanded computer reduction	105
54	Back force link: typical raw data	105

ILLUSTRATIONS (Cont'd)

Figure		Page
55	Back force link: typical full-event computer reduction.....	106
56	Back force link: typical expanded computer reduction.....	107
57	Typical displacement- and velocity-time results	
	(a) Displacement-time data.....	108
	(b) Velocity-time data.....	108
58	Position-time plot, fitting velocity lines.....	110
59	Position-time plot, fitted velocity curves.....	111
60	Wave- and particle-velocity relationship.....	112
61	Wave-velocity and strain relationship.....	113
62	Dynamic stress-strain curve.....	114
63	Dynamic-to-static comparison: dense, high-ambient stress...	118
64	Dynamic-to-static comparison: dense, middle-ambient stress.	119
65	Dynamic-to-static comparison: dense, low-ambient stress....	120
66	Dynamic-to-static comparison: medium-dense, high-ambient stress.....	121
67	Dynamic-to-static comparison: medium-dense, middle-ambient stress.....	122
68	Dynamic-to-static comparison: medium-dense, low-ambient stress.....	123
69	Dynamic-to-static comparison: loose, high-ambient stress...	124
70	Input stress read in Test V, 253-1200.....	126
71	Universal relationship between stress angle and stress ratio	129
72	SFC constitutive relationship.....	130
73	Universal relationship between inert-ϕ_p function and stress ratio.....	132
74	Stress angle, ϕ_p.....	134
75	SFC wave-velocity function, N_p.....	135
76	Effect of ambient stress on wave velocity.....	136
77	Particle-velocity function, Q_p.....	139

ILLUSTRATIONS (Cont'd)

Figure		Page
78	Kinetic-energy function, S_p	140
79	Potential-energy function, M_p	142
80	Total-energy function, U_p	144
81	Energy partitioning	146
82	Reflection factor, R_p	149
83	Reflected waveform	150
84	Reflection function, W_p	153
85	Effect of density on stress ratio, L_p	154
86	Effect of density on stress angle, ϕ_p	155
87	Effect of density on inert-ϕ_p function, $f(\phi_p)$	156
88	Effect of density on slope function, $d\phi_p/d\varepsilon_p$	157
89	Effect of density on modulus function, $f(\phi_p)\ d\phi_p/d\varepsilon_p$	159
90	Effect of density on wave-velocity function, N_p	160
91	Effect of density on particle-velocity function, Q_p	161
92	Effect of density on kinetic-energy function, S_p	162
93	Effect of density on potential-energy function, M_p	163
94	Strength-density relationship	165
95	Seismic-velocity vs. strength relationships	167
96	Drawing of specimen mold (each segment has two halves, identical except for mating pins or holes)	
	(a) End view	174
	(b) Plan	174
	(c) Section A-A	174
97	Axial-load test on foam bed	177
98	Lateral resistance of foam beds	177
99	Drawing of specimen cradle	
	(a) Section A-A	178
	(b) Side elevation	178
100	Drawing of expansion chamber	180

ILLUSTRATIONS (Cont'd)

Figure		Page
101	Crystal temperature and stability effects	
	(a) Temperature effects	182
	(b) Stability effects	182
102	Input-voltage sensitivity	184
103	Possible errors due to flag-to-crystal misposition	185
104	Details of transverse positioning errors (0.375-in. flag only)	187
105	Transverse positioning errors (all for 1/4-in. flag-to-crystal spacing)	188
106	Crystal rise time test	189
107	Static tests: typical raw data	194
108	Static tests: typical full-event computer reduction	195
109	Static tests: typical expanded computer reduction	196
110	Static tests: typical actual and averaged data	197
111	Static tests: typical uniform-strain analysis	199
112	Static tests: typical extended uniform-strain analysis	199
113	Static comparison: dense, high-ambient stress	201
114	Static comparison: dense, middle-ambient stress	202
115	Static comparison: dense, low-ambient stress	203
116	Static comparison: medium-dense, high-ambient stress	204
117	Static comparison: medium-dense, middle-ambient stress	205
118	Static comparison: medium-dense, low-ambient stress	206
119	Static comparison: loose, high-ambient stress	207

TABLES

Table		Page
I	Schedule of vacuum triaxial tests	77
II	Density results from all tests	80
III	Summary of static long-specimen tests	98
IV	Summary of wave-propagation tests	100
V	Summary of computations	211

ABBREVIATIONS AND SYMBOLS

BFL	back force link
c	wave velocity
c_a	wave velocity of rod A
c_b	wave velocity of rod B
c_d	dilatational-wave velocity
c_e	elastic-wave velocity
c_o	seismic-wave velocity
c_p	plastic-wave velocity
c_{pi}	plastic-wave velocity at specified strain (ε_i)
c_{po}, c_{p1}, c_{p2}...c_{pn}	plastic-wave velocity corresponding to stress or strain level 1, 2, 3...n, respectively
c_s	shear-wave velocity
c_w	velocity of input wave
c_1, c_2	wave velocities consistent with simplified bilinear stress-strain curve corresponding to Young's moduli E_1 and E_2, respectively
d	diameter
D	dense
E	Young's modulus
E_o	seismic modulus (based on initial tangent of stress-strain curve)
E_p	tangent or plastic modulus
E_{pi}	tangent or plastic modulus at specified strain (ε_i)
E_1, E_2	Young's moduli for simplified bilinear stress-strain curve
fps	feet per second
$f(\phi_p)$	unique function of ϕ_p (inert-ϕ function)
FFL	front force link
gm	gram(s)
G	shear modulus

Hg	mercury
ips	inches per second
I.D.	inside diameter
kc	kilocycle(s)
kfps	kilofeet per second
Kohm	ohm x 10^3
l	length
lb	pound(s)
low	low-ambient stress
L	loose
L_p	subfailure-coulombic stress ratio applicable to specific plastic strain, ε_p: deviator/ambient
L_{pi}	incident stress ratio for SFC materials
L_{pr}	reflected stress ratio for SFC materials
L_s	strength ratio (ratio of strength to ambient stress)
LVDT	linear variable differential transformer
L_x	external-energy losses
mil	inch x 10^{-3}
min	minute(s)
mm	millimeter(s)
msec	millisecond(s)
mt	megaton(s)
mv	millivolt(s)
mv/lb	millivolt(s) per pound(s)
M	constrained or dilatational modulus
MD	medium dense
Mohm	ohm x 10^6

M_p	SFC potential-energy function
M_{pr}	reflected potential-energy function for SFC materials
N_p	SFC wave-velocity function
O.D.	outside diameter
p	subscript to denote plastic
pcf	pounds per cubic feet
P	prophylactic membrane
P-wave	dilatational wave
Q_p	SFC particle-velocity function
R_p	reflection factor for subfailure coulombic materials
R-wave	Rayleigh wave
s	strength
S	surgical membrane
SFC	subfailure coulombic materials
S_p	SFC kinetic-energy function
S-wave	shear wave
$t, t_1, t_2, t_3 \ldots t_n$	time variables
t_r	rise time
T_e	elastic kinetic-energy density
T_p	plastic kinetic-energy density
T_{pi}	plastic kinetic-energy density at specified strain (ε_i)
u	axial-particle displacement
$\dot{u}$	axial-particle velocity
u_i	i-th component of displacement
$\dot{u}_i$	particle velocity in i-th direction
U_p	SFC total-energy function

U_{pi} incident total-energy function for SFC materials

U_{pr} reflected total-energy function for SFC materials

v particle velocity

v_e elastic-particle velocity

v_p plastic-particle velocity

v_{pi} plastic-particle velocity at specified strain (ε_i)

$v_{po}, v_{p1}, v_{p2} \ldots v_{pn}$ plastic-particle velocities corresponding to stress or strain level 1, 2, 3...n, respectively

V_e elastic potential-energy density

V_p plastic potential-energy density

V_{pi} plastic potential-energy density at specified strain (ε_i)

W_p reflection function for SFC materials

x axial coordinate

x_j space coordinate in j-th direction

$x_0, x_1, x_2 \ldots x_n$ displacement-measuring stations designating position 0, 1, 2, 3...n, respectively

$x_{01}, x_{02}, x_{03} \ldots x_{0n}$ position of wavefront at time $t_1, t_2, t_3 \ldots t_n$, respectively

$x_{p1}, x_{p2}, x_{p3} \ldots x_{pn}$ position of stress σ_p at time $t_1, t_2, t_3 \ldots t_n$, respectively

°F. degrees Fahrenheit

Δt_w time delay of input function for stress level, σ_p

Δv_{pi} plastic-particle-velocity increment

$\Delta \varepsilon_{pi}$ plastic-strain increment

$\Delta \sigma_a$ reflected portion of incoming axial stress in rod A

ε axial strain

$\dot{\varepsilon}$ strain rate

ε' specified strain consistent with simplified bilinear stress-strain curve

ε_o seismic strain

ABBREVIATIONS AND SYMBOLS (Cont'd)

ε_p	plastic axial strain
ε_{pi}	incident plastic strain or any specified plastic strain
ε_{pr}	reflected plastic strain
λ	wavelength
μv	microvolt(s)
μs	microsecond(s)
ν	Poisson's ratio
ξ	elastic total energy
ξ_e	elastic total-energy density
ξ_p	plastic total-energy density
ρ	mass density
ρ_a	mass density of rod A
ρ_b	mass density of rod B
σ	axial stress
σ'	specified stress consistent with simplified bilinear stress-strain curve
σ_{af}	total axial stress in rod A after reflection
σ_{ao}	any increment of incoming axial stress in rod A
σ_{bf}	transmitted (refracted) portion of incoming axial stress in rod B
σ_{dp}	deviator stress applicable to specific plastic strain, ε_p
σ_{ij}	stress on i-th plane in j-th direction
σ_o	seismic stress
σ_p	plastic stress (at specific strain, ε_p)
σ_{pi}	incident stress of SFC materials
σ_{pr}	reflected stress for SFC materials
σ_1	major principal stress
$(\sigma_1)_p$	major principal stress applicable to specific plastic strain, ε_p

ABBREVIATIONS AND SYMBOLS (Cont'd)

σ_3	minor principal stress (ambient stress)
τ	shear stress
ϕ_p	subfailure coulombic stress angle at specific plastic strain, ε_p

This page intentionally left blank.

SECTION I

INTRODUCTION

1. Statement of Problem.

For many years there has been intensive interest in determining the dynamic properties of soils and in predicting the form of a given input wave after it has propagated a distance through a soil of known dynamic properties. The most urgent interest has been generated by the need to defend against nuclear blasts, but also of pertinent interest to engineers are vibrating machinery and structures, earthquake effects, blasting and blast-induced excavation, and high-speed subsurface penetration. The problem to be solved is essentially the same in all cases and may be stated concisely as follows: *given the soil properties and the input function, predict the waveform and its effect at a specified point in space and time.* Thus it is necessary to determine the following: (1) the effects of soil properties; (2) the effects of the input function; (3) the method of predicting the waveform; and (4) the method of predicting the effects of the waveform for the particular engineering situation.

Experimental studies that measure the effects of ambient stress, stress and strain level, and soil condition were required to determine the first two--the effects of soil properties and input function. To establish the last two--methods of predicting the waveform and its effects--theoretical studies that adequately consider the effects of soil properties and problem geometry and that include soil-structure interaction effects pertinent to the particular situation were required.

2. Scope of Study.

In this study pertinent elements of wave-propagation theory and the dynamic properties of soils were summarized. The theory of plastic waves was extended in order to develop general methods for the analysis of strain-rate-insensitive but constitutively unique materials. In this extension it was assumed that the wave velocities depend only on material properties, expressed by the mass density and the shape of the stress-strain curve.

Experimental devices and techniques were developed so that both static and dynamic experiments could be performed on long, slender, unconstrained rods of sand. The wave-propagation experiments were designed mainly around the concept of using displacement rather than stress measurements. Soil-property and

wave-propagation experiments were performed on the long rods, and the static tests were augmented by standard static triaxial tests. The static and dynamic test results were compared on the basis of their stress-strain curves to determine the effects of stress condition and sand properties on the wave-propagation parameters.

As an engineering simplification, the concept of a material following Coulomb's failure law at subfailure stresses was introduced. For such subfailure coulombic (SFC) materials, simplifications in wave-propagation theory were possible. In addition, for such SFC materials some general laws of the dependence of waveform parameters on stress condition were established. For the sand used in the study, some specific empirical relationships of the dependence of waveform parameters on material properties were developed.

Stress reflections from a rigid interface were studied by using energy-density and energy-partitioning concepts.

Finally, the possibility and the conditions of a correlation between seismic velocity and static triaxial parameters are presented.

SECTION II

REVIEW OF LITERATURE

1. Wave-Propagation Laws.

a. Continuity and Motion Equations.

Two basic laws govern any continuum; they are the conservation of mass and the equality of applied force and time-rate change of momentum. These laws are usually expressed in the form of the *equation of continuity*

$$\frac{d\rho}{dt} + \rho \frac{\partial \dot{u}_i}{\partial x_j} = 0 \tag{1}$$

where

ρ = mass density
$\dot{u}_i$ = particle velocity in i-th direction
t = time variable
x_j = space coordinate in j-th direction

and the *equation of motion*

$$\frac{\partial \sigma_{ij}}{\partial x_j} = \rho \frac{\partial^2 u_i}{\partial t^2} \tag{2}$$

where

σ_{ij} = stress on i-th plane in j-th direction
u_i = i-th component of displacement

In these general laws body forces have been neglected and no assumptions have been made for either geometry or material properties. For the problem of this study, which involves transient waves traveling in a long rod that is *unconstrained* in the lateral direction, considerable simplification can be achieved. The exact solution, even for an ideally elastic material, is extremely difficult. If there were no lateral deformations, owing either to constraint or to the rod having a Poisson's ratio of zero, the rod would be *constrained*. Although the mathematics for the constrained case are quite simple, the experimental techniques of achieving a constrained condition are overwhelming. Classical

theoretical developments of the elastic problem (Ref. 1) ignore the dynamic effects of the lateral deformations (Poisson's effect) for the unconstrained case to achieve rather simple linear solutions. The theoretical developments to follow will also implicitly assume the mathematics of constrained geometry. Insofar as possible the errors involved in this assumption will be assessed in comparison with experimental results from unconstrained rods.

With this assumption of one-dimensional geometry there are no lateral kinematics. If only an axial compressive stress is applied, the equations of the governing laws simplify to

$$\frac{d\rho}{dt} + \rho \frac{\partial \dot{u}}{\partial x} = 0 \tag{3}$$

where

$\dot{u}$ = axial-particle velocity

x = axial coordinate

and

$$\frac{\partial \sigma}{\partial x} = \rho \frac{\partial^2 u}{\partial t^2} \tag{4}$$

where

σ = axial stress

u = axial-particle displacement

The subscripts have been dropped with the understanding that only axial (x) components are to be considered. For this one-dimensional case the axial strain (ε) may be defined as

$$\varepsilon = \frac{\partial u}{\partial x} \tag{5}$$

Then the strain rate ($\dot{\varepsilon}$) becomes simply

$$\dot{\varepsilon} = \frac{\partial \varepsilon}{\partial t} = \frac{\partial^2 u}{\partial x \partial t} = \frac{\partial \dot{u}}{\partial x} \tag{6}$$

Substitution of this result into Eq. (3) simply leads to the definition of natural strain (Ref. 2) on the assumption of negligible area change, and forecasts numerical errors only if the unit strains considered exceed perhaps 0.20. Such unit strains are not anticipated; therefore the equation of continuity may be taken in the form of either Eq. (3) or (5).

b. Constitutive Relationships.

To interpret Eq. (4), it is necessary to have some constitutive relationship between the variables stress and displacement. In view of Eq. (5), a stress-strain curve would serve this purpose exactly. The stress-strain curve for soil is not necessarily unique; stress is in general a function of strain, strain rate, and previous history. Some simplifications can, however, be made for the experiments to be studied. First, consider only *first-loading* cycles so that the effects of previous history become trivial. Second, assume that the material is *constitutively unique;* that is, any two of the variables stress, strain, or strain rate will uniquely determine the third to define a unique constitutive point. Finally, assume that the sand to be studied is strain-rate-insensitive (based on data from the literature cited later in this section and on the results of the experiments to be reported). Then the stress-strain curve is unique (as shown in Fig. 1) and may be expressed in the general form

$$\sigma = \sigma_p (\varepsilon) \tag{7}$$

where

σ_p = plastic stress (at specific strain, ε_p)

If either the stress σ_p or the strain ε_p is specified, the other is uniquely fixed by the constitutive point on the stress-strain curve. For the same point the tangent or *plastic modulus* (E_p) is:

$$E_p = \left.\frac{\partial\sigma}{\partial\varepsilon}\right|_p = \frac{d\sigma_p}{d\varepsilon_p} \tag{8}$$

is also uniquely defined; for a specified constitutive point, therefore, the stress, strain, and plastic modulus are uniquely determined and may be treated as (empirical) constants for that specified point.

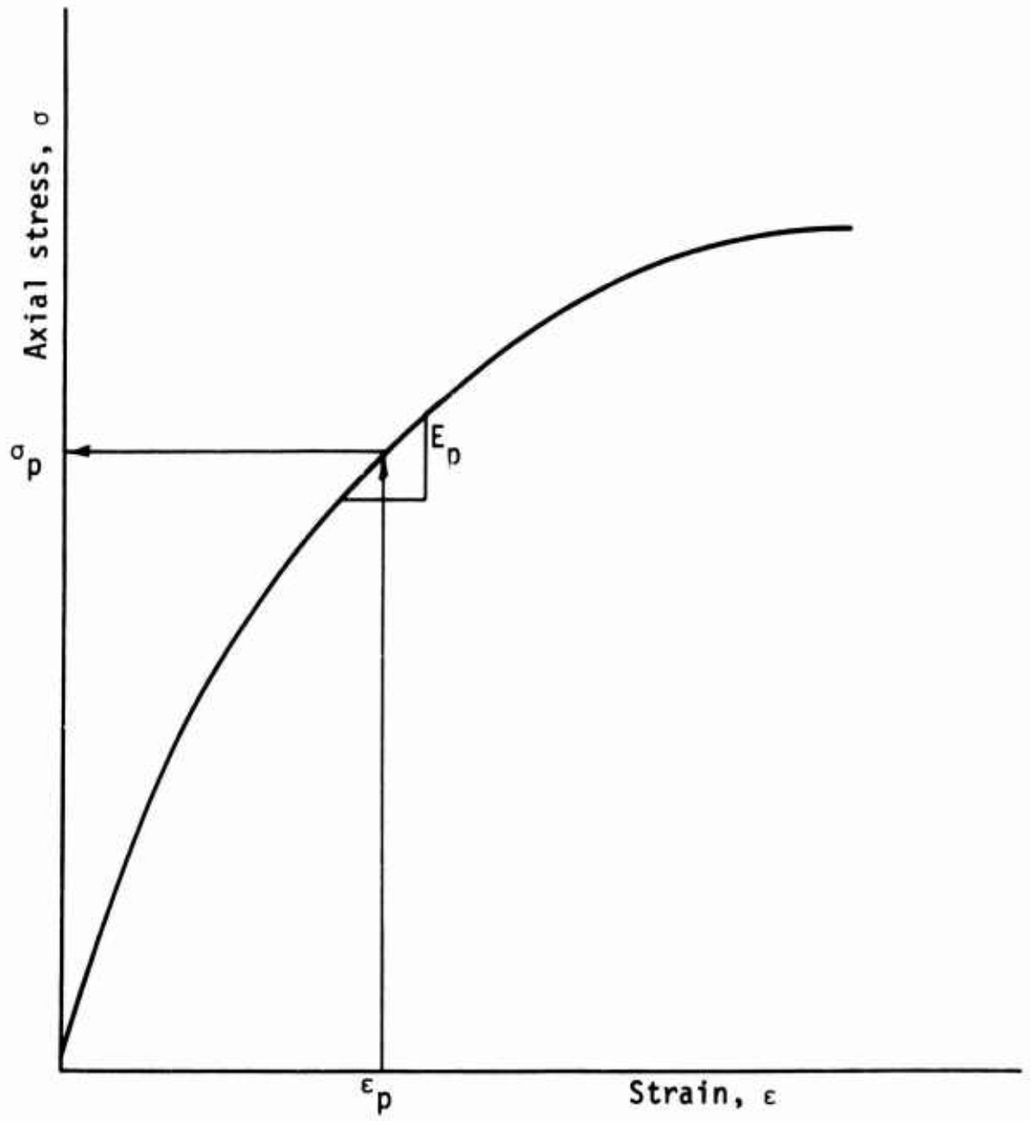

Figure 1. General stress-strain curve for conditions of single loading, constitutive uniqueness, and strain-rate insensitivity

c. One-Dimensional Wave Propagation.

With these simplifications, it is permissible to operate on Eq. (7), utilizing Eqs. (5) and (8) for a specified constitutive point

$$\frac{\partial \sigma_p}{\partial x} = \frac{d\sigma_p}{d\varepsilon_p} \frac{\partial \varepsilon_p}{\partial x} = E_p \frac{\partial^2 u}{\partial x^2} \tag{9}$$

When substituted into Eq. (4) and rearranged, the result is

$$\frac{E_p}{\rho} \frac{\partial^2 u}{\partial x^2} = \frac{\partial^2 u}{\partial t^2} \tag{10}$$

Equation (10) is the general equation governing one-dimensional wave propagation. An explicit solution is not generally possible (exception: the elastic case discussed later), although it is possible to operate on the equation in order to deduce the form to which a solution must conform. This is done by *assuming* that the plastic-wave velocity (c_p) at which the wave travels

$$c_p = \frac{\partial x}{\partial t} \tag{11}$$

depends uniquely on the constitutive properties of the material. This is the basic assumption of plastic-wave theory. By making certain functional substitutions, it is possible to operate (Ref. 3) on the second-order partials in Eq. (10) to deduce that each specific stress, σ_p (or its corresponding strain, ε_p) travels at a specific and unique *wave velocity*

$$c_p = \sqrt{\frac{E_p}{\rho}} \tag{12}$$

For soils in the unconstrained geometry the plastic modulus (E_p) decreases with increasing strain; therefore the wave velocity must also decrease with increasing strain. This means that a stress wave in an unconstrained rod of soil will become progressively softened because the low-stress components will tend to outrun the high-stress components.

d. Particle Velocity.

In the above a relationship was established between the constitutive properties of a plastic material and the velocity at which a *wave* will propagate through a rod of that material. Each element or *particle* in the rod will travel at a slower velocity, relatable to constitutive properties.

Because plane-transverse sections are assumed to remain plane throughout this work, a particle may be thought of as a thin wafer transverse to the long axis of the rod. This wafer concept is utilized in designing and interpreting the experiments that are described later.

The kinematics of a particle can be described in terms of any or all of the three fundamental quantities--displacement, velocity, or acceleration. It is simplest here to use the plastic-particle velocity (v_p), which is defined in general as

$$v_p = \frac{\partial u}{\partial t} \tag{13}$$

If Eqs. (12), (11), (5), and (13) are substituted into the basic Eq. (10), the results simplify to

$$c_p = \frac{\partial v_p}{\partial \varepsilon_p} \tag{14}$$

For a given plastic- and strain-rate-insensitive material, c_p being uniquely related to strain, the equation may be treated as an ordinary differential and integrated to yield

$$v_p = \int_0^{\varepsilon_p} c_p d\varepsilon_p \tag{15}$$

e. Energy Relationships.

Consider a rod in which a wave is traveling. Select some point x that lies in the swarm of the wave. At a given time the stress at point x will be some value σ_p, and this stress will be moving across point x with a wave

velocity c_p given by Eq. (12). According to the uniqueness of the stress-strain curve (Fig. 1) the strain will have a corresponding value ε_p. In addition, the wafer or thin lamina at x will be in motion at a particle velocity given by Eq. (15).

In the process of being strained, the wafer at point x has consumed some potential energy. From the unique stress-strain curve given in Figure 1, either the stress or strain is uniquely defined if the other is specified; therefore the plastic potential-energy density V_p is also uniquely defined as the area under the stress-strain curve up to the specified constitutive point

$$V_p = \int_0^{\varepsilon_p} \sigma_p d\varepsilon_p \tag{16}$$

This consumed potential-energy density may or may not be recoverable and for soil materials is undoubtedly not recoverable. Recoverability is not, however, pertinent to the problem being studied because only the first loading (with no unloading) is to be considered.

Since at the specified strain ε_p the wafer at x is in motion with a particle velocity v_p (Eq. 15), the wafer also possesses kinetic energy. The plastic kinetic-energy density (T_p) may be expressed as

$$T_p = \frac{1}{2} \rho \, v_p^2 \tag{17}$$

The plastic total-energy density (ε_p) is the sum of these potential and kinetic-energy densities, plus a general term L_x which accounts for any external losses that may be taking place

$$\xi_p = V_p + T_p + L_x \tag{18}$$

f. Reflections.

In all of the above a rod of semi-infinite length has been assumed. If the rod is of finite length, the wave characteristics must be compatible with the boundary conditions at the end of the rod. Because the wave is not aware of the end until it hits it, the compatibility must be achieved by reflections of a

wave from the end. For example, if the rod were rigidly supported at the end, no motion could exist, and a wave would have to reflect from the end back into the bar in order to develop stresses and strains to meet this no-motion condition.

It is not generally possible to develop explicit expressions for the reflected wave in nonlinear materials, even for the constitutively unique and strain-rate-insensitive plastic case considered above; but for an ideally linear elastic material such an explicit expression will be given below. In addition, for the simplified conditions set down, utilization of the energy equations given above will yield the reflected wave for nonlinear materials. The method is developed in the sections to follow.

2. Waves in Elastic Materials.

a. Assumptions.

A constitutively elastic material is assumed here to meet all ideal assumptions, that is, that the material is homogeneous, isotropic, linear, nonhysteretic, and strain-rate insensitive. The geometry will be taken as one-dimensional for the theoretical review because the governing equations become linear. The errors resulting from applying one-dimensional solutions to unconstrained experimental data are assessed in the subsection on dispersion below. In recognition of this assessment, the constitutive parameter for an elastic material will be loosely taken as Young's modulus (E) although a notation for the one-dimensional modulus would be correct.

b. Elementary Results.

On the assumption of linearity, the constant E may be substituted into Eq. (12) to derive the velocity at which a wave will travel in an elastic material

$$c_e = \sqrt{\frac{E}{\rho}} \tag{19}$$

where

c_e = elastic-wave velocity
E = Young's modulus

Because E is the same for all stresses, the wave velocity is the same for all stresses; therefore there is no change in the shape of a wave in a truly constrained elastic material, a conclusion which can also be reached from first principles (Ref. 1).

Because the wave velocity is a constant, its substitution into Eq. (15) yields a simple expression for the particle velocity associated with a wave in a truly constrained elastic material

$$v_e = c_e \varepsilon \tag{20}$$

where

v_e = elastic-particle velocity

Note that the particle velocity is not a constant, but depends on the strain level.

c. Energy Partitioning.

For the truly one-dimensional case the energy-density Eqs. (16), (17), and (18) reviewed above simplify to

$$V_e = \frac{1}{2} \sigma \varepsilon \tag{21}$$

$$T_e = \frac{1}{2} \rho v_e^2 \tag{22}$$

$$\xi_e = V_e + T_e \tag{23}$$

where

V_e = elastic potential-energy density
T_e = elastic kinetic-energy density
ξ_e = elastic total-energy density

on the assumption of no external losses (Ref. 1). Note that the energies are not constants, but depend on strain level. By identification, the kinetic-energy density T_e may also be written as

$$T_e = \frac{1}{2} \rho (c_e \varepsilon)^2 = \frac{1}{2} E \varepsilon^2 = \frac{1}{2} \sigma \varepsilon$$

to conclude that the *potential and kinetic energies are equal* for a wave traveling undisturbed by other waves in a truly one-dimensional elastic material (Ref. 1).

d. Reflection.

Consider Figure 2, which shows a rod of uniform cross-section, but made up of two different materials A and B abutting at a plane interface. Consider some increment of incoming axial stress, σ_{ao} (which can be imagined as one level of a general stress wave) moving to the right and impinging on the boundary. Upon hitting the boundary, some portion of the incoming stress will reflect back on itself as $\Delta\sigma_a$, and a certain stress σ_{bf} will be transmitted (refracted) into rod B. If the boundary is plane, has no mass or elasticity of its own, and if it remains intact throughout the reflection and refraction operation, then two conditions must obtain directly at the boundary: (1) the sum of the incoming and reflected stresses in rod A must be precisely balanced by the refracted (transmitted) stress in rod B; and (2) the particle velocities in rods A and B just at the boundary must be equal. One can, by applying these conditions (Ref. 1), obtain an expression for the total stress in rod A at the boundary after reflection:

$$\sigma_{af} = \sigma_{ao} \frac{2\,\rho_b c_b}{\rho_a c_a + \rho_b c_b} \tag{24}$$

where

σ_{af} = total axial stress in rod A after reflection
σ_{ao} = any increment of incoming axial stress in rod A
ρ_a = mass density of rod A
ρ_b = mass density of rod B
c_a = wave velocity of rod A
c_b = wave velocity of rod B

The total stress in rod A at the boundary after reflection is, therefore, simply a function of the relative elastic properties of rods A and B. The product ρc is the *acoustic impedance* of the material. For an elastic material it is a constant, but for nonlinear materials it is a variable, depending on the strain or stress level.

The concept of acoustic impedance leads to some conclusions that at least bracket the reflections possible in a nonlinear material. Two possible limits are that rod B is rigid, so that the acoustic impedance of B is infinitely greater than A, or that rod B is nonexistent (a free boundary), so that the acoustic impedance of B is much smaller than A. In the first case--a rigid reflector--

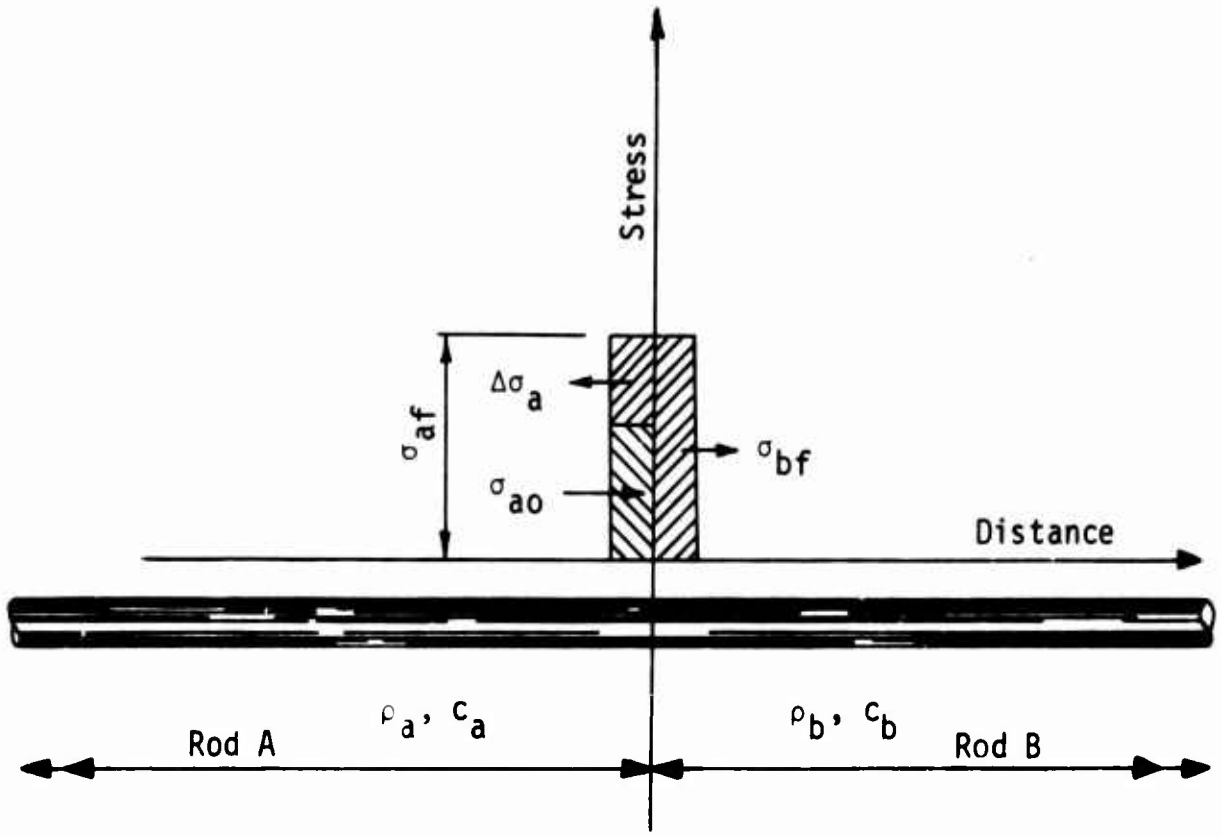

Figure 2. Reflection

manipulation of Eq. (24) shows that reflected stress in A will be double the incident stress. In the second case--a free boundary--the final stress in A will be zero, a conclusion in agreement with the end-boundary conditions.

e. Dispersion.

The theory for one-dimensional wave propagation requires that there be no lateral strain at all; but because this case is practically impossible to create in the laboratory, experimenters have been forced to work with unconstrained uniaxial rods. Clearly, all unconstrained rod experiments interpreted by the simple one-dimensional theory involve a greater or lesser degree of error. The rigorous and complete theoretical analysis of a rod is an extremely difficult problem (Ref. 4).

The basic reason for the difference between one-dimensional and unconstrained wave-propagation problems is the lateral expansion (Poisson's effect) that must take place in the unconstrained case. As a wave propagates down an unconstrained rod, there is a difference between the time rate of motions in the axial and in the lateral directions. This phase difference leads to two effects: (a) at a given instant of time an originally plane section is no longer plane

(Ref. 5), thus negating one of the key assumptions in the simple one-dimensional approach; and (b) to meet the stress-free boundary conditions at the lateral surface, *surface waves* are created. These surface waves travel at velocities less than either the rod (unconstrained) elastic-wave velocity (c_e) or the dilatational-wave velocity (c_d). The effect of these surface waves is (a) to slow down the overall wave velocity under steady-state vibration, and (b) to cause the front of a transient wave to vanish.

Assume that the rod is unconstrained and is infinitely long. At some point a train of pure sinusoidal waves is introduced and sustained. The problem is to determine the velocity at which the waves will travel. In the unconstrained case the highest possible wave velocity (Ref. 1) is the rod velocity c_e from Eq. (19). The rigorous solution of this problem was first undertaken by Pochhammer in 1876 and Chree in 1889. Their work was organized and presented by Love (Ref. 6). The exact solution to the problem was obtained by Bancroft in 1941 (Ref. 7) and is given in Figure 3, which shows the relationship between the given frequency of a given steady-state sinusoidal wave and the velocity at which that wave travels. For convenience the frequency is expressed nondimensionally as the ratio of rod diameter (d) to sinusoidal wavelength (λ), and the wave velocity (c) is expressed in terms of its ratio to the simple-theory rod velocity c_e from Eq. (19). Bancroft's solution yields a major conclusion: the wave velocity decreases with increasing frequency.

It is important to keep in mind that the material is assumed to be ideally elastic with no hysteretic losses, and that the dispersion described is due only to the geometry of the situation; that is, the bar is free to expand laterally, and the inertia of the lateral expansion changes the simple theory. At very low frequencies a sinusoidal wave will propagate at essentially the simple-theory rod velocity c_e, and at very high frequencies a sinusoidal wave will propagate at essentially 0.6 of the c_e. Note that if one is willing to accept perhaps 5 percent errors in wave velocity and at a nominal value of Poisson's ratio (ν) of 0.3, the simple theory gives adequate results at frequencies so low that the diameter-to-wavelength ratio approaches 0.4. To express this conclusion in more usable form, simple theory is reasonably valid for wavelengths greater than 2.5 times the diameter ($\lambda \geq 2.5d$). Although this conclusion applies only to an infinite bar subjected to an infinite sinusoidal train, it may be taken as a guide in the design of experiments utilizing rods of finite length and transient pulses.

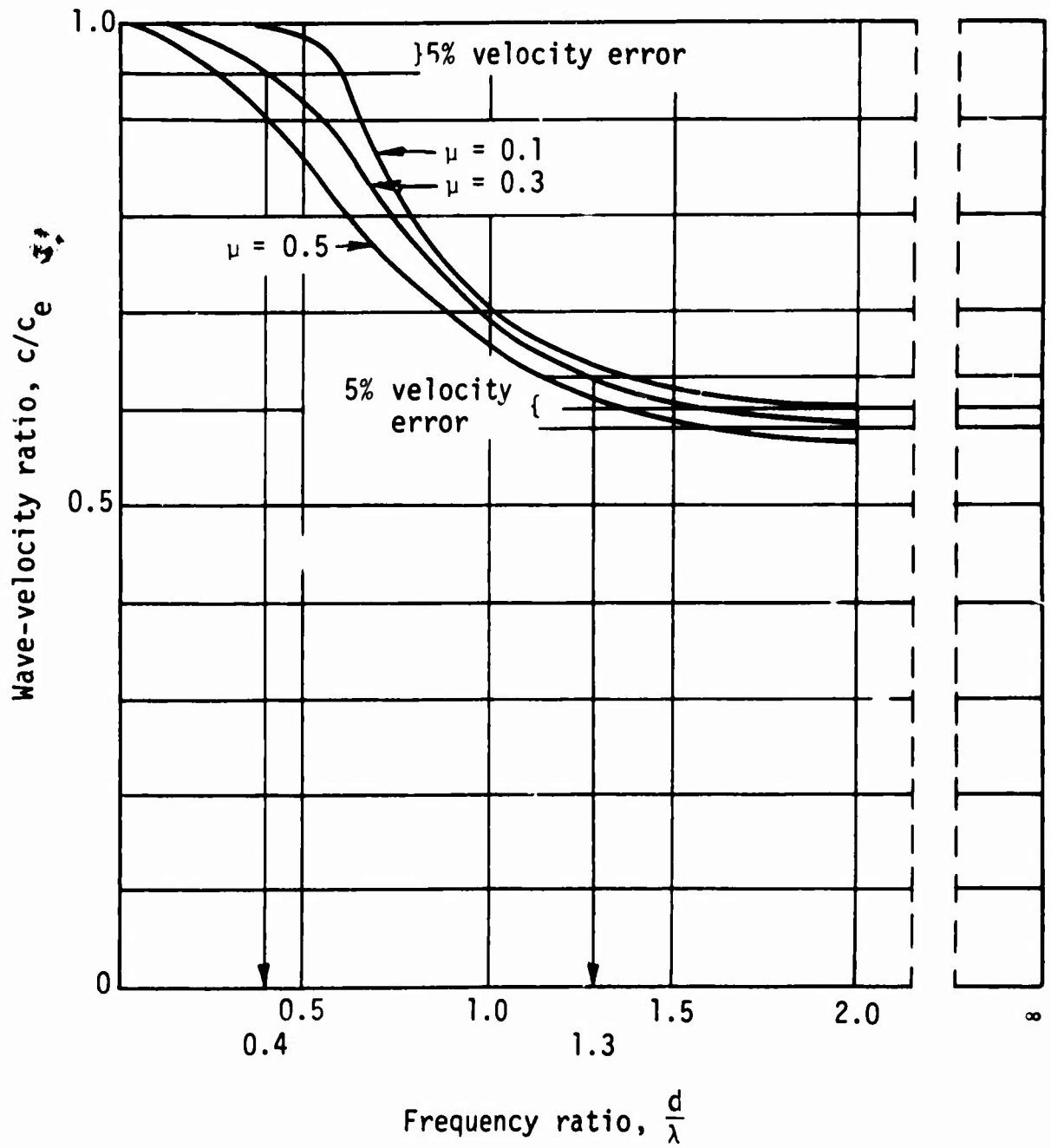

Figure 3. Exact-phase velocities in an infinite elastic rod--longitudinal mode and infinite sinusoidal train (Fig. 1, p. 590 in Ref. 7)

3. Waves in Plastic Materials.

a. Phenomenology.

The basic phenomenology of plastic-wave propagation was developed mathematically at the beginning of this section. The discussion here will deal with the history of the development and the changes in waveform that take place during propagation of a plastic wave.

The first development of plastic-wave propagation theory was apparently the intuitive approach published by Donnell (Ref. 8). As a result of his development of elastic-wave theory, Donnell suggested that if the stress-strain curve for a plastic material could be approximated by two straight lines (Fig. 4a), then the time history of a wave could be deduced for a rod of that material. Since each of the straight lines has a slope (different Young's moduli E_1 and E_2) and by recalling Eq. (19) for the elastic case, Donnell deduced that for strains (or stresses) less than ε' (or σ'), the wave velocity would be

$$c_1 = \sqrt{\frac{E_1}{\rho}} \quad \begin{cases} \varepsilon < \varepsilon' \\ \sigma < \sigma' \end{cases}$$

while for strains greater than ε' the wave velocity would be

$$c_2 = \sqrt{\frac{E_2}{\rho}} \quad \begin{cases} \varepsilon > \varepsilon' \\ \sigma > \sigma' \end{cases}$$

where

E_1, E_2 = Young's moduli for simplified bilinear stress-strain curve

c_1, c_2 = wave velocities corresponding to Young's modulus E_1 and E_2, respectively

ε' = specified strain

σ' = specified stress

Thus, at some specific time t_1 the *front* of the wave ($\varepsilon < \varepsilon'$) would have traveled to a position $x_1 = c_1 t_1$, whereas the remainder of the wave ($\varepsilon > \varepsilon'$) would have traveled only to a position $x_2 = c_2 t_2$. This is shown in Figure 4b. From Donnell's deductions, therefore, one would expect the higher strain levels to travel at lower velocities, with the result that a sharp-fronted wave would rapidly become softened in a bar of plastic material.

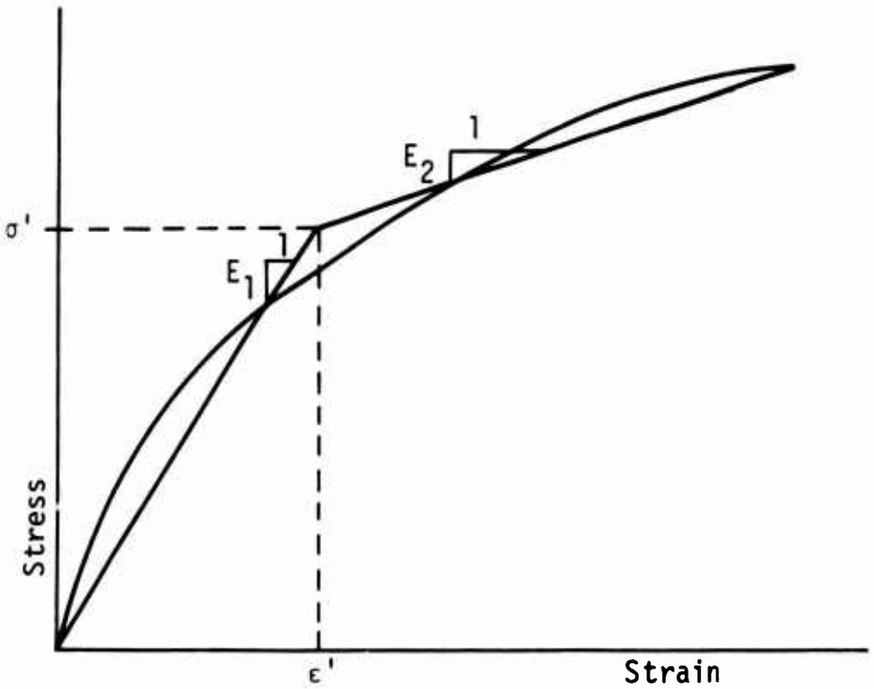

(a) Stress-strain curve

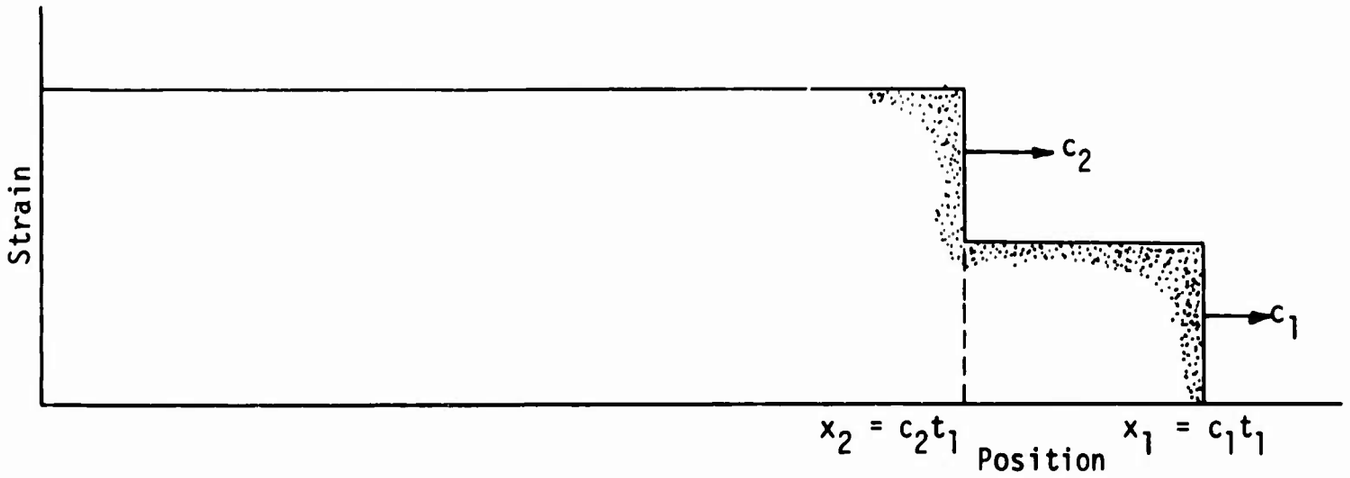

(b) Wave position plot

Figure 4. Donnell's simplification for wave-propagation phenomena (Ref. 8)

Donnell's simplification of the problem lay largely unused for 10 years even though, as described at the beginning of the section, it contained the germ of the method of solution of wave-propagation problems in plastic, strain-rate-insensitive materials.

The problem was not solved mathematically until World War II when solutions were obtained secretly and almost simultaneously by von Karman (U.S.), Taylor (U.K.), and Rakhmatutlin (U.S.S.R.). After the war numerous experimental investigations were undertaken to verify the mathematical solutions. Because the solutions all assumed a strain-rate-insensitive material, some of the experimental investigations failed to reproduce the theoretically predicted results.

b. Constitutive and Geometric Assumptions.

In the foregoing subsection on elastic waves it was possible to separate the effects of constitutive properties and geometry (constraint). For example, in the elastic case a simple modulus substitution would make the constitutive conversion for different constraints, and the result would still be linear; the effects of constraint would then be cared for separately (Fig. 3). In the plastic case, however, such a separation cannot be made *because the constitutive relationship depends on the constraint.*

In the developments described at the beginning of this section it was implicitly assumed that the stress-strain curve was *concave downward.* This is usually true only for the unconstrained case, which applies to the theoretical and experimental work of this report. Most real materials when in a truly one-dimensional configuration yield a concave-upward stress-strain curve as shown in Figure 5; some materials naturally yield such a curve even in the unconstrained configuration. It should be noted that the tangent to such a curve *increases* with increasing strain; therefore higher strains will propagate at *higher* velocities. This means that the high-strain components will tend to outrun the low-strain components forming a discontinuous *shock front* at which the strains are required to rise almost instantaneously from the zero to the maximum strains. This action creates a point at which the results of rod wave-propagation tests may be misinterpreted with respect to one-dimensional waves: shocks do not and cannot be created in rods of materials with concave-downward stress-strain curves. Because shocks are a study in themselves, extrapolation from rod results to one-dimensional shock cannot and should not be made at present.

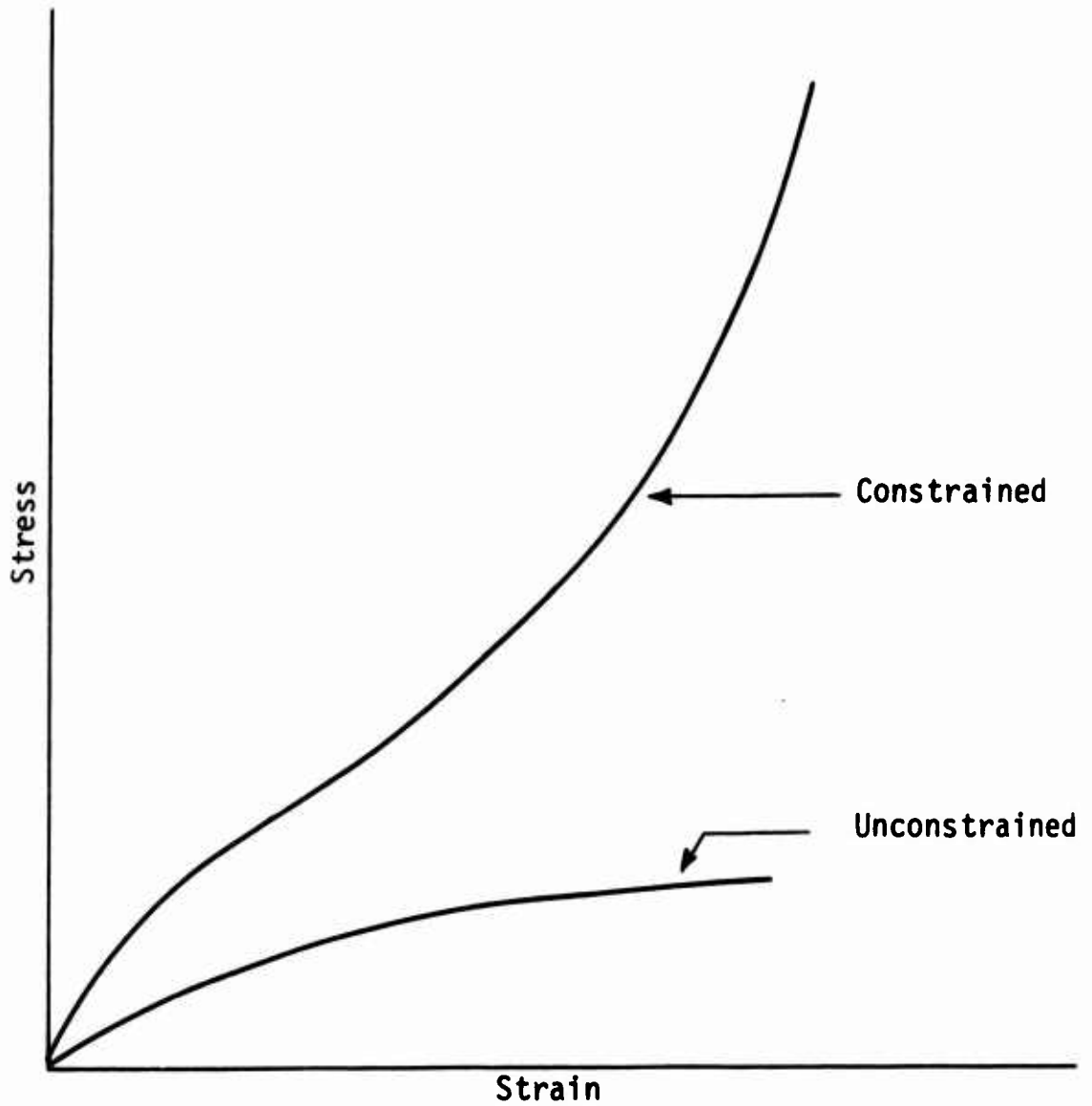

Figure 5. Constrained stress-strain curve

c. Dispersion.

The input implicitly discussed thus far is a step-type stress or strain pulse of infinite duration, as in Figure 6. The effects of dispersion (cf., elastic case, Fig. 3) are unknown for a plastic material, although Plass and Ripperger (Ref. 9) did cast a mathematical solution to include the effect; however, since the computer solutions to the problem have not been completed at this writing, the exact effects of geometric dispersion cannot yet be studied. It should be clear that in a plastic material dispersion or softening of the wave occurs owing both to the constitutive relationship of the material and to geometric dispersion; therefore, if plastic properties are to be studied by wave propagation, or if wave effects are to be predicted from plastic properties, the geometrical dispersion must be eliminated as a variable because its effect cannot presently be assessed. This means that *step-type pulses are to be avoided.* By taking a qualitative guide from the elastic result, negligible geometric dispersion may be expected if the rise time of the input pulse is kept such that the front appears as a long wavelength, $\lambda \geq 2.5d$. If the front in Figure 6b is taken as approximately a quarter-sine wave, this means that the rise time (t_r) should be at least

$$t_r \geq \frac{2d}{3c_o} \tag{25}$$

where the seismic-wave velocity (c_o) is computed by Eq. (19) based on the initial tangent modulus (E_o) to the stress-strain curve (stress approaching zero) (Fig. 7).

d. Seismic Parameters.

The near-zero stress or strain condition defines the *seismic* range. Workers in the field of seismology and geophysics have developed a great wealth of seismic theory based on purely elastic assumptions and have accumulated a sizable store of seismic data (e.g., Refs. 10,11,12,13,14), the use of which has yielded a wealth of information about the internal constitution of the earth; the techniques are used in geophysical exploration for oil and for solving foundation problems. By measuring the seismic-wave velocity, a seismic modulus may be computed by solving Eq. (19). Predictions of ground motions under high-stress conditions (e.g., nuclear blasts) are sometimes made using a modulus computed in this way (Refs. 15,16). Reference to Figure 5 shows that for either the constrained (one-dimensional) or unconstrained (applied to two-dimensional--plane strain--problems in normal soil mechanics practice) case there may be little

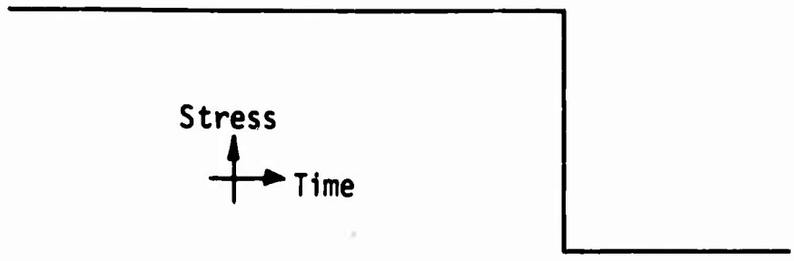

(a) Step-pulse input

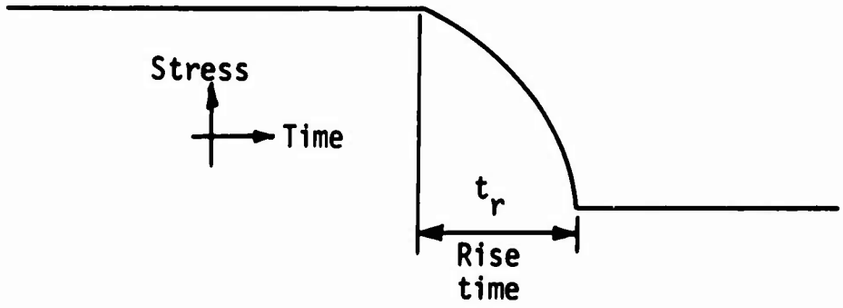

(b) Soft-pulse input

Figure 6. Input stress pulses

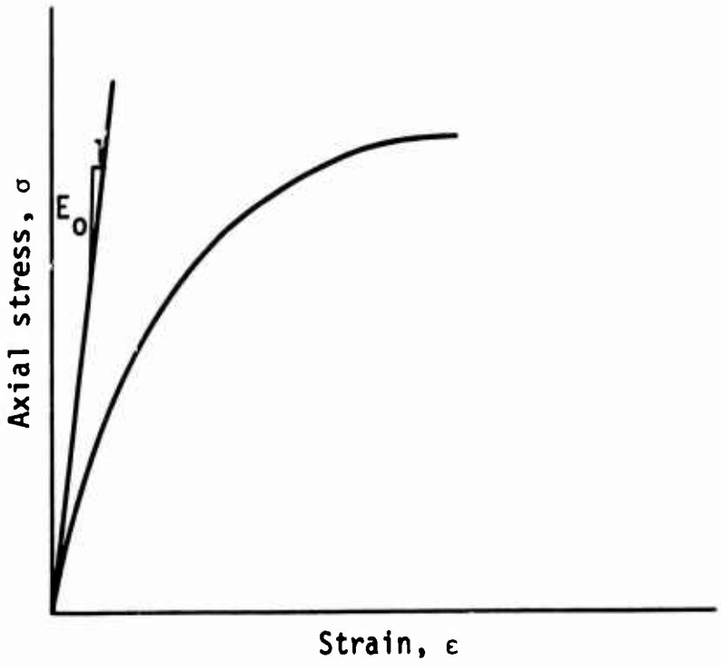

Figure 7. Near-zero parameters

relationship between the seismic modulus and the stress-strain curve. In other words, it may be incorrect to specify the constitutive properties by a single initial-tangent seismic modulus. Seismic parameters will be further discussed in the explanatory material and descriptions of experimental work below.

e. Unloading Waves.

Thus far the effects of an unloading plastic wave have not been discussed because they are not directly pertinent to this study. For completeness, however, a brief discussion is included here. Kolsky (Ref. 3) has given a particularly clear treatment of the subject.

Figure 8 shows the complete loading-unloading stress-strain curve for a plastic material. Recalling the general principle developed above that each stress level in a plastic wave travels at a velocity dictated by the tangent modulus at that stress, and noting that the slope of the unloading portion of the curve is steeper than the loading portion, it is obvious that an unloading wave travels faster than a loading wave; therefore an unloading front must sooner or later overtake a loading front. Because the loading and unloading fronts are generating different particle velocities, when the unloading front overtakes the loading front, it is reflected back into itself, and the loading front continues. This is the phenomenon of internal reflection.

The conclusions to be drawn are: (1) internal reflections can lead to grossly nonuniform strain patterns due to the high stresses induced during reflection; (2) even for a strain-rate-insensitive material, unloading and internal reflection can grossly complicate an experimental problem and can mask fundamental conclusions; and (3) for strain-rate-sensitive materials the problem becomes extremely complicated by internal reflection. One is led to conclude, therefore, that for initial, fundamental, phenomenological experimental studies infinitely long stress pulses should be used to avoid internal reflections. In fact, the early literature contains examples of tenuous or even incorrect conclusions drawn from experimental data (on simple materials, such as metals) in which the effects of internal reflection were not realized.

4. Wave Propagation in Soil Masses.

a. Elements of Seismology.

The one area of soil dynamics that has received a great deal of attention is that in which the stress excursions are exceedingly small, at *seismic* levels. This area has been popular because the relatively direct and well-developed

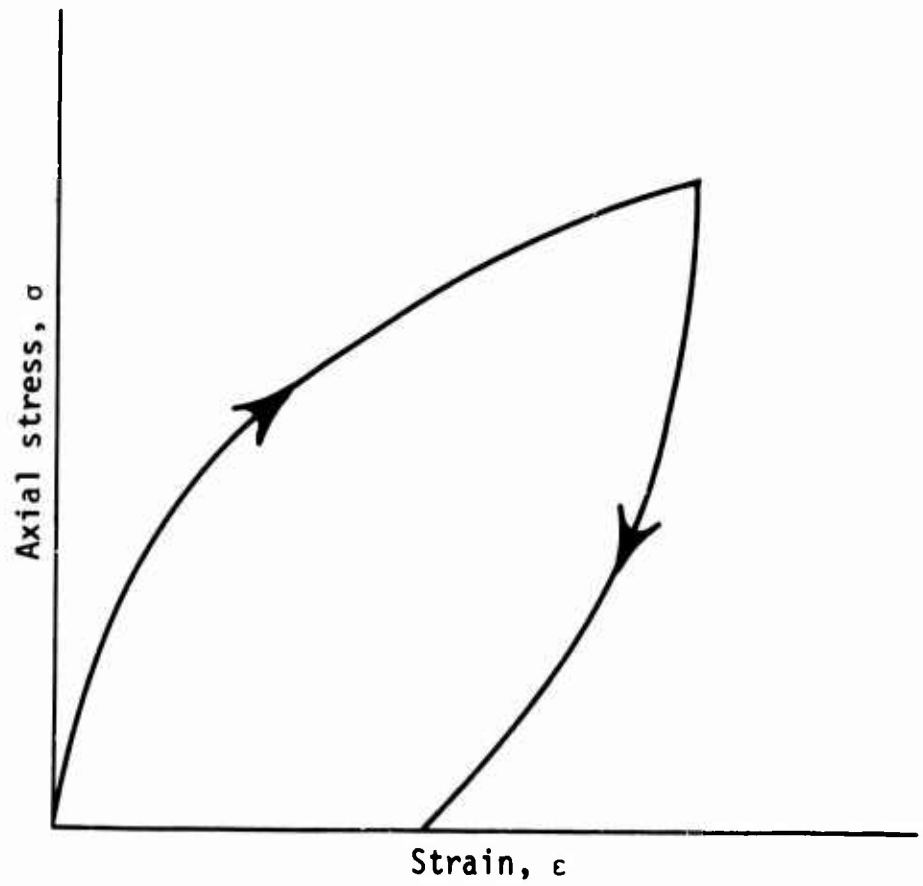

Figure 8. Plastic loading-unloading curve

theory of three-dimensional elastic waves, termed *seismology*, is available. The developed theory is well covered in the references (e.g., Refs. 10,11,12). In this subsection only a brief review will be given for continuity with the material to follow.

For all ideal elastic assumptions it is possible to derive a wave equation that can be separated into two decoupled wave equations, which show that there must exist in the body of an elastic mass two *body waves:* (1) the *dilatational* or P-wave, in which the particle motion is in the direction of propagation; and (2) *shear* or S-waves, in which the particle motion is transverse to the direction of propagation. Decoupling of the wave equation is the result of the assumed linear constitutive nature of the material; therefore the two waves travel at velocities which depend on those linear properties

$$c_d = \frac{M}{\rho} = \frac{E}{\rho} \frac{(1 - \nu)}{(1 - 2\nu)(1 + \nu)} \tag{26}$$

$$c_s = \frac{G}{\rho} \tag{27}$$

where

c_d = dilatational-wave velocity

c_s = shear-wave velocity

M = constrained or dilatational modulus

G = shear modulus

These results do not necessarily apply for a nonlinear material; the existence of the shear wave cannot be demonstrated mathematically for such materials, and the relationship between the constitutive properties and the wave velocity are not precisely derivable, except by analogy to the methods presented above.

When a body wave contacts a surface (either free or interface), the compatibility conditions at the surface must be met. These conditions require the generation of *surface waves*. Although there are many types of surface waves (Refs. 11,14), the *Rayleigh wave* is generally felt to be the most important for free-surface conditions. In the Rayleigh wave the particle motion is in the form of an ellipse whose plane is perpendicular to the surface and whose minor axis is along the direction of propagation. The P- and S-waves are body waves, but can travel along the surface, and the R-wave is a surface wave that decays in amplitude with depth. Each of the waves travels at a specific velocity, governed only by the assumed linear properties of the medium. The P-wave travels the fastest, and the S- and the R-waves travel slower and at almost the same velocity.

b. Low-Stress, Steady-State Problems.

These problems are concerned with estimating the response and frequency of vibrating massive foundations, such as machinery pedestals, radar towers, and stable tables; in these cases the vibratory stress excursion must be small. This class of problem is idealized to the vibration of a plate on an elastic half-space. The idealized problem was first solved by Eric Reissner, whose results were corrected and extended by T. Y. Sung (Ref. 17). Sung's results were later extended and put into engineering form by Richart (Ref. 18), and were simplified to the well-known forms of finite-degree vibration by Hsieh (Ref. 19). The theory and practice have been developed to the point that text and reference books have been written (Refs. 20,21,22).

By utilizing this elastic theory, reasonable solutions can be obtained for this class of engineering problem. The interpretation of the solution is a different matter; the engineer must assess the limitations of the solution on the basis of his experience, but such experience is usually quite limited. Considerable research in this area is underway (Refs. 23,24).

The two most obvious general limitations on the method are the range of stress excursion permissible and the validity of the constants used in the computations. Studies of the latter have led to some rather interesting field and laboratory wave-propagation experiments.

Although some field experiments have been performed to delineate the fundamentals of foundation vibrations (Refs. 22,20,24), most field experiments have been designed to determine the elastic soil constants. The simplest approach utilizes Eqs. (26) and (27): a disturbance (e.g., a blast) is created at a known distance from a set of kinematic instruments (seismometers), and the arrival time of the P- and S-waves are used to compute c_d and c_s. The equations are then solved simultaneously with the relation $E = 2(1 + \nu)G$ to arrive at any convenient set of elastic constants. This method, though simple in approach, is difficult in practice and is little used for two reasons: the S-wave signal arrives after the P-wave signal and is often lost in the swarm of the P-wave signal; and most sites are layered, with the result that reflections from underlying layers may completely obscure the S-wave.

For these reasons the following somewhat more complicated method is practiced: c_d is measured from a dynamite test as described above, and Rayleigh waves are created by driving a vibrator at the surface. Then, taking advantage of the known theoretical relationship between the Rayleigh and shear velocities, the elastic constants are computed. The theory has been described by Jones (Ref. 25), and the field techniques and equipment are discussed in the literature (Refs. 26,27,28,29). The field methods cannot, however, be used to predict soil behavior under changed conditions of loading or drainage. For these and other reasons laboratory experiments have been performed which have brought to light some fundamental dynamic soil properties, to be discussed further.

c. High-Stress Problems.

In this class are included the engineering problems associated with nuclear blasts. Because of the large area and depths loaded by such blasts (Ref. 30), for tractability the problem is often simplified to the one-dimensional case. In this case the constrained constitutive relationship must be assumed. The problem is to predict the time history of motion of a surface or subsurface structure and the loadings to be felt by the structure. The approach to the problem is rather imperfectly developed; the constitutive parameters presently used in the predictions are soil density, seismic velocity, and constrained modulus

(Refs. 15,16); the equations used are semi-empirical, based on scaled results of field tests under severely limited soil conditions. The logical extension of the present study would be a parallel fundamental study of wave propagation in the constrained case.

Engineering problems in this high-stress class are also associated with the propagation of earthquake waves, with waves at great distances from a nuclear blast, and with initial times at shorter distances from a nuclear blast. In these cases the problem is taken as two-dimensional. Although data are lacking, there are reasons to believe that these problems can be handled to engineering accuracy by use of the accepted soil mechanics methods of analysis based on constitutive parameters from unconstrained or plane-strain tests. Although earthquake problems are usually handled by elastic theory, efforts are made by engineers and seismologists to account more accurately for the plastic and dynamic properties of the soil materials.

5. Dynamic Properties of Sand

All tests to determine the high-stress dynamic properties of soils have been conducted under *transient* loadings; that is, a single load that may or may not cause failure and that may or may not unload the sample is applied. There is recent evidence that the conclusions drawn from such tests may be quite misleading for oscillatory high-stress loadings, such as those resulting from earthquakes and from outrunning or direct-induced ground motions caused by nuclear explosions.

High-stress tests have usually been conducted on a cylindrical specimen of soil. The load is created by a piston either pushing on or impacting onto one end of the sample. Stress is computed by measuring the load at one or both ends of the specimen and dividing the measured load by the specimen area on the assumption of *uniform stress*. This assumption requires that the loading be slow enough so that lateral-inertia effects are not appreciable. In other words, the rise time of a pulse should be greater than $2d/3c_o$ from Eq. (25). It should be noted that this requirement is a function only of the *diameter* of the specimen.

Strain is computed by measuring the change in length of the specimen and then dividing the change by the original length on the assumption of *uniform*

strain. This assumption requires that the specimen be short enough so that any one increment of stress or strain travels back and forth through the specimen many times during the test. A rule often used is that the wave should travel through the specimen about 10 times during the test. Note that this requirement is a function only of the *length* of the specimen.

The dynamic properties of *dry sands* under high-stress transient loadings have been reported by Casagrande and Shannon (Ref. 31), Taylor and Whitman (Refs. 32,33), Whitman (Ref. 34), and Whitman and Healy (Refs. 35,36,37). A particularly good summary is given in Ref. 37. Figure 9 summarizes the known facts about the behavior of dry sands. As shown in Figure 9a, the stiffness is essentially unchanged, and the strength may increase from 5 to as much as 20 percent between slow (usual static) and fast (with no wave-propagation effects) strain rates. These conclusions are sharpened by Figure 9b (Ref. 37). As a general rule, for all sands tested there was no strain-rate effect until the strain rate reached perhaps 5 percent per second. Above this rate the strain-rate effect caused an increase in strength of perhaps 5 to 20 percent for strain rates up to about 700 percent per second, at which point wave-propagation effects began to appear. Data from all investigations showed scatters as great as or greater than the reported effect of 5 to 20 percent. The conclusions drawn were, therefore, the result of the averaging of many tests. It is interesting to note that although a strict interpretation of the averaging would indicate a slight *decrease* in strength in the strain-rate range from static to 5 percent per second, this decrease is not shown in Figure 9b.

In understanding the behavior of *saturated sands*, it is helpful to be able to measure the pore water pressures in the specimen during the dynamic test. For this reason dynamic pore pressure gages have been developed (Refs. 32,33,38,39,40). Seed and Lundgren (Ref. 41) have studied the dynamic behavior of saturated sands by performing a detailed and careful study of the effects of drainage in a static test (effective stresses) compared with the effect of nondrainage in static tests (total stresses), and by comparing these results with dynamic tests in which, as a practical matter, no drainage could occur.

The typical behavior of a dense, saturated sand is as follows: at low-strain rates the pore pressure decreases as *dilation* proceeds; finally the water fails in tension or *cavitates*; the (deviator) stress-strain curve shows a stiffening at low strains, but the curve breaks rapidly when the cavitation occurs. The same general pattern is evident at high-strain rates, except that the

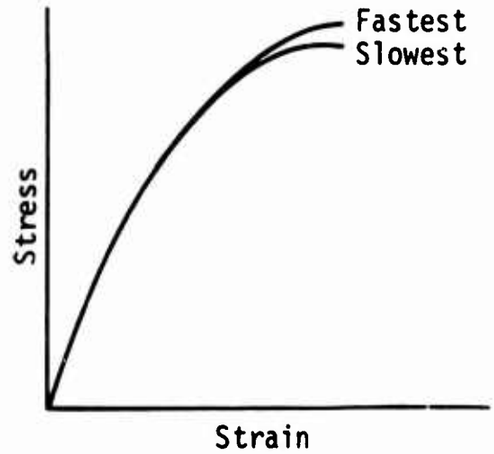

(a) Influence of rate of loading on stress-strain curve

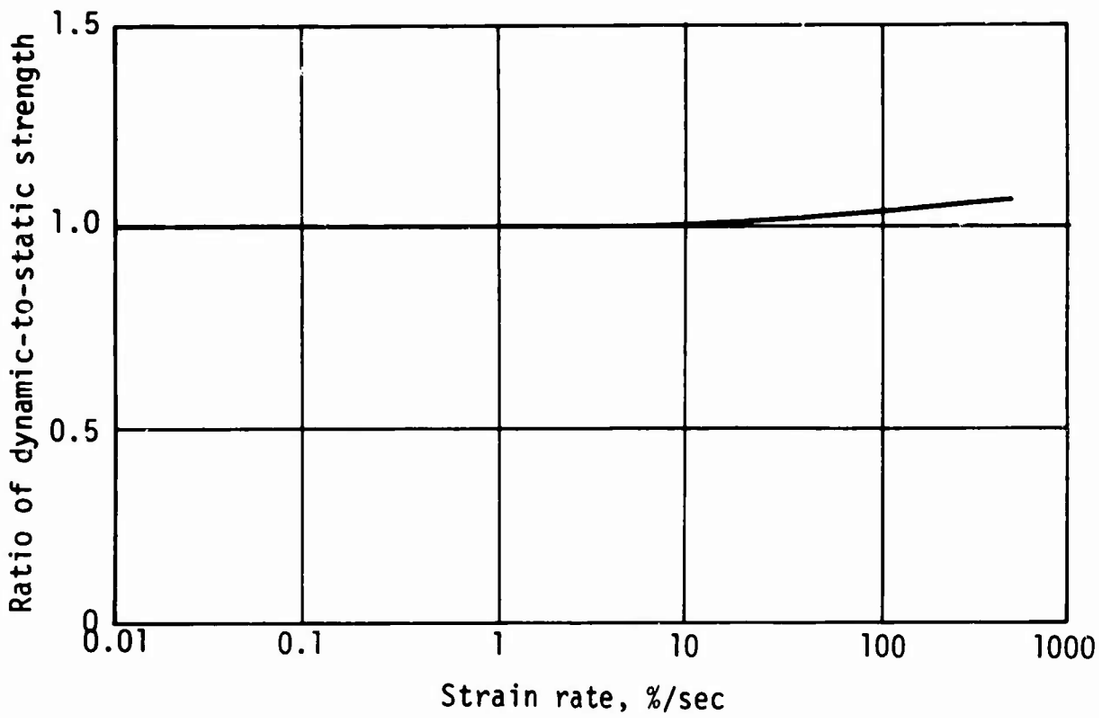

(b) Relationship between strain rate and strength

Figure 9. Strain-rate effect for dry sands

cavitation may occur at a slightly higher strain. The fact that cavitation occurs allows the computation of the dynamic strength of a saturated sand. Since the pore pressure is a known value (the cavitation pressure), the effective stresses can be computed. The known, small, strain-rate effect can be applied to these stresses to compute the strength increase. Loose saturated sands tend to compress at low strains and to dilate slightly at high strains; therefore loose sands appear to become stronger and stiffer when dynamically loaded.

Detailed studies under transient loadings have been conducted (Refs. 42,43,44) to verify the same behavioral patterns for other cohesionless soils. The results may be summarized by noting that the high *apparent* strain-rate effect in saturated sands is caused by the fact that since the soil cannot drain in a dynamic test, pore pressures develop. Because most sands dilate at realistic void ratios, the developed pore pressures are negative, leading to higher strengths. The true strain-rate effect (on effective stresses) is the same (5 to 20 percent) as in the dry sand. The *apparent* strain-rate effects in saturated sands are greater for loose sands because of the near equality of the strength and the cavitation pressure for these weak materials.

6. Previous Unconstrained Wave-Propagation Experiments on Sands.

a. Steady-State Vibration.

It is fundamental to this type of test that the *stress excursions* must be exceedingly small, even though the state of stress may have an appreciable value. All idealized elastic assumptions are made, with these resulting simplifications: tests may be designed on the assumption of simple linear response, and all the *elastic parameters* (constants) may be computed if any two can be determined experimentally. The basic variables to be studied are the *condition* of the soil and the *state of stress* as they affect the elastic constants. For a given sand the condition is completely controlled by the density and (to a lesser degree) the degree of saturation. The state of stress can be simplified for the unconstrained case to the combination of the triaxial ambient and deviator stress. For the results to be reviewed below, the soil conditions and states of stress are rather restricted; the density has been varied, but only the completely dry and the completely saturated states have been studied; and only isotropic (i.e., ambient stress only, with no deviator) states of stress have been studied for the unconstrained geometry. Within this limited framework some interesting experiments have been designed, and some very useful data have been obtained.

The key to all the low-stress testing equipment is that only two elastic parameters have to be measured. In the unconstrained geometry the two parameters usually measured are the axial and torsional natural frequencies of a rod of the soil. From these two frequencies the Young's modulus and the shear modulus, respectively, are computed from elementary dynamics (Ref. 45). For a sensible range of soil properties and a long specimen with low-resonant frequencies, it can be shown (Ref. 46) that the effects of dispersion are negligible. Thus the major problem is to design testing equipment that will not have spurious resonances in the range of frequencies to be measured. This problem has proved to be formidable.

One approach, taken by Wilson (Refs. 46,47), is to place the specimen on a vibrating table (which is, in fact, a thick circular plate fixed at its edges) and to vary the frequency until maximum response is achieved at the top of the specimen. The table is driven in the axial and torsional modes by separate loudspeakers. The table is the base of a triaxial cell into which ambient pressure may be introduced as a controlled variable. The test method presents theoretical difficulties because neither end of the sample is truly fixed nor free. Since, however, the amplitudes at the top are large compared with the input amplitudes at the bottom, the error involved in assuming complete fixity at the bottom is probably small for all but the most rigid of soils, and the values obtained are generally felt to be adequate for engineering. The device is designed for soil samples of usual sizes, and has been used a great deal for pertinent engineering problems.

In another approach, taken by Richart and his associates (Refs. 18,48,49), the base of the specimen is truly fixed, and the driving and response measurements are both accomplished at the top, which is taken to be free. The specimen is long and thin, in contrast to the normal geometry of soil samples. The setup is placed inside a special triaxial cell so that the ambient pressure may be controlled. This device has proved to be a powerful research tool; many of the data to be presented were obtained in it.

Note that both of the devices described depend on placing a specimen into axial and torsional resonance, and that owing to the nature of the test the effects of deviator stress cannot be studied.

By using the mathematical model of a close packing of elastic spheres, it has been demonstrated (Refs. 49,50,51,52, and references therein) that there

should be a 1/6-power relationship between wave velocity and ambient stress. While such an idealized relationship is not expected to exist for soils, the theoretical result does indicate that some approximate power relationship between wave velocity (or modulus) and ambient stress may exist; this conclusion is borne out by experimental data.

Figure 10 shows an envelope of the data for dry 20-30 Ottawa sand from the work of Richart and his associates (Refs. 48,49). The results show that for both shear and compression waves the velocity increases with increasing ambient stress and with increasing density, and that the relationship between wave velocity and ambient stress is close to a power function. Richart also demonstrated (Ref. 49) that for a given ambient stress and for a limited range of densities the relationship between wave velocity and density for the 20-30 Ottawa sand is essentially linear (Fig. 11). On the basis of Richart's demonstration the data in Figure 10 have been used to construct the curves shown in Figure 11, to which reference will be made when the experimental data are discussed. These

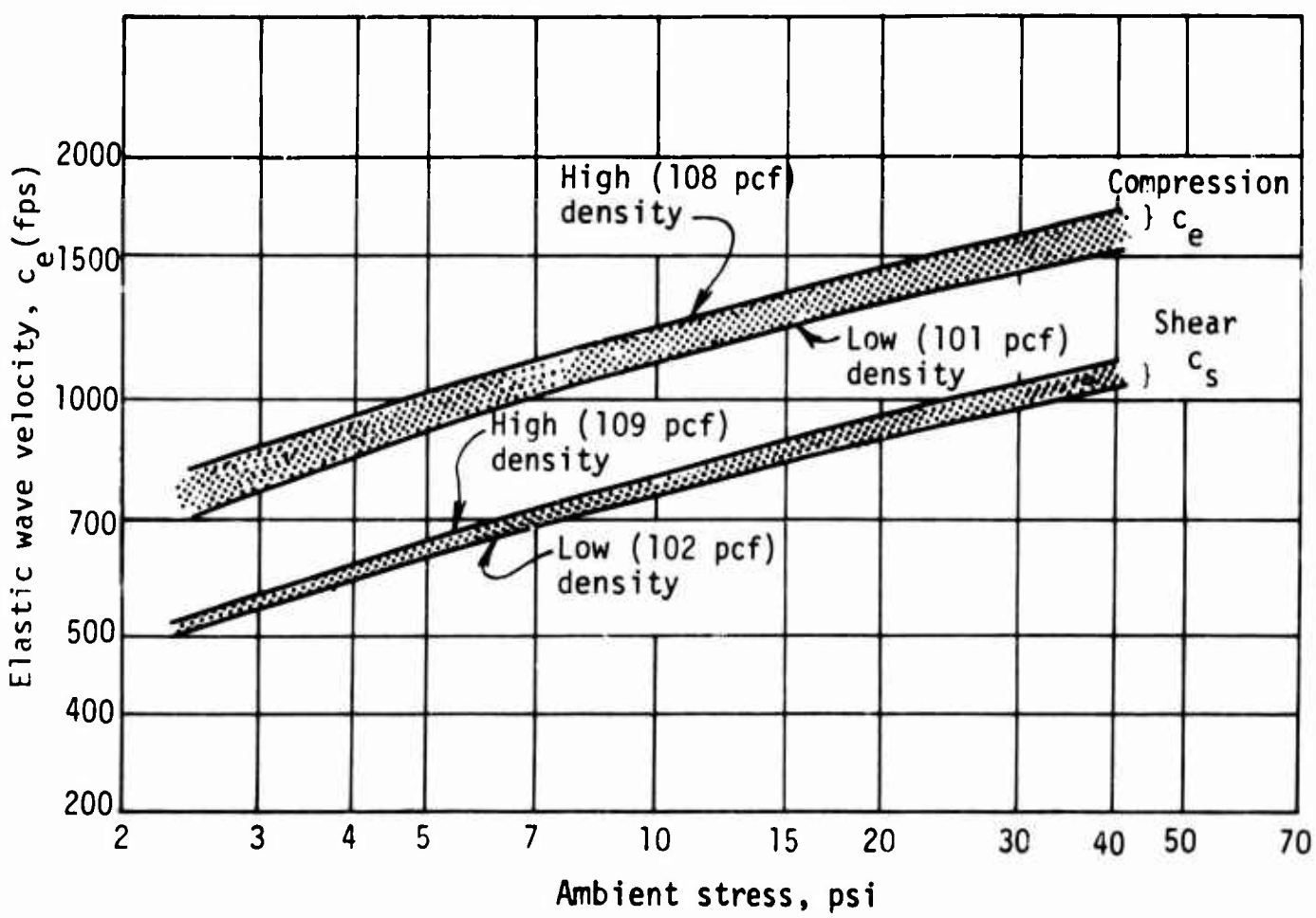

Figure 10. Wave velocities in dry 20-30 Ottawa sand (Ref. 49)

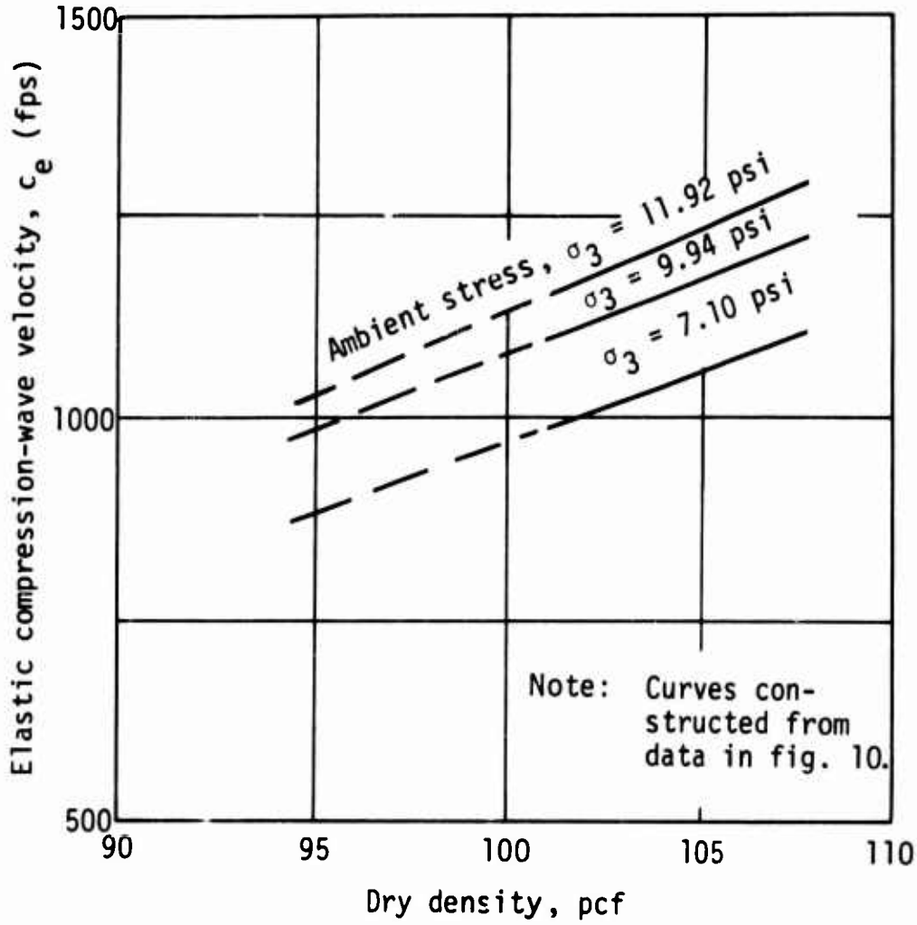

Figure 11. Velocity-density relationships for dry 20-30 Ottawa sand at selected ambient stresses

curves allow one to estimate the seismic-wave velocity in this sand at a given condition (density) and a given state of stress (ambient only).

Wave propagation in saturated sands is complicated by the waves carried in the water. Experimental data show that the wave velocity in a saturated sand is slightly less (up to 15 percent) than in a dry sand, presumably because of the increased mass and the small reduction in stiffness of the sand caused by the wetting (Ref. 49).

Experiments (Ref. 48) have shown that as the strain excursion is increased from a small value, the wave velocity decreases and the hysteretic damping increases. The decrease in wave velocity follows directly from the usual shape of the unconstrained stress-strain curve (Fig. 1), according to the principles expressed in Eq. (12). By hysteretic damping is meant that the nonlinearities of the soil are becoming important and simple elastic approaches are of decreasing validity.

b. Transient Loadings.

Pioneering efforts in transient wave propagation were done in the early 1950's at the Massachusetts Institute of Technology (MIT) under the direction of D. W. Taylor (Refs. 32,33), and R. V. Whitman (Ref. 34). The tests were performed on 2-inch-diameter specimens of dry 20-30 Ottawa sand in lengths from 7 to 32 inches. The initial condition of the sand and the state of stress were the same in all tests, a density of 108-109 pcf and a vacuum-induced ambient stress of 14 psi.

The specimens were suspended by gravity in cellophane slings inside a specially built triaxial cell. Thus support was provided only against downward lateral motions; and horizontal and vertical upward lateral motions (instabilities) were possible during the tests. For this reason inverted slings were provided in later tests. The input wave was created by releasing a spring-loaded mass so that it could impact a loading piston in contact with the end of the specimen. The reaction end of the specimen butted against an essentially rigid spacer. Three types of measurements were made during the test: (1) stress at the impact and reaction ends; (2) motion of the impacted end; and (3) strain within the specimen near the impact ends.

The stress gages were total-load gages, for which stress could be computed on the assumption of uniform stress. They worked by communicating the stress from the specimen through a thin membrane into a sealed, thin, oil-filled chamber. The back side of the chamber was a plate, instrumented with wire strain gages; the pressure generated in the oil caused the back to deflect, yielding an output from the strain gages. The gage was reported to have a natural frequency of 8 kilocycles (kc) but to be somewhat less sensitive than desirable and presumably was linear. The motion of the impacted end was measured with a linear variable differential transformer (LVDT). Transverse core motions were presumably minimized by fixing the core on a long shaft connected directly to the massive loading head. The internal strain gages were made by gluing sand to ordinary wire strain gages. In static triaxial proof tests these gages yielded a constant ratio to the externally recorded strains up to a strain of about 0.4 percent, above which the ratio became smaller, approaching zero. Owing to lack of time these gages and the way in which they are used could not be fully exploited. All readout was taken by photographing the traces on oscilloscope screens; nonlinearities and drift in the traces caused some uncertainty in the data.

Regardless of the impact velocity, the velocity of the first (near-seismic) arrival was a constant at about 1,300 fps. Reference to Richart's data in Figure 10 shows precise agreement. From static triaxial tests the compressive strength of the sand was estimated to be 28 psi. The measured stress at the impact end, however, showed pronounced initial spikes, which ranged from about 20 psi at low-impact velocities (15 ips) to about 90 psi at high-impact velocities (90 ips). The existence of these stresses in excess of the failure strength has been explained by the authors (Ref. 34) as a hypersensitivity to lateral inertia, by Smith and Newmark (Ref. 53) as a lateral-inertia effect, and by Parkin (Refs. 54,55,56) as a strain-rate sensitivity according to Malvern's law (Ref. 57). As pointed out by Whitman in his discussion in Refs. 55 and 56, the latter may be a rather unlikely explanation in view of the known small strain-rate sensitivity of this sand. After the initial peak the load decayed to essentially the compressive strength, or the buckling strength for longer specimens that buckled. The reaction end did not in any case show the peak like the impact end; instead, the stress at the reaction end built up slowly, showing that the wavefront had softened during its propagation. Owing to the short length of the specimens the serious reflection returns allowed study only of the initial front. The internal strain-gage readings showed an almost linear buildup to a maximum value, which then held constant. The impact-end particle velocity was continually decreasing during this time. Thus the strain versus particle-velocity relationship would have a negative slope, an impossible result for the unconstrained configuration.

This result leads to one or two possible conclusions: (1) the impact end, on account of lateral-inertia hypersensitivity, was constrained throughout a great deal of the test; and (2) the peaked stress wave had attenuated between the impact end and the strain gage (a distance of 6 to 9 inches). Of the two, the second conclusion seems the more likely, as was borne out by some very approximate computations using a simple viscoelastic model (Ref. 34); the impact-stress peak, if caused by lateral inertia, should have attenuated within a nominal distance of 6 inches. In the study of the data the authors (Ref. 34) assumed perfect elastic-rigid reflection, with the result that the reaction gage was taken to read twice the incident stress. The authors recognized that for longer specimens the chances of a vagrant inclusion or pocket of looser material are substantially greater than for a short specimen.

An extension of the MIT work recently undertaken by Selig (Ref. 58) at the Illinois Institute of Technology (IIT). Selig's experiments were similar to the MIT experiments with the exception that loading was accomplished by air-shock blast from a shock tube; stresses inside the specimen were measured with nonlinear but calibrated piezoelectric gages; the specimen was 2.8 inches in diameter and 64 inches long; and the material was a 20-40 Ottawa sand. Prior to the wave-propagation tests some dynamic, vacuum triaxial tests were performed to determine the strain-rate sensitivity of the material. These tests showed strain-rate sensitivities as high as 25 percent, but the author felt that in view of the data scatter only 10 percent was justified. In order to reduce wave-propagation effects, the specimens were somewhat short compared with their diameter (4:2.8, L/D = 1.43, cf. usual value of 7.5). When assembled and in the testing apparatus, each wave-propagation specimen was subjected to a number of tests at different ambient stresses and different shock inputs. The first loading was either a static load or low-stress shock in order to calibrate the stress gages. For the subsequent multiple wave-propagation tests the ambient stress, peak-shock pressure, and positive-phase duration were varied. It was not possible to evaluate the changes in the condition of the specimen from test to test.

It was found that the input shock front lost its zero-rise characteristic by the time it reached the first stress gage, 8 inches inside the specimen, and that considerable softening of the front and degradation of the stress amplitude occurred with further propagation. These effects were most pronounced for low-ambient stresses and low densities. Even though the specimens must have densified and stiffened under the multiple impacts, Selig found that the first-arrival (seismic) wave velocity did not change substantially. The results agree quite well with those plotted in Figure 10. The disagreements usually showed Selig's values to be the higher, presumably because of evanescence from the dilatational velocity initially induced by the shock input. By performing several cycles of static loading, it was found that an initial tangent modulus could be used which would predict the wavefront velocities according to Eq. (19). Selig analyzed his data by using position-time plots such as Heierli (Ref. 59) had previously used for the analysis of constrained experiments.

c. Discussion of Previous Work.

The MIT and IIT projects were both admirably performed pioneering efforts in an admittedly difficult experimental and theoretical area. The results demonstrated several important facts to guide future research. These facts

will be reviewed as they pertain to this research. The theory of strain-rate-insensitive plastic materials gives reasonable quantitative and qualitative agreement (Refs. 58,59). Guided by these previous efforts, a portion of the present effort has been devoted to extending the theory of plastic waves for strain-rate-insensitive materials for much simpler analyses under limited conditions. This is done in Section III.

Both of the efforts described utilized a sharp-fronted input pulse, velocity in the MIT work and stress in the IIT work. From the theoretical results shown in Figure 3 it is apparent that the wave velocities and (more important) the stress and strain distributions are not uniform for a sharp-fronted pulse. In fact, recent theoretical studies (Ref. 4) show that the distortions of sharp-fronted pulses may be even worse than those indicated by the figure. Thus the analysis of such results, based on plastic theory which presupposes plane sections, cannot be expected to show precise agreement.

In addition, the hypersensitivity of a sand to lateral-inertia effects must be considered: if under a sharp impact the sand cannot expand laterally in phase with its axial deformations, then the inertia of the lateral expansion has the effect of creating an additional ambient stress on the sand specimen. The existence of such an effect was brought out most clearly in the MIT experiments, where although the measured impact stresses exceeded the strength (at the nominal ambient stress) by three times, failures apparently did not occur until late in the event. Both projects also included unloading waves, which obscured the front, led to peak-stress attenuations, and generally made the final results difficult to analyze. For these reasons it was decided to use a soft-fronted, loading-only pulse in the experiments for this report.

Both projects relied on stress measurements rather than kinematic measurements (exception: the pilot MIT work with the internally embedded strain gage). As a result of his careful study and extensive development work Selig (Ref. 58) determined that stress gages in soils would be nonlinear even under restricted conditions. By judicious interpretations of his stress-gage data Selig was able to study the phenomenon, but in neither the MIT nor the IIT effort was the entire wave-propagation event able to be related to the basic constitutive properties of the material; therefore the theoretical and experimental efforts of this project were designed to make this relationship apparent.

These combined conditions have led to a certain direction for the theoretical developments and experimental work to be undertaken: (1) the analysis should be on the basis of plastic theory; (2) the input pulse should be soft fronted and should contain no unloading so that basic wave-propagation phenomena can be studied; and (3) the main intelligence should come from kinematic (rather than dynamic) measurements.

SECTION III

EXTENSION OF THEORY OF PLASTIC WAVES FOR STRAIN-RATE-INSENSITIVE MATERIALS

1. Basic Concepts.

The material in this section is developed so that the same methods can be used either to compute waveform parameters from a given input and a set of constitutive properties or to compute the input and constitutive properties from a set of measurements of waveform parameters. The effects of dispersion will be ignored, plastic behavior will be assumed, and only loading waves will be considered. Within these three limitations some very powerful analytical tools can be developed.

The review in Section II demonstrated that a wave in a plastic material travels at a different velocity for each strain (or stress) level, and that the wave velocity for a given strain depends on the tangent modulus at that strain and the mass density according to Eq. (12). Those developments also lead to relationships involving particle velocity and the kinetic- and potential-energy densities, summarized by Eqs. (14), (15), (16), (17), and (18).

The front of the wave at near-zero strains will travel at the seismic velocity (c_o).

$$c_o = \sqrt{\frac{E_o}{\rho}} \tag{28}$$

For a sand, the near-zero strain seismic modulus (E_o) will depend on the density and ambient stress (Figs. 10,11). If the modulus and the mass density are known, the front velocity c_o is computed by Eq. (28). For all soils, however, it turns out that E_o is extremely difficult to determine (Refs. 46,47,48,49), even with unusually careful and precise measurements (Ref. 60). For this reason c_o is usually determined directly by the low-stress vibration techniques described in Section II. It will therefore be assumed in the following that c_o is a known quantity. Then, for a specified constitutive relationship (mass density and stress-strain curve) the plastic-wave velocity (c_p) can be computed by Eq. (12).

By similar processes the plastic-particle velocity (v_p) is computed by Eq. (15)--once the c_p is known--and the potential- and kinetic-energy densities also follow directly. By manipulations of this type the waveform parameters can

be computed for a given input wave; and by reversing the procedure, the original constitutive relationships can be computed from given waveform parameters.

Usually, however, the pertinent functions (constitutive relationships, input, waveform parameters) are available only in the form of graphical representations, which can be handled by curve-fitting methods, or by semigraphical procedures, which can be carried out either manually or by a computer. Either approach is approximate at best; the semigraphical method has been used here and is described in the following because it leads to more physical insight into the problem.

2. Waveform Computations.

a. Computation of Waveform Parameters.

Figure 12 was prepared to illustrate the graphical adaptation of the simple procedures outlined above; in it are outlined the typical preliminary operations in preparation for computation of waveform parameters. For this and all other (soil) work to follow, the mass density is a trivial variable that will be taken as a constant in any given wave-propagation test.

Figure 12a contains the basic constitutive data, the mass density, and the stress-strain curve. By selecting an adequately fine strain mesh, the plastic modulus (E_p) can be computed as a tangent or chord slope. As a practical matter, the mesh should be chosen so that the difference between the tangent and chord slope is negligible. In this way Figure 12b of the modulus as a function of strain is constructed. The values on that plot are divided by the mass density, and the square root is taken to obtain the wave-velocity versus strain plot in Figure 12c.

By inspection of Eq. (15) it is apparent that for a strain-rate-insensitive, plastic material there must exist a unique but nonlinear relationship between particle velocity and strain. This relationship is expressed by Eq. (15) and can be obtained by integration of the wave-velocity versus strain plot, as shown in Figure 12d. Similarly, there must exist unique relationships between potential-energy density and strain, and kinetic-energy density and strain: the potential-energy density is the area under the stress-strain curve, and the kinetic-energy density depends on the square of the particle velocity. Thus these relationships can be constructed from the stress-strain curve and the particle-velocity versus strain curve, as shown in Figure 12e.

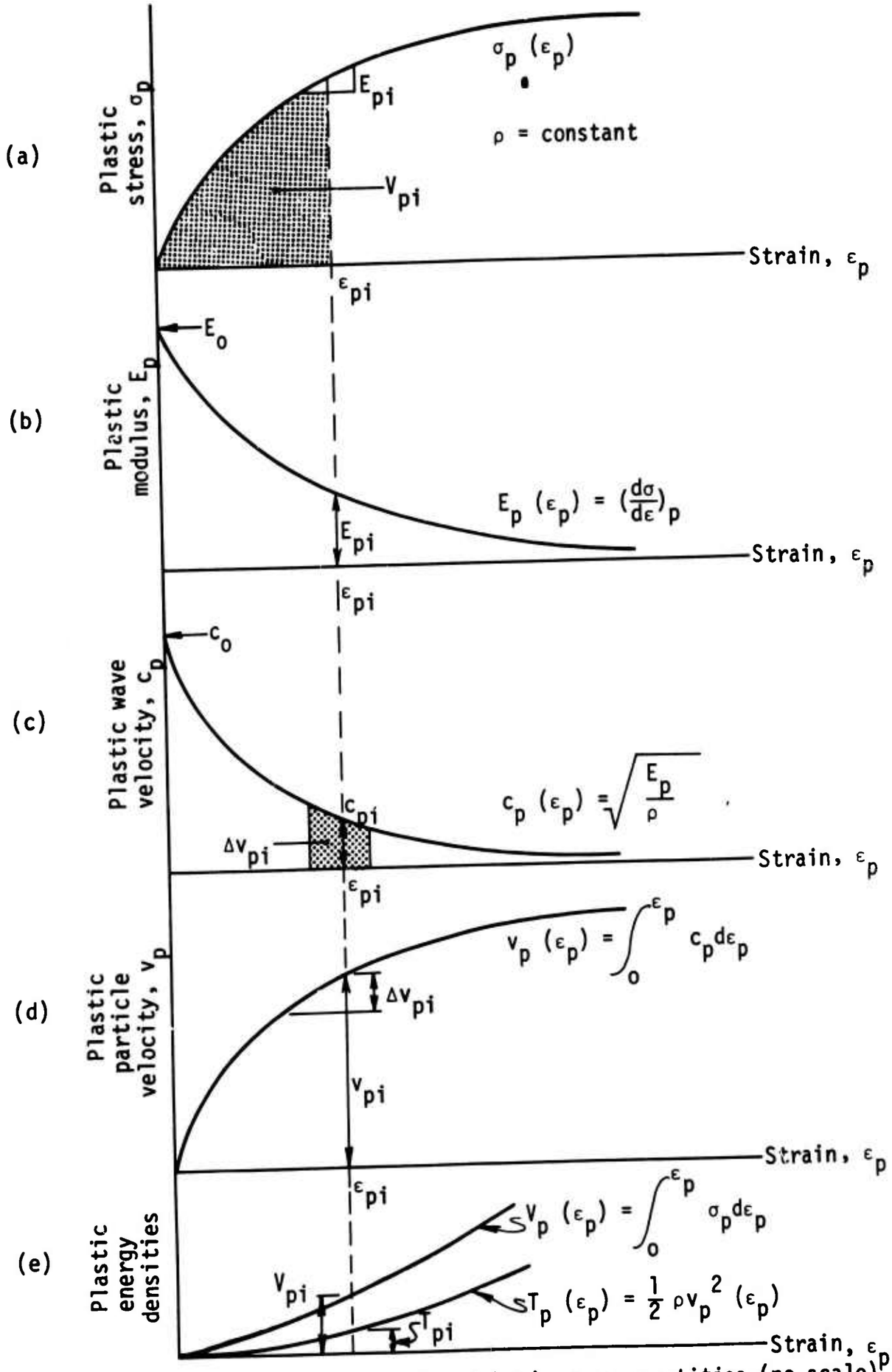

Figure 12. Initial computation of basic wave quantities (no scale)

Two obvious and significant conclusions follow directly from examination of the sketches in Figure 12: (1) wave velocity is not constant, and particle velocity and strain are not linearly related as in the elastic case; and (2) the energies are not equally partitioned as in the elastic case.

For consistency with the experimental material to follow, strain was taken as the independent variable in Figure 12. In wave-propagation problems, it is usually simpler to imagine stress as the independent variable; however, due to the uniqueness of the stress-strain curve, either stress or strain may be taken as the independent variable.

For example, Figure 13b shows a wave-velocity versus stress curve computed from the stress-strain curve shown in Figure 13a. Once this diagram has been drawn, the stress-position history can be computed for any time, and the stress-time history can be computed for any position. For example, Figure 14a shows a linearly fronted stress pulse with a maximum value of two stress units. Since the front travels with a velocity c_o from Eq. (28), at any time (t_1) the front will be at position $x_{o1} = c_o t_1$. If the time delay of input of a certain stress σ_p is Δt_w, then the position of stress σ_p at t_1 is $x_{p1} = c_p t_1 - c_w \Delta t_w$ where c_w is the velocity of the input wave. After the positions of several stress levels are computed in this way, the shape of the wave at t_1 can be sketched, as in Figure 14a. In the same way, the shapes at other times (t_2) can be computed, as shown. The result is a series of pictures of the wave in the rod at various times. If it were possible in a rod experiment simultaneously to measure the stress at many points in a rod, the resulting data would be that shown in Figure 14a. If, on the other hand, the stress at a point or points were measured as a function of time (the usual experimental condition, see Refs. 34,58), the result would be the stress-time plots of Figure 14b. These plots may be deduced either by vertical interpolation of the top sketch, or by computation of the time required for a given stress level to reach a given position (x_1) $t_{p1} = \Delta t_w + x_1/c_p$.

This discussion has been in terms of stress because stress is a simple and useful engineering concept. Since stress is, however, difficult to measure in rod wave-propagation experiments and virtually impossible to measure under any conditions in soil, a more reliable experimental procedure may be to measure either strain or displacement at a particular position as a function of time. A reverse graphical procedure for analyzing displacement- or strain-time experimental records for the computation of the stress-strain curve will be explained.

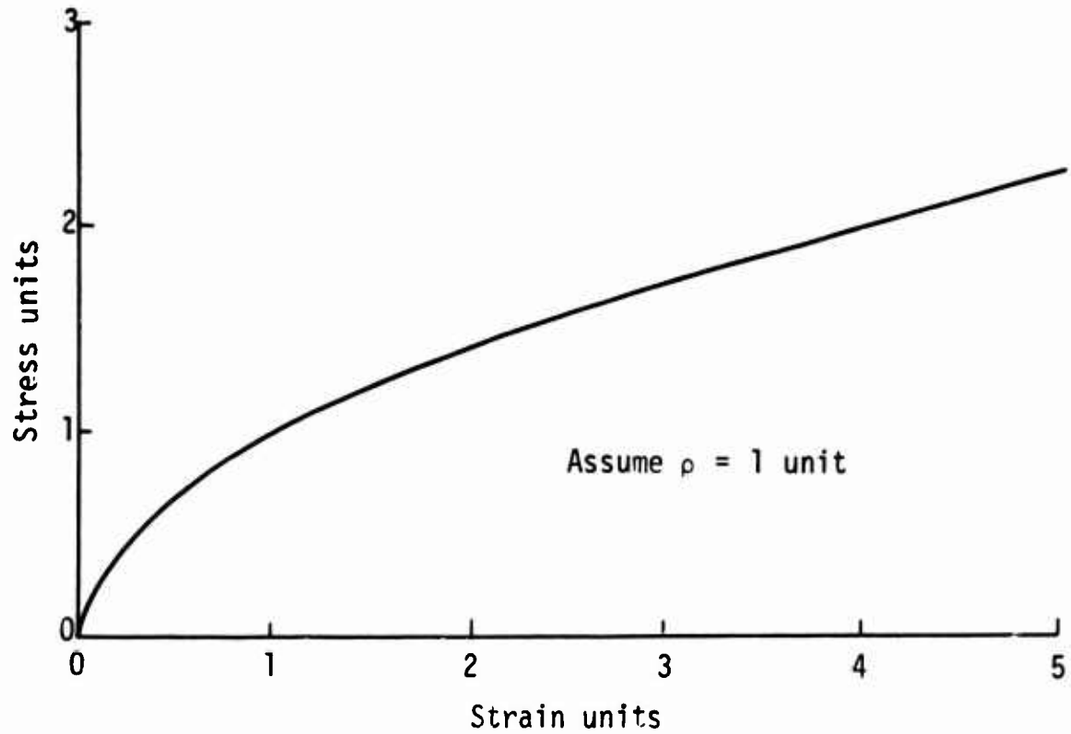

(a) Stress-strain curve

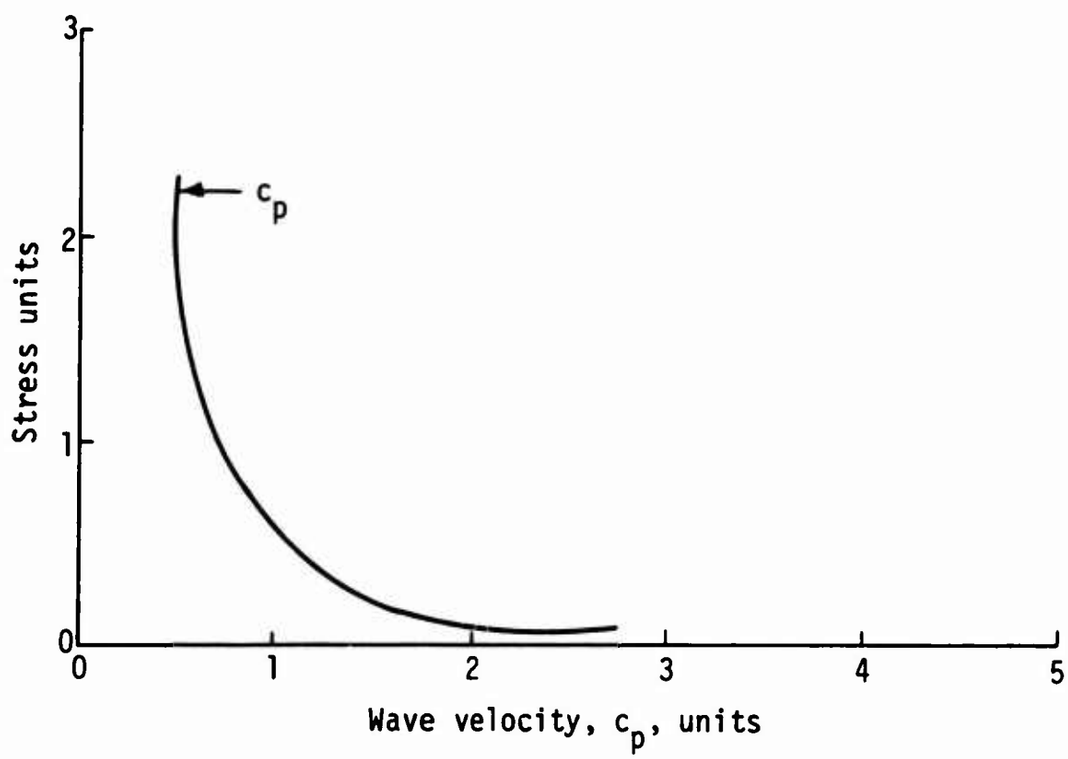

(b) Stress-wave velocity curve

Figure 13. Computation of stress-dependent basic wave quantities (sketch, no scale)

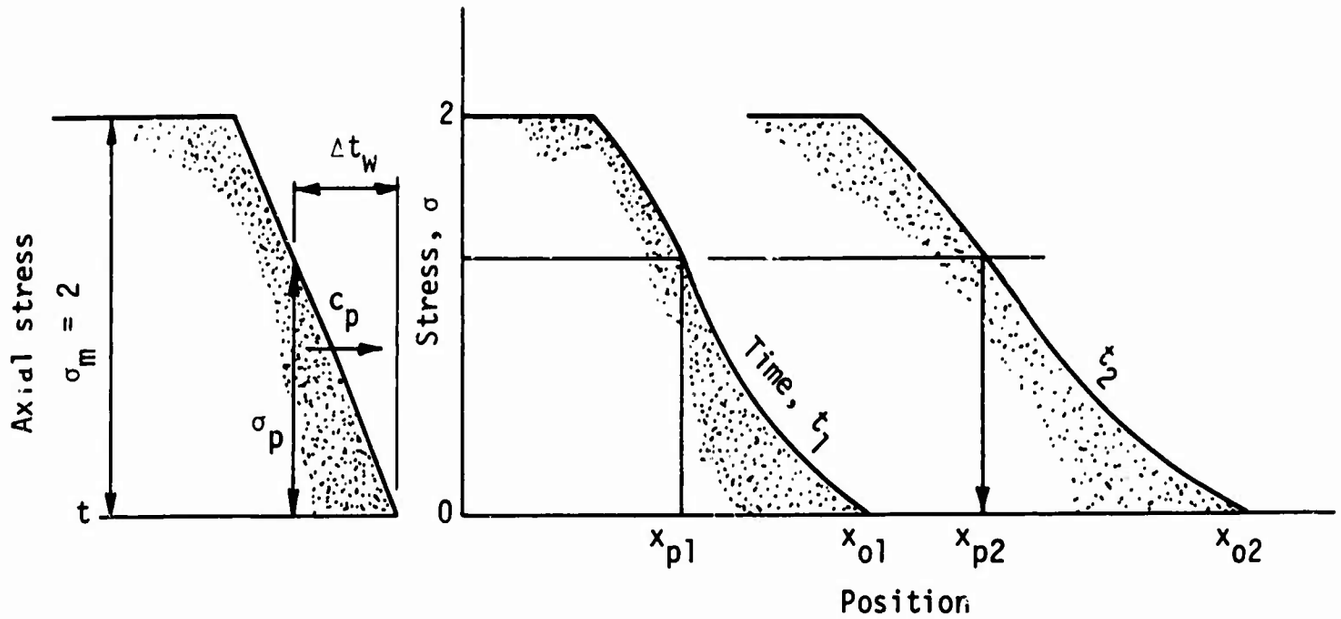

(a) Stress-position plots at different times

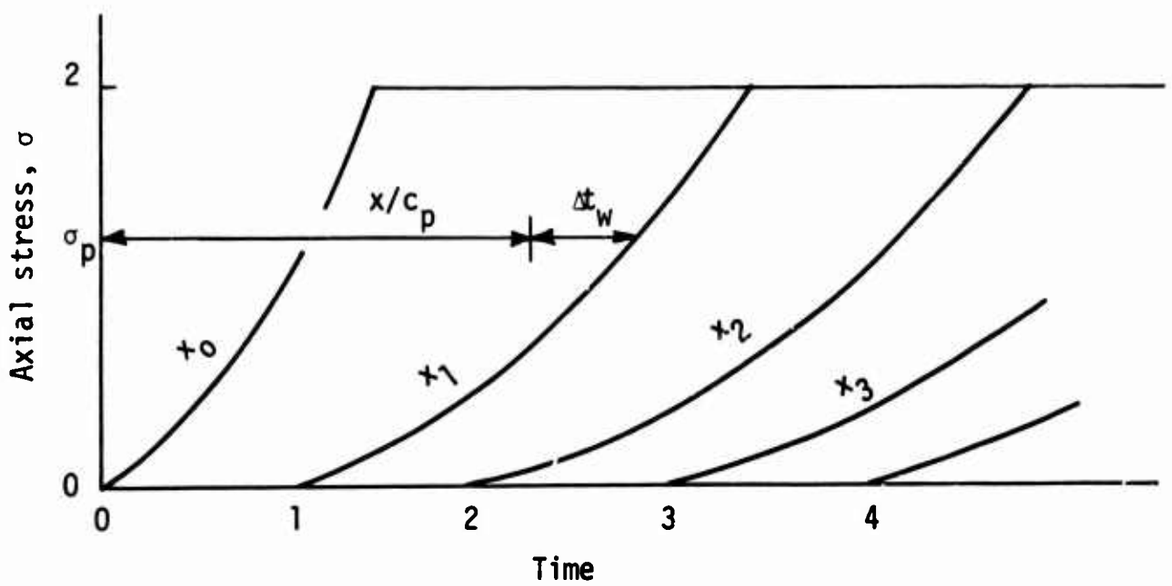

(b) Stress-time plots at different positions

Figure 14. Plastic waveforms (sketches, no scale)

Some additional concepts, however, will now be introduced. Two representations of the computed waveform are given in Figure 14: a stress-position plot, parametricized on time, and a stress-time plot, parametricized on position. Simplification can be achieved by constructing a position-time plot, parametricized on stress, as shown in Figure 15. On a position-time plot the slope of any line is, by the definition in Eq. (11), a wave velocity. For example, the line labeled *front* represents the position-time history of the near-zero seismic signal traveling at c_0. The stress value of 1/2 travels at a slower velocity, according to the construction on the figure, and therefore has a flatter slope as shown. The position-time histories of some other stress--1/2, 1, 3/2, 2--are shown, along with the slope indicating their respective velocities. The usefulness of the simple position-time plot for this strain-rate-insensitive, no-unloading case is that each stress *travels* at a constant-wave velocity, allowing the waveform to be represented in a linear form. In addition, because of the unique relationship between stress and strain it can be said that each strain travels, or is *generated*, at a constant-wave velocity. Finally, because of the unique relationship between particle velocity and strain it can also be said that each particle velocity is generated at a constant-wave velocity. Similar arguments could be made for the partitioned-energy densities.

This principle of linearity of waveform (wave velocity on a position-time plot) provides an extremely helpful and simple check on computations and graphical operations leading to construction of the waveform at a given point in space and time. It also provides a direct method for analyzing experimental data, as explained next. The method is useful, though tedious, for the analysis of unloading and reflection waves in a strain-rate-insensitive material (Ref. 58) and can be adapted to the analysis of constitutively nonunique materials by an experimental, graphic, iterative procedure (Ref. 59).

b. Simple Analysis of Kinematic Waveform Data.

In the experiments in this report displacement as a function of time as a wave passes through a rod of soil will be measured at several points along the rod. For a soft-fronted input-stress pulse with no unloading the resulting data will form a monotonically increasing smooth curve of displacement as a function of time for each position. Expected results for several positions are sketched by the heavy lines in Figure 16a. As a practical matter, these data usually contain two deficiencies: (1) the displacement measurements cannot be taken close enough together to allow accurate *strain* computations; and (2) there

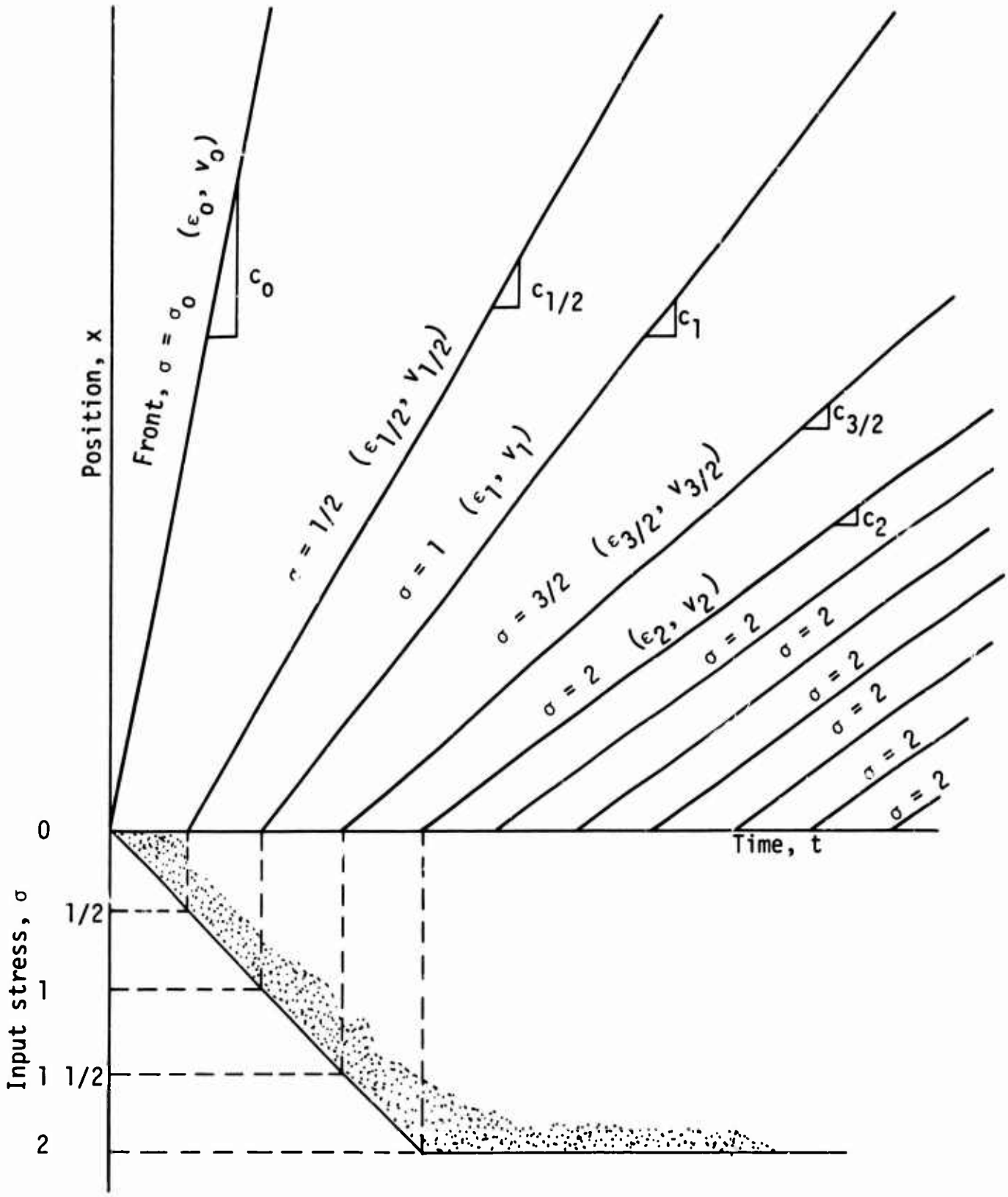

Figure 15. Interpretation of position-time plot

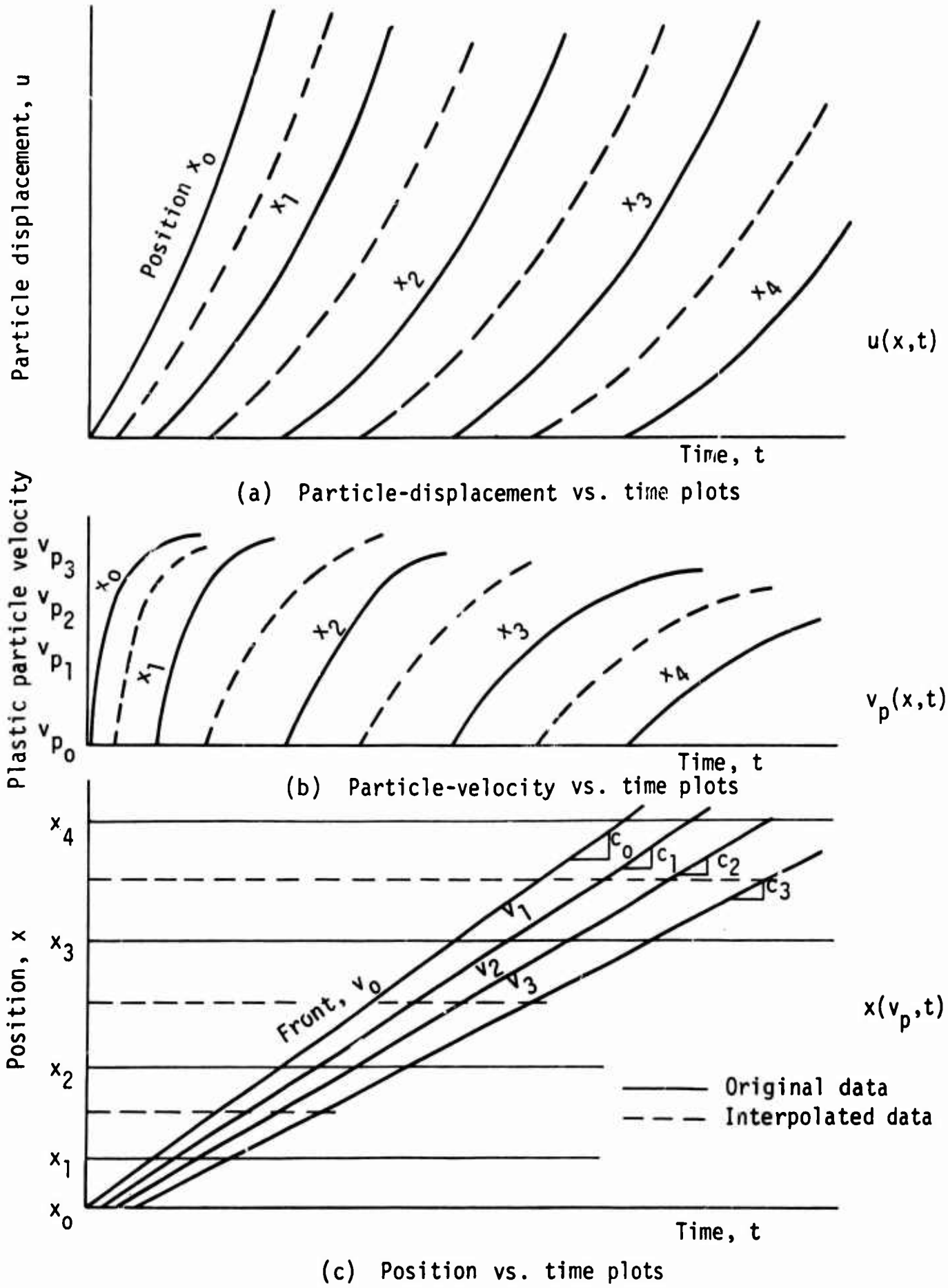

Figure 16. Preparing experimental raw data

is no guarantee that the readings are *internally consistent* (i.e., meet the combined geometric and kinematic compatibility conditions expressed by Eq. 14), because one or more gages may be reading incorrectly. The data, therefore, should be *prepared* for analysis in such a way as to yield more accurate strain computations and ensure internal consistency. Both conditions can be met by making use of the linearity of waveform quantities on a position-time plot, as will be explained.

In Figure 16 the original (heavy line) data can be differentiated to yield velocity because the curves are smooth and monotonic. The result is the particle-velocity versus time curves parametricized on position (Fig. 16b). From these curves one can find the point in position and time at which a particular particle velocity is generated; the results can be used to locate data points on the position-time plot (Fig. 16c). Then, for each v_p the slope of a best-fit straight line will yield the c_p at which each particle velocity is being generated. Each of these computed wave velocities can then be plotted as a function of its corresponding particle velocity as in Figure 17, and a best-fit smooth curve can be drawn through the resulting points.

The data on the curve (Fig. 17) may be *incorrect* owing to inaccurate gage readings, but they are at least internally consistent according to the required kinematic and geometric compatibility conditions of plastic theory for strain-rate-insensitive materials. This operation forces the data to be plastic and strain-rate insensitive, and it adjusts the data within themselves so that they are internally consistent. On the basis of the fitted curve of Figure 17, the straight lines on the position-time plot (Fig. 16c) may have to be adjusted slightly and may be augmented to gain a finer velocity-parameter mesh. That position-time plot may then be used to construct a new velocity-time plot (Fig. 16b), but with a finer position-parameter mesh (dotted lines).

These curves, in turn, may be integrated to obtain a set of displacement-time curves with a finer position-parameter mesh (Fig. 16a). These curves may now be considered as the prepared experimental data, ready for analysis. It is to be emphasized that these operations are done to obtain a finer position-parameter mesh for accurate strain computations and to ensure internal consistency of the data; the data are not forced to conform to any conditions of theory, *except* that the material be strain-rate insensitive and plastic.

With the data prepared, they may be analyzed to yield either the constitutive properties of the material or the waveform parameters in any quantity

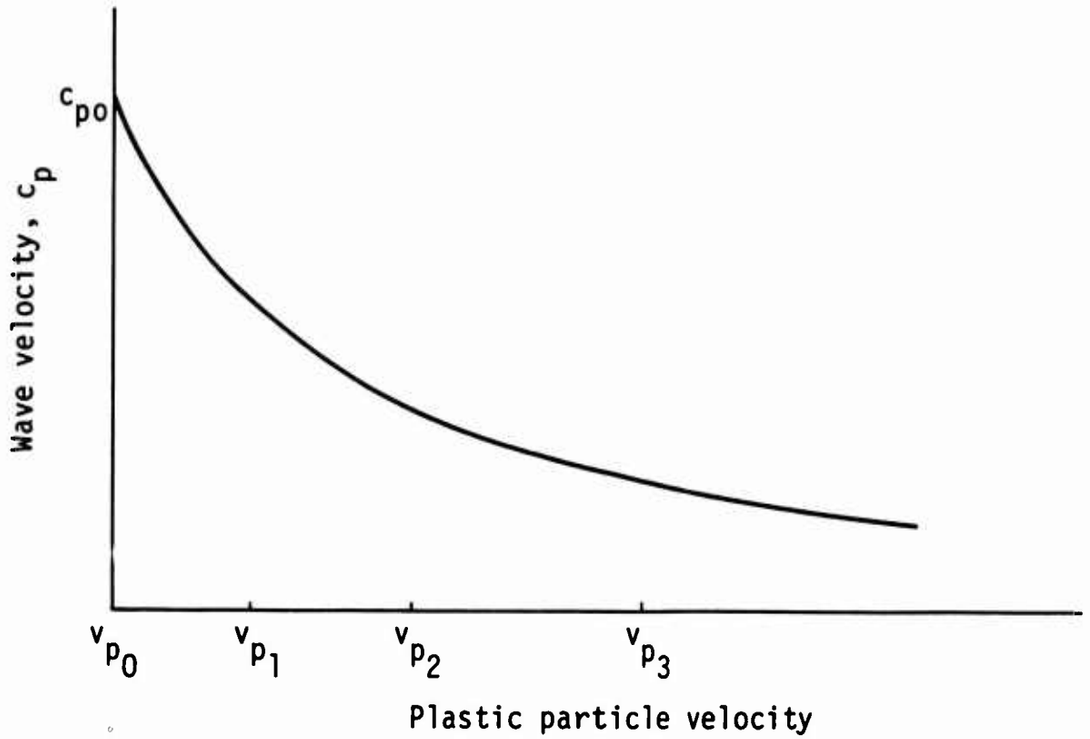

Figure 17. Compatibility fitting

desired. To do the latter, it is usually most flexible to construct the stress-strain curve from these displacement-time data.

There are two basic methods for deriving the stress-strain curve. One, the more tedious method (Ref. 61), relies on the accuracy of computed strains to obtain wave velocities; it can be extended to strain-rate-insensitive materials. The other, a simpler method, makes use of the results of the data-preparation exercise above. This method, which is the only one that will be developed here, preserves the internal consistency of the data by relying on Eq. (14) solved in the form

$$\varepsilon_p = \int_o^{v_p} \frac{1}{c_p} \, dv_p \tag{29}$$

where

ε_p = plastic axial strain

Thus in the wave-velocity versus particle-velocity plot of Figure 17, the reciprocals of the ordinates c_p are computed and plotted as a function of v_p as in

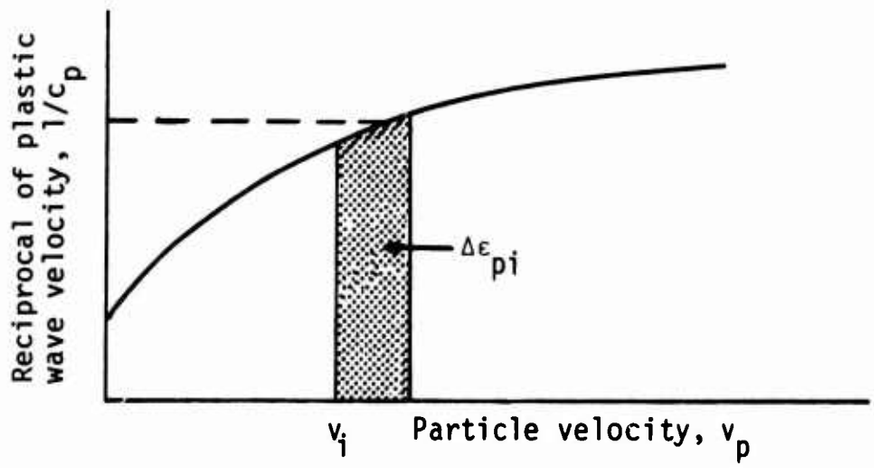

(a) Reciprocal of wave-velocity vs. particle-velocity plot

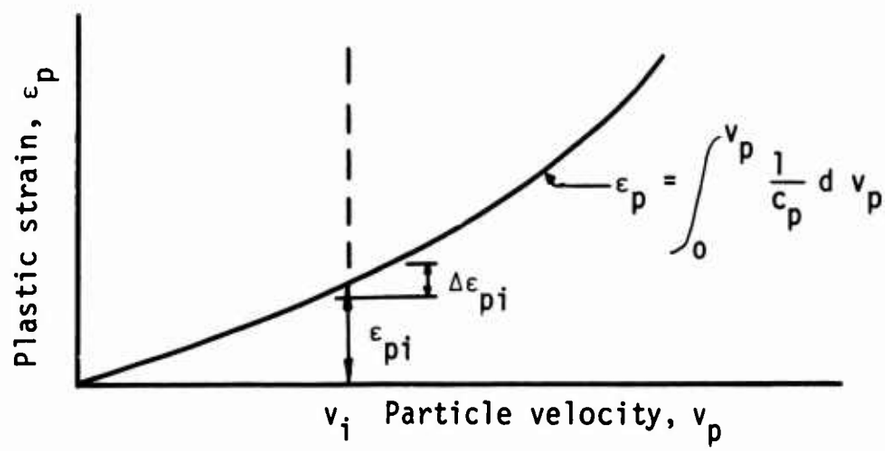

(b) Plastic-strain vs. particle-velocity plot

Figure 18. Simple data analyses

Figure 18a. The resulting curve is then integrated as shown to obtain plastic strain as a function of particle velocity, Figure 18b. This curve is then operated on according to the reverse of the operations shown on Figure 12 to obtain the stress-strain curve. As well as preserving the internal consistency of the data this method allows close and accurate study of the results and detection of invalid or inconsistent results.

SECTION IV

EXPERIMENTAL EQUIPMENT

1. General Description.

A short overall description of the experimental setup will be given here, followed by a description of key items of the experimental gear. Appendix A, which is subdivided just like this section, contains detailed descriptions of the development and verification of tests on the equipment.

Specimens of dry Ottawa sand, contained in rubber membranes, were fabricated in 1-inch-diameter, 5-foot-long rods. The specimens were subjected to one of three different vacuums and were fabricated so as to be as near as possible to one of three different densities; thus the behavior of the sand could be studied in terms of its condition (the density) and the state of stress (ambient only) in both static and wave-propagation tests. The specimens were contained in a special foam material, which was held at working level by a stout frame. The specimen was loaded by a shock tube modified for application of a soft-fronted, flat-topped pulse of essentially infinite duration.

The motions of the specimen, as the wave propagated, were measured by light-sensitive crystals at seven stations along the specimen. The crystals sensed the changes in light caused by the motions of triangular flags secured to the specimen at each station by hypodermic needles passing through the specimen. The time-history of the forces at the ends of the specimen was measured by force links; and because the quantitative performance of these links was uncertain (they were intended primarily as time-of-arrival sensors), the input force was also measured by a proving ring in the static tests. The signals from all transducers were amplified and recorded remotely on magnetic tape.

Three types of tests were performed over the range of densities and ambient stresses considered: (1) essentially standard, static, vacuum triaxial tests to failure; (2) static tests to failure on the long sand rods; and (3) wave-propagation tests at just less than the failure stress on the long sand rods. Each specimen was used only once, and no preloading or conditioning sequence was applied.

2. Specimen.

a. Mold and Membrane.

The mold was a split, thick-walled aluminum tube. It was mounted vertically, fitted with a membrane and bottom cap, subjected to vacuum, and filled with sand according to the procedures to be described. Drawings of the mold are shown in Appendix A.

The membranes were a flexible surgical-rubber tubing, described in Appendix A.

b. Soil.

The soil used was a uniformly graded, clean, standard Ottawa sand. Figure 19 shows the distribution of grain sizes. This material is called 20-30 Ottawa sand because most of its grains are passed by the No. 20 sieve (0.840 mm) and retained on the No. 30 sieve (0.590 mm).

The maximum and minimum densities to which the sand can be fabricated depend on the grading, the specific gravity, and the method of placement, including the mold geometry. For these experiments the minimum density obtained was 93.4 pcf, but the maximum was only 106.1 pcf because of the small diameter of the long mold. This is somewhat less than the usual maximum density for this material; a maximum density on the order of 114 or 115 pcf is common for more usual geometries (Ref. 58). This constitutes one experimental limitation on the results to be given: the highest densities could not be studied because they could not be attained in the small-diameter long mold.

The specimens were fabricated nominally to three densities: loose (95 pcf), medium dense (100 pcf), and dense (105 pcf). It was not, of course, possible to fabricate the specimens precisely to these densities each time. The actual densities were, however, carefully computed and can be compared by an interpolation process to be described.

3. Specimen Containment.

a. Foam.

Because of the buckling noted in earlier experiments (Ref. 34), and because the thinness of these specimens would make buckling even more possible, extensive preliminary work was performed to develop a specimen-containment scheme that would minimize buckling while disturbing the experimental conditions to a minimal degree.

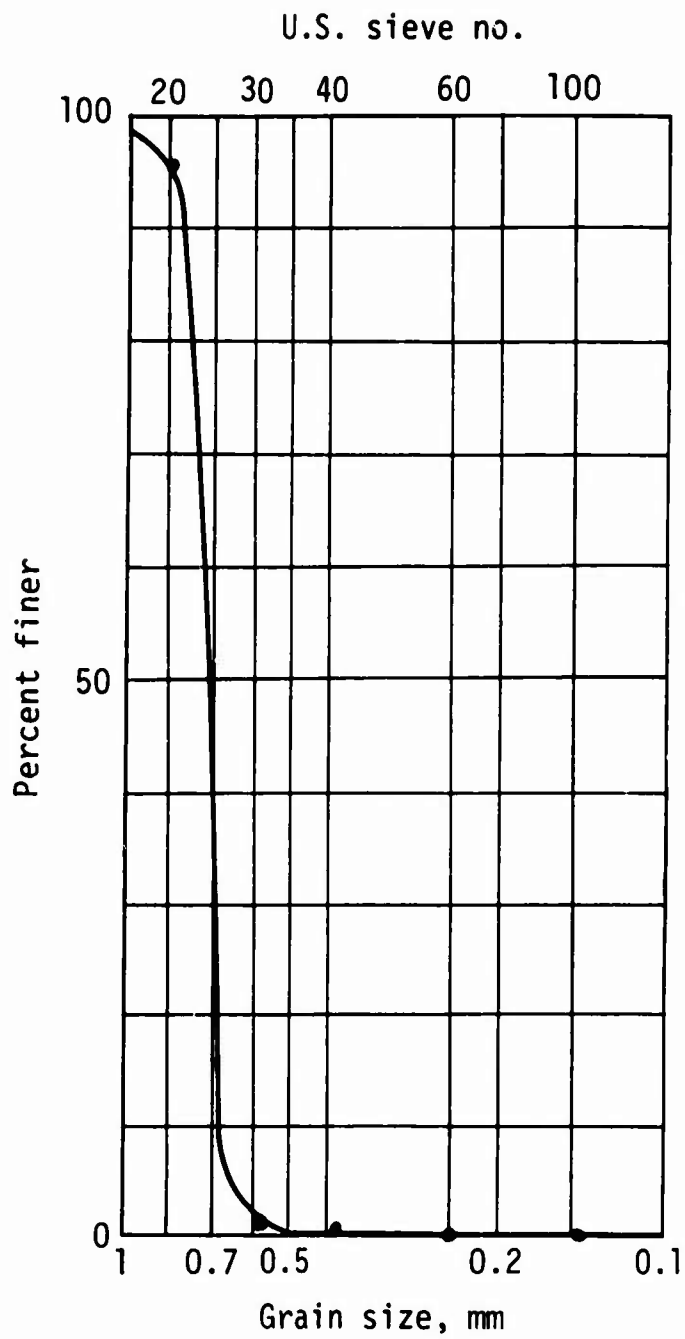

Figure 19. Grain-size distribution of 20-30 Ottawa sand

The results were the slotted foam beds shown in Figure 20. By this scheme the axial specimen motions were opposed only by the small cantilever resistances of the supporting members, but the lateral (buckling) specimen motions were opposed by the generous short-post compression resistance of the supporting members.

Figure 20a shows the typical section of foam placed under and over the specimen. As will be explained, it was necessary to cut out some of the foam at the displacement-measuring (light) stations. Tests showed that the lateral resistance at these cutout stations was seriously reduced. To reduce the tendency for buckling, special shapes (Fig. 20b) were cast with thicker cantilevers at the cutout sections; the small additional lateral resistance at these stations was accepted as an unavoidable experimental limitation.

The development and verification tests of the foam bed are described in Appendix A.

b. Cradle and Frame.

The upper and lower foam beds were placed into the upper and lower cradles (Appendix A), which were made of wood. The lower cradle was attached to a hardwood baseboard, which was wedged tightly into steel angles that were a part of the stout steel-support frame that held the entire setup at working level. The steel frame had several intermediate legs and was generously crossbraced. Each leg was fitted with an adjusting screw at its base so that the frame could be leveled and straightened for each test. The upper cradle was removable and was made in short sections for that purpose. It was held in place during the test by heavy lead ingots placed on top of it. Figure 21 shows the cradle and frame with the bedded specimen ready for testing.

4. Loading Device.

The load was created by a 3-1/2-inch O.D., 3-1/4-inch I.D., 20-foot-long, air-charged shock tube with a special short expansion chamber designed to create a soft-fronted pulse. The entire length of the tube was used as a charging chamber to create an infinite duration for the purposes of this experiment. The tube was supplied with legs and adjusting screws just as the frame was.

The diaphragm was burst by firing a hypodermic needle into it. For details of the expansion chamber and firing mechanism, see Appendix A.

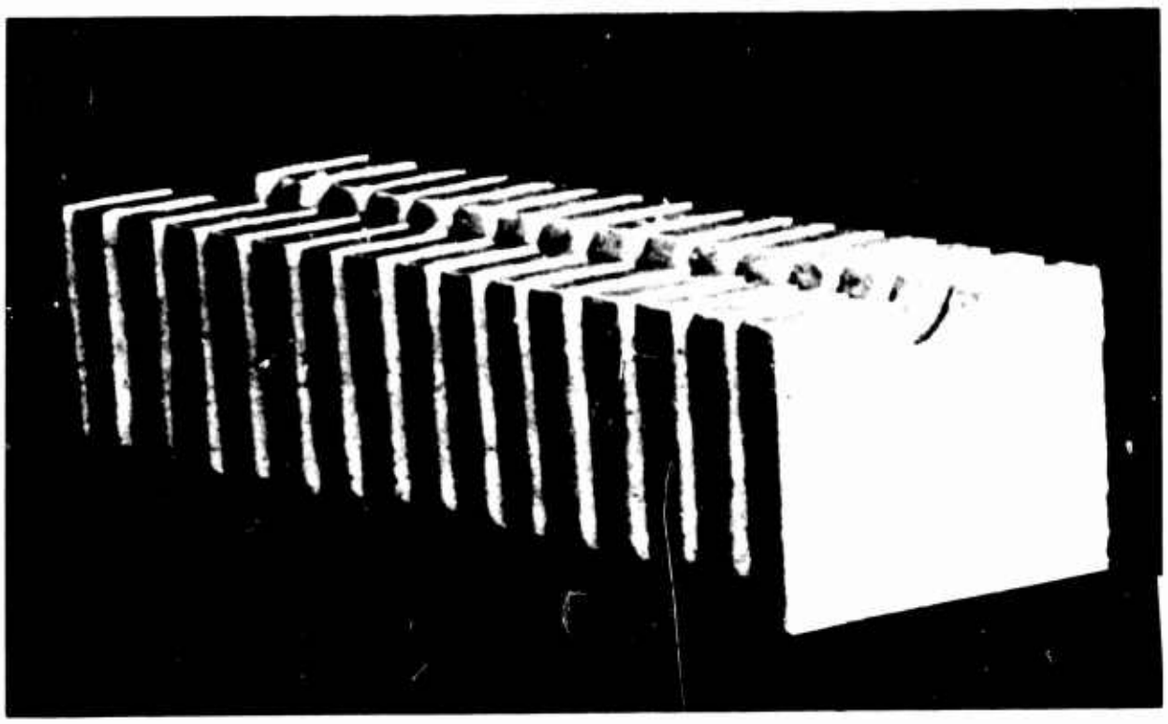

(a) Normal section

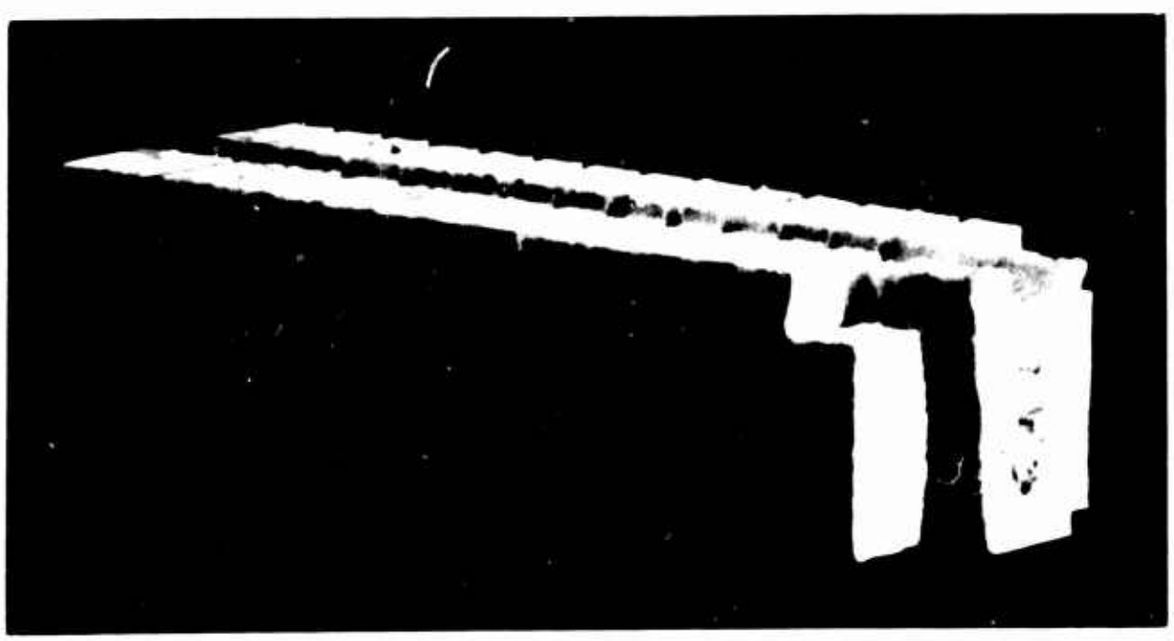

(b) Section showing one cutout at light station

Figure 20. Typical sections of foam bed

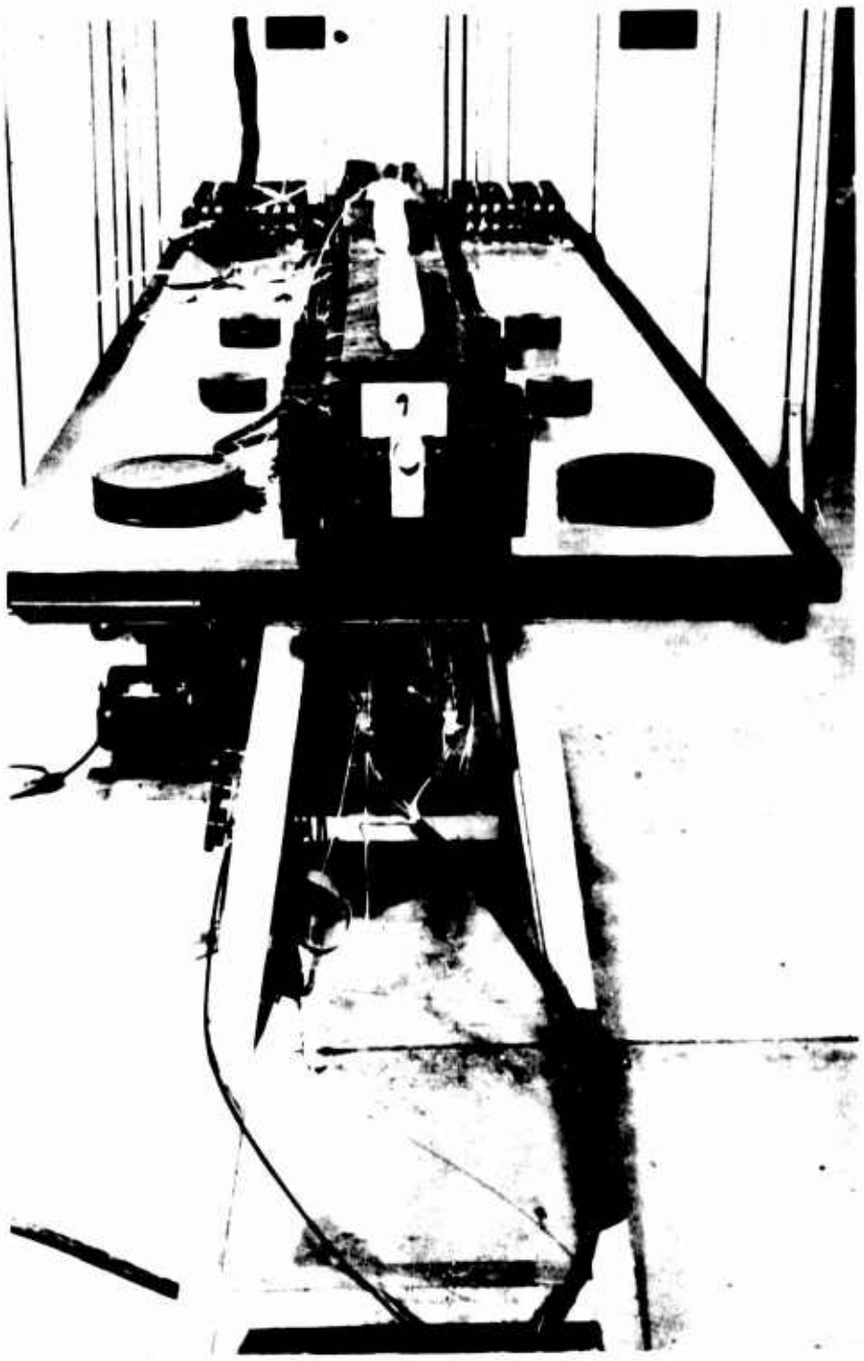

Figure 21. Frame and cradle

The expansion chamber contained a removable piezoelectric gage. This gage was used as a common-time event for the wave-propagation tests only and was not used to measure the load on the specimen.

5. Displacement Measurements.

a. Light System.

Particle displacements of the specimen were measured by allowing opaque flags to intercept a light beam, causing a linear change in the light to fall on a photodiode crystal to create an electrical signal, which was measured.

The flags (Fig. 22) were cut from 0.012-inch (photographic) film and were sprayed on both sides with flat black paint for opacity. The interior of each flag was cut out to a butt dimension of 0.50 inch and to a length depending on the amount of travel expected in a particular experiment. For comments on the fabrication of the flags, see Appendix A.

The photodiode (Hoffman, 52-C) was a light-sensitive, current-generating silicon crystal, shown in Figure 23. The output from the crystal was sensed by measuring the voltage change across a 75-ohm resistor in parallel with the crystal.

The light source was a microscope bulb (GE 1493), housed in an aluminum tube, shown in Figure 24. The tube was reduced in section so that it would fit into the cradle between the cantilevers of the foam bed. To prevent the bulb from projecting its own filament shadow onto the photodiode, a thin diffuser of translucent Mylar plastic was placed over the bulb at the point of section reduction in the tube.

Although the light should have been precisely collimated for instrumentation work, the procurement of a point-source light and a proper collimating-lens system would have created great expense and delay for the number of measuring stations required in this experiment. For this reason parallel-slit collimation was attempted and was found adequate. The slit was made by mounting a pair of razor blades at the top of the light cell (Fig. 24). The insides of the tubes were painted flat black to reduce spurious reflections. The light bulbs were seriated in pairs; and the pairs were circuited in parallel to a common 12-volt power supply. For ease of mounting and handling in the experimental setup, each crystal was mounted with conducting epoxy onto a clear plastic carrier (Fig. 25).

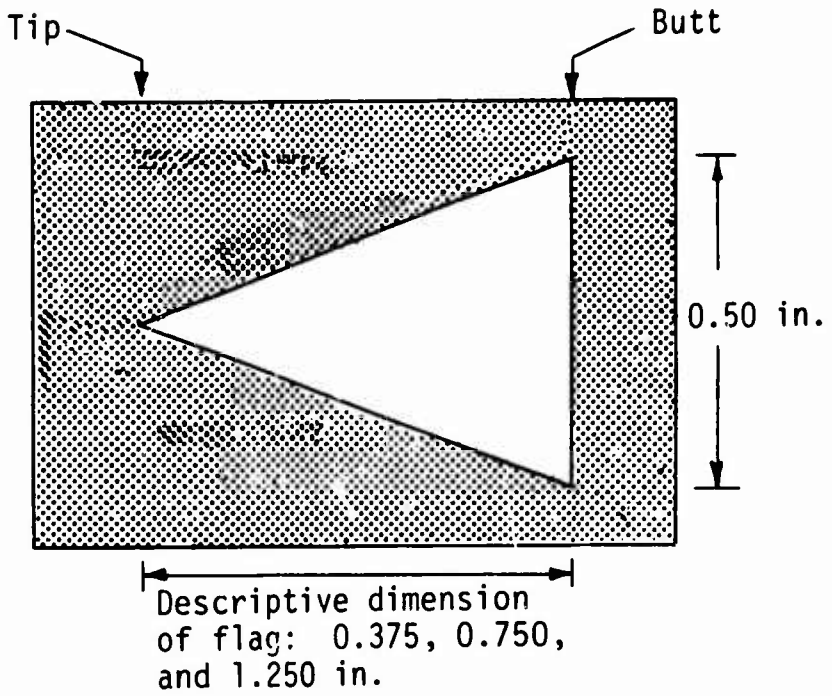

(a) Dimensions of displacement flags

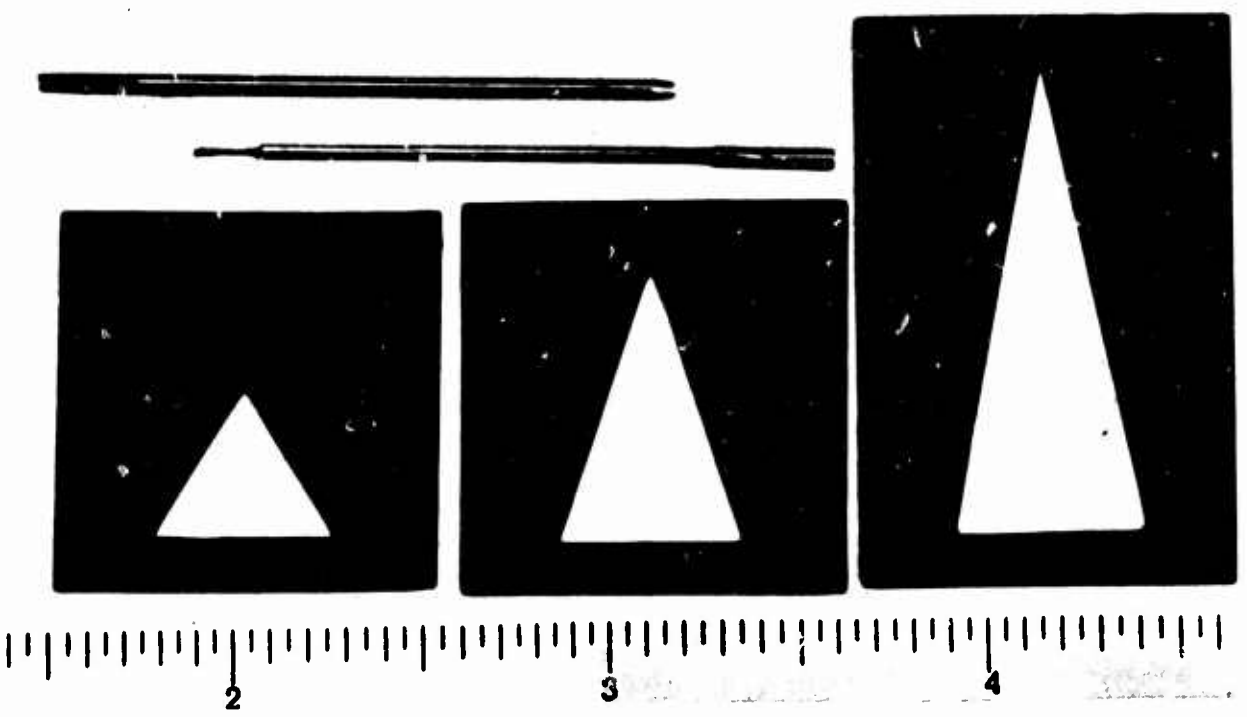

(b) Different-sized displacement flags

Figure 22. Displacement flags

Figure 23. Light-sensitive crystal

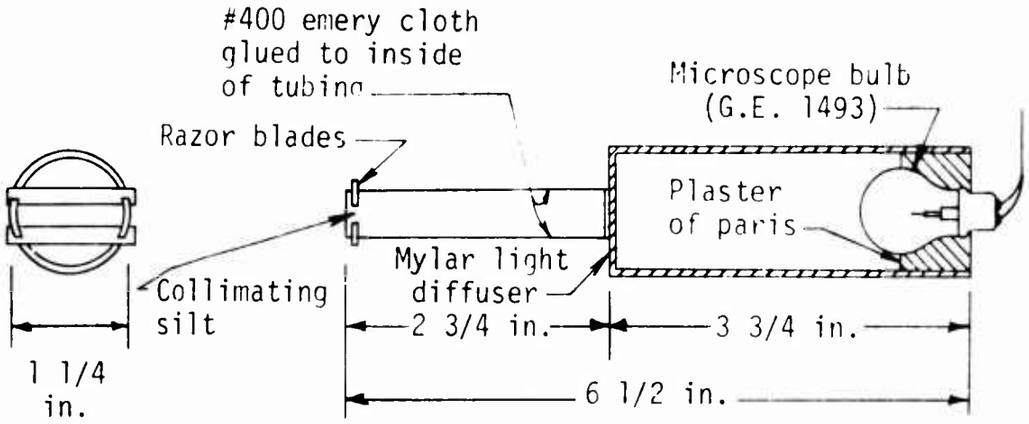

(a) Details of light source

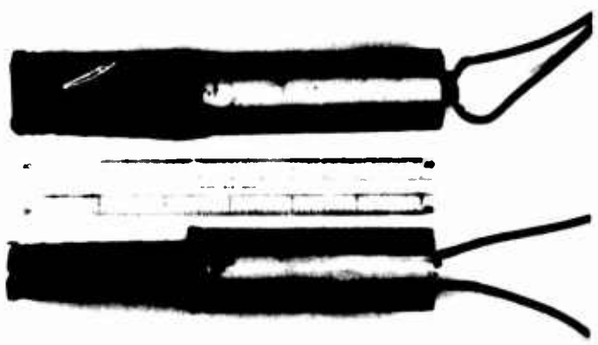

(b) Photograph of light source

Figure 24. Light source

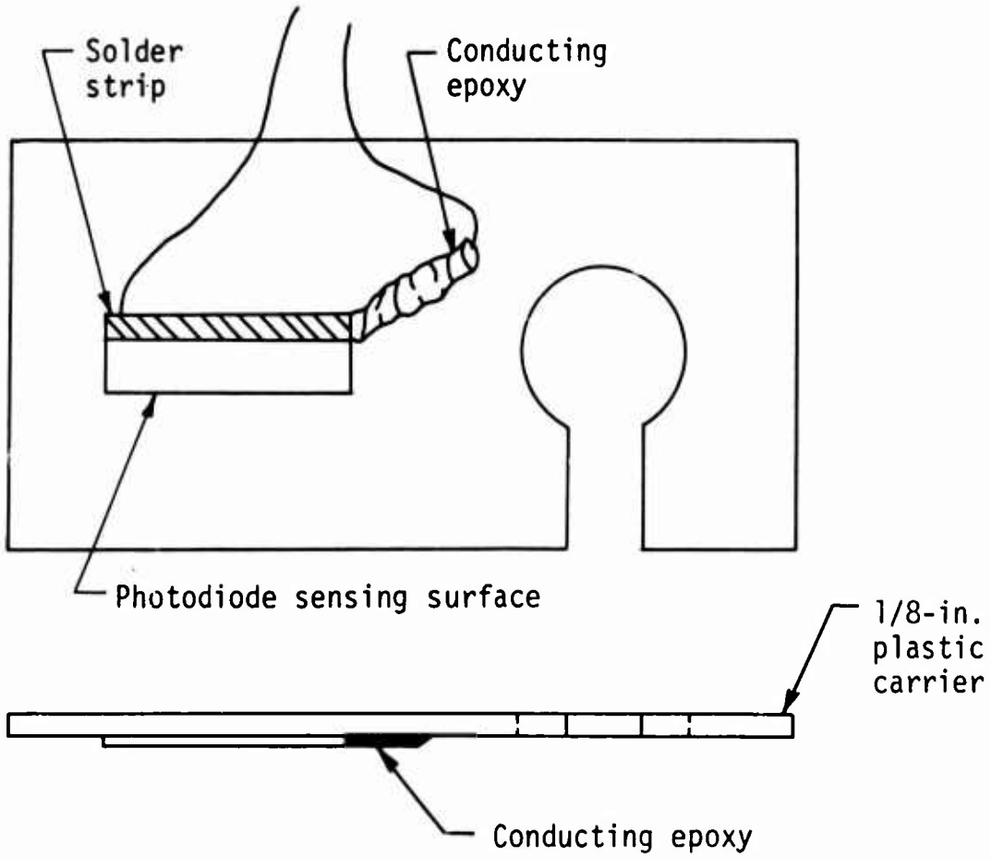

Figure 25. Photodiode and carrier

The setup of the light-source, flag-photodiode, displacement-measuring system is shown in Figure 26. The light beam projecting vertically upward onto the crystal was intercepted by the flag. Each displacement-measuring station contained two such systems, the pair of flags being supported by a slotted hypodermic needle (Fig. 22) that passed through the soil specimen. The total weight of each flag pair and the hypodermic needle was about 1.25 gm, roughly equivalent in mass to an 0.07-inch-thick wafer of the soil specimen. The motions of the particles in the soil specimen carried the flag pair along, changing the amount of light impinging on the respective photodiodes and generating electrical signals as described.

b. Sensitivity Calibration.

Each crystal-flag pair was calibrated before each experiment. To reduce unknown errors, the calibration was done directly in the experimental setup with all conditions as nearly the same as possible during an actual test. All lights in the entire setup were turned on, and neighboring lights were shielded (the entire inside of both cradles, as well as all calibration fixtures, were painted flat black). The calibration device had three components (shown

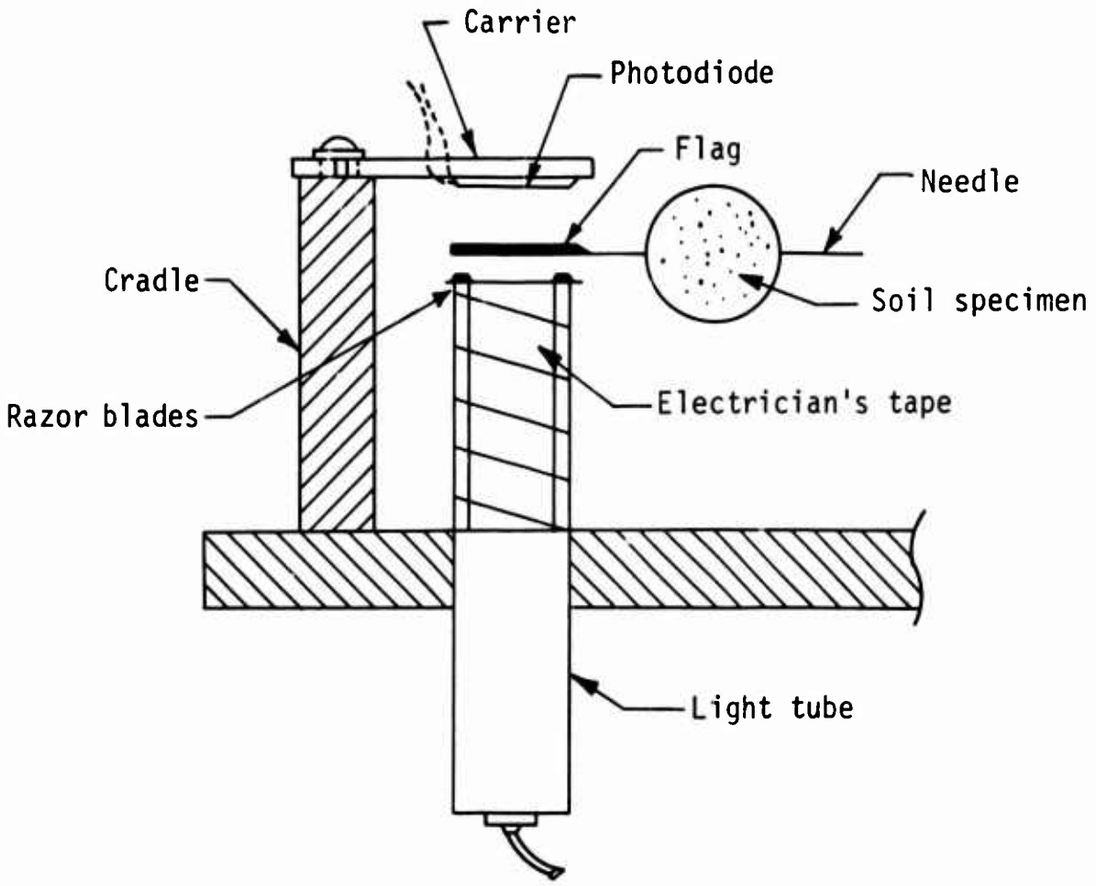

(a) Detailed drawing of displacement-measuring system

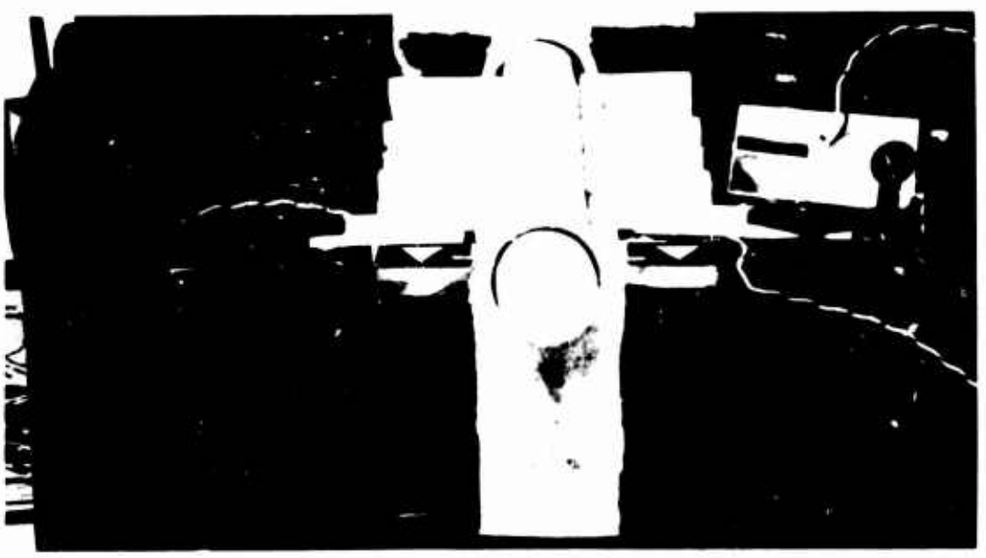

(b) Photograph of displacement-measuring system

Figure 26. Displacement-measuring system

removed from the cradles in Fig. 27): (1) the *monorail*, which fitted into the lower cradle and had a machined plane rail on top; (2) the *carrier* designed to carry the flags at their proper elevation (flag-to-crystal spacing) during the calibration; and (3) the *potentiometer*, a calibrated precision linear potentiometer used to measure the calibration displacements. For ease of calibration the potentiometer was connected to the horizontal plates of an oscilloscope, and the photodiode crystal output was connected to the vertical plates.

This setup, as well as a typical calibration picture, is shown in Figure 28. The flags were positioned so that they would move butt first during the test. This was done so that if the flag were mispositioned axially before the experiment the initial portion of the signal would be in the wrong direction (see Fig. 28); even though the data would be lost for an improperly positioned flag, time would not be wasted in analyzing erroneous data. The flags were positioned axially before the test by adjusting them until an oscilloscope record showed that the nadir, point 3 in Figure 28, had been to some point A in the linear portion of the output. For maximum travel an attempt was made to adjust the flag as closely as possible to the nadir. The pretest, transverse flag positioning was to assure that the geometrical center of the flag coincided with the illumination center of the light-crystal system; in this way maximum output could be obtained.

After the calibration was completed, the calibration device was removed from the cradle, the displacement crystal was removed, the foam replaced, and the displacement-measuring system was reassembled for the experiment.

c. Placement.

The displacement-measuring system (flags and crystals) was finally reassembled and adjusted after the specimen had been fabricated and placed in its foam bed as described below.

The first reassembly operation was done to position the flags. The flags were carried by a slotted mating pair of hypodermic needles (Fig. 22), which were pushed through the center of the specimen. The pushing was done with a long needle insert, which was guided by permanent bushings built onto the lower cradle. Before insertion the membrane around the specimen was generously greased to avoid vacuum leaks. The larger of the two needles was then inserted through the specimen. Next, the smaller needle was inserted into the protruding end of the larger needle. Note in Figure 22 that the smaller needle was tongued on its

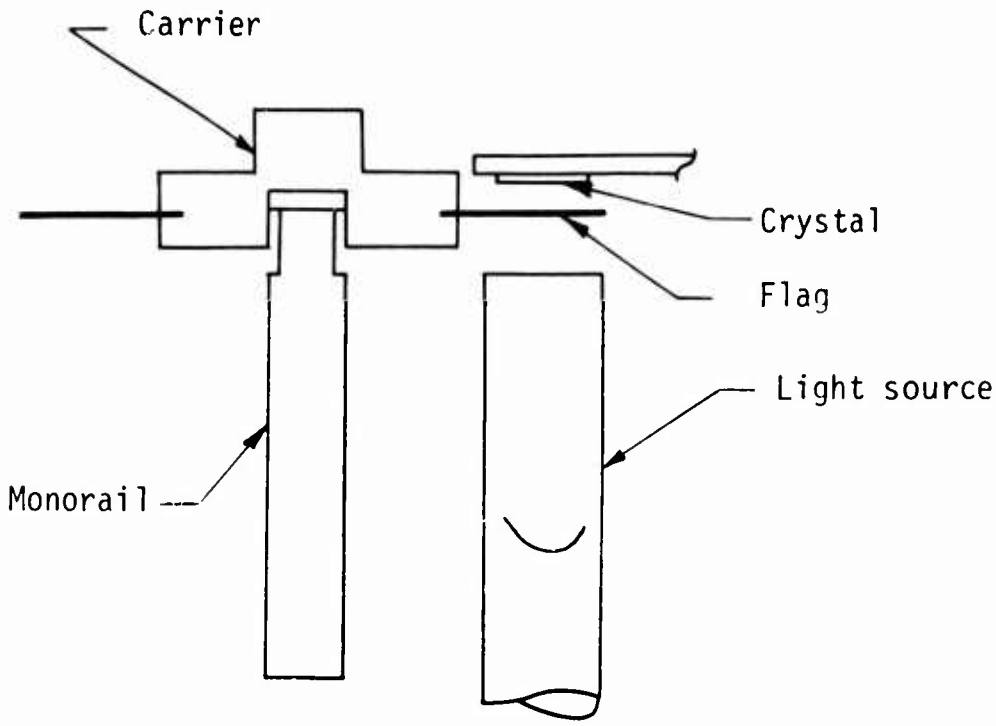

(a) Detailed drawing of calibration device

(b) Photograph of calibration system

Figure 27. Output-displacement calibration device

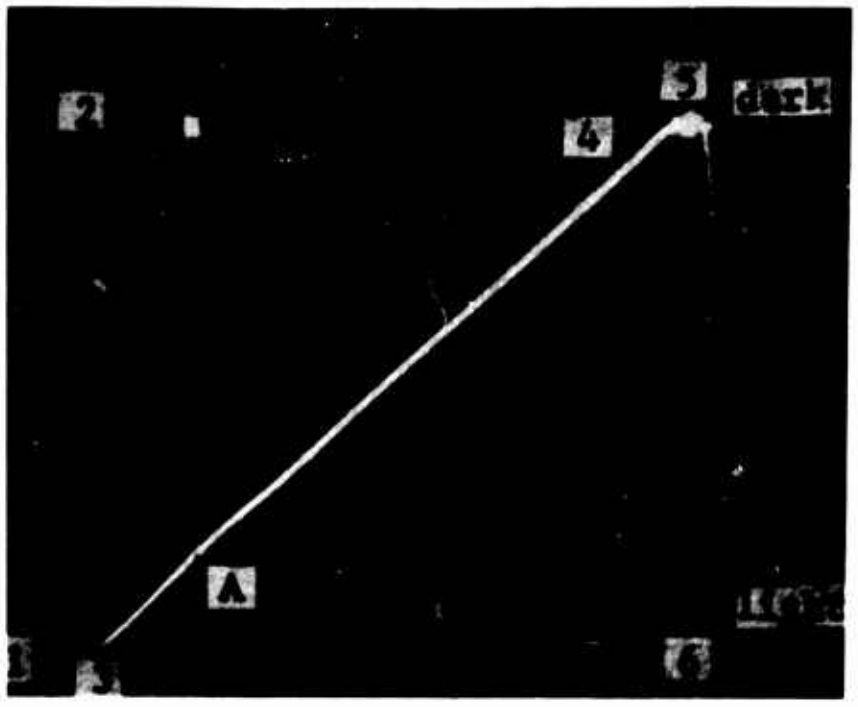

1. Flag not in field.
2. Leading edge enters field.
3. Butt just past edge of crystal (nadir).
4. Nonlinearity begins as tail moves onto crystal.
5. Trailing edge covers crystal.
6. Flag past field.

A. Adjustment before test.

(a) Photograph of output-displacement calibration

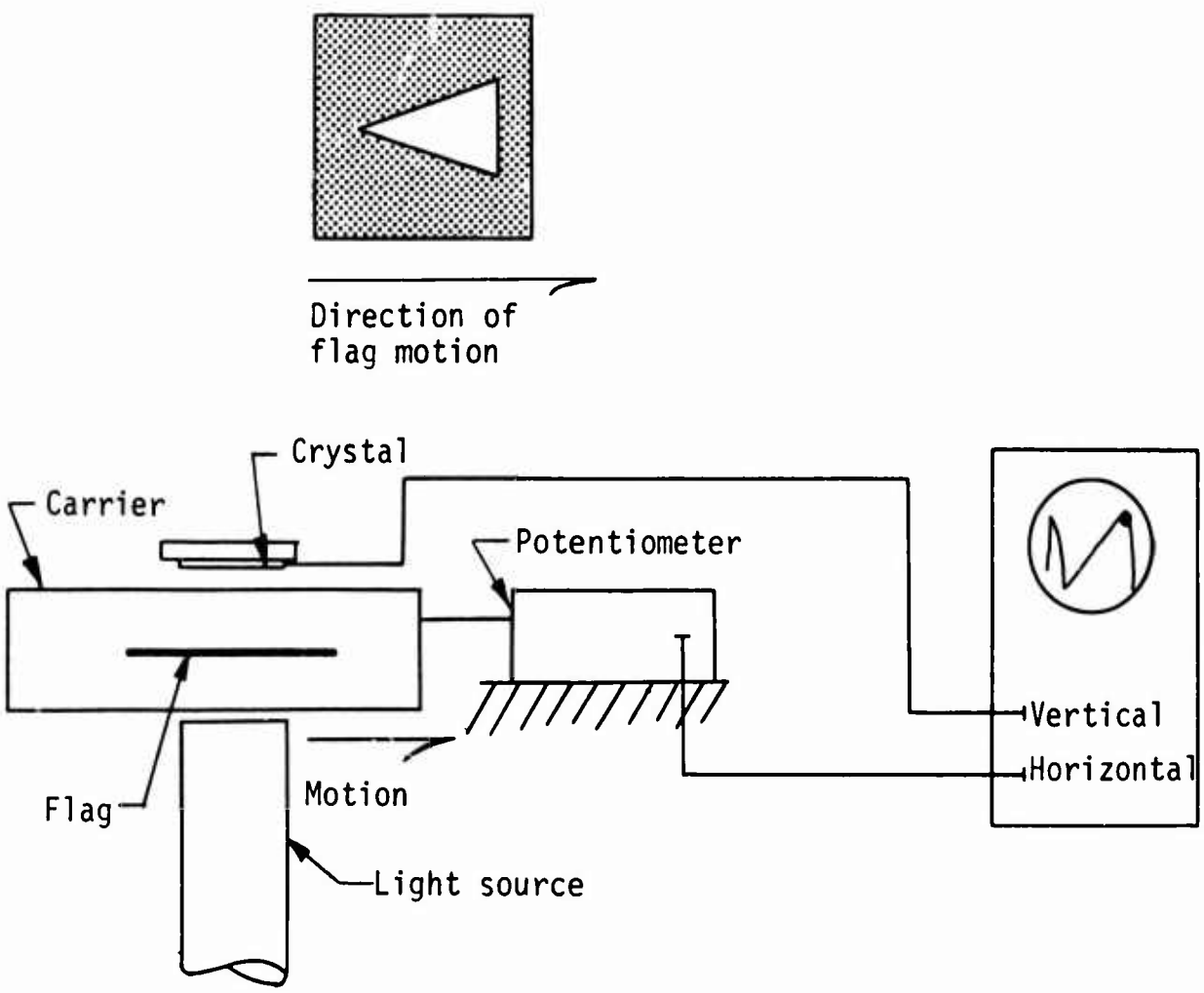

(b) Drawing of output-displacement calibration

Figure 28. Output-displacement calibration

insert end so that it would properly engage a groove inside the larger needle, ensuring that the slots in both needles were in the same plane. The flags were then placed gently into the slots.

Next, the light crystals were placed in position and secured with screws. The lights were turned on and each flag in turn was positioned on a scope to point A in Figure 28. The upper bed and cradle were then placed over the specimen, and the entire setup was covered by a sheet of black polyethylene plastic to exclude any vagrant ambient light during the test.

d. In-Place Calibration.

Once the flags were placed, their direct sensitivity calibration was known; but it was necessary to be able to scale this calibration through the amplifying and recording states without relying on the veracity of dial settings. This could be done by some sort of signal substitution, preferably by the signal itself (Ref. 62). It was done here simply by turning the lights off and on twice, once with direct voltage readout on a scope and again on the recording tapes just before the event. A typical result is shown in Figure 29. By comparing the voltage outputs from the direct and the remote calibrate pulses, the recording-system gain was easily computed.

e. Verification Tests.

The light-flag-crystal scheme was tested for temperature effects, short-term stability, long-term stability, and errors in vertical and lateral flag positioning. The results of these tests are given, along with descriptions of the test methods, in Appendix A. It is concluded that the errors do not exceed about 5 percent.

6. Force Measurements.

The forces in the static tests were measured with a proving ring whose linearity and stability were verified by frequent check tests.

The vacuums were measured with a manometer and the leakage checked by placing a vacuum gage at other positions along the various lines leading to the sample.

The force links at the ends of the specimen were intended only to be time-of-arrival gages but, insofar as was practical, an attempt was made to obtain some force-time data from them. Obtaining a suitable design for these gages would have required an extensive and unwarranted digression from the main topic

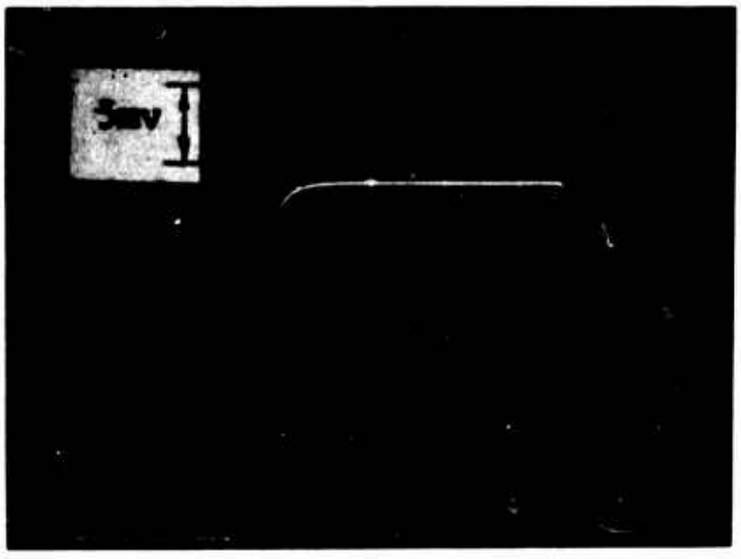

(a) Direct CRO calibrate

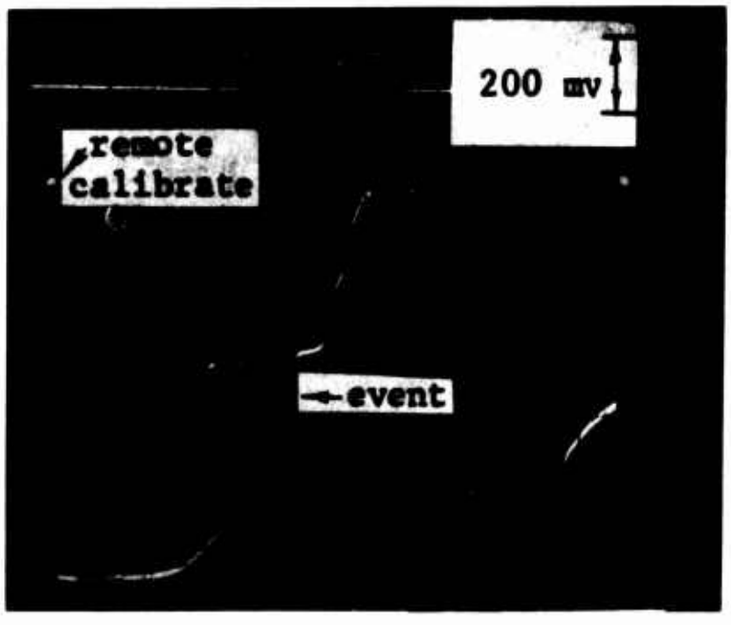

(b) Remote calibrate

Figure 29. Preexperiment calibrations

in order to gain secondary information. The front link would have had to be completely insensitive to accelerations, to have a high sensitivity for measuring the small loads, to have a high natural frequency so that its wave velocity would be considerably higher than that of the soil, and to be completely insensitive to bending; the back force link would have had to exhibit all the same characteristics except the acceleration sensitivity (because the specimen abutted a massive lead block).

A compromise of sorts was reached simply by potting ordinary carbon resistors in epoxy. These elements were quite sensitive, easily developing 1 to 2 millivolts per pound (mv/lb) output. They were also electrically stable, as shown by the results of three 20-megohm calibrate pulses in Figure 30. They were, however, somewhat sensitive to bending. Figure 30 also shows the results of a particularly severe calibration test in which dead weights were purposely placed on the link with an eccentricity just less than complete unbalance. The points shown are the results of several exercises of this type and indicate that vagrant eccentricities during a test could lead to perhaps 10 percent errors in the force-link readings. Owing to lack of appropriate equipment it was not possible to perform a valid quantitative acceleration-sensitivity test on the force links. The gage did, however, show only minor outputs when shaken violently by hand.

For these secondary data, and for approximate analyses only, these bending and acceleration errors were accepted as experimental limitations. For this reason no further force-link studies were undertaken.

7. Fabrication and Placement of Specimen.

The membrane was inserted in the assembled mold and made fast at the ends. The mold was then placed vertically in a stand, and the bottom cap (the back force link) was inserted. A vacuum was applied to the space between the membrane and the mold, drawing the membrane snug. After the membrane had been inspected for twists or wrinkles, the sand placement was begun. The sand was placed in three ways, depending on the nominal density desired: for *dense*, the material was placed in thin (1-inch) layers and vibrated; for *medium dense*, the material was poured through a funnel and tube from a height of 24 inches above the exposed sand surface; and for *loose*, the material was allowed to flow gently out of a funnel and tube held directly at the exposed sand surface. Placement was stopped when a precise distance below the top was reached. The top cap (a nylon plug) was inserted to that depth, and the membrane was sealed against the cap. The test vacuum was then introduced into the specimen through the bottom

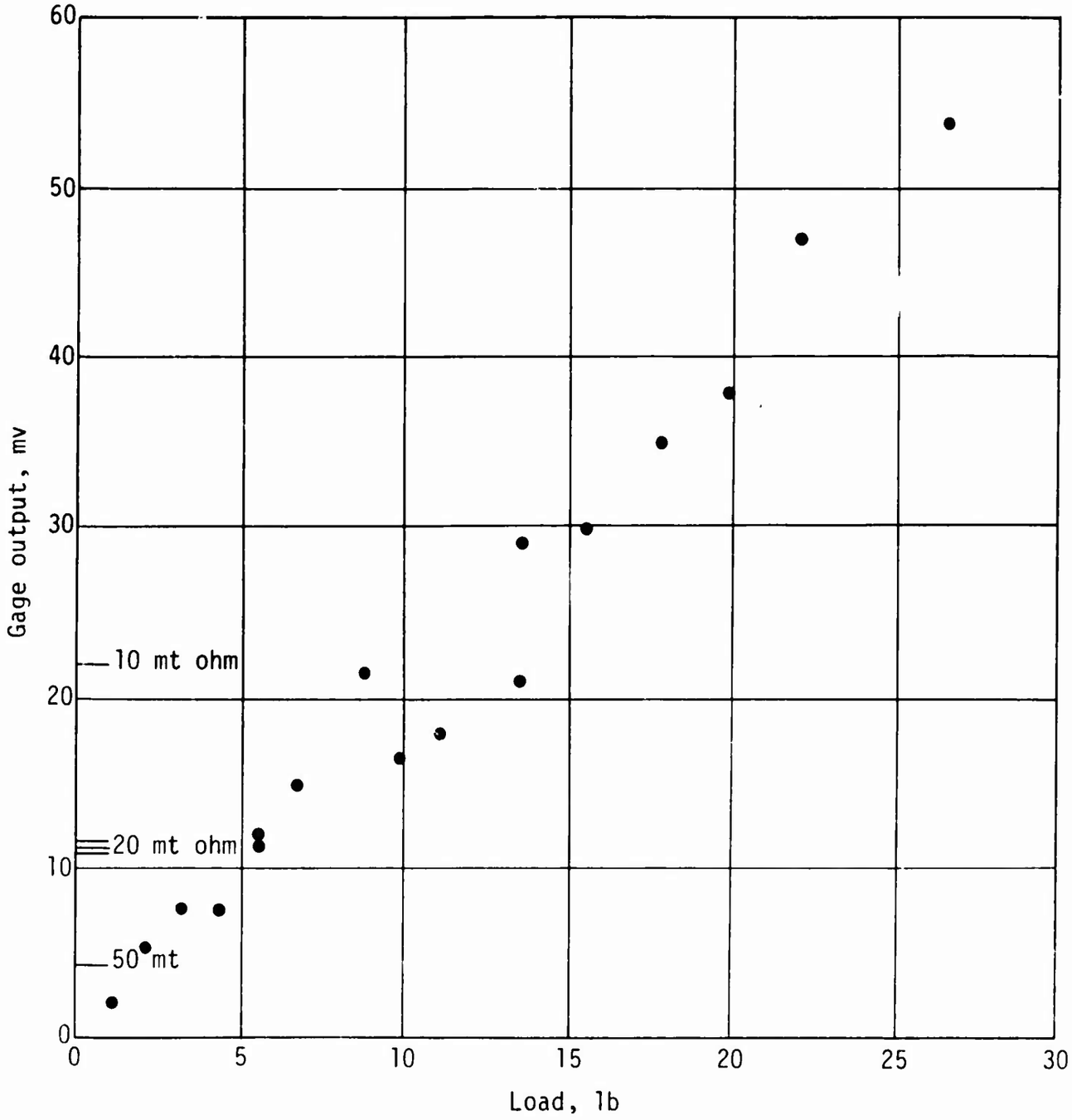

Figure 30. Force-link calibrate with eccentricities

cap, and the outside vacuum was terminated. The mold and specimen were removed from the stand and placed horizontally on a table to be prepared for placement in the foam bed.

Preparation was started by gentle removal of the upper half of the mold. Numerous bands of bookbinder's tape were wrapped around the specimen and lower half of the mold. With the bands in place the sample could be inverted, with the half of the mold used for support, and lowered into its bed, as shown in Figure 31. The mold was then removed.

With the specimen in place the lead backup block and the back force link were brought into tentative contact, and the needles were inserted. The flags were placed in the needle slots and positioned with the aid of a scope. The lead block and the back force link were then brought into careful contact, and the foam cantilevers were cocked forward a nominal 1/8 inch. The top bed and cradle were gently lowered into place and secured by the weight of lead ingots. The setup at this stage is shown in Figure 21.

The shock tube was then fitted with a diaphragm and was moved into position in line with the sample end. At this time the tube was adjusted for position and alignment, and the loading cap (containing the front force link) was inserted into the expansion chamber. The tube was then moved forward until the end of the specimen and the loading cap made gentle contact. Alignment inside the expansion chamber was checked with a dental mirror, and the necessary adjustments were made. The entire specimen container was then covered with the polyethylene sheet. The lights were turned on and allowed to reach equilibrium temperature, and the direct on-off light, in-place calibration was performed. The tube was then charged to the desired test pressure. Actual firing was done by the remote-record system. The firing sequence consisted of the on-off light calibration, followed by actual firing, with an abort option at any point in the sequence. After the test the apparatus was carefully disassembled, and the specimen was inspected.

The foregoing is a description of the actual wave-propagation tests. The sequence was the same for the static tests to failure with these exceptions: a proving ring was placed between the loading head and the sample end, the diaphragm was not put in the shock tube, and the load was applied by a slow buildup of pressure in the shock tube.

Figure 31. Lowering specimen into bed

For these experiments seven displacement stations were used, as shown in Figure 32, yielding sixteen data channels (14 displacement and 2 force) and one common-event channel. For the dynamic tests the common event was the piezoelectric gage in the expansion chamber. For the static tests the common event was a manually actuated electrical pip, generated each time the proving-ring dial traversed 0.0010 inch. Although the data were collected on different tapes in the remote-record system, the common-event channel was always recorded on all tapes in a given test.

8. Remote-Recording System.

The experimental data were all remotely recorded on tape, through utilization of an automatic control system that performed the immediately preshot functions. So that both static and dynamic tests could be performed, the photodiodes and the force links were dc-coupled to the recording system; therefore a dc-balance network was required. Figure 33 is a diagram of the remote-record setup. The dc-balance network was simply a battery-powered potentiometer (bucking) circuit, which, after ample time for warmup, was adjusted in the final few minutes before an experiment. The signal was preamplified before the remote-record system, which also applied a small amplification. The automatic control system was used to turn the lights on and off about 3 seconds before the shot to yield the remote calibration pulse. By comparing of the remote to the direct calibrates (Fig. 29), the recording-system amplification was directly computed, with no reliance on indicated amplifier gains. The tape-recorded data were read on an oscilloscope. Several pictures were usually taken so as to expand, in time and amplitude, certain areas of interest in the signal. After these were studied, the tapes were duplicated by direct recording, and the duplicates were sent to the computer laboratory for reduction. Although a computer program for data analysis has been written, the data were analyzed manually to gain feeling for the phenomena involved.

9. Triaxial Tests.

These tests were done for comparison with the static and dynamic long-specimen experiments. At first it was felt that if the triaxial and the static long-specimen tests did not agree, overriding weight would be given to the static long-specimen results because of the known undesirable seating and boundary effects in triaxial tests on small specimens. In fact, the data agreed quite well, and some rather interesting facts about triaxial tests on small specimens were noted.

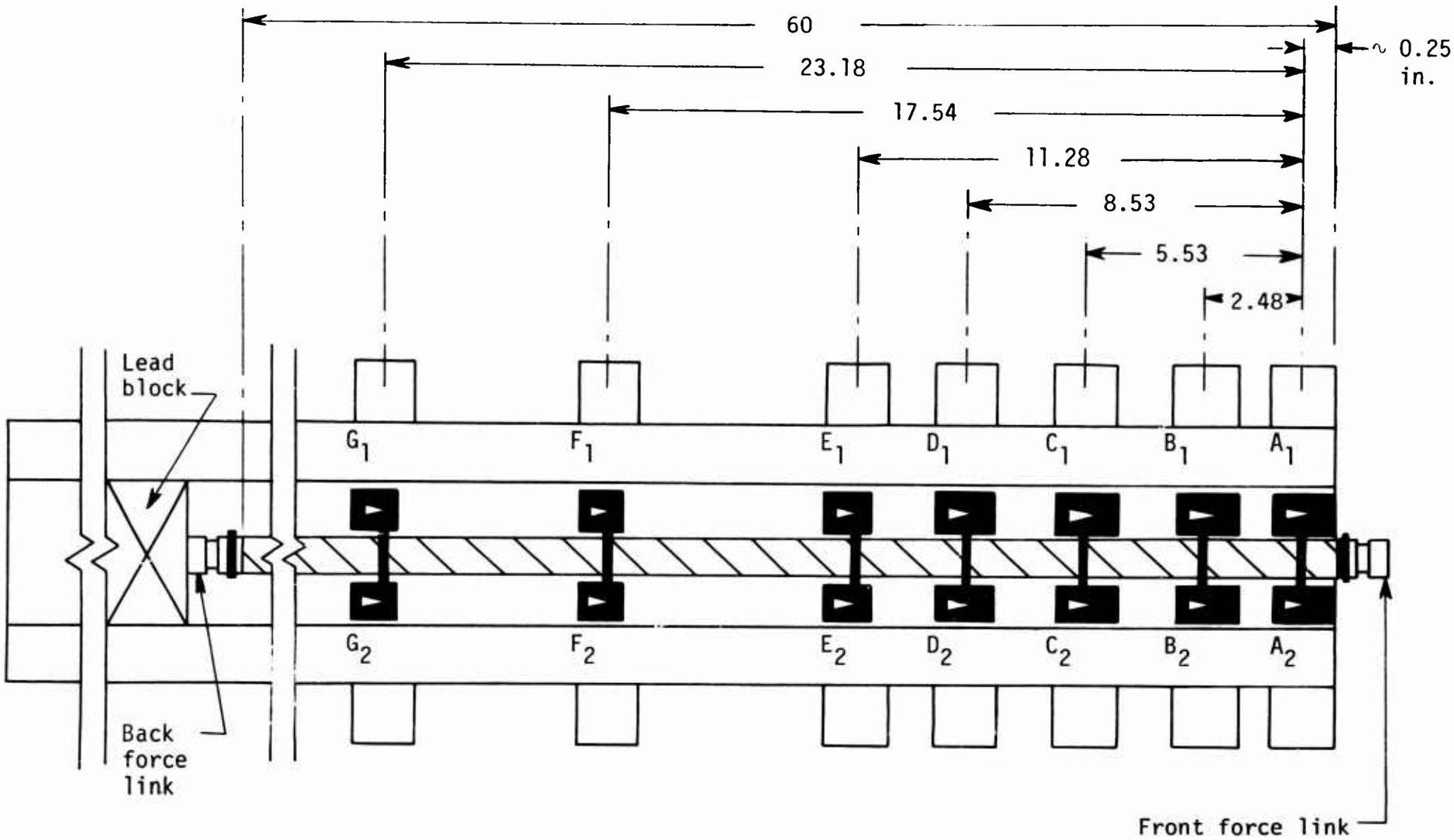

A-G = displacement-measuring stations
1 and 2 = side 1 and side 2 of displacement-measuring stations
Dimensions= inches

Figure 32. Locations of displacement-measuring stations

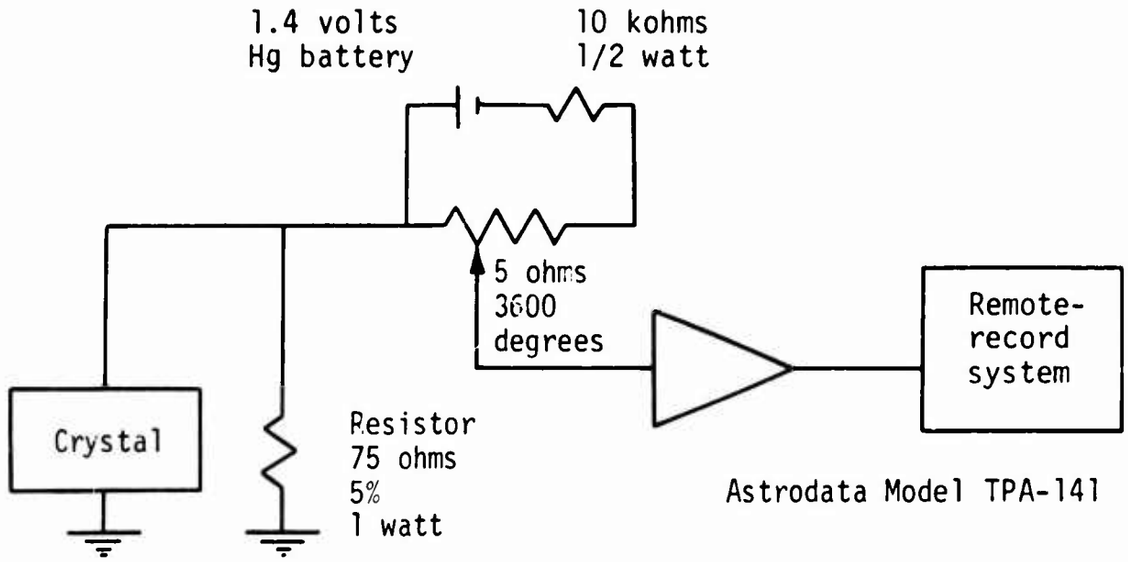

Figure 33. Remote-record circuitry

The triaxial specimens were fabricated in the same way as the long specimens (described in the foregoing), except that they were 3.6 inches long if 1 inch in diameter, or 4 inches long if 1.4 inches in diameter. They were loaded uniformly to failure in about 5 minutes in an air-actuated commercial unconfined-compression tester. The load was measured with the same proving ring used in the static long-specimen tests. The displacements were measured with an 0.001-inch dial gage. The vacuum was created by the same pump and was measured by the same manometer; it was measured at both ends of the specimen so that any leaks could be detected and corrected.

When the internal vacuum was applied, the loose specimens shrank measurably. The reduced area was used for stress computations, but no further area corrections were made. The strain was computed by dividing the overall displacement by the reduced length. The original, as-compacted density was used for comparative purposes.

Before starting the main triaxial test, it was decided to ascertain that the stiffness of the surgical membrane was not affecting the results. For this purpose, what was intedned to be a short comparative series of tests was planned: at several densities and ambient stresses two identical specimens were fabricated, one in a surgical membrane and the other in the more common 1.4-inch (prophylactic) thin membrane used in triaxial testing, but allowed here to fold and wrinkle

to accommodate to the 1-inch-specimen diameter. A comparison of the stress-strain curves would show immediately if any membrane effect existed: if the stiffness of the surgical membrane were adverse, the stress-strain curves for specimens tested in this membrane should lie above those for comparable specimens tested in the prophylactic membrane.

As shown in Figure 34, the initial results were appalling: clearly, at limiting densities (dense and loose) and ambient stresses there was a gross difference between the results obtained by each of the two membranes. It now remained to show whether the effect was a strengthening, caused by the stiffness of the surgical membrane, or a weakening, caused by the wrinkling and end effects of the prophylactic membrane. After an exhaustive series of tests, described in Appendix A, it was concluded that the effect was a weakening, caused by the wrinkling and end effects of the prophylactic membrane. Figure 34 also shows the results of tests on specimens at the normal triaxial size of 1.4 inches. The larger specimens at higher densities (similar fabrication techniques did not yield similar densities for these larger specimens) yielded slightly stiffer stress-strain curves. All the tests to be reported in later sections were performed on specimens jacketed in the 1-inch-diameter surgical membranes.

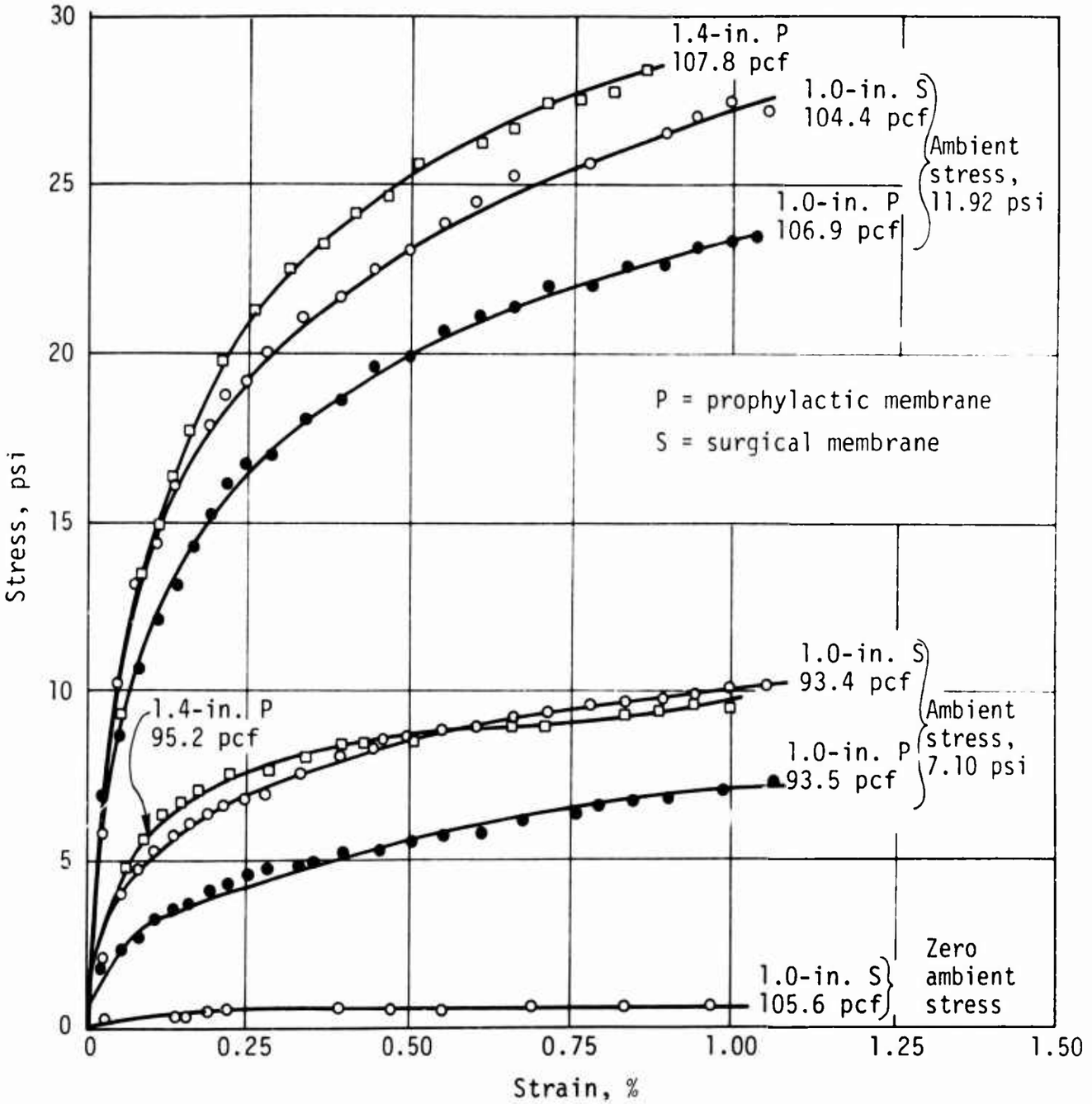

Figure 34. Initial tests of membrane effects

SECTION V

EXPERIMENTAL RESULTS

1. Vacuum Triaxial Tests.

a. Scope of Tests.

A total of 48 triaxial tests was performed, of which 25 yielded data directly usable in this report. Table I lists all tests, test purposes, test conditions, and test methods (described in Section IV, 9).

First-load stress-strain curves from sands are notoriously vagrant; even under the best test conditions with skilled and careful operators, discouragingly large scatters in data points must be expected. For example, Figure 35 shows the results of such carefully performed tests, reported in Reference 58; only two full stress-strain curves and 10 ultimate strengths were reported. The data from the two reported stress-strain curves are typical of the vagrancies; the looser specimen appears stiffer at low strains and softer at high. The inner of the shaded bands is in this case the scatter band for two tests on specimens fabricated and tested, to all appearances, under precisely similar conditions. Based on 10 strengths reported, the large darkened band shown in Figure 35 indicates the range of scatter of the data. As has been emphasized in the literature (Refs. 34,38,58), because the scatter band in this type of test is in fact larger than the strain-rate sensitivity, any precise analysis is at best approximate and of questionable utility for application to practical problems.

The data from these experiments showed the same vagrancies and will be discussed.

Table I

SCHEDULE OF VACUUM TRIAXIAL TESTS

Test	Membrane	Ambient stress, psi	Density, pcf	Purpose	Density classification
2A	S	11.92	105.7	T	D-high
A2	S	11.92	104.2	T	D-high
A3	S	11.92	94.4	T	L-high
B1	S	9.94	105.1	T	D-middle
B2	S	9.94	103.6	T	D-middle
B3	S	9.94	86.6	T	--
B4	S	9.94	94.5	T	L-middle
C1	P-1	7.10	106.1	M(t)	--
C2	S	7.10	104.6	T	D-low
C3	S	7.10	100.1	T	MD-low
C4	S	7.10	94.6	T	L-low
D1	S	11.92	105.0	T	D-high
D2	S	11.92	109.4	T	--
E1	S	11.92	104.4	T	D-high
E2	P-1	11.92	106.2	M(t)	--
E3	S	7.10	93.4	T	L-low
F1	S	11.92	104.7	T	D-high
F2	S	11.92	98.4	T	MD-high
F3	S	0	105.6	M(t)	--
F4	P-1	11.92	107.1	M(t)	--
F5a	S	11.92	105.6	T	D-high
F5b	P-1	11.92	107.7	M(t)	--
F6	P-1	11.92	106.9	M(t)	--
F7	P-1	11.92	106.7	M(t)	--
F8	P-1	11.92	105.7	M(t)	--
G1	P-1.4	11.92	107.0	M(t)	--
G2	P-1.4	11.92	107.5	M(t)	--
G3	P-1.4	11.92	108.2	M(t)	--
G4	P-1.4	7.10	95.7	M(t)	--
G5	P-1.4	9.94	103.1	M(t)	--
G6	P-1.4	7.10	107.6	M(t)	--
G9	P-1.4	7.10	95.2	M(t)	--
H1	S	7.10	106.1	T	D-low
H2	S	9.94	105.5	T	D-middle
H3	S	11.92	105.5	T	D-high
L1	S	7.10	104.7	T	D-low
L2	S	7.10	100.5	T	MD-low
L3	S	9.94	98.3	T	MD-middle
L4	S	11.92	98.6	T	MD-high
M1	S	7.10	96.2	T	--
M2	S	9.94	96.8	T	--
M3	S	11.92	97.0	T	--
N1	S	11.92	109.2	T	--
N2	S	9.94	109.4	T	--
N3	S	7.10	110.0	T	--

Table I (Cont'd)

SCHEDULE OF VACUUM TRIAXIAL TESTS

Test	Membrane	Ambient stress, psi	Density, pcf	Purpose	Density classification
01	S	11.92	94.1	T	L-high
02	S	9.94	93.8	T	L-middle
03	S	7.10	93.8	T	L-low

S = surgical membrane used in long-specimen tests
P-1 = prophylactic membrane, forced to 1-in. diameter
P-1.4 = prophylactic membrane used in normal 1.4-in. diameter
T = soil-property test
M(t) = test to evaluate anomalous membrane effect
D = dense (105 pcf)
MD = medium dense (100 pcf)
L = loose (95 pcf)
high = 11.92-psi ambient stress
middle = 9.94-psi ambient stress
low = 7.10-psi ambient stress

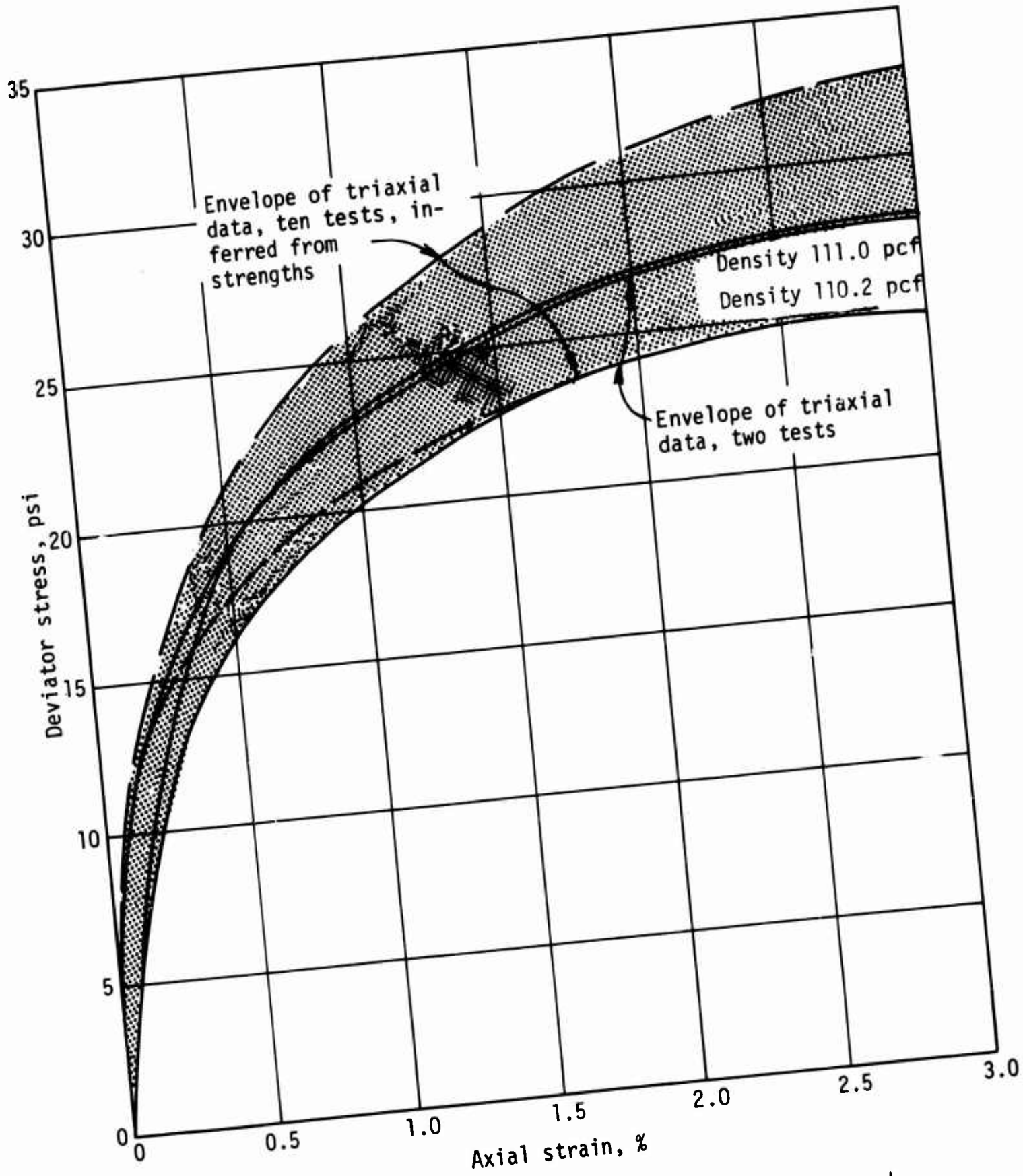

Figure 35. Typical scatter in first-load tests on sand

b. Results of Tests.

As explained in Section IV, the specimens were fabricated in three different ways to yield three densities, arbitrarily referred to as dense, medium dense, and loose. The density results from all tests--triaxial and long specimen--are presented as follows:

Table II

DENSITY RESULTS FROM ALL TESTS

Density classification	Desired density, pcf	Average density from all tests pcf (no. of tests)	Lowest density, pcf	Highest density, pcf
Dense	105	104.9 (22)	103.6	106.1
Medium dense	100	100.1 (11)	98.3	102.0
Loose	95	94.4 (9)	93.4	95.4

Note that, using the best and most careful techniques, the scatter in densities obtained is nevertheless appreciable. In fact, the data reported are somewhat selective; if any specimen evidenced an obvious anomaly, it was destroyed and refabricated without further question. In view of the scatter in simple densities under these ideal conditions, one would be surprised if the stress-strain data did not show some scatter, particularly when the experiences of other researchers are taken into account.

Such scatter did indeed occur, as shown in Figure 36, which contains the largest scatter band of this test series. Shown are the results of seven tests, along with the scatter band or envelope into which they fall. Note that the envelope is broad simply because of the large number of tests used to define it; if Tests 2A and F1 had been discarded--as they might well have been because they diverged grossly from the other tests--the envelope would have been much thinner. The data presented are, however, intended to be realistic rather than complementary. All of the pertinent triaxial data for the nine conditions--three densities and three ambients--are given in Figures 36 through 44. Shown on these figures are the data (corrected for seating errors if required), the envelope, and a best-fit smoothed curve found by analytic procedures and described in the following.

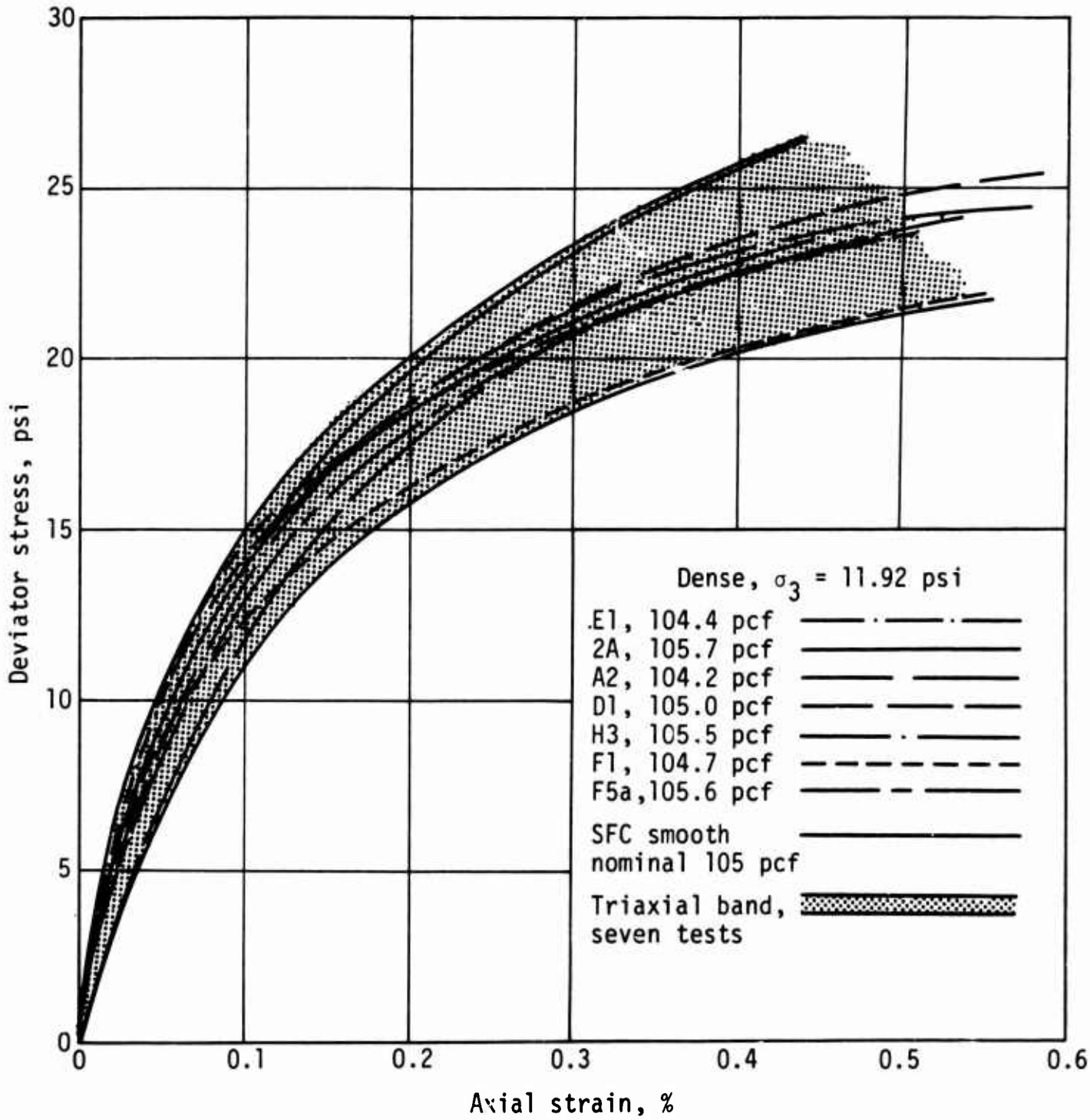

Figure 36. Triaxial results: dense, high-ambient stress

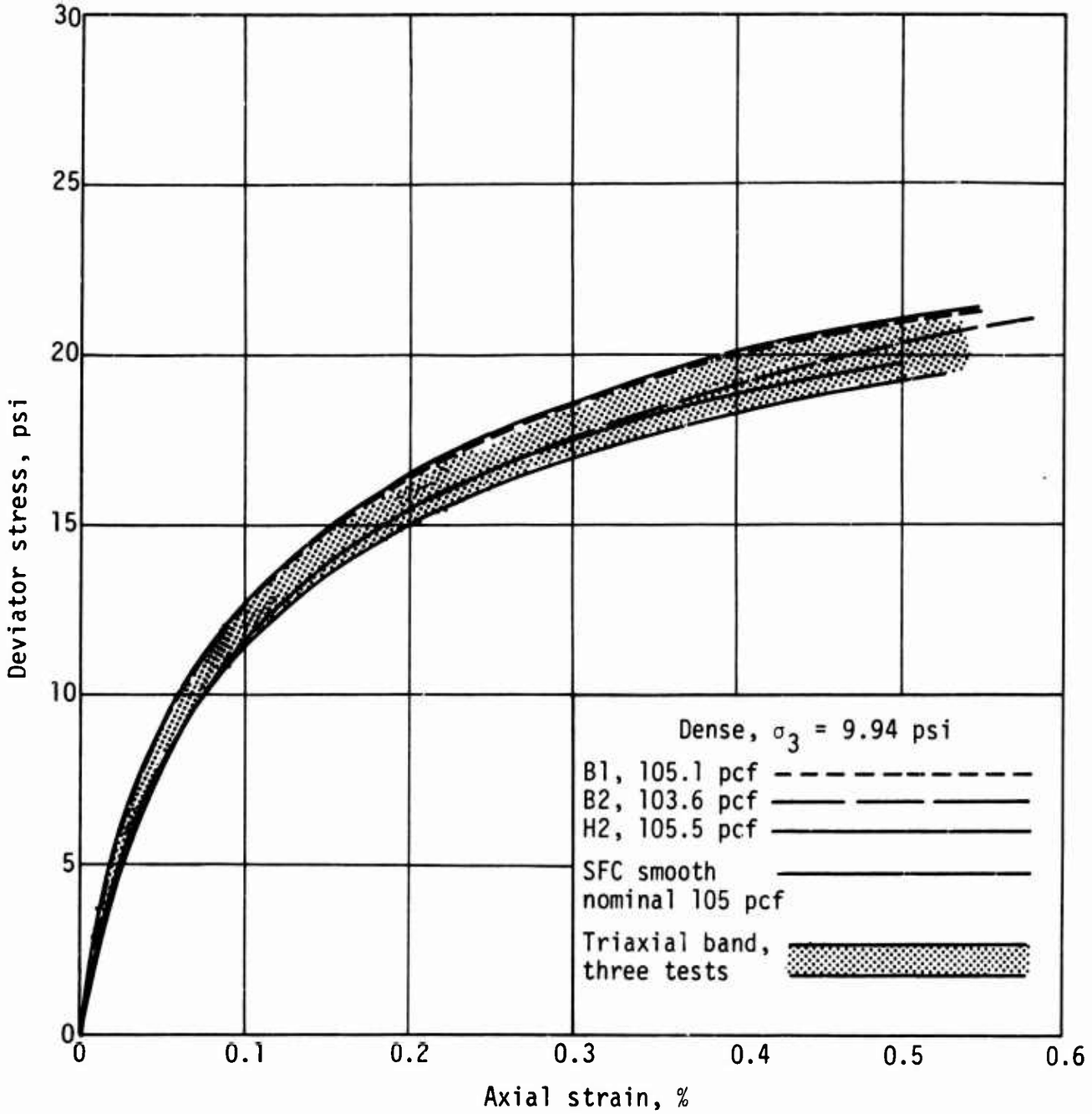

Figure 37. Triaxial results: dense, middle-ambient stress

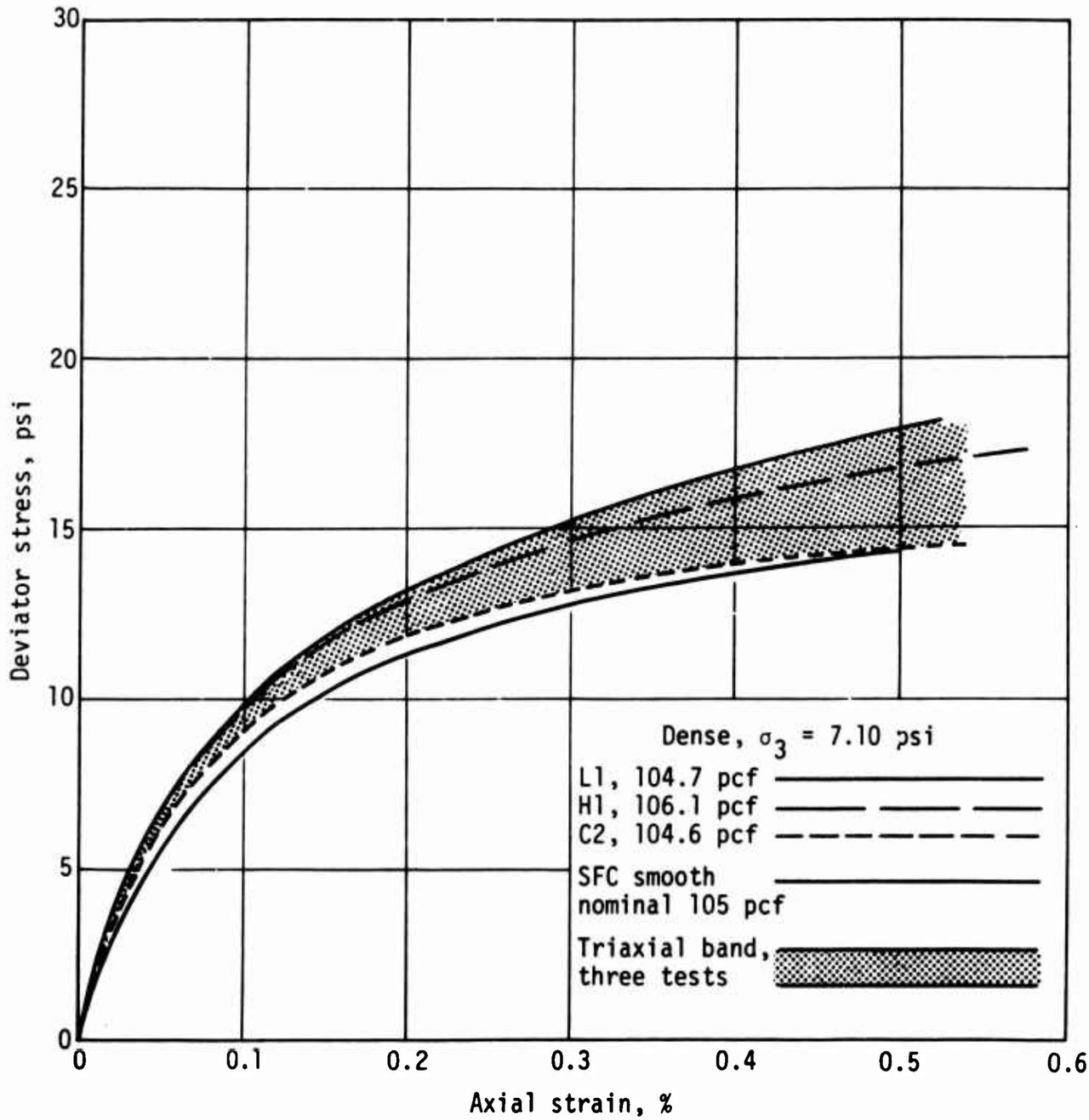

Figure 38. Triaxial results: dense, low-ambient stress

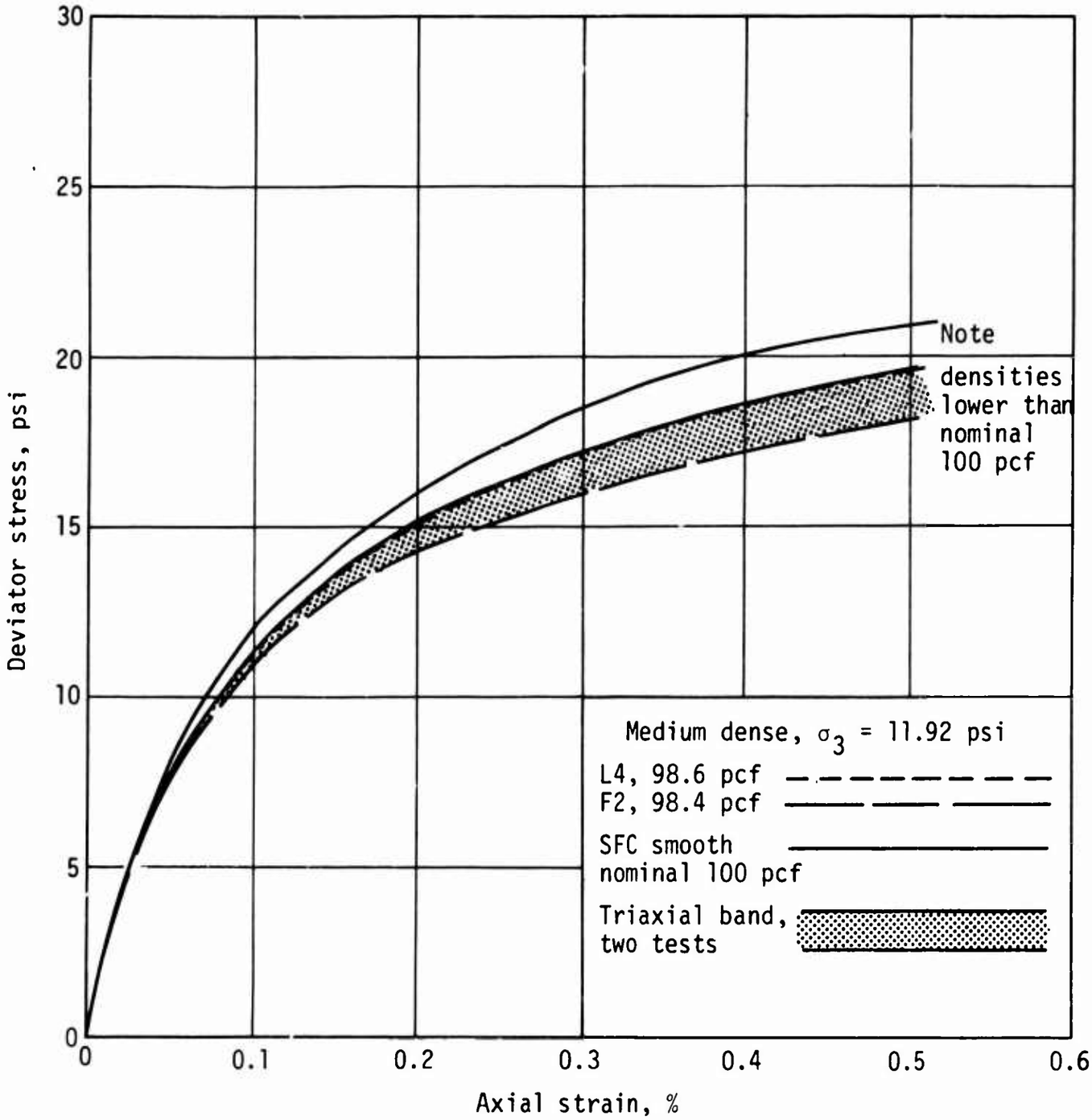

Figure 39. Triaxial results: medium-dense, high-ambient stress

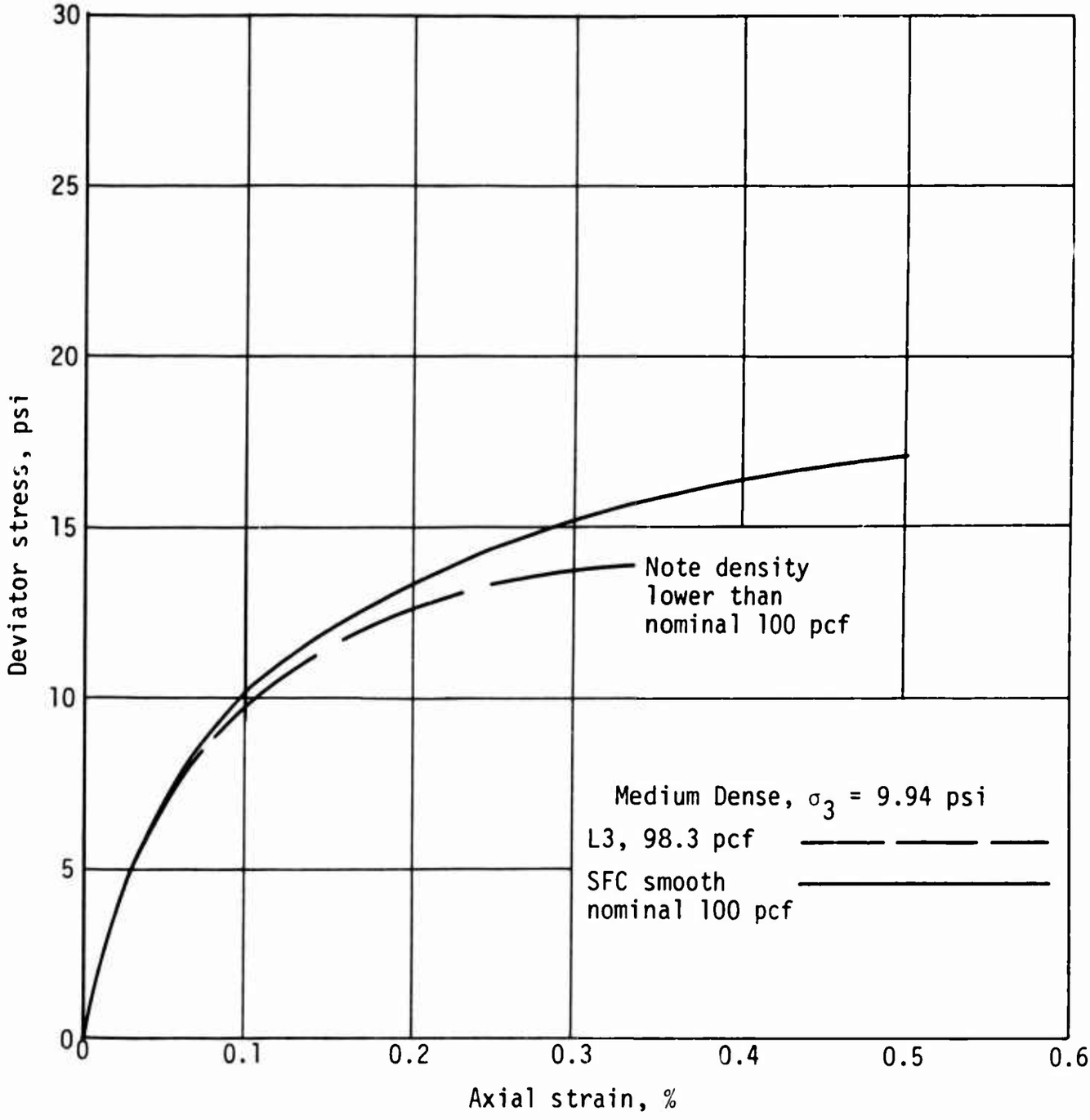

Figure 40. Triaxial results: medium-dense, middle-ambient stress

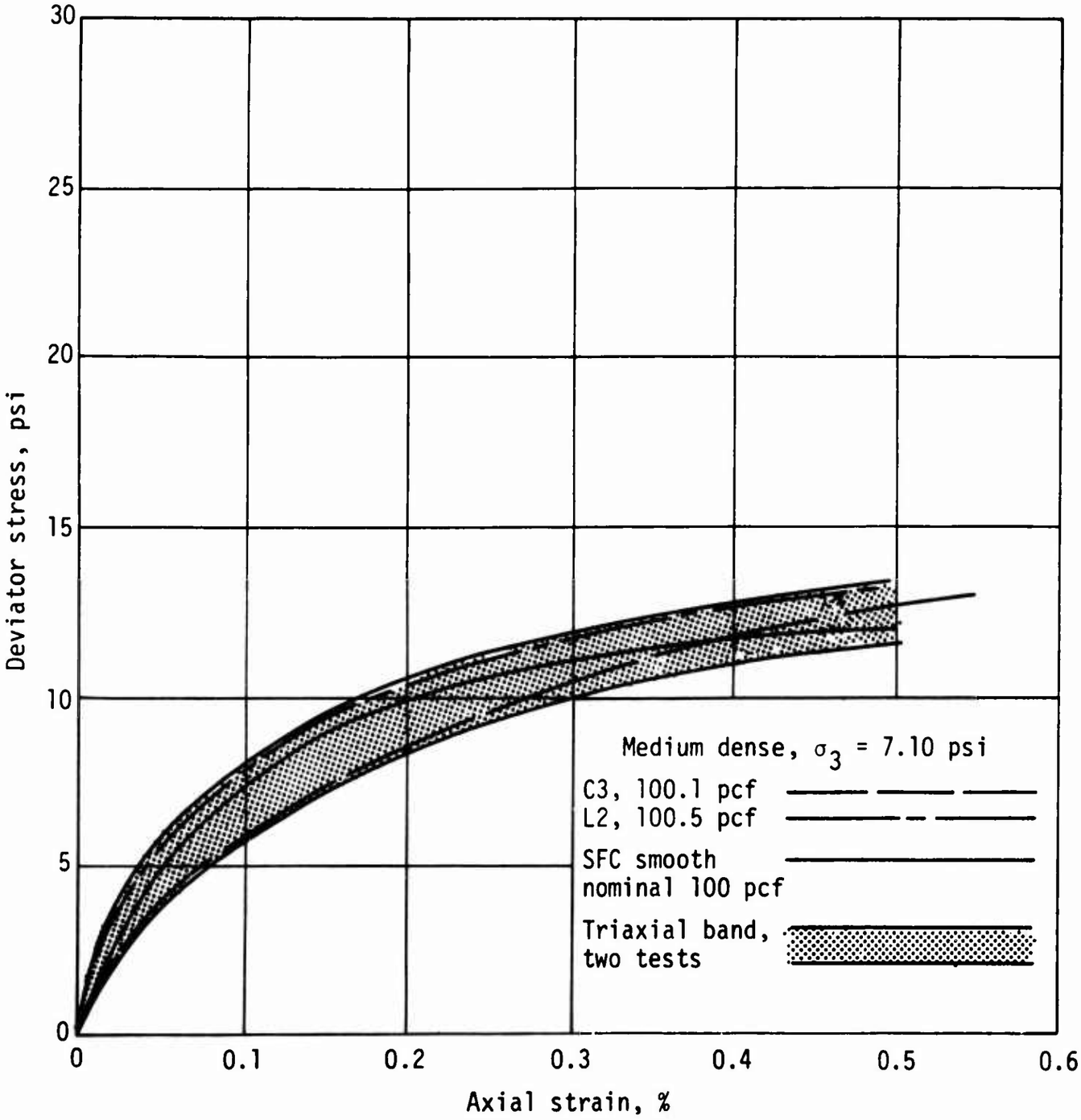

Figure 41. Triaxial results: medium-dense, low-ambient stress

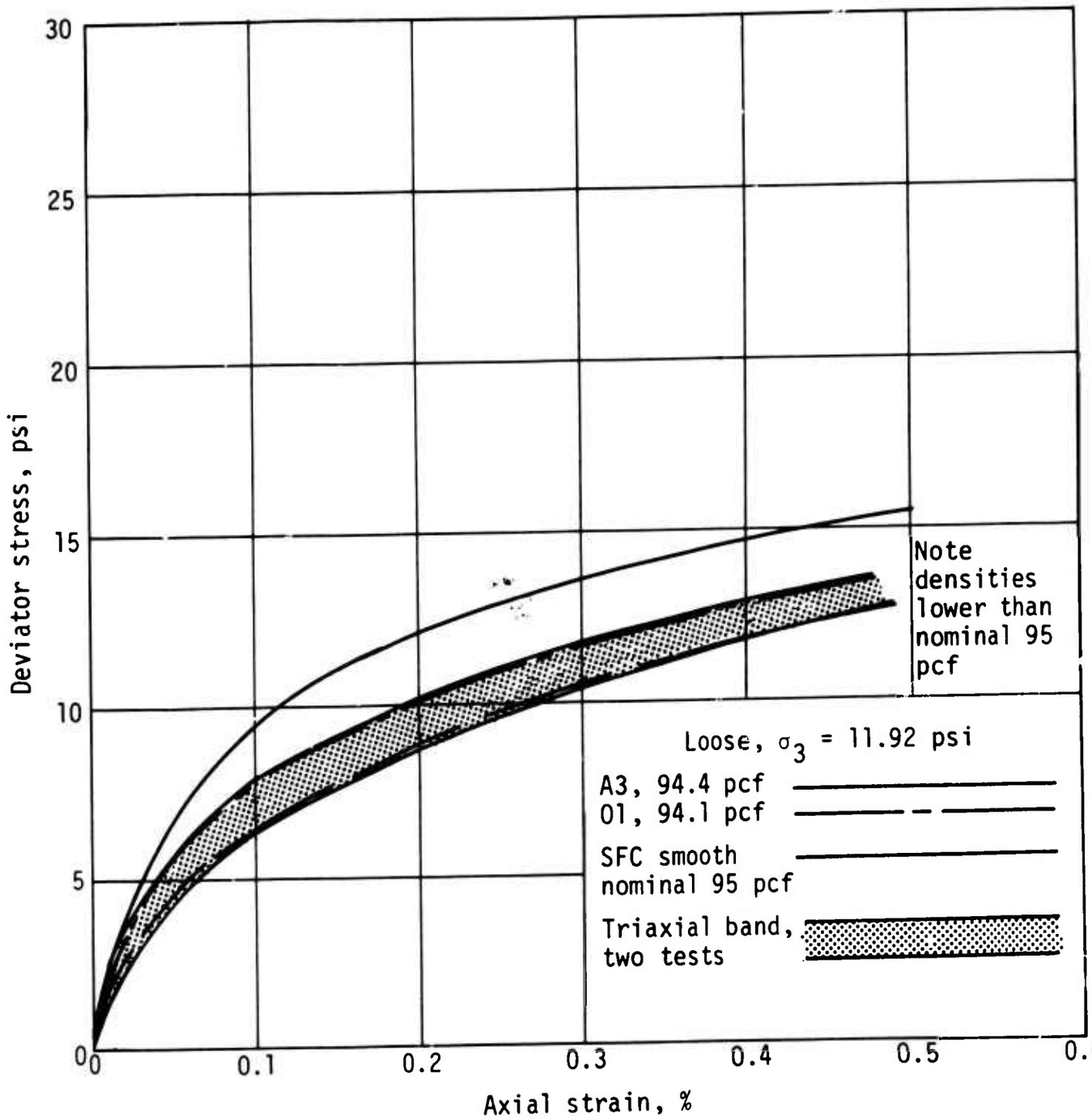

Figure 42. Triaxial results: loose, high-ambient stress

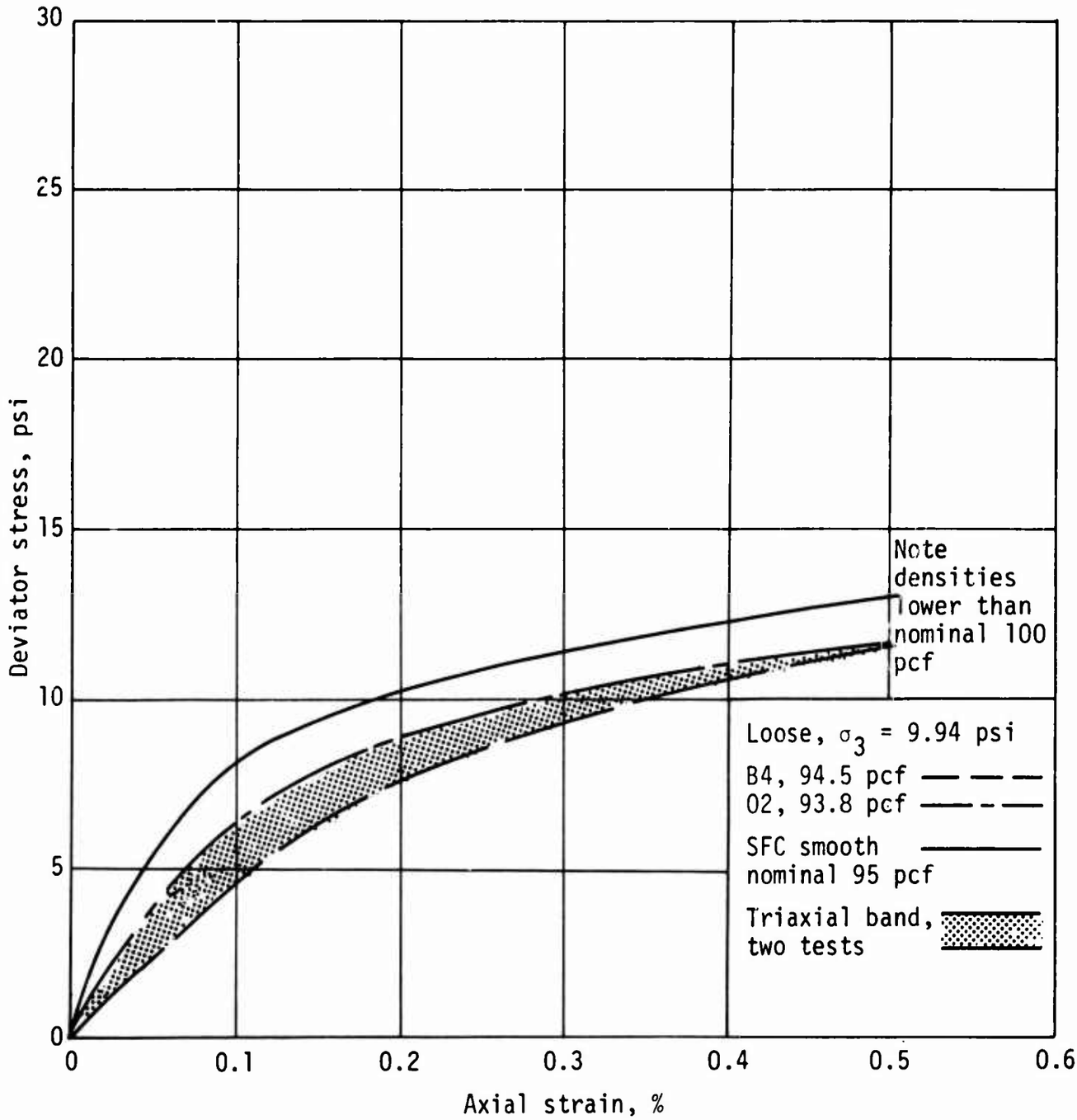

Figure 43. Triaxial results: loose, middle-ambient stress

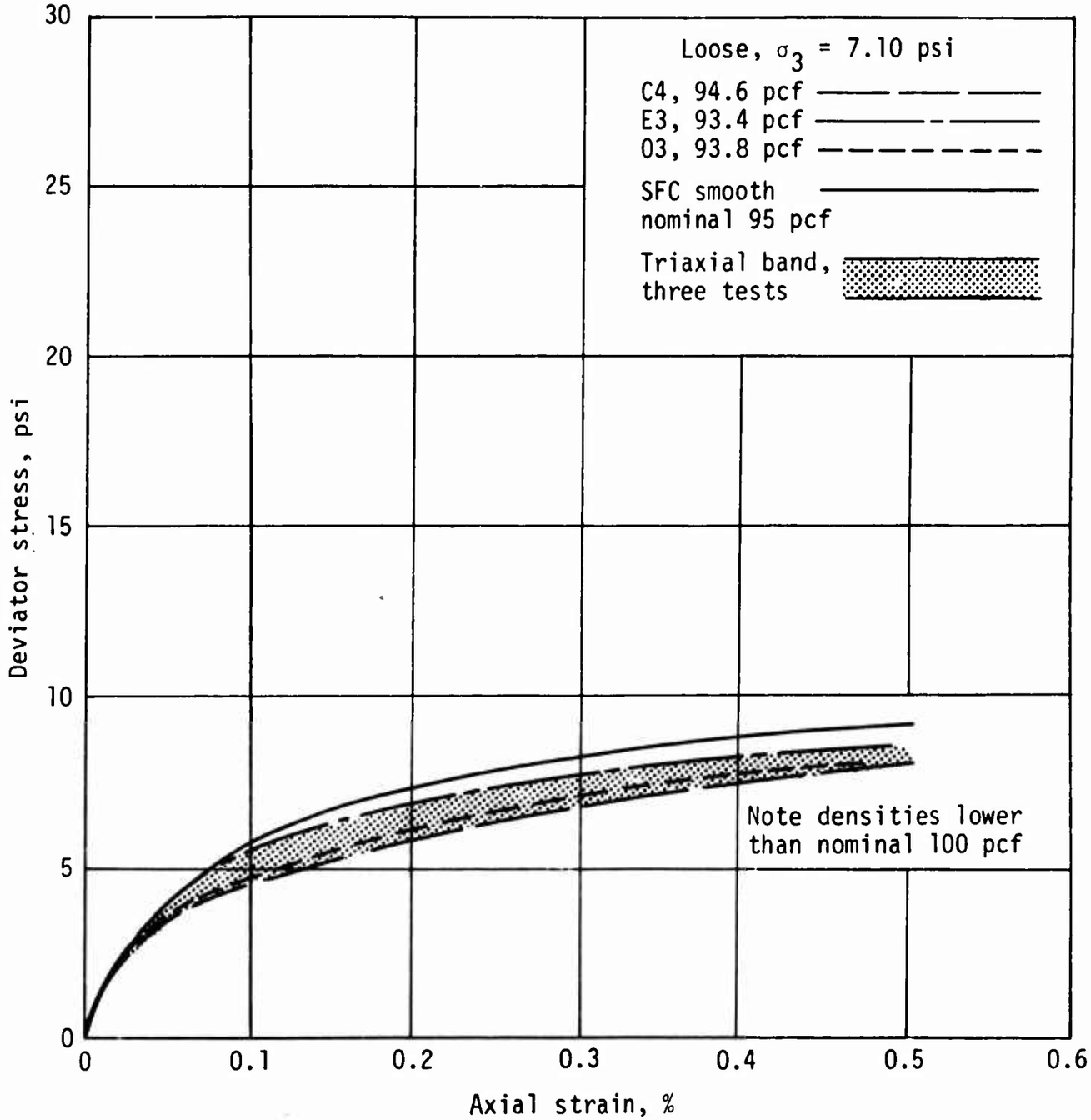

Figure 44. Triaxial results: loose, low-ambient stress

2. Analysis by Subfailure Coulombic (SFC) Method.

a. The SFC Method.

There are several ways in which the data could be analyzed to arrive at a single best-fit curve:

(1) by drawing a line through the center of the envelope;

(2) by taking an arithmetic average of the tests available for that envelope;

(3) by forcing a fit to an explicit mathematical curve, using the tests available for that envelope.

These three approaches were rejected because they would have depended on the number of tests available for any one density-ambient condition. For example, any of the three approaches might have been adequately accurate using the seven tests of Figure 36, but none of them could have done much with the single test on Figure 40. Furthermore, all of these three methods would have depended on the conditions being the same for all the tests defining the envelope. Specifically, this dependence is erroneous when applied to the densities, as shown by Table II and data recorded on the figures (such methods, especially the third, have been applied with success, however, as reported in Refs. 55,56,58). For these reasons it was decided to use another approach to analyze these data.

The approach should include all variables--stress, strain, density, and ambient stress--from all tests in such a way that the trends of the entire test series could be used to adjust or guide the analysis of one test. The presumption is that the behavior will always vary smoothly and consistently as the variables are varied. Having presumed this, it was necessary to assume some pattern that the behavior might logically follow.

For example, experience with cohesionless soils demonstrates the fact that the stress-strain curve is steeper for higher densities; or more precisely, the stress required to cause a given strain is higher for higher densities. This fact was recognized in the following analysis (to be explained with the aid of the sketches in Fig. 45). Because the three ambient stresses were invariant quantities for all the tests, the data for each of the three ambient stresses were plotted together, yielding three sets of stress-strain curves, each of which differed only in density (Fig. 45a). Then, for each ambient stress, with the use of fine strain mesh, a plot was made of the stress required to cause a specific strain as a function of density (Fig. 45b). From that plot a fitted stress-strain curve could be drawn for any density (Fig. 45c). Such curves would

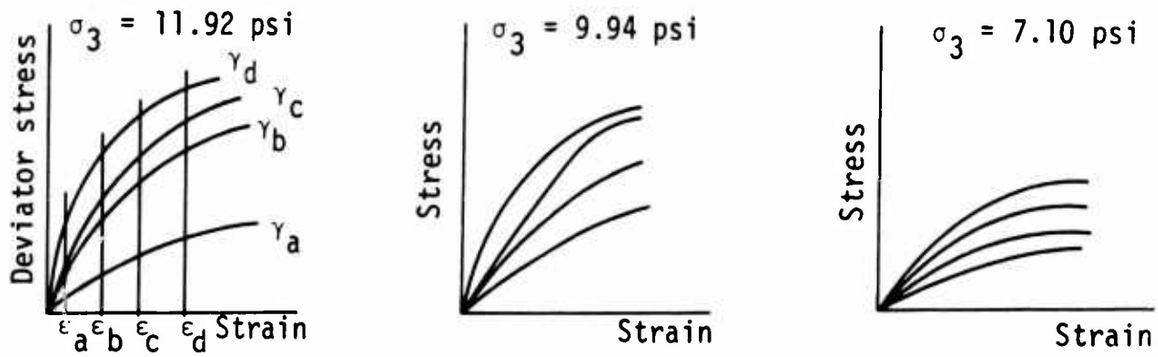

(a) Parametricizing on ambient stress

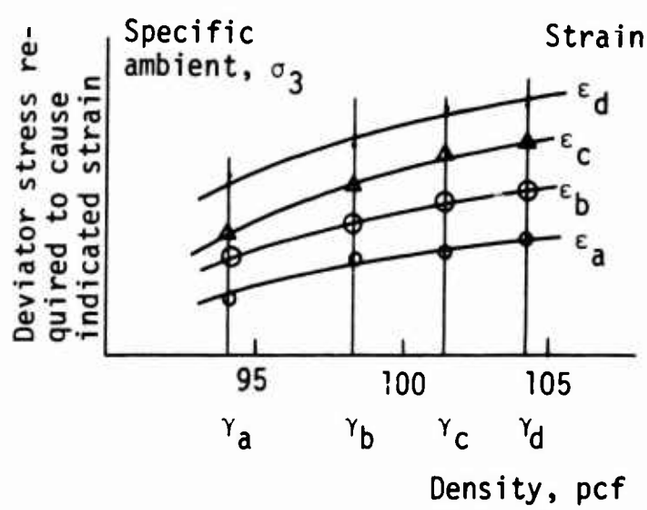

(b) Smoothing stress-density curves

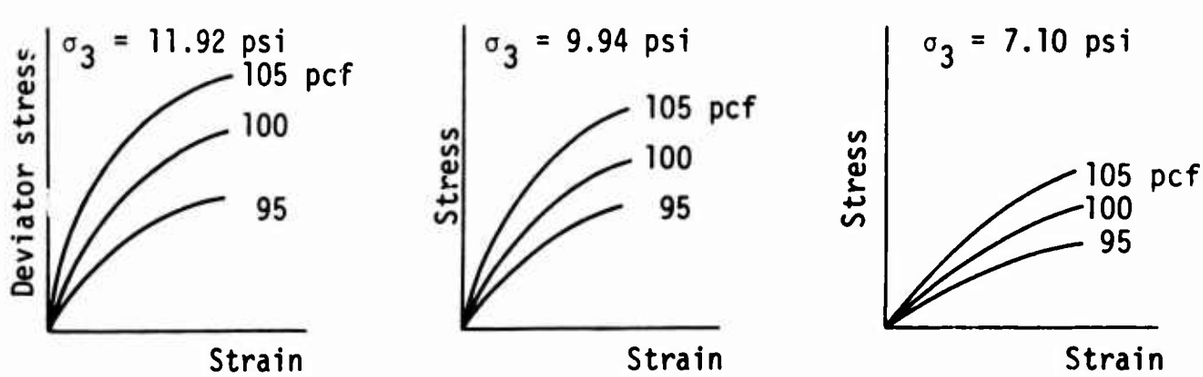

(c) Semi-smooth stress-strain curves

Figure 45. Preparatory analysis of triaxial results

be consistent for density, but not necessarily for ambient stress. For this cohesionless sand, however, an additional smoothing on ambient stress was attempted.

The second smoothing requires the assumption that the material is *subfailure coulombic* (SFC): that is, at stresses *below* failure the stress required to cause a given strain is controlled by Coulomb's equation.

$$\tau = \sigma_p \tan \phi_p \tag{30}$$

where

τ = shear stress

ϕ_p = subfailure coulombic stress angle at specific plastic strain

An important observation of the application of the SFC technique is that the Mohr's circles of stress for a given strain with different ambient stresses become tangent to the same straight line passing through the origin for all tests on material possessing the same density. This fact was utilized to force ambient-stress consistency by the SFC method on specimens of the same density. To prepare for the analysis, the data of Figure 45b (which are actually three plots, one for each ambient) were interpolated at the three arbitrary densities--95, 100, 105 pcf--and used to draw semismooth stress-strain curves (Fig. 45c). Those curves were then used, with a fine strain mesh, to draw Mohr's circles to which a straight line, Coulomb envelope could be fitted for each specific density, as in Figure 46. The fitted envelope was then used for each ambient stress to backcompute the stress required to cause the strain represented by the envelope. With these fitted data available, it was possible to construct a stress-density curve similar to that in Figure 45b. Each set of such curves formed a consistent and smooth family, from which the stress-strain curve could be constructed for any combination of density and ambient stress. For example, Figure 47 shows the nine curves for the three arbitrary densities and the three ambient stresses.

This smoothing technique forces consistency on the variable density and ambient stress for the entire test series and does not necessarily yield results closely consistent with an individual test or two for one set of density versus ambient-stress conditions. For example, note that the smoothing agrees quite well with the enveloped data in Figures 36, 37, and 41; falls above the envelopes in Figures 39, 40, 42, 43, and 44, where the test densities were *lower* than the *arbitrary value* of the SFC-smoothed curve; and falls slightly below the envelope in Figure 38.

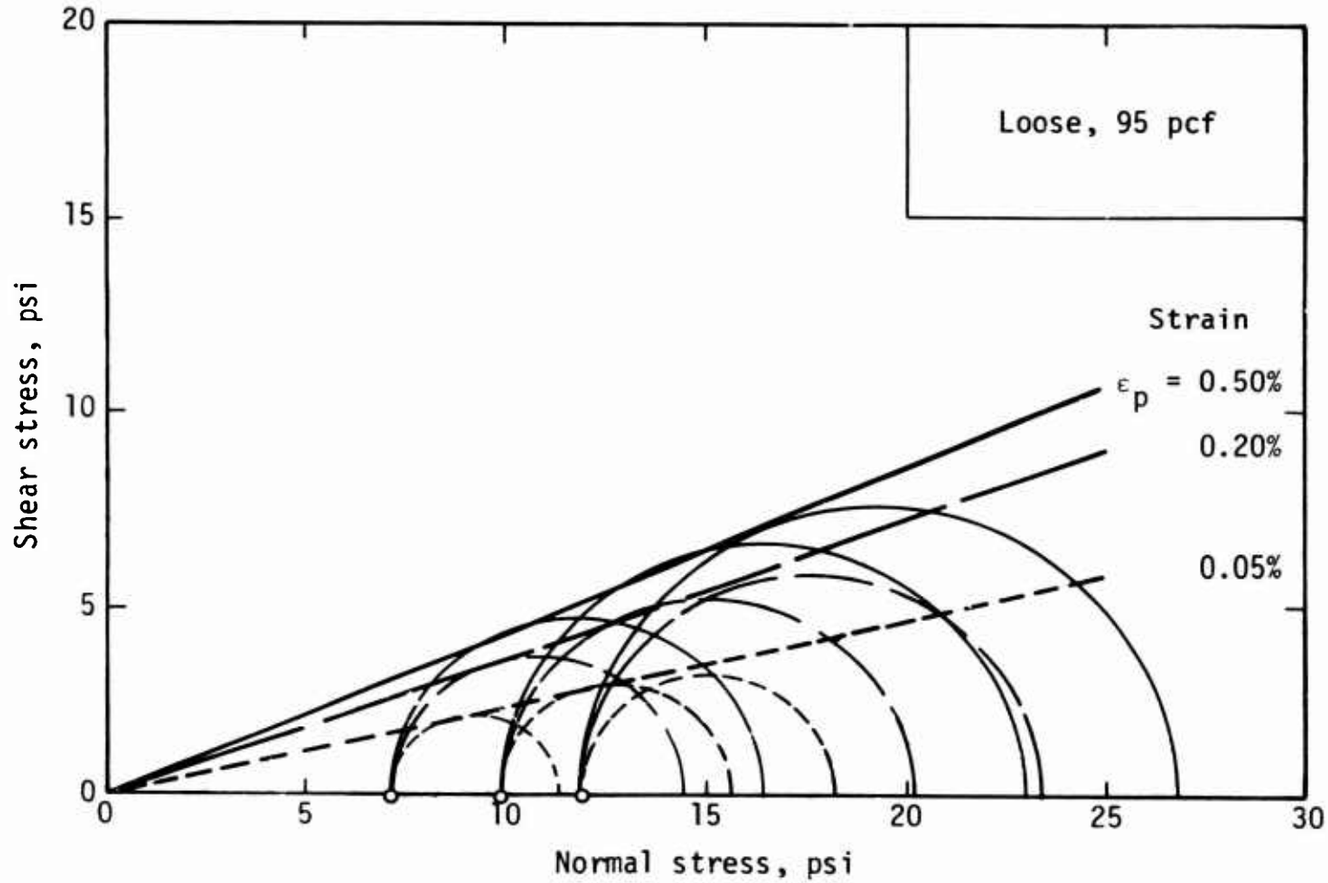

Figure 46. SFC smoothing of triaxial results

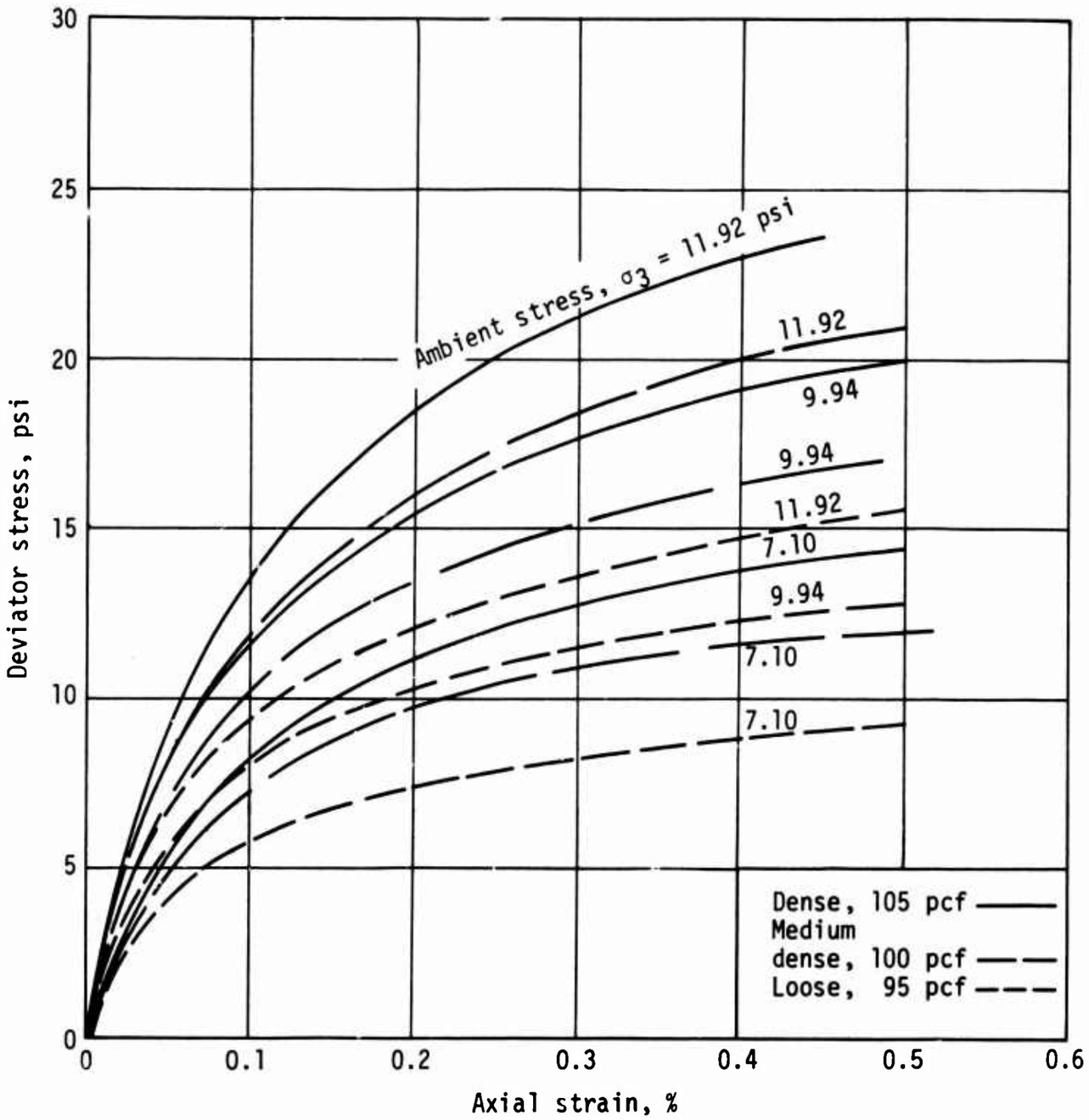

Figure 47. SFC-smoothed stress-strain curves

Although the application of the SFC method to the lower strains has not been strictly verified by previous experiment, it was used here because

(1) it obviated the objections to approaches 1 through 3 above;

(2) it forced consistency between ambient stress and density;

(3) it allowed, for the analyses to follow, the computation of low-strain seismic parameters directly from the data in Figure 10;

(4) it seemed to yield a close approximation to the actual stress-strain curves; and

(5) it resulted in some sweeping simplifications in waveform computations for those soils that exhibited the SFC property to an engineering approximation (see Section VI).

b. Summary of Analyzed Results.

The bands in Figures 36 through 44 and the SFC-smoothed stress-strain curves are the basic comparative data results from this set of triaxial tests.

3. Pilot Wave-Propagation Tests.

a. Series A.

This test series was designed only to check out the equipment and instrumentation, to verify the specimen-handling techniques, and to obtain some rough data to see if any problems existed. To these ends a single dense specimen was fabricated and subjected to the high-ambient stress. The specimen was fabricated as described in Section IV. The needle-and-flag placement and positioning technique were tried several times to perfect it and to train the operators. Since after this practice the specimen was in something less than an undisturbed condition, no quantitative significance was assigned to this test.

The data were recorded on scopes, with the use of makeshift triggers for the practice run. The specimen was shot several times at progressively increasing stresses until failure by buckling occurred at slightly less than the failure strength as found in the literature (Ref. 34). The data were only partially recorded because some of the scopes would fail to trigger from time to time. At this time the displacement-measuring stations were located at about 6-inch centers along the specimen. Because cursory analysis of the data from this preliminary test showed that closer spacings were required for accurate data reduction, steps were initiated to acquire and install those additional stations.

When the corrections indicated by this first pilot series were partially complete, a second pilot series was performed.

b. Series B.

For this second series, better specimen-placement techniques, more adequate scope triggers, and some of the additional displacement-measuring stations were in hand. Since there were not enough scopes available to read all instruments simultaneously, 12 shots were performed on the specimen so that each instrument could be verified.

Analysis of the data showed that, using the internal scope amplifiers, the signals were essentially noise free and were completely adequate in amplitude for accurate reduction. Scope recording was inadequate, however, for four reasons:

(1) if the amplitude of duration of the event were estimated incorrectly, the resulting readout could be too cramped or could miss the main data entirely;

(2) because the readout was only from one Polaroid picture per scope, detailed study of a part of the event was possible only by tedious and rather inaccurate projection techniques;

(3) time referencing of all the channels was somewhat difficult to achieve with the limited number of scopes available; and

(4) even after a warmup period of several hours most channels would drift between the setup and calibration procedure and the actual shot (30-60 minutes).

It was decided, therefore, to build a panel of bucking (potentiometer) circuits to dc-zero each instrument immediately before firing, and to record on magnetic tape so that the event could be read and studied in expanded detail. These decisions were necessary in order that the 17 channels of instrumentation could be obtained simultaneously, properly coordinated in time. The decisions did, however, create a problem that was not fully appreciated until the main experiments began. This was electrical noise, which was apparently created by the bucking circuits, the high preamplification needed for the tape recorders, and the long lines needed to reach the recorders, which were remote from the test area. This electrical noise and the limitations it imposed will be discussed with the presentation of the main data.

Although the specimen was shot many times at just below its failure strength, it buckled in only a few of the shots. The buckles were minor and were simply pushed back into place for this practice series.

c. Conclusions from Pilot Tests.

On the basis of these two pilot tests, specimen fabrication and placement techniques and needle-flag placement and positioning techniques were perfected. Additional displacement-measuring stations were installed, and the design of the force links was slightly modified to minimize the eccentricities and to make handling and operation easier. It was decided that the foam bed was adequate to prevent buckling. As will be explained, this conclusion proved somewhat incorrect when more cutouts for the additional displacement-measuring stations were installed, and a new foam-bed design was required; unfortunately, this was not apparent until almost half of the main experiments were completed; at that time the cutout points were reinforced to eliminate the buckling. It was further decided that all instruments were yielding adequate, noise-free signals. This conclusion was found to be somewhat in error with respect to noise when the main experiments were remote recorded.

In summary, all procedures and systems functioned more than adequately except for the buckling of the foam bed (which was corrected halfway through the main experiments) and the noise in the remote system (which could not be corrected with the equipment available and the conditions prevailing at the time of the main experiments).

4. Static Long-Specimen Tests.

The static long-specimen tests that were performed are summarized in Table III. The method for performing the long-specimen tests is described in Section IV. Detailed test data, along with the analysis and complete results, are given in Appendix B. Only the conclusions of these tests are given here.

Results of the early tests, performed before the additional cutouts in the form were reinforced, agreed closely with SFC curves at their density up to stresses just under 10 psi (about half the strength), at which point buckling occurred, with the result that the static long-specimen stress-strain curve dropped below the SFC curve. Results of the later tests, performed after the cutouts were reinforced, agreed well with the SFC curves, and usually lay above the SFC curves if disagreement existed.

On the basis of the agreement between these tests and the SFC curves, it was concluded that either could be used as a basis for static comparison with the dynamic experiments. Because the SFC curves provided more data extending all the way to shear failure, and because those curves would allow construction of

Table III

SUMMARY OF STATIC LONG-SPECIMEN TESTS

Test	Time code*	Ambient stress, psi	Density, pcf	Density classification†
C	244-0800	11.92	104.7	D-high
D	244-0900	11.92	104.9	D-high
E	244-1000	11.92	95.4	L-high
F	244-1100	11.92	98.8	MD-high
L	252-0900	9.94	105.0	D-middle
P	252-1200	7.10	104.6	D-low
S	253-0900	9.94	100.9	MD-middle
U	253-1100	7.10	100.7	MD-low

*Reference code for tape-recorded data

†Classification according to nominal density and ambient stress:
D = dense (105 pcf)
MD = medium dense (100 pcf)
L = loose (95 pcf)
high = 11.92 psi
middle = 9.94 psi
low = 7.10 psi

the stress-strain curve for each dynamic experiment at its own density and ambient stress, it was decided to use the SFC curves as the basis for static comparison with the dynamic experiments.

5. Wave-Propagation Tests.

a. Scope of Tests.

Table IV summarizes the wave-propagation experiments.

Since Test G (248-0800) clearly buckled early in the event, it was redone as Test K (252-0800). Test M (not shown in the table) yielded no data because the diaphragm preruptured; it was redone as Test N (252-1100). Notice that all three ambient stresses were used for two of the densities, dense and medium dense, but that only the high-ambient stress was used for the loose specimen. The middle- and low-ambient stresses were not used for the loose specimens for two reasons: since the specimens at these ambients were extremely soft and difficult to handle, the results would have been of questionable validity; and the extremely soft behavior might have had little engineering significance.

b. Data from Experiments.

The methods of performing the wave-propagation tests and of recording the data were described in detail in Section IV: the specimen was loaded by a soft-fronted pulse (1 to 2 msec) generated by rupturing the diaphragm in a shock tube; the loads were recorded on force links at the front and rear of the specimen; and displacements were measured by light gages. A piezoelectric pressure gage in the expansion chamber of the shock tube was used to provide a common-time event.

Typical photographic readout is shown in Figure 48. The upper trace is the piezoelectric gage in the expansion chamber; its initiation is taken as zero time. The lower trace is typical of the raw data for a displacement gage (here, B-1). These data were processed on the computer for more accurate interpretation (as was done for the static tests), and two computer readouts were obtained: one to show the entire event (Fig. 49), and one with the initial part of the event expanded in amplitude and time (Fig. 50).

The same types of typical raw and computer-reduced data are shown for the front force link in Figures 51 through 53 and for the back force link in Figures 54 through 56. Although complete faith should not be placed in the exact amplitude readings from these force links, the time histories should be correct.

Table IV

SUMMARY OF WAVE-PROPAGATION TESTS

Test	Time code*	Ambient stress, psi	Density, pcf	Density classification†
G	248-0800	11.92	105.2	D-high
H	248-0900	11.92	101.8	MD-high
J	248-1100	11.92	95.1	L-high
K	252-0800	11.92	104.5	D-high
N	252-1100	9.94	105.0	D-middle
R	253-0800	7.10	104.2	D-low
T	253-1000	9.94	99.9	MD-middle
V	253-1200	7.10	102.0	MD-low

*Reference code for tape-recorded data

†Classification according to nominal density and ambient stress:
D = dense (105 pcf)
MD = medium dense (100 pcf)
L = loose (95 pcf)
high = 11.92 psi
middle = 9.94 psi
low = 7.10 psi

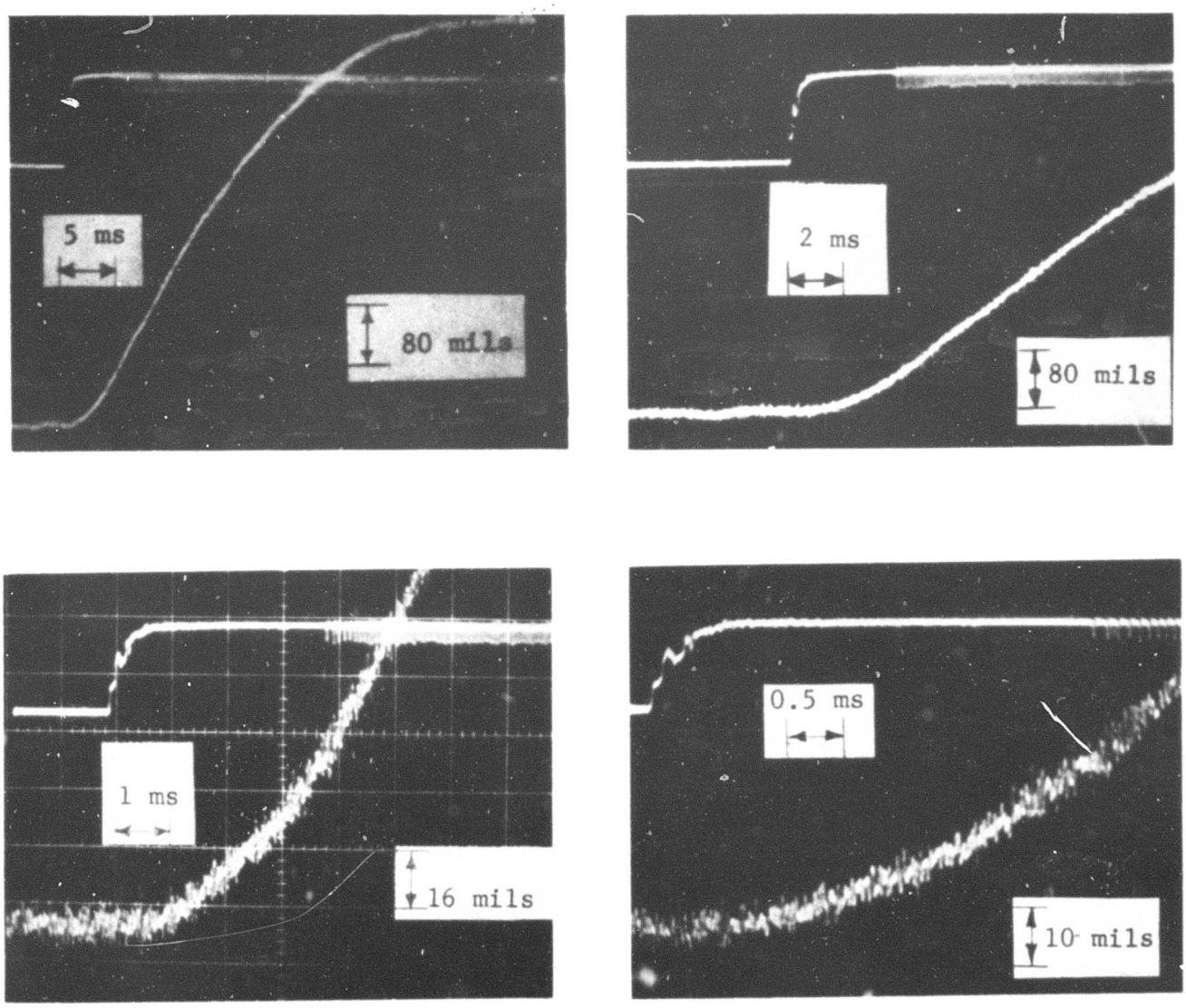

Figure 48. Displacement gages: typical raw data

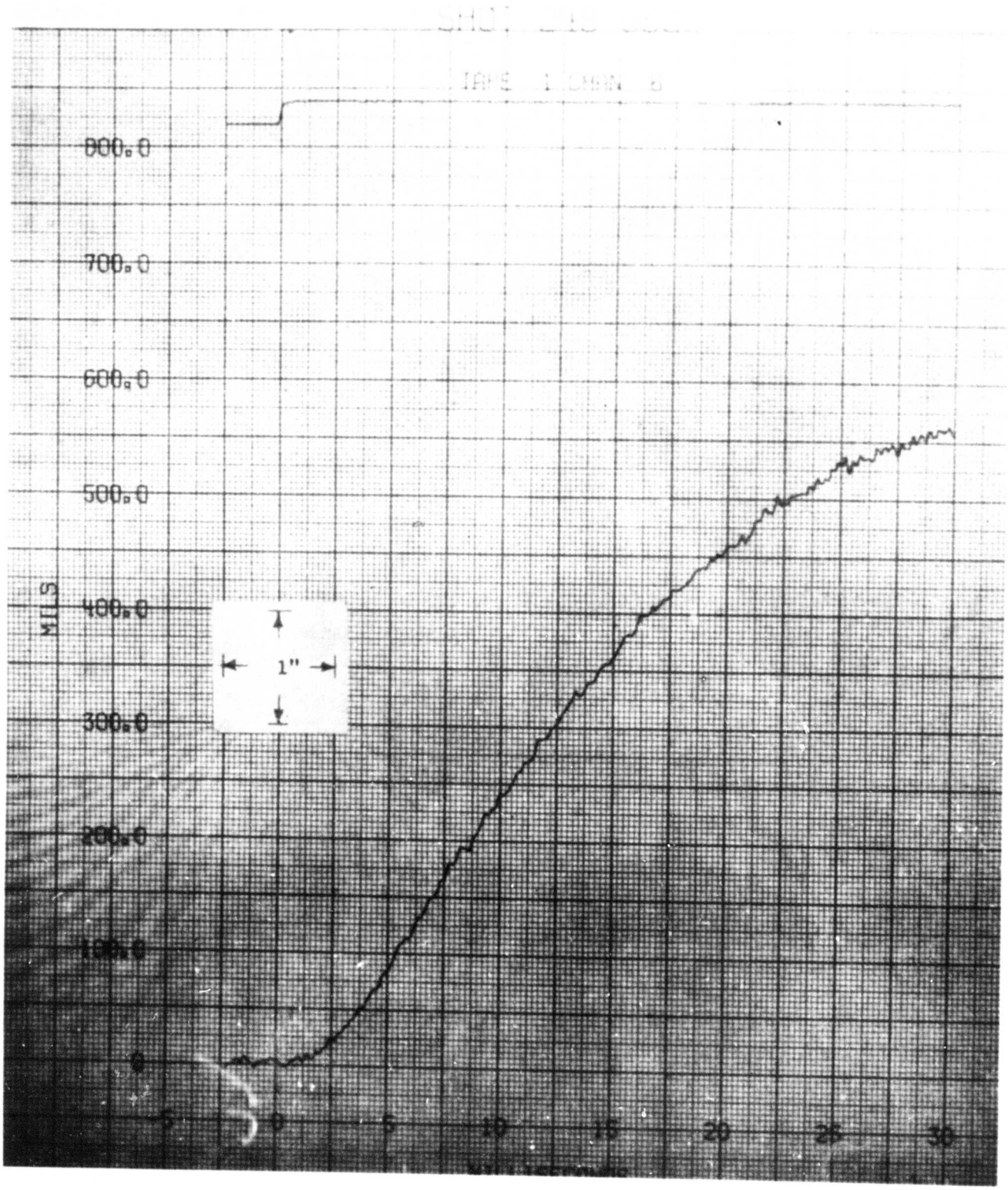

Figure 49. Displacement gages: typical full-event computer reduction

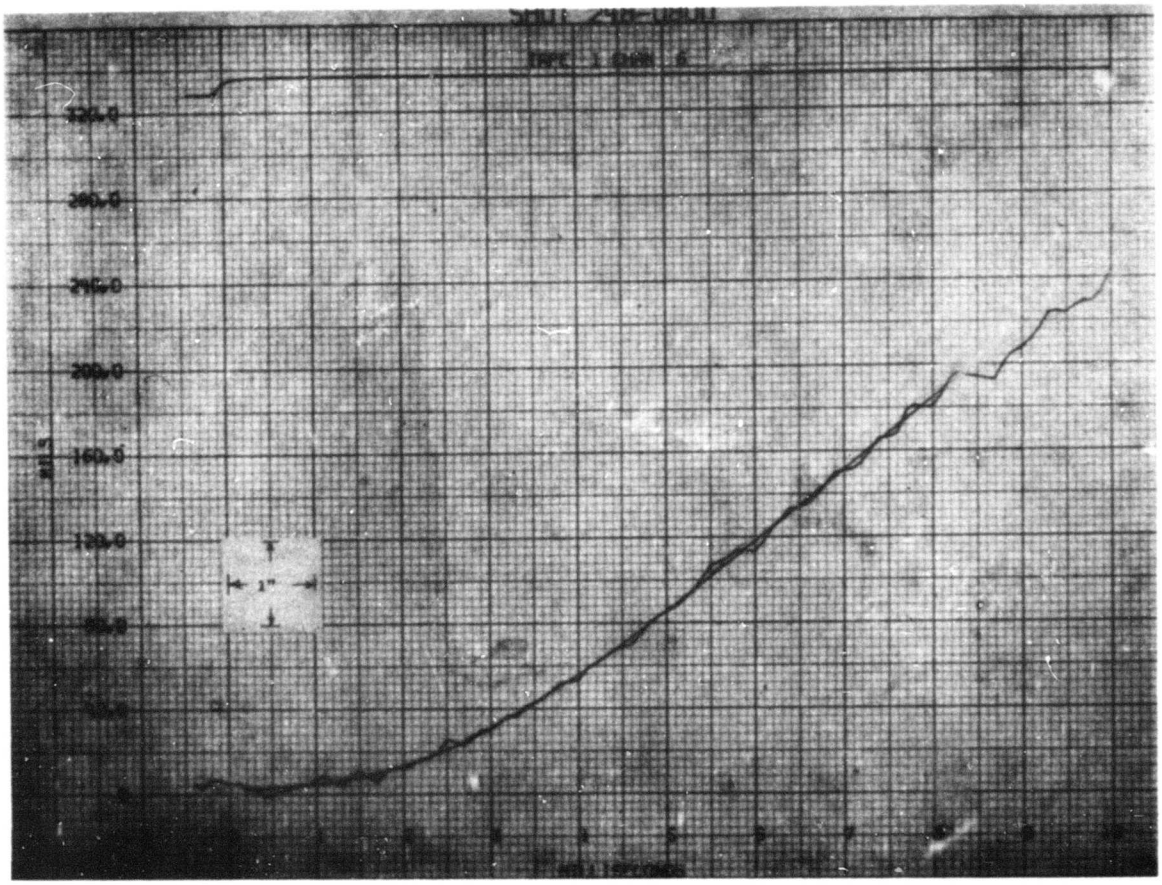

Figure 50. Displacement gages: typical expanded computer reduction

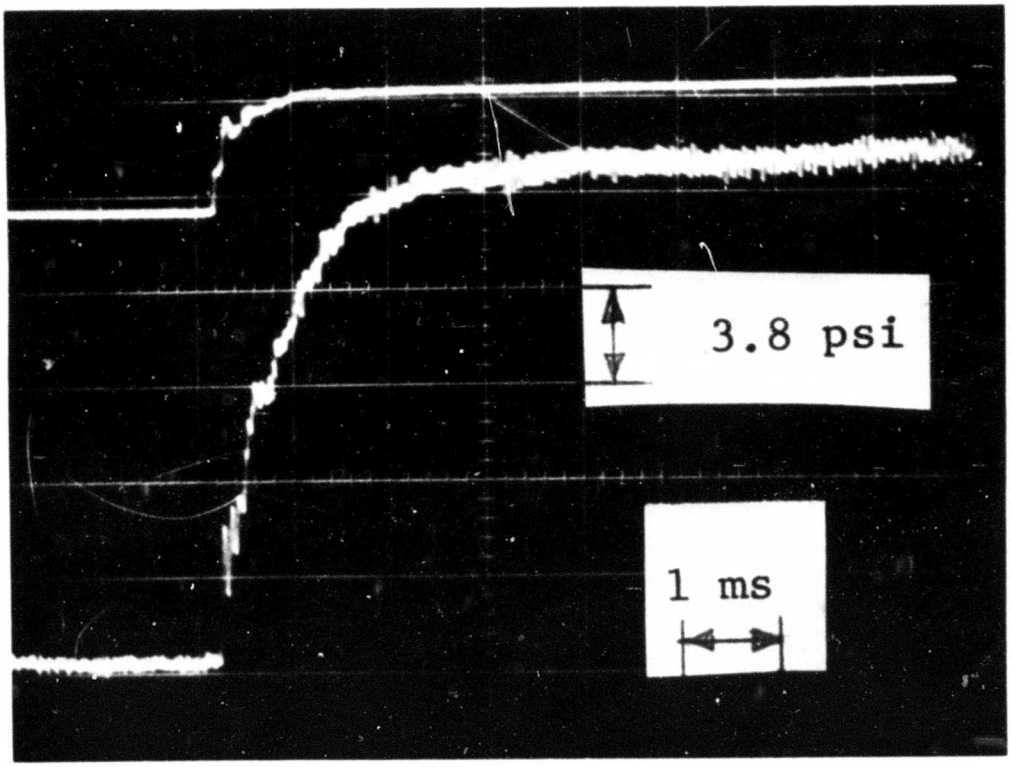

Figure 51. Front force link: typical raw data

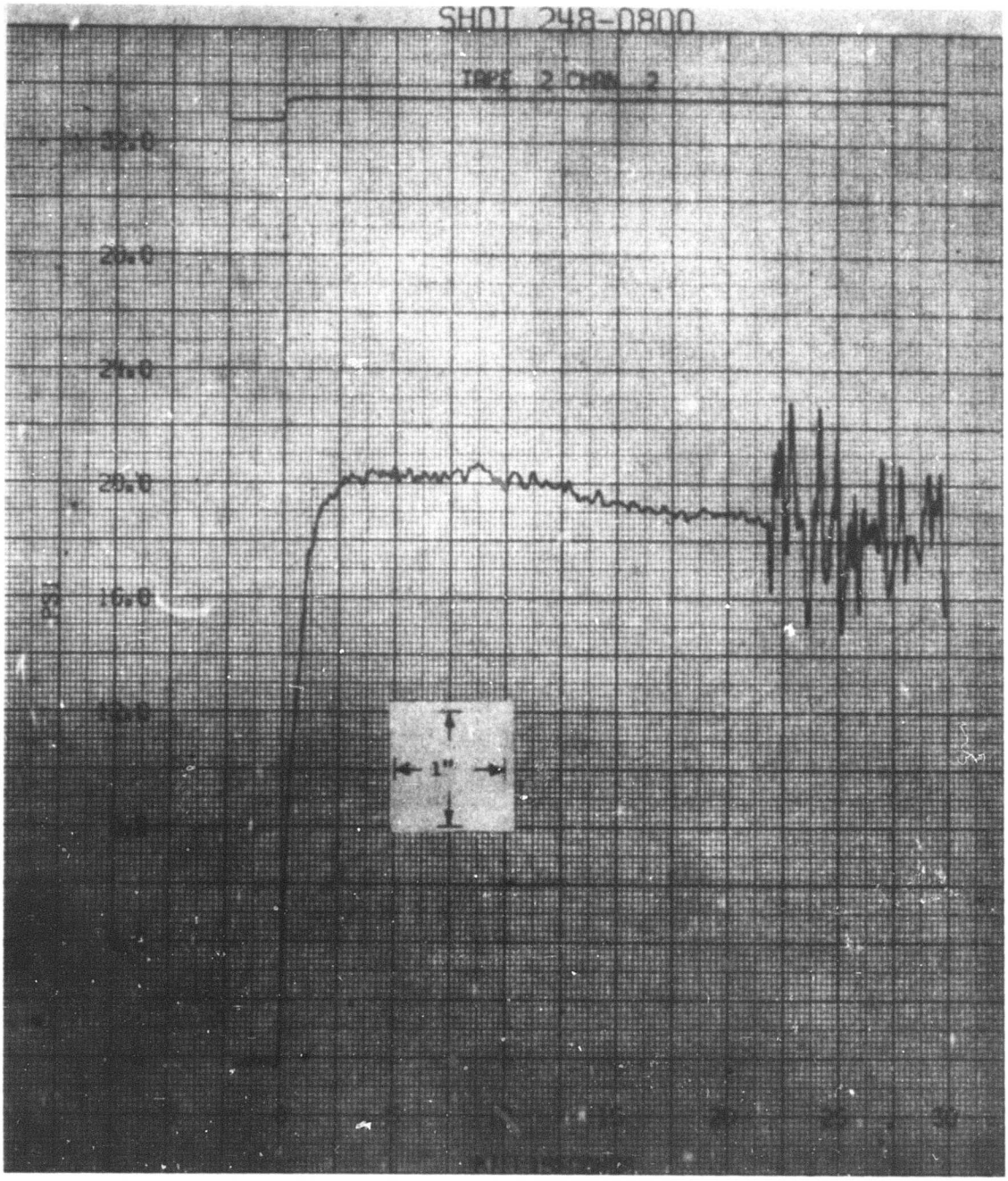

Figure 52. Front force link: typical full-event computer reduction

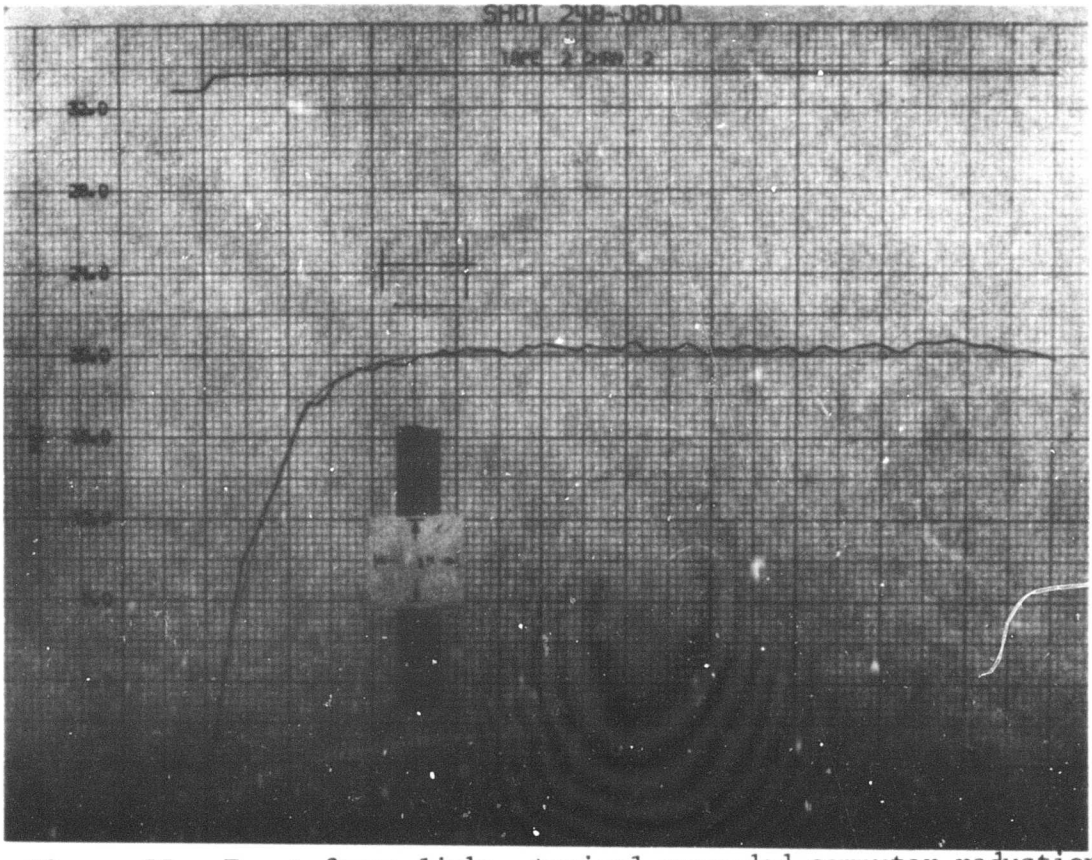

Figure 53. Front force link: typical expanded computer reduction

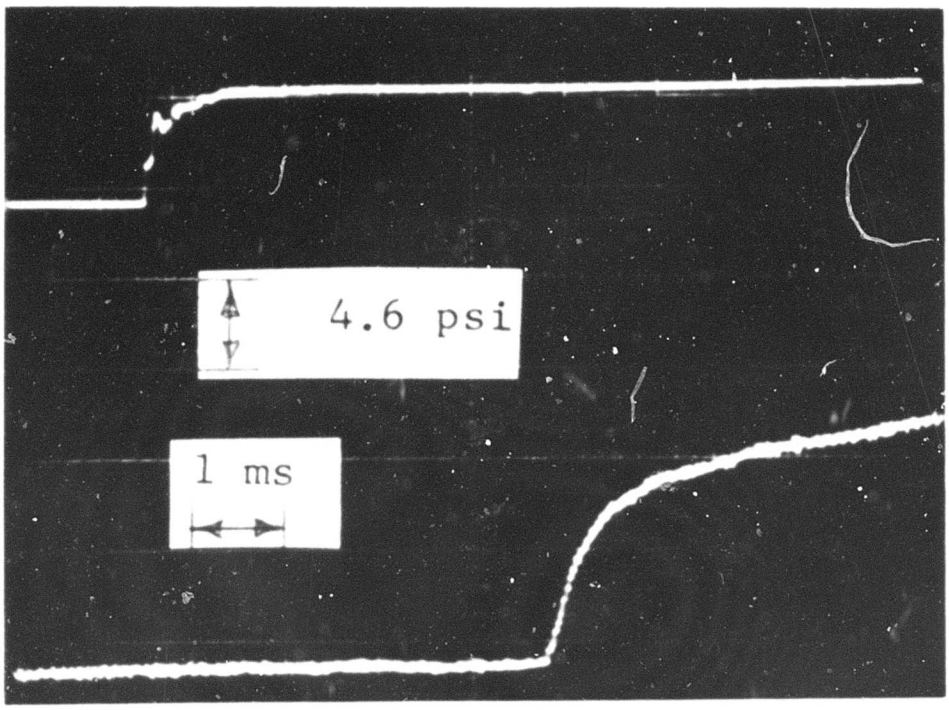

Figure 54. Back force link: typical raw data

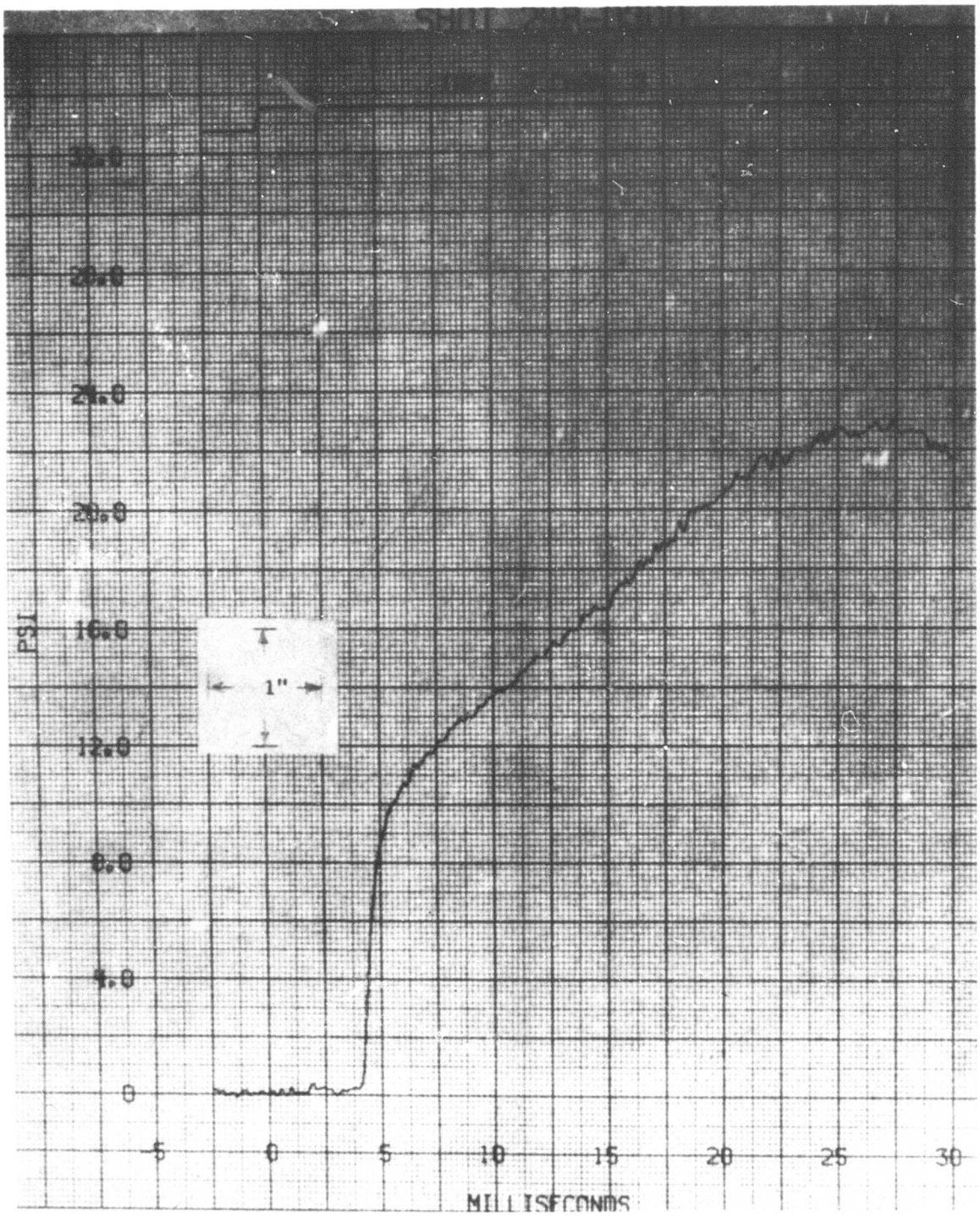

Figure 55. Back force link: typical full-event computer reduction

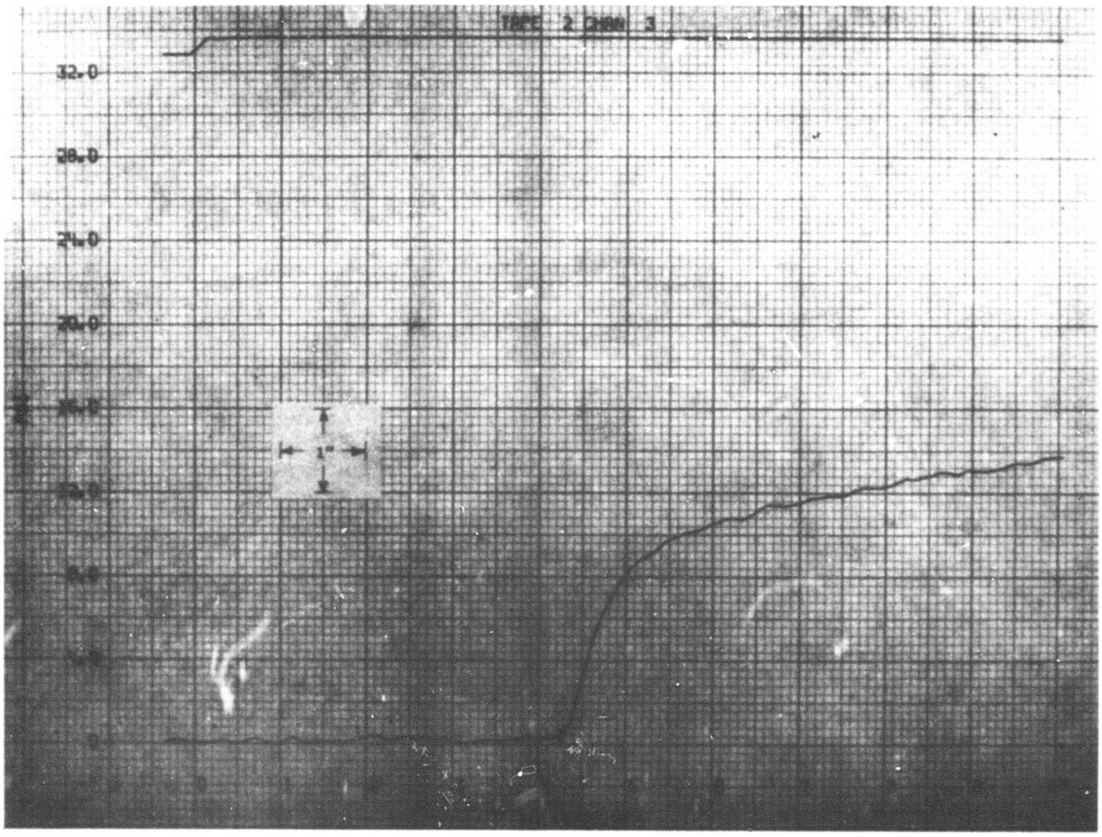

Figure 56. Back force link: typical expanded computer reduction

Note that the front force link indicates a rise time of about 2 msec, and, as expected, the back force link indicates a considerably softer pulse. Some analysis of the force-link data will be given below. First, however, the displacement readings will be analyzed because they are the basic data from the experiment.

c. Detailed Reduction of Test Data.

The gage readings in mils were plotted as a function of time as in Figure 50, and the readings for the two sides at each station were averaged (just as for the static tests). Because the phenomenon was dynamic, the readings at the front end of the specimen could be 10 times those at the last gaging station at a given instant of time. These displacement-time data were differentiated to yield particle-velocity versus time curves. A typical result is given in Figure 57. As explained in Section III, these data may contain inconsistencies which can be minimized, on the assumption of a plastic and strain-rate-insensitive material, by taking advantage of the fact that a given particle velocity is generated at a unique wave velocity.

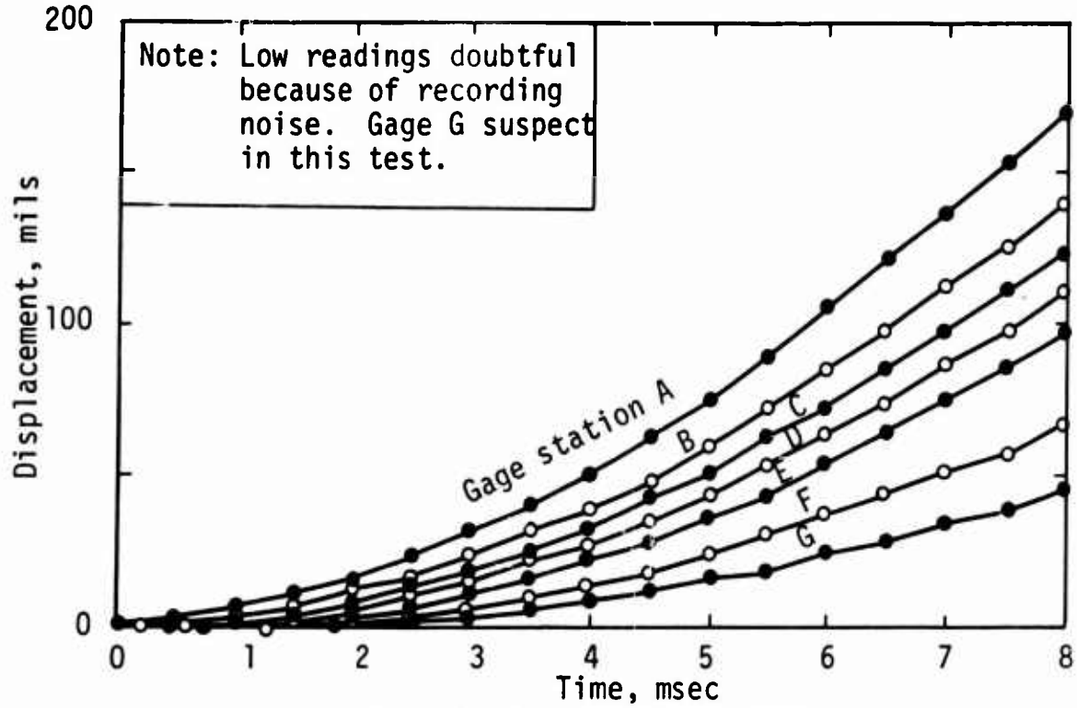

(a) Displacement-time data

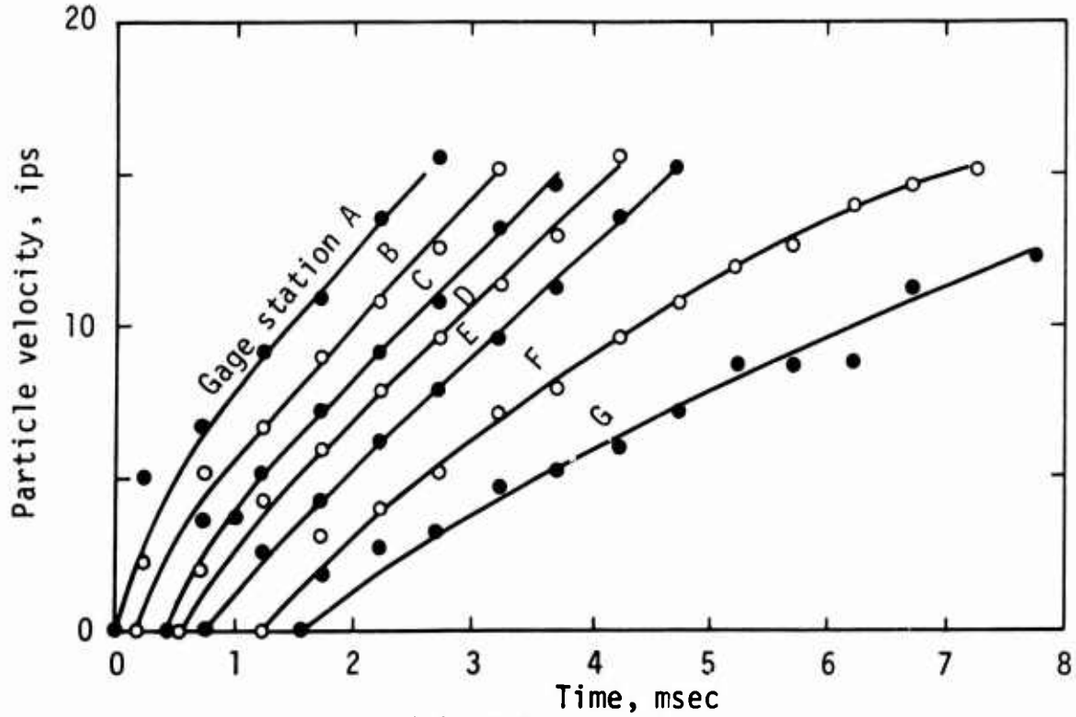

(b) Velocity-time data

Figure 57. Typical displacement- and velocity-time results

Data from a plot such as Figure 57 were therefore rearranged in a plot of position time for a given particle velocity. Such a plot is given in Figure 58. The slope of any line on a position-time plot is, by definition, a wave velocity. From the known density and the Richart data in Figure 10, the seismic-front line can be drawn as shown. This value was checked from the force-link readings, and the differences were in all cases trivial. The points for several velocities are shown on the figure. The straight line was drawn as a best fit, utilizing the fact that station G seemed to be misreading in this shot. The best-fit straight lines were similarly but independently fitted to the other velocity data from Figure 57 to obtain the family of straight lines in Figure 59. The wave velocity for each particle velocity was computed as the slopes of these lines, and the results were conveniently plotted as Figure 60. Then, following the method outlined in Section III, the results were rearranged and graphically integrated according to Eq. (29)

$$\epsilon_p = \int_0^{v_p} \frac{1}{c_p} \, dv_p$$

The results of the integration are most conveniently displayed for subsequent operations in Figure 61, which shows wave velocity as a function of strain. Because of the compatibility smoothing done on the wave-velocity versus particle-velocity relationship (typically as shown in Fig. 60) the resulting wave-velocity versus strain curve is smooth for fine increments of graphic integration. The stress-strain curve was then obtained directly by integrations of the ρc_p^2 curve, computed from the data in Figure 59, according to the solutions of Eqs. (8) and (12)

$$\sigma_p = \int_0^{\epsilon_p} \rho c_p^2 \, d\epsilon_p \tag{31}$$

The result for this case is shown in Figure 62.

d. Discussion of Reduction.

It is apparent that this method of data reduction forces the results to be strain-rate insensitive and to exhibit plastic behavior; but it also forces

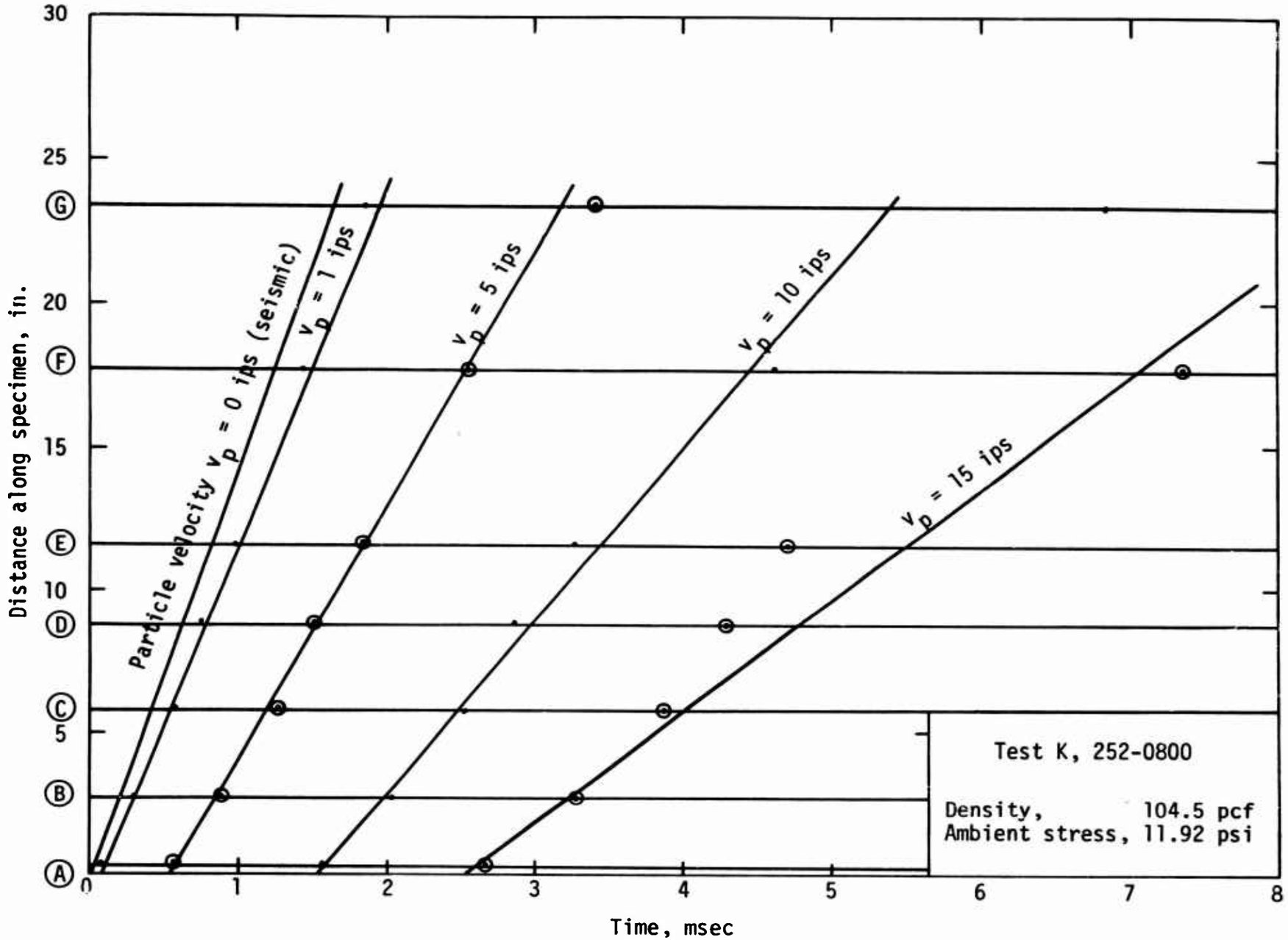

Figure 58. Position-time plot, fitting velocity lines

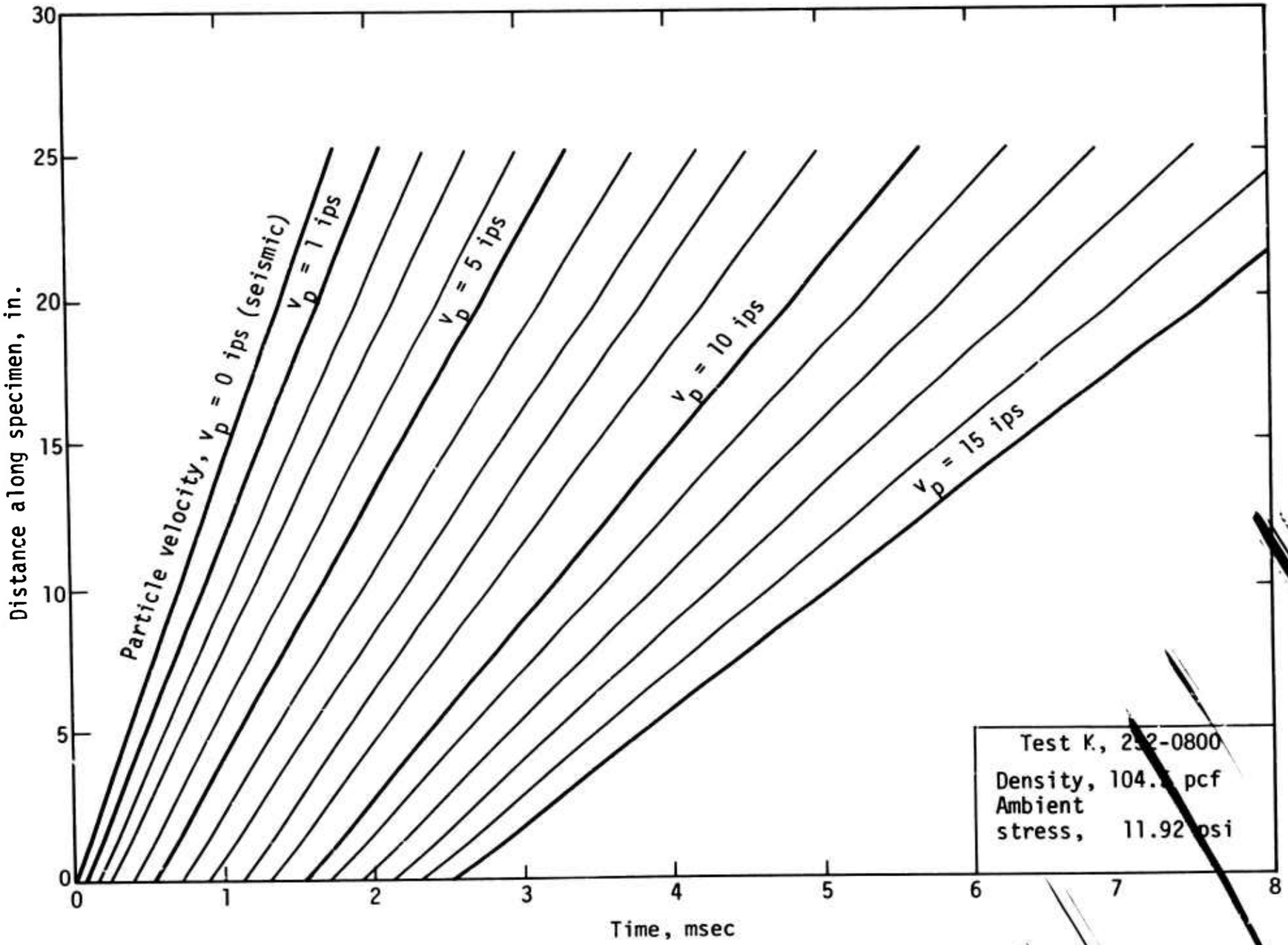

Figure 59. Position-time plot, fitted velocity curves

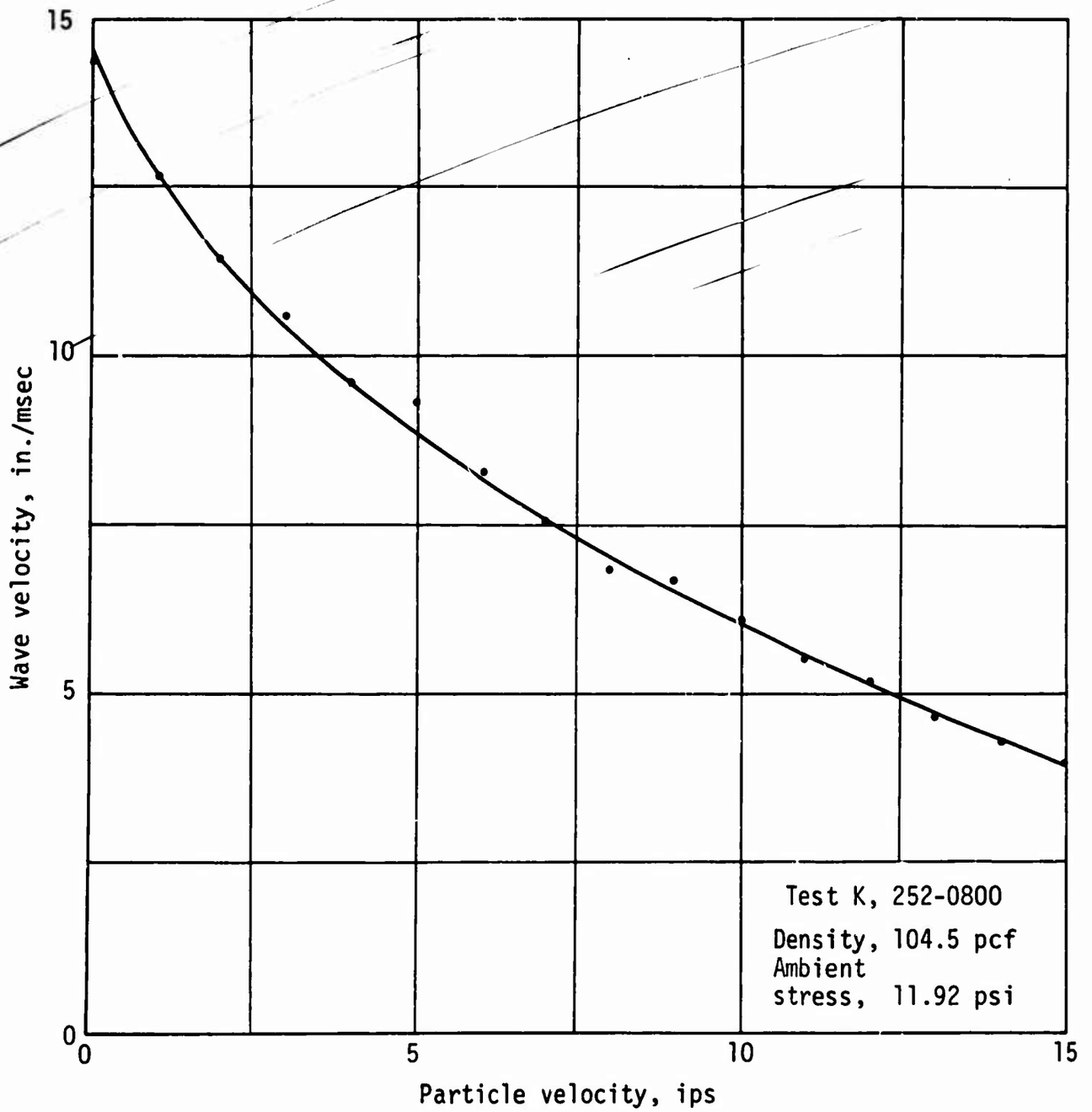

Figure 60. Wave- and particle-velocity relationship

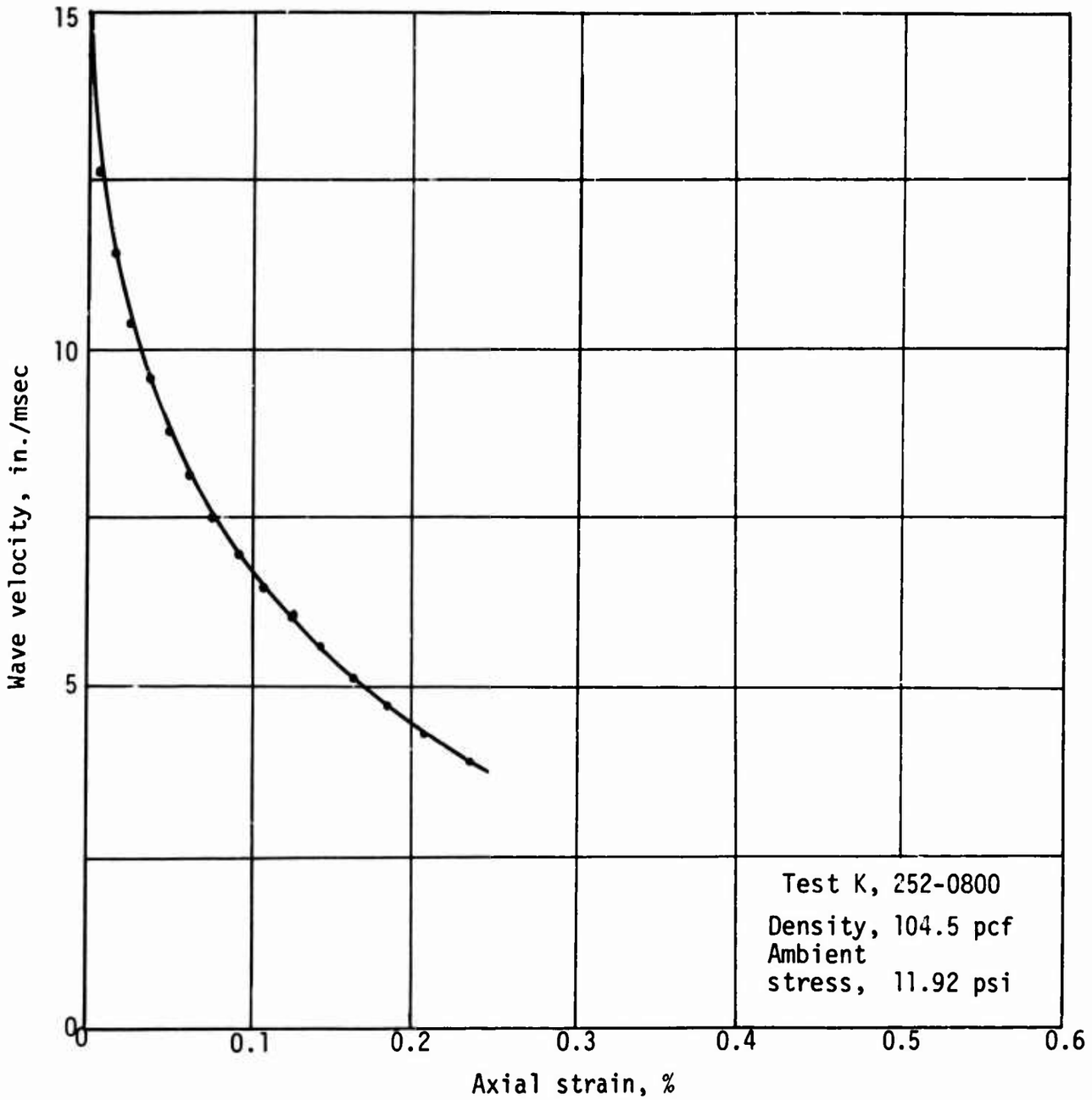

Figure 61. Wave-velocity and strain relationship

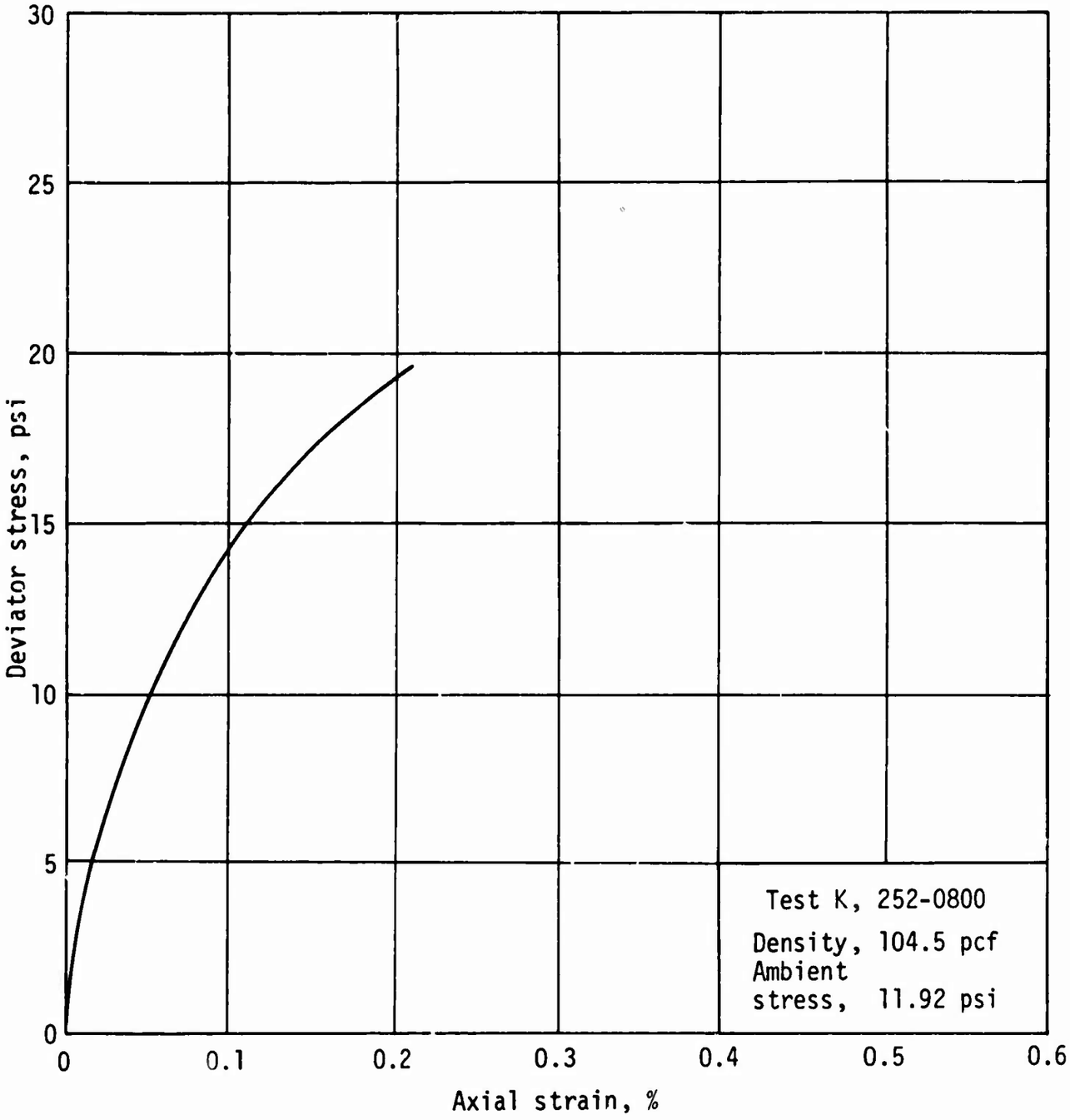

Figure 62. Dynamic stress-strain curve

the data to be kinematically consistent. If the material were in fact appreciably strain-rate sensitive, then this procedure would have the effect of making the leading gages (e.g., station A) appear to be reading too *low*; and perhaps, but certainly to a lesser degree, might make the rear gages (e.g., station G) appear to be reading too *high*.

Reverse computations were made to check this effect, and precisely the opposite was found to be true: station A, when it disagreed with the back-computation from the smoothed data, always read high, and station G usually read low. For this reason it was concluded that any discrepancies between actual and backcomputed data were not caused by neglect of an appreciable strain-rate effect. Instead, the discrepancies, when they occurred, were handled by scaling the actual data geometrically against time on the assumption that the calibrations might have been in error. Except for station A, no large corrections were necessary. When large corrections had to be applied to A, those data were rejected on the assumption that buckling or failure might be occurring, air leakage around the loading head might be disturbing the flags, or some ambient light might be leaking in.

It is also apparent that some curve fitting was done in three places: the velocity-time plot, Figure 57; the position-time plot, Figure 58; and the wave-velocity versus particle-velocity plot, Figure 60. It would have been possible to use computer-smoothing methods to make so-called best-fit curves to the data points; in particular, the straight lines of the position-time plot could have been fitted by least squares or some other common procedure. None of these fitting schemes was used, however, for the following reasons: the value of each point had to be judged individually, and one of the main purposes of the effort was to gain experience with the phenomena taking place. If computer-fitting methods had been used, it would have been necessary to assume that all gages and their ancillary systems were functioning perfectly at all times. Realistically speaking, this would have been a highly unlikely circumstance for so many gages of a new type. In addition, had computer-fitting methods been used, a great deal of experience would have been lost. For these reasons the curves were fitted by hand, using the experience and judgment that developed after analyzing a few tests.

Finally, it should be recognized that the initial part of the final stress-strain curve depends somewhat on the intercept chosen on the wave velocity versus particle velocity and the wave-velocity versus strain plots: that is, the seismic velocity. This value could have been computed from the readings of the two force links. It was somewhat difficult, however, to pick off the first

time-of-arrival at the back force link (Fig. 56). In general, the computed seismic velocities agreed with or differed only by small amounts from Richart's data (Figs. 10,11). When there was a disagreement, the present data led to lower velocities than Richart's. It is felt that this was owing to the sensitivity of the force link (designed to read in pounds rather than micropounds). Because Richart's instruments were much more sensitive to seismic-wave velocity than were the force links used here, Richart's data were used. No serious errors were introduced, apparently, since the intercept always fitted smoothly to the remainder of the data.

e. Results of Experiments.

A typical result is given in Figure 62. All results are discussed in the next section.

SECTION VI

ANALYSIS AND DISCUSSION

1. Study of Dynamic and Static Tests.

a. Comparison of Results.

The dynamic and static test results can be compared in two ways: (1) on the basis of method of fabrication, assuming that vagrant errors should more or less cancel; or (2) on the basis of properties, assuming the use of some method to force consistency on the properties (here, the SFC method).

As has been pointed out, all specimens--triaxial, static long specimen, and wave propagation--were fabricated by the use of similar methods; if something unusual happened during fabrication (e.g., a large shot in an adjacent shock tube while a loose specimen was being made or tested), or if the specimen or test did not appear correct for any reason, the specimen was destroyed and another made. Although comparing results on the basis of method of fabrication does not provide proper knowledge of soil property, it does help in assessing the limitations of the results and in guiding future researchers in similar materials.

Two basic properties must be used in a static-to-dynamic comparison, actual density and ambient stress. For the static basis of comparison these two were combined by the SFC method described in Section V. Using this method, it is possible to construct the static stress-strain curve for any density and any ambient stress. For each dynamic test, therefore, the comparable static stress-strain curve can be constructed from the test data (density and ambient stress) in Table IV.

The bases for comparison are the stress-strain curves. The dynamic stress-strain curves are compared (Figs. 63-69) with static curves as follows: (1) for *method* comparison, the triaxial band; and (2) for *property* comparison, the SFC curve constructed for each test at the density and ambient stress of the dynamic experiment.

In general, the dynamic stress-strain curves compared more favorably by method with the static stress-strain curves than did the results of the static long-specimen tests. Exceptions were Tests G and J (Figs. 63,69) which buckled, and Test V (Fig. 68) which is discussed below. (Recall that Test G was repeated as K.) The results are usually within the errors seen in the scatter envelopes,

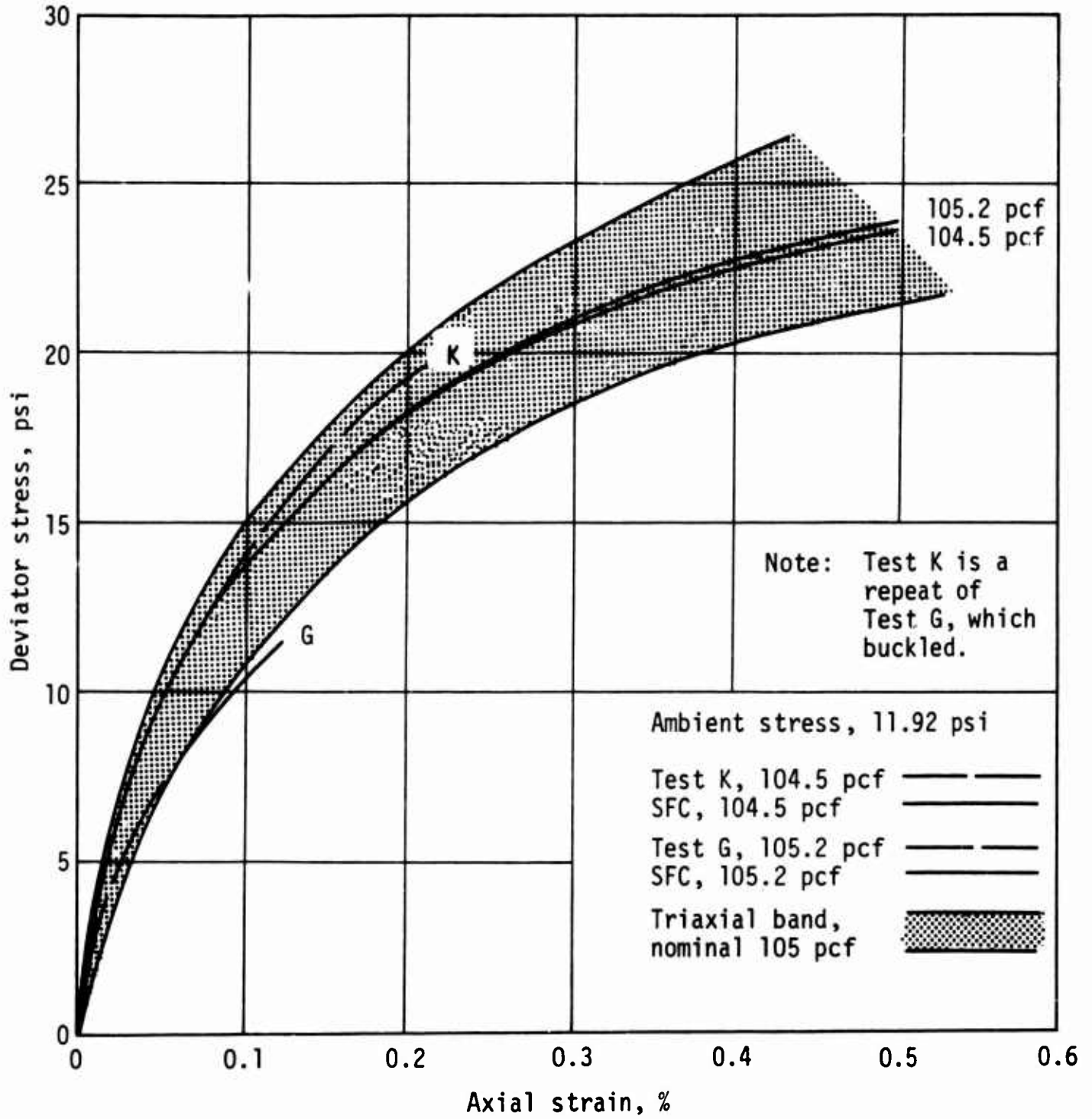

Figure 63. Dynamic-to-static comparison: dense, high-ambient stress

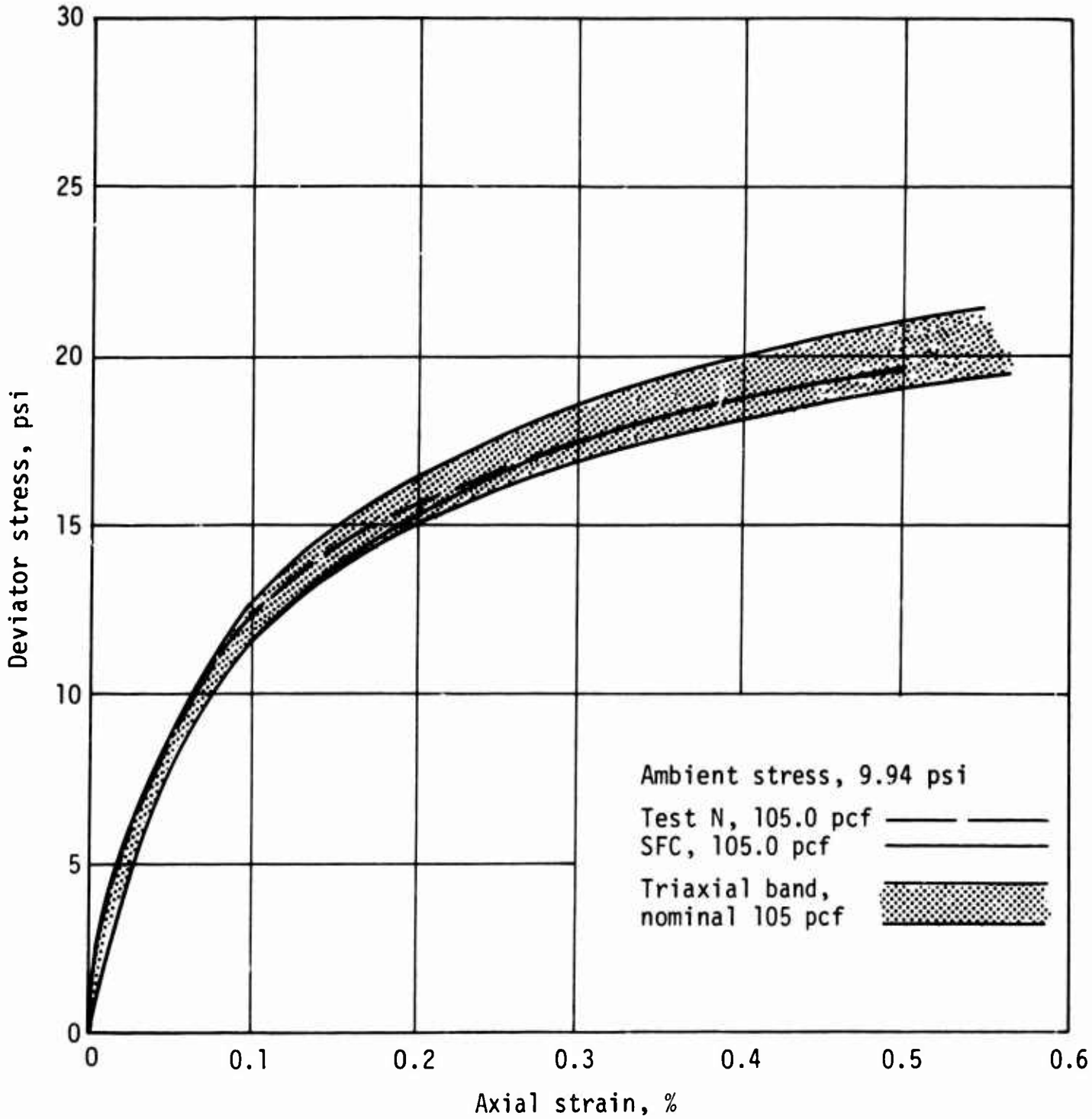

Figure 64. Dynamic-to-static comparison: dense, middle-ambient stress

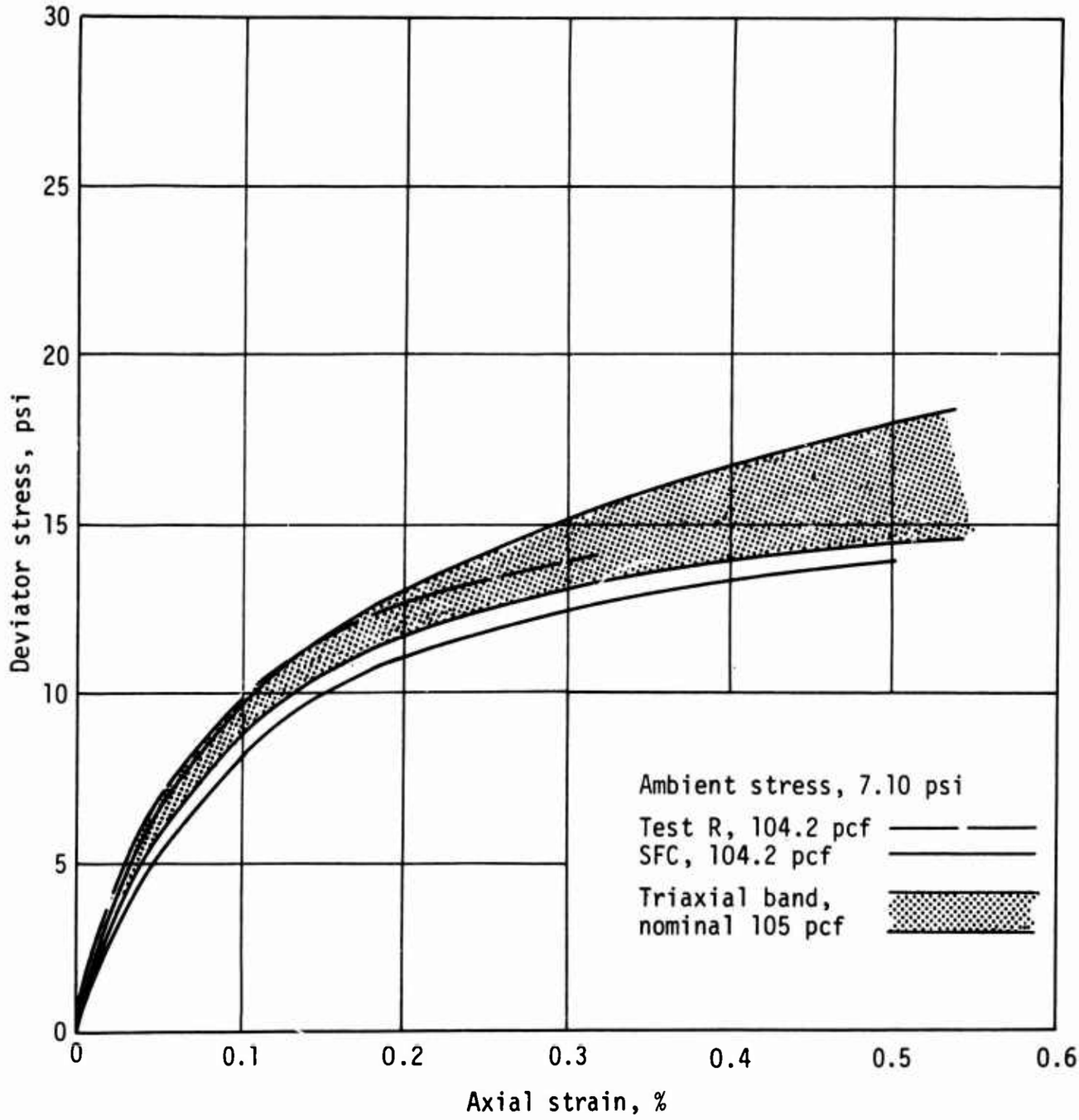

Figure 65. Dynamic-to-static comparison: dense, low-ambient stress

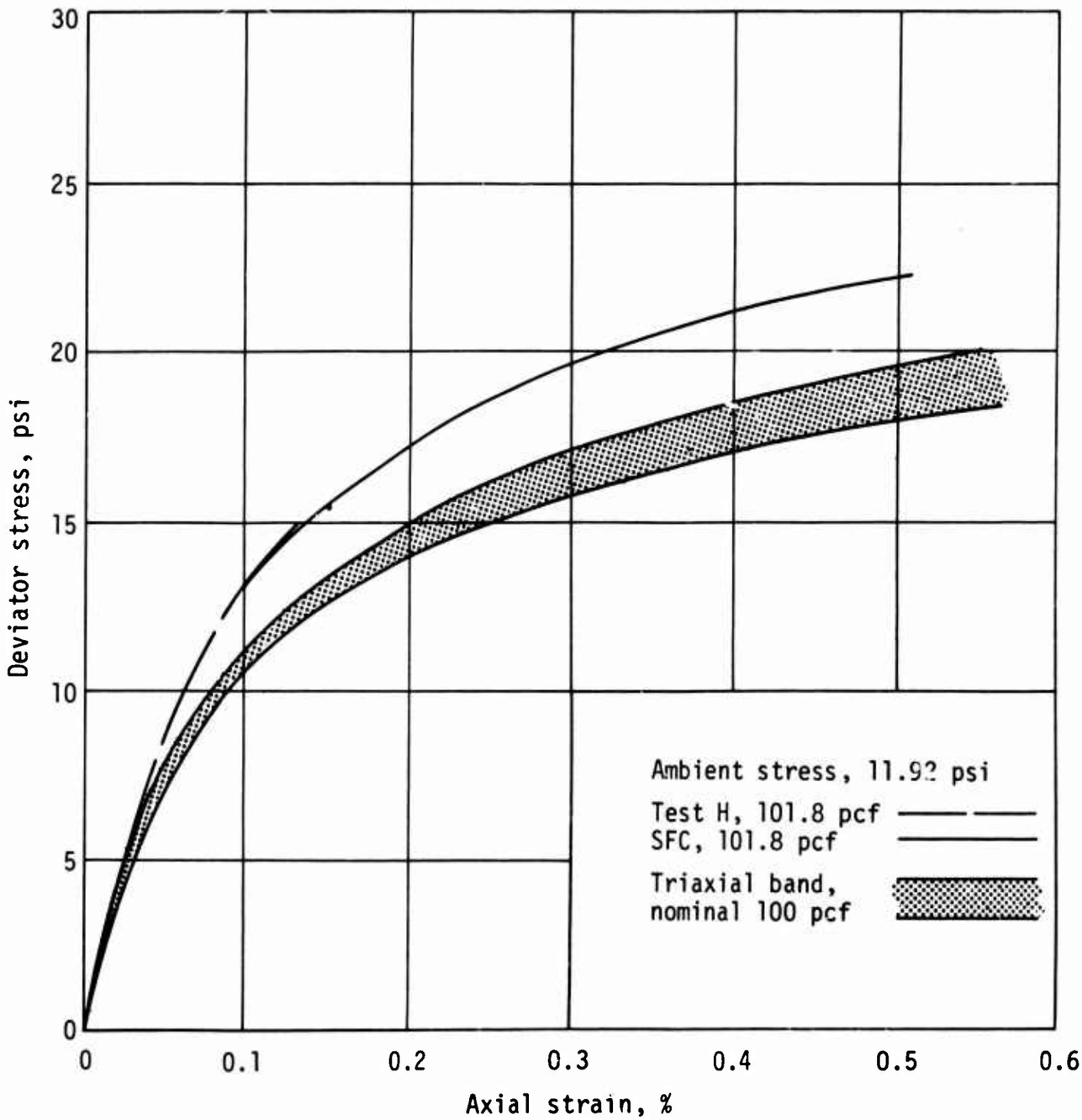

Figure 66. Dynamic-to-static comparison: medium-dense, high-ambient stress

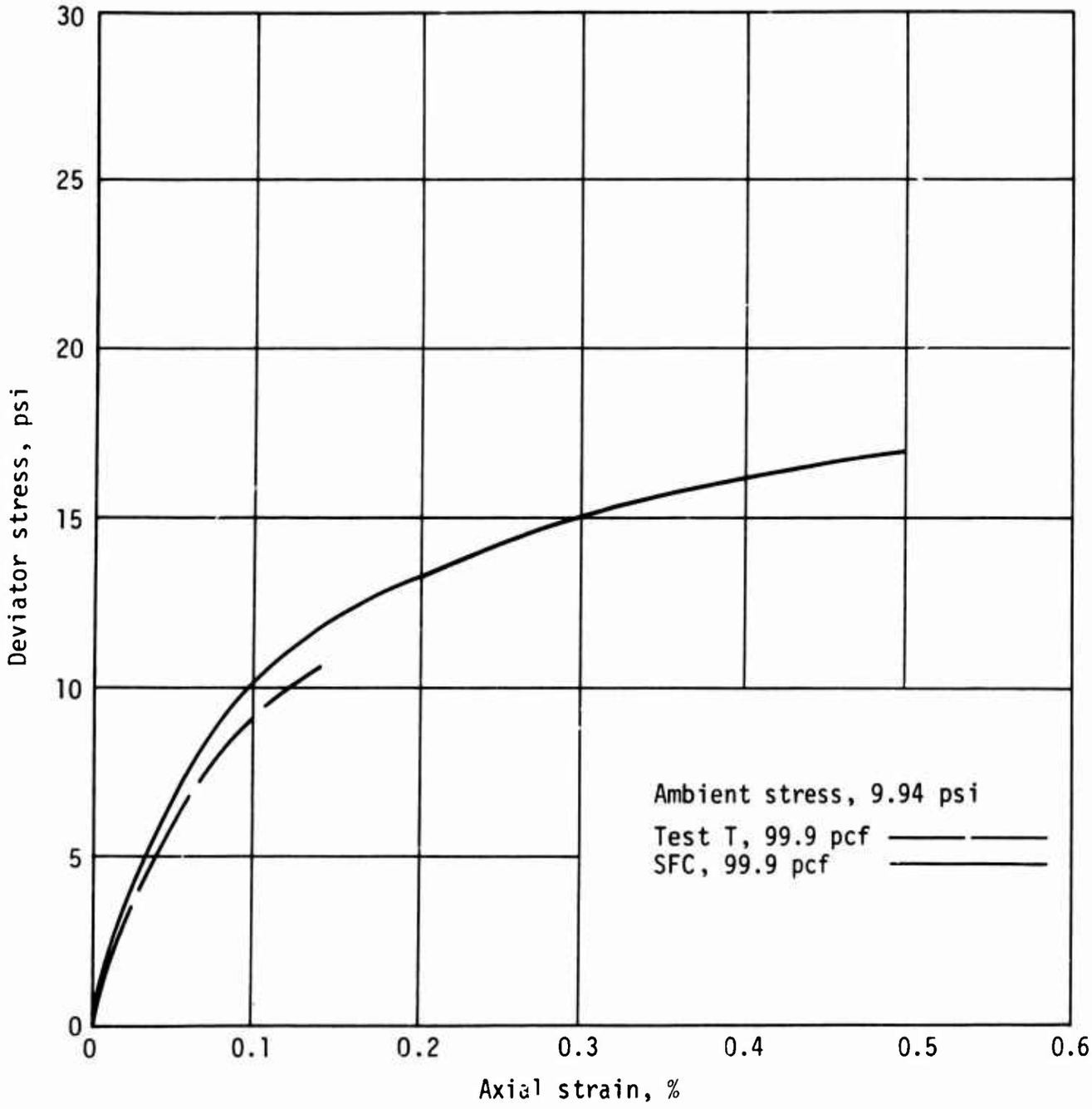

Figure 67. Dynamic-to-static comparison: medium-dense, middle-ambient stress

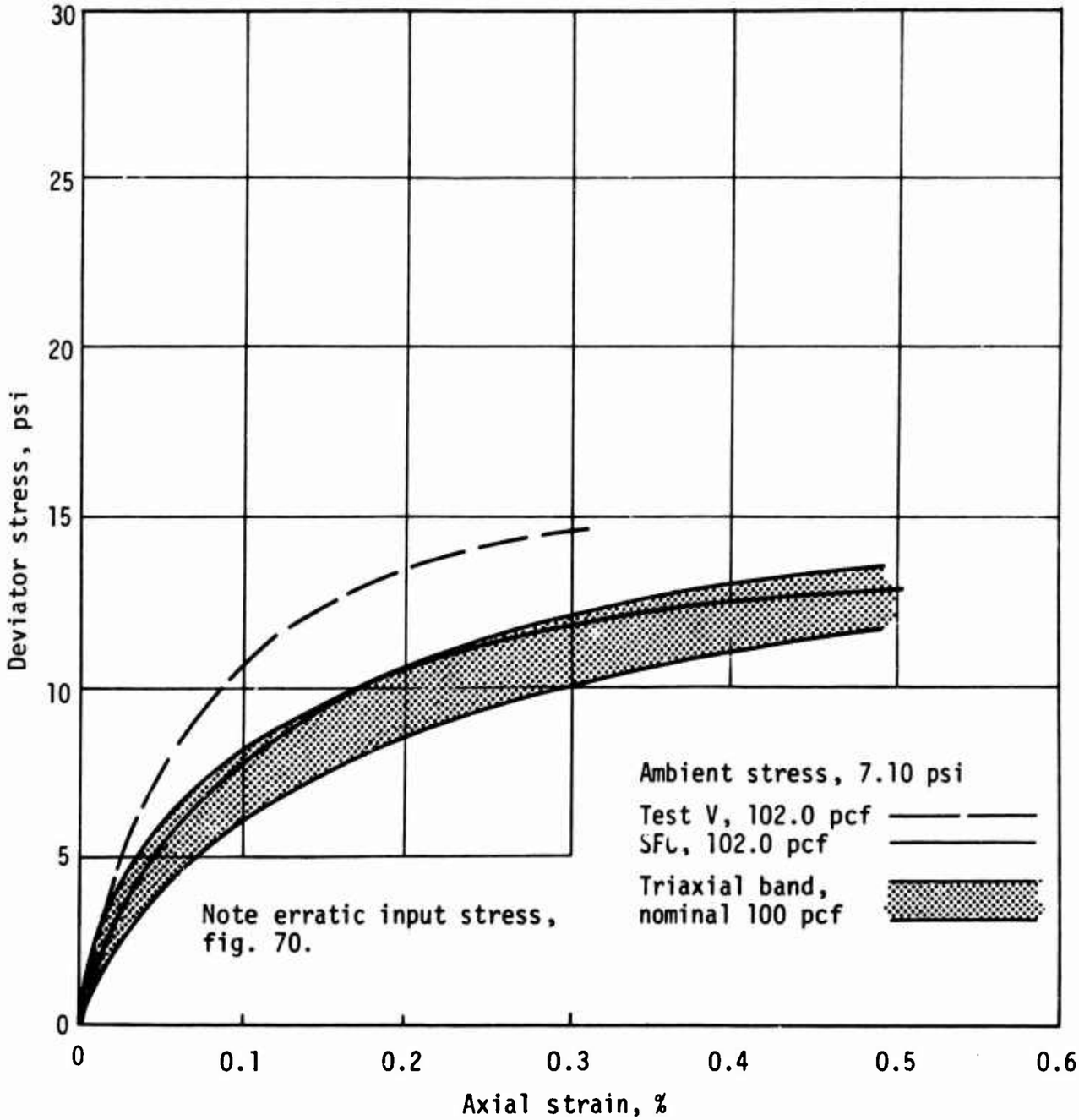

Figure 68. Dynamic-to-static comparison: medium-dense, low-ambient stress

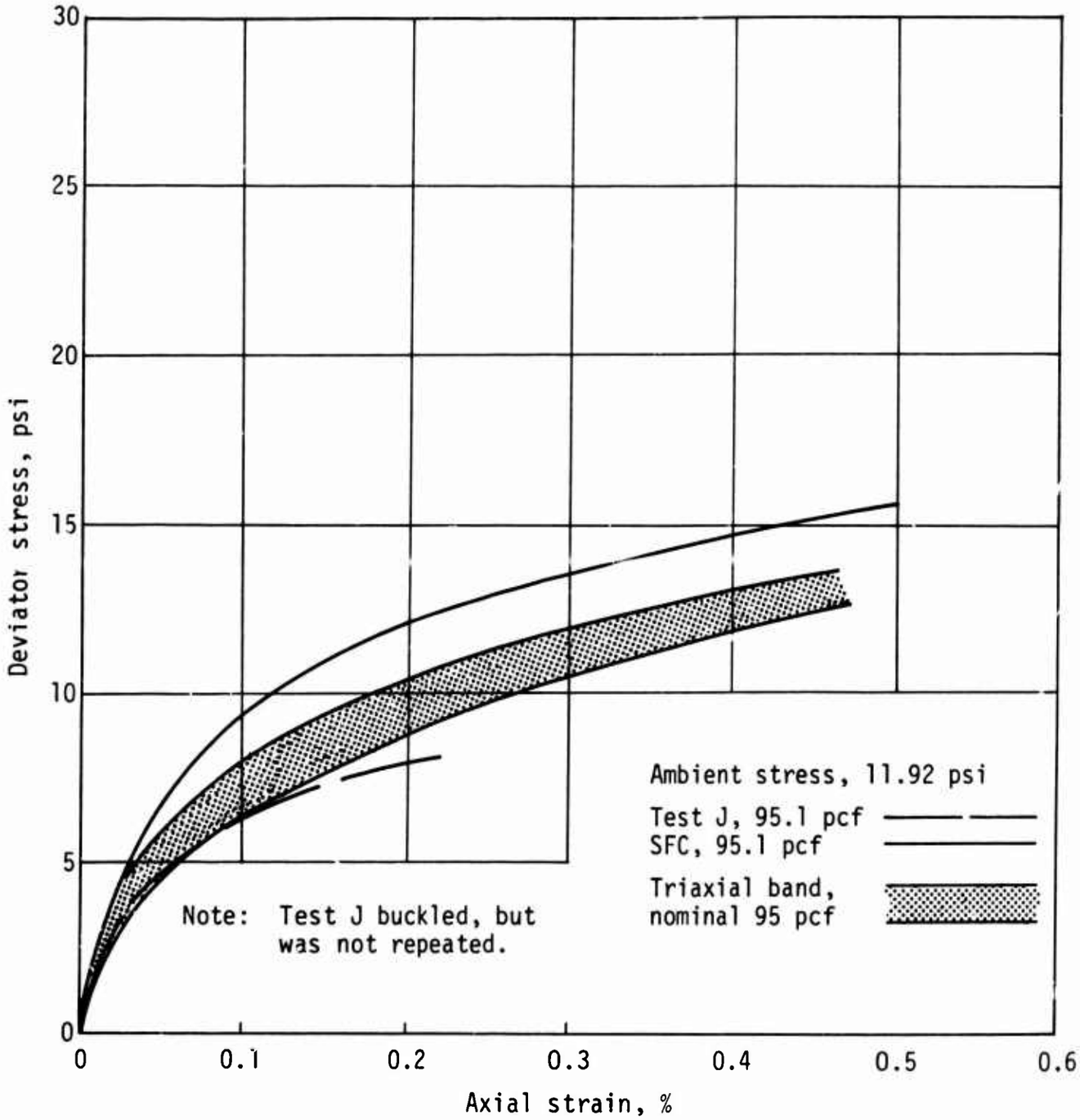

Figure 69. Dynamic-to-static comparison: loose, high-ambient stress

which in turn represent the scatter seen in the results of carefully performed tests and caused by the vagrant nature of sands.

Detailed quantitative significance should not be assigned to these plots of comparison by method; recall that many of the triaxial envelopes were obtained for specimens *below the nominal densities*, and many of the specimens for dynamic tests were *higher than the nominal density* (e.g., Test V, Fig. 68). Nevertheless, since many of the bands exceeded the reported maximum strain-rate sensitivity of this material, these plots do allow two tentative conclusions: the material appears to be only slightly strain-rate sensitive, and the computed dynamic stress-strain curves appear reasonable.

From the comparison by properties with the SFC curves, excepting the curves for G and J (Figs. 63,69, for reasons noted above), it can be seen that (1) the dynamic curves agree with their SFC static curves more closely than the envelopes of data from which the static curves were derived; and (2) there is no clearly consistent difference between the curves to indicate a large strain-rate sensitivity. For example, Tests K, H, and N lie very near but slightly above their curves, Tests R and V lie appreciably above, but Test T lies below.

It should be noted that the softer the specimen (i.e., lower density, lower ambient stress), the greater the disagreement between the dynamic curves and their SFC static curves; the results from the softer specimens lie farther above their comparable static curves. Although this observation may be taken to indicate a strain-rate sensitivity proportional to softness, the research does not support such a conclusion. It should be recalled that Tests G, H, and J were performed before the foam bed was reinforced; two of these--G and J--buckled, and the other--H--showed excellent agreement (Fig. 66). The other tests, K, N, R, T, and V--were performed after foam reinforcement. Of these, Tests K, N, and T showed excellent agreement (Figs. 63,64,67), while tests R and V only showed stiffer behavior (Figs. 65,68). The disagreement in Test R was not serious, amounting to perhaps 20 percent at the most. The disagreement in Test V was, however, more serious, amounting to as much as 50 percent at low strains. In Test V the input stress was not the smooth function usually obtained, but instead was that shown in Figure 70. Note that after the peak was reached, the stress decreased by about one quarter, then fluctuated erratically during the remainder of the loading. The effects of such an arbitrarily shaped pulse are not included in the analysis of the test data and are not the subject of this report.

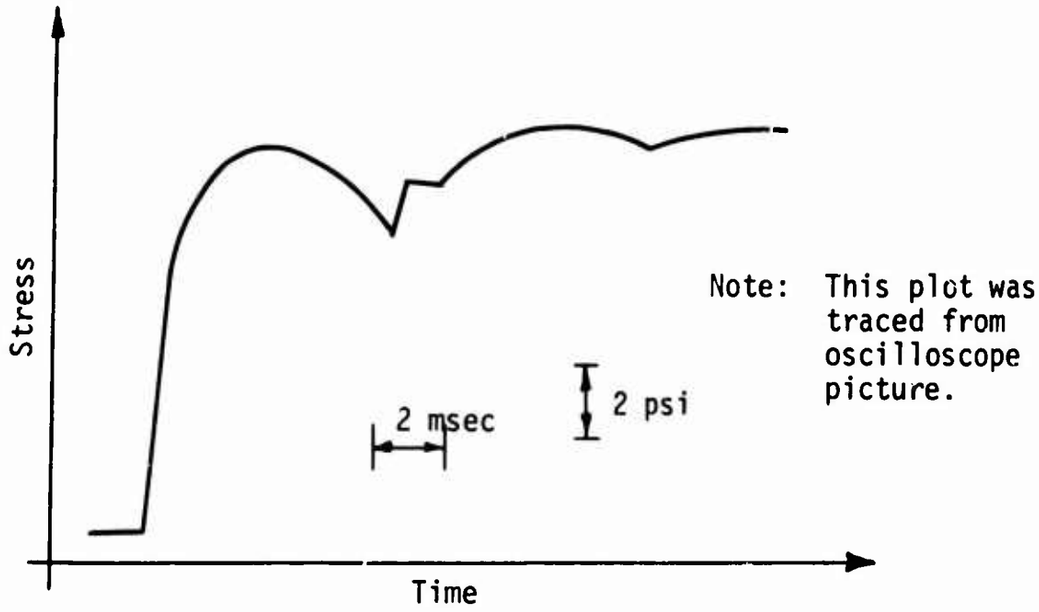

Figure 70. Input stress read in Test V, 253-1200

Because of the vagrant nature of the input stress, the results of Test V are tentatively rejected as being invalid for the program at hand.

The results shown, tempered by the experiences of the experiments, indicate that Tests H, K, N, R, and T provided the valid and analyzable results of this series of experiments. In most cases the results agreed with the SFC static curves within 10 percent; in only one case (Test R) was the disagreement up to 20 percent. The disagreements, with the exception of Test T (Fig. 67), showed the dynamic results to yield a stiffer stress-strain curve than the static, indicating a minor strain-rate sensitivity. The average of the maximum sensitivities is less than 5 percent for this test series as reduced, however.

b. Conclusions Regarding Static and Dynamic Properties of Sand.

The static tests were reduced to a best-fit single curve by application of the SFC method to the results of about thirty triaxial tests. When compared with these static curves, the dynamic curves showed excellent agreement, disagreeing slightly in favor of increased stiffness. Although use of the data-analysis method forced strain-rate insensitivity when there is likely to be strain-rate sensitivity, this method will yield a single stress-strain curve that is stiffer for high-strain rates than for low. In other words, this method yields a stress-strain curve that is crudely an average of the lowest and highest strain rates. The maximum strain-rate sensitivity, therefore, is somewhat higher than that yielded by a dynamic-to-static comparison. On the basis of these comparisons,

for a soft-fronted pulse and for the range of densities and ambient stresses studied, five major conclusions may be drawn:

(1) *This sand is, for all engineering purposes, strain-rate insensitive.* The sensitivity can be as high as 20 percent, but averages only 3 percent. This conclusion verifies the findings of some investigators (Refs. 34,53,58), but contradicts others (Ref. 55).

(2) *The seismic arrivals are consistent with the Richart data (Ref. 49).*

(3) *The theory of wave propagation for plastic strain-rate-insensitive materials accurately models the behavior of this sand.*

(4) *This sand behaves statically as an SFC material.*

(5) *This sand behaves dynamically as an SFC material* to an engineering approximation, except at the lowest strains approaching seismic conditions.

On the basis of these conclusions the following simplifications are possible: (1) static tests will accurately predict dynamic behavior; (2) the results of a few static tests can be used to construct the stress-strain curves for a variety of densities and ambient stresses; (3) the seismic velocity depends only on density and ambient stress; and (4) the wave-propagation parameters can be considerably simplified.

2. Wave Propagation in Strain-Rate-Insensitive SFC Materials.

a. Some Fundamental Concepts.

In Section V, 2a, it was pointed out that if a material were subfailure coulombic (SFC), then the Mohr's circles of stress for a given strain but for different ambient stresses would all have to be tangent to the same straight line passing through the origin. From the geometry of the circle and origin-centered straight line, it follows that the relationship between the major principal stresses is

$$\frac{(\sigma_1)_p}{\sigma_3} = \tan^2 \left(45 + \frac{\phi_p}{2}\right) \tag{32}$$

where

$(\sigma_1)_p$ = major principal stress applicable to specific plastic strain, ε_p

σ_3 = minor principal stress (ambient stress)

ϕ_p = subfailure coulombic stress angle at specific plastic strain, ε_p

and where the subscript p implies that the parameters are applicable to a specific strain level (ε_p). Recalling the soil mechanics definition of deviator stress

$$\sigma_{dp} = (\sigma_1)_p - \sigma_3 \tag{33}$$

where

σ_{dp} = deviator stress applicable to specific plastic strain, ε_p

one may define the more useful *stress ratio* L_p

$$L_p = \frac{\sigma_{dp}}{\sigma_3} = \tan^2 \left(45 + \frac{\phi_p}{2}\right) - 1 \tag{34}$$

where

L_p = subfailure-coulombic stress ratio applicable to specific plastic strain, ε_p

and where the subscripts p imply that the parameters L_p, σ_p, ϕ_p are applicable to a given strain, ε_p. The stress ratio L_p is uniquely related to the *stress angle* ϕ_p, for any and all SFC materials. For ease of later reference, this unique relationship is given in Figure 71. Then if ϕ_p is known, L_p is known; and Eq. (34) may be rewritten in the more useful form

$$\sigma_{dp} = L_p \sigma_3 \tag{35}$$

to state that the deviator stress σ_{dp} required to cause a given strain ε_p under a specified ambient stress σ_3 may be computed if L_p is known. It turns out that L_p is extremely simple to compute: from a few tests at different ambient stresses the deviator stress at each strain is divided by the (constant) ambient stress of each test to arrive at L_p according to Eq. (34). When this is done, the values of L_p may be plotted as a function of the strain to obtain the *SFC constitutive relationship* for that material.

As an example, these computations were performed for the static triaxial experiments of this report. The results are given for later reference in Figure 72. There are three curves because there are three nominal conditions of density--105, 100, and 95 pcf. This simplified constitutive relationship has far-reaching significance in wave-propagation problems.

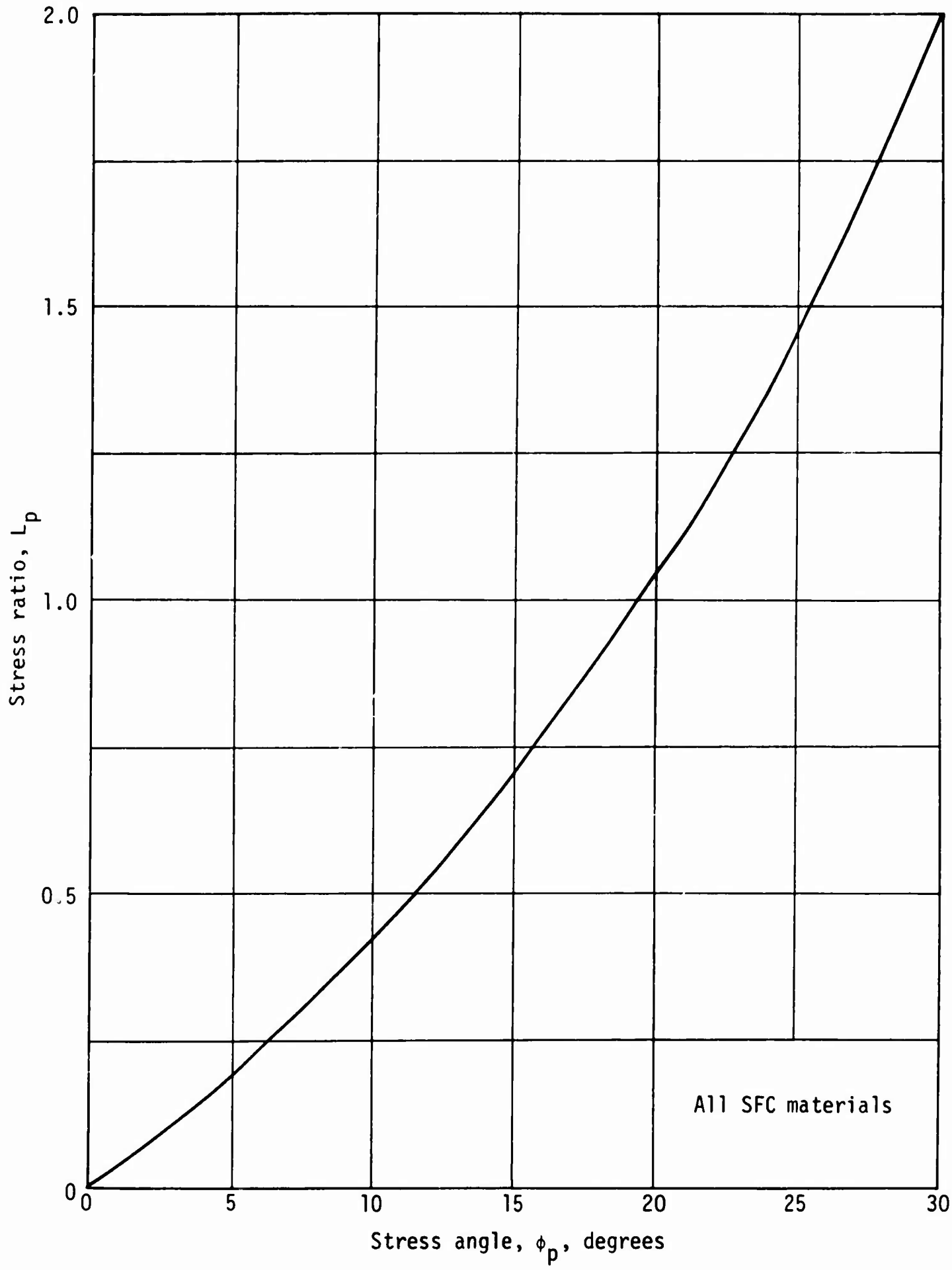

Figure 71. Universal relationship between stress angle and stress ratio

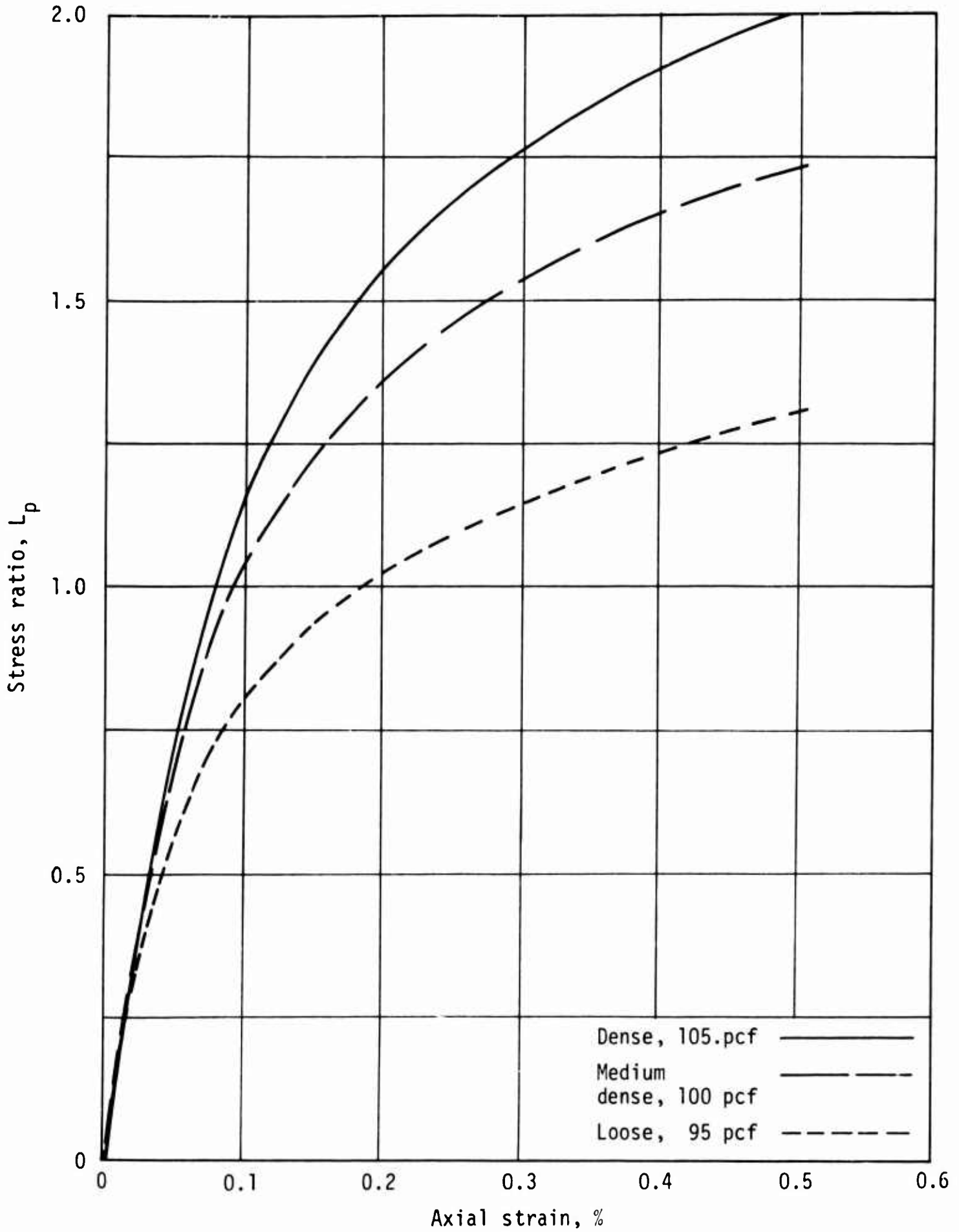

Figure 72. SFC constitutive relationship

b. Wave Velocity in SFC Materials.

In Section II, Eqs. (8) and (12), it was shown that the wave velocity and constitutive properties can be related by

$$c_p = \sqrt{\frac{1}{\rho} \frac{d\sigma_{dp}}{d\varepsilon_p}} \tag{36}$$

For SFC materials, this may be simplified by recalling Eq. (35) and operating

$$\frac{d\sigma_{dp}}{d\varepsilon_p} = \frac{d}{d\varepsilon_p} (L_p \sigma_3) = \sigma_3 \frac{dL_p}{d\varepsilon_p}$$

noting that σ_3 is a constant. Substituting from Eq. (34), differentiating, and simplifying, the result is

$$\frac{d\sigma_{dp}}{d\varepsilon_p} = \sigma_3 \left[\frac{\tan^2 (45 + \frac{\phi_p}{2})}{1/2 \cos \phi_p} \right] \frac{d\phi_p}{d\varepsilon_p} \tag{37}$$

The expression can be further simplified by noting that the bracketed term is unique on ϕ_p and is inert insofar as wave propagation is concerned. It is therefore convenient to define the inert-ϕ function $f(\phi_p)$

$$f(\phi_p) = \left[\frac{\tan^2 (45 + \frac{\phi_p}{2})}{1/2 \cos \phi_p} \right] \tag{38}$$

and to write

$$\frac{d\sigma_{dp}}{d\varepsilon_p} = \sigma_3 \, f(\phi_p) \frac{d\phi_p}{d\varepsilon_p} \tag{39}$$

Because both L_p and $f(\phi_p)$ are unique functions of ϕ_p, they can be solved simultaneously and related for any and all SFC materials. This has been done for later reference; the results are given in Figure 73. Thus for any material at a given strain ε_p, $f(\phi_p)$ is a known value because L_p is known. Similarly, because

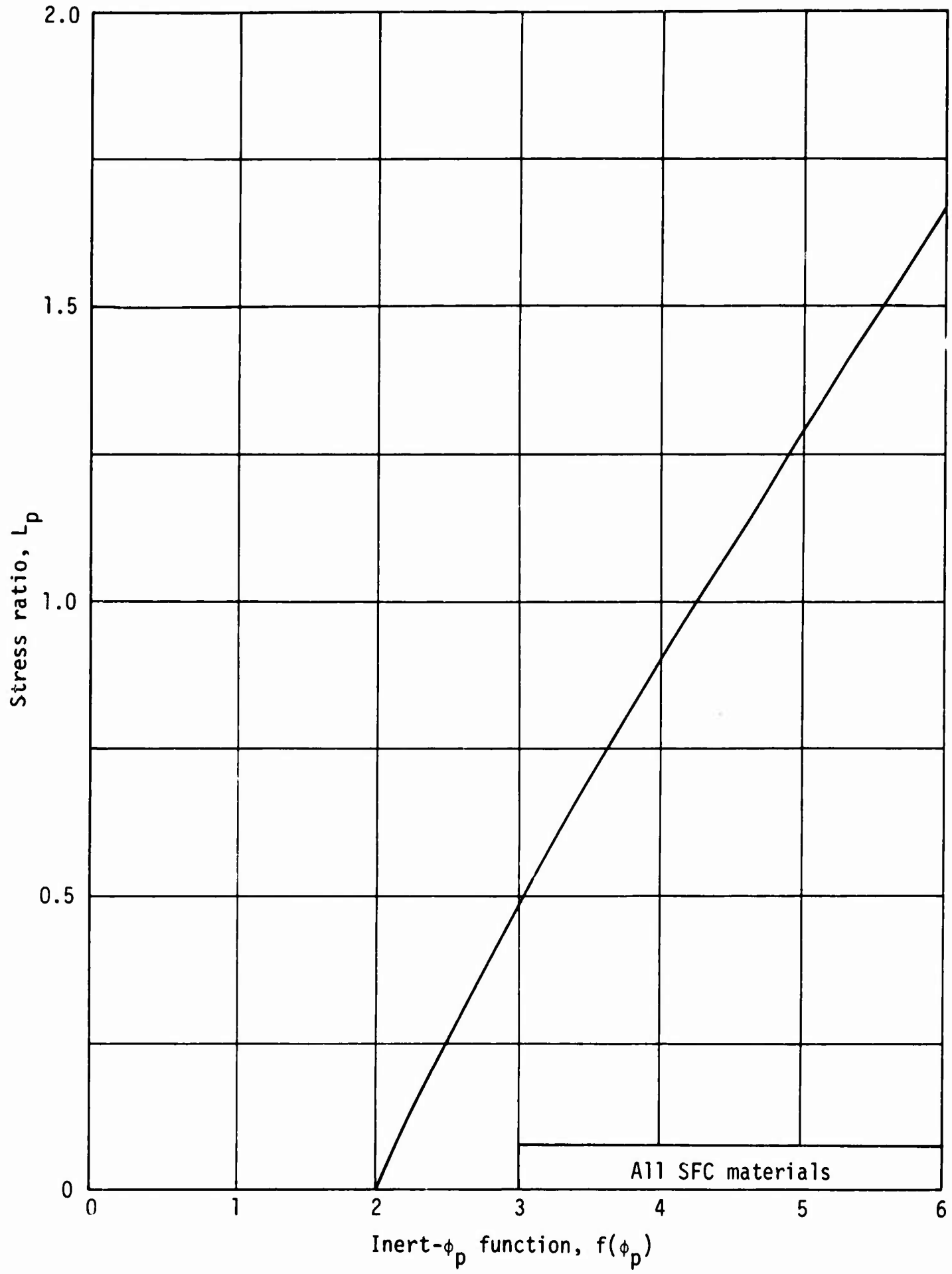

Figure 73. Universal relationship between inert-ϕ_p function and stress ratio

L_p is known for any strain ε_p by an SFC constitutive relationship such as in Figure 72, and because L_p and ϕ_p are uniquely related for all SFC materials, as shown in Figure 71, the relationship between the stress angle ϕ_p and strain ε_p may be constructed, as has been done in Figure 74 for the three material conditions in this report. Direct differentiation of the curves in Figure 74 yields the term $d\phi_p/d\varepsilon_p$ in Eq. (39), with some obvious uncertainties at low strains due to the steepness of the curves. Thus all terms in the differential of Eq. (39) are known. When Eq. (39) is substituted back into Eq. (36), the result is

$$c_p = \sqrt{\sigma_3}\sqrt{\frac{1}{\rho} f(\phi_p) \frac{d\phi_p}{d\varepsilon_p}} \tag{40}$$

Note that all the terms under the second root sign are known. One may therefore simplify the problem by defining the SFC wave-velocity function (N_p)

$$N_p = \sqrt{\frac{1}{\rho} f(\phi_p) \frac{d\phi_p}{d\varepsilon_p}} \tag{41}$$

so that the equation for wave velocity in an SFC material becomes simply

$$c_p = N_p \sqrt{\sigma_3} \tag{42}$$

As an example, the N_p is given in Figure 75 for the three material conditions in this report.

The implication of Eq. (42) is that for an SFC material the wave velocity c_p at which a given strain ε_p is generated is proportional only to the square root of the ambient stress acting. In other words, *wave velocity is a simple power function of ambient stress for a given strain; but the power function is the same for all strains.* This observation simplifies design and analysis problems in SFC materials simply because power functions plot as straight lines on log-log scales.

For example, Figure 76 shows that the wave velocities for a strain of 0.2 percent represent an intermediate stress condition and for a strain of 0.5 percent they represent a near-failure condition. The lines are parallel because the power is 1/2 in both cases, and they differ in vertical position only by the

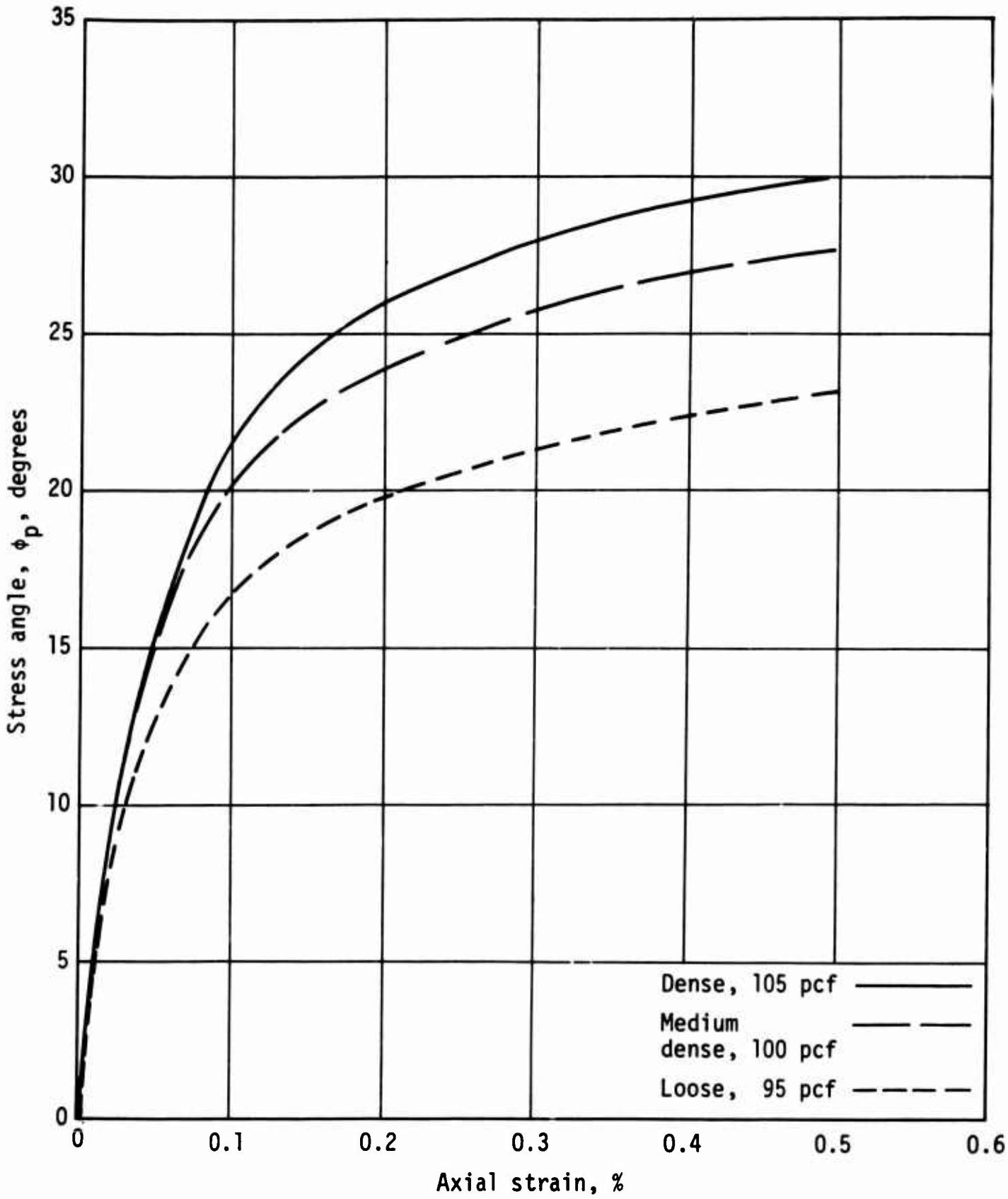

Figure 74. Stress angle, ϕ_p

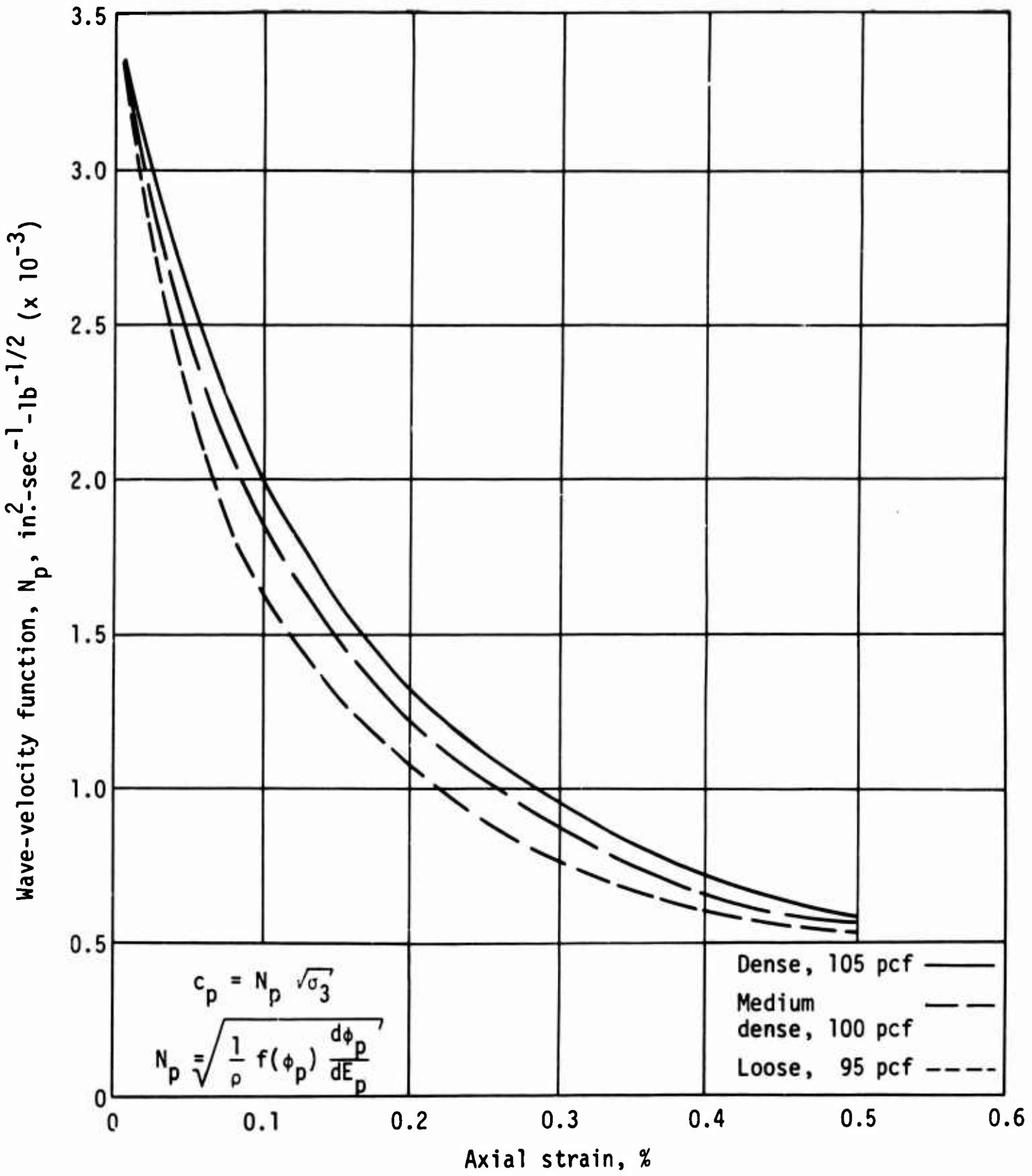

Figure 75. SFC wave-velocity function, N_p

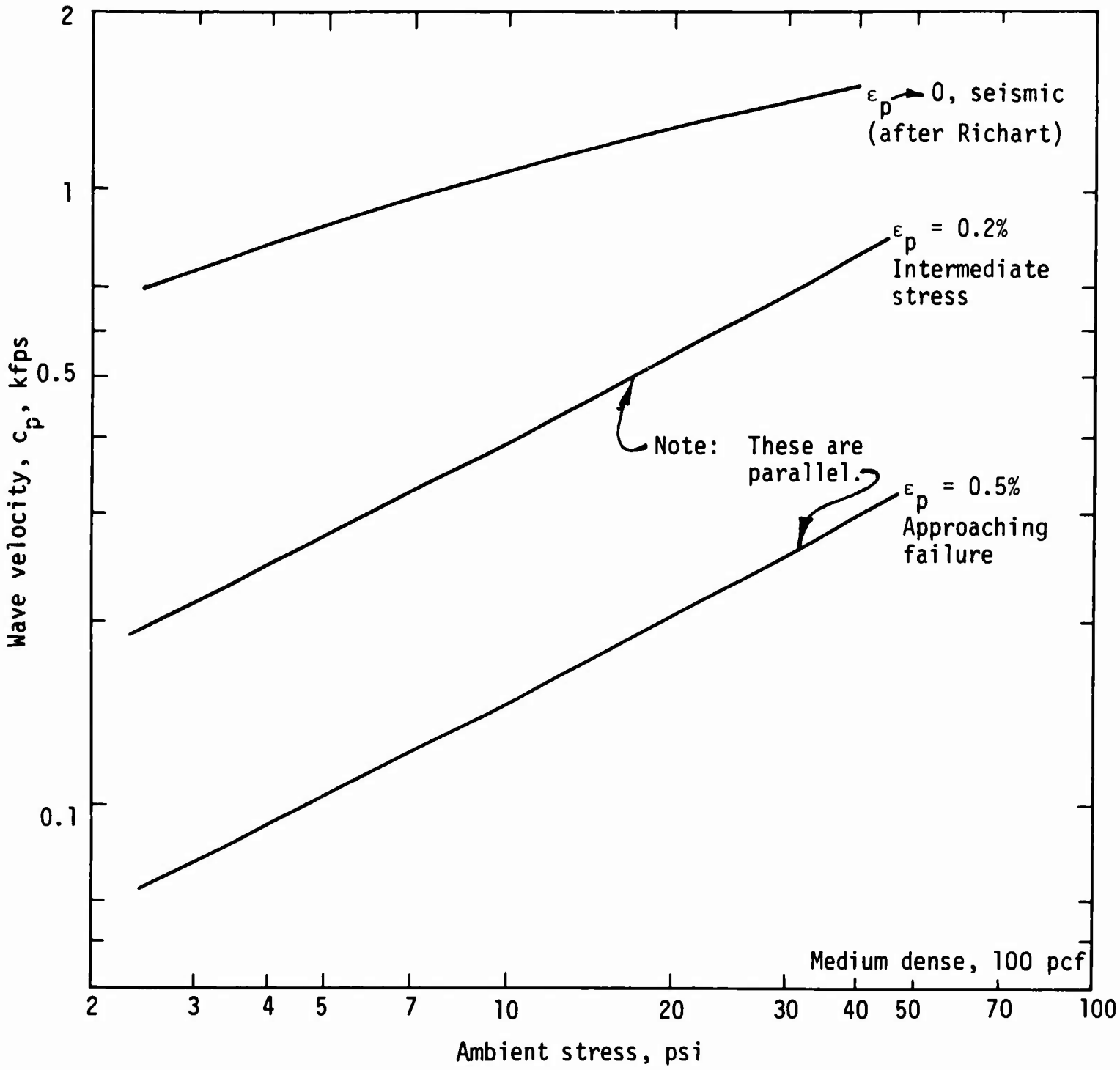

Figure 76. Effect of ambient stress on wave velocity

N_p values from Figure 75 used to compute them. This log-log linearity should not be carried to unusually small strains approaching seismic conditions, however, for two reasons. First, experience with the analysis presented shows that the computed term $d\phi_p/d\varepsilon_p$ can be quite unreliable at low strains (e.g., 0.005 percent). Second, the SFC mechanism is felt to be similar to friction, and is probably not applicable when friction is not dominant. At low strains the major transmission of energy is probably by point contact, where some lower power for the power function controls (Ref. 50). For this sand specifically the 1/4-power apparently applies at seismic strains (Ref. 49). This low-strain limitation is emphasized in Figure 76 where Richart's seismic data are also plotted (some semi-empirical simplifications on seismic velocity are given later in this section).

c. Particle Velocity in SFC Materials.

Recall the basic relationship between wave velocity, strain, and particle velocity

$$v_p = \int_0^{\varepsilon_p} c_p d\varepsilon_p \tag{15}$$

Identifying with Eq. (42), substituting, and simplifying, the result is

$$v_p = \sqrt{\sigma_3} \int_0^{\varepsilon_p} N_p d\varepsilon_p \tag{43}$$

Note that the integral is simply the integration of known functions, as in Figure 75. Thus the integral may be defined as the SFC particle-velocity function (Q_p)

$$Q_p = \int_0^{\varepsilon_p} N_p d\varepsilon_p \tag{44}$$

and the particle-velocity expression becomes simply

$$v_p = Q_p \sqrt{\sigma_3} \tag{45}$$

The function Q_p is a simple integral, shown in Figure 77 for the three material conditions in this report.

Thus the particle velocity in an SFC material is also a simple power function on ambient stress.

d. Kinetic Energy in SFC Materials.

Recall the basic definition of kinetic-energy density pre[illegible]ly noted

$$T_p = \frac{1}{2} \rho v_p^2 \tag{17}$$

Now identify with Eq. (45), substitute, and define the SFC kinetic-energy function (S_p)

$$S_p = \frac{1}{2} \rho Q_p^2 \tag{46}$$

The resulting simple expression for kinetic-energy density is

$$T_p = S_p \sigma_3 \tag{47}$$

The function S_p is shown in Figure 78 for the three material conditions in this report.

This result, Eq. (47), is particularly interesting: it implies that the *kinetic energy in an SFC material is linearly proportional to ambient stress.*

e. Potential Energy in SFC Materials.

Recall the basic definition of potential (strain) energy

$$V_p = \int_0^{\varepsilon_p} \sigma_p d\varepsilon_p \tag{16}$$

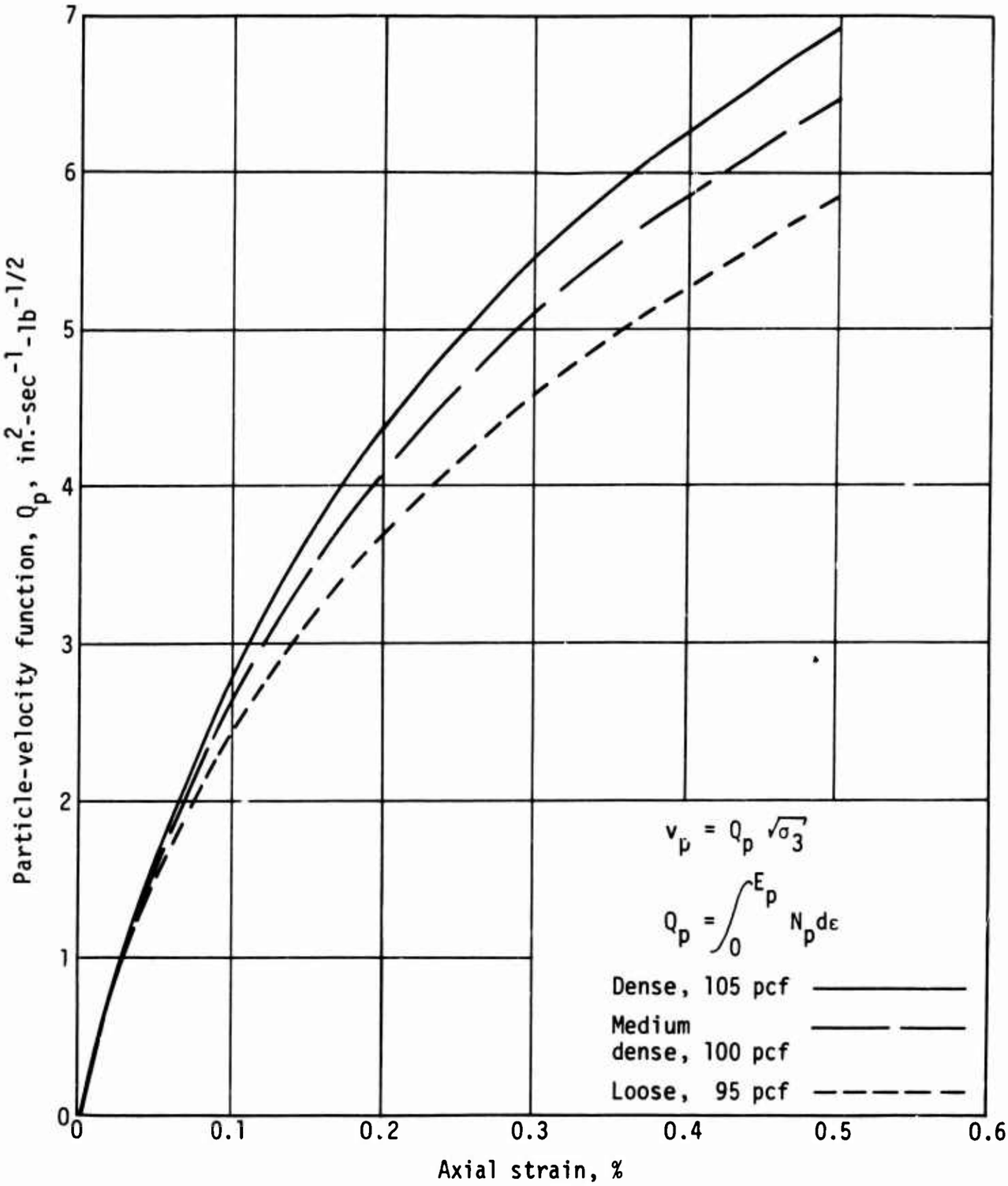

Figure 77. Particle-velocity function, Q_p

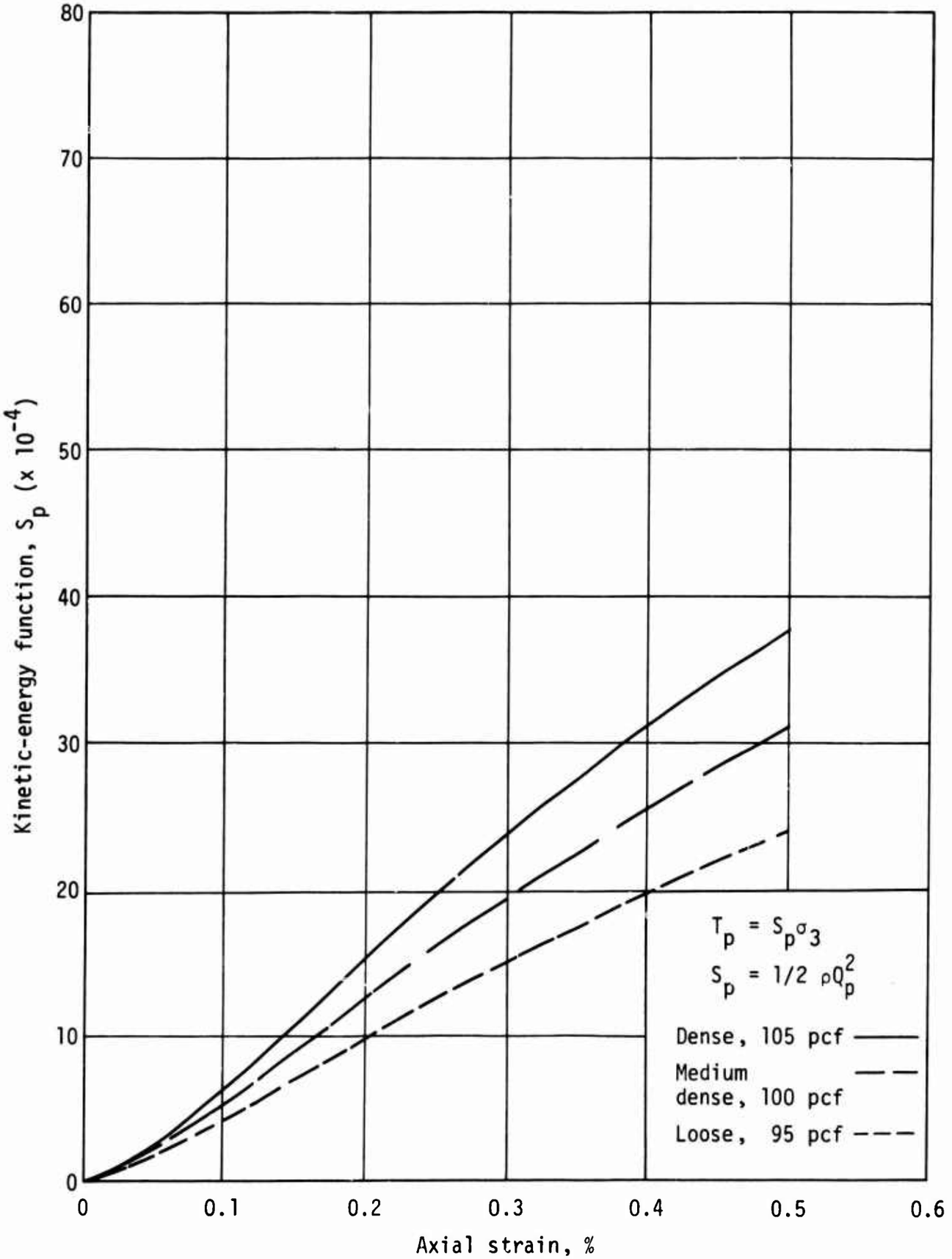

Figure 78. Kinetic-energy function, S_p

Now identify with Eq. (35), substitute, and define the SFC potential-energy function (M_p)

$$M_p = \int_0^{\varepsilon_p} L_p d\varepsilon_p \tag{48}$$

The resulting simple expression for potential energy is

$$V_p = M_p \sigma_3 \tag{49}$$

The function M_p is simply the integration of the SFC constitutive relationship (Fig. 72), the results of which are given in Figure 79 for the three material conditions in this report. The result, Eq. (49), shows that potential energy is also linearly proportional to ambient stress.

f. Total Energy in SFC Materials.

It is fundamental to the following development that only *loading* functions are considered in this report. For the general case of any strain-rate-insensitive plastic material, it was shown in Section III (specifically in Fig. 12) that both the potential and the kinetic energies follow directly from the stress-strain curve and the mass density. If the mass density is assumed constant, the foregoing may be stated more explicitly: the kinetic and potential energies depend uniquely on the shape of the stress-strain curve. The shape of the stress-strain curve, in turn, is an expression of the stress required to cause strain. In the process of applying stress to cause strain, the total available energy is transferred to the soil sample. The shape of the stress-strain curve reflects this stress transfer. Now clearly, and particularly for soils, some of the transferred energy is lost. Thus the previously derived expression for total energy is applicable.

$$\xi_p = V_p + T_p + L_x \tag{18}$$

For loading only, the loss term L_x in Eq. (18) must represent only those losses *external* to the specimen.

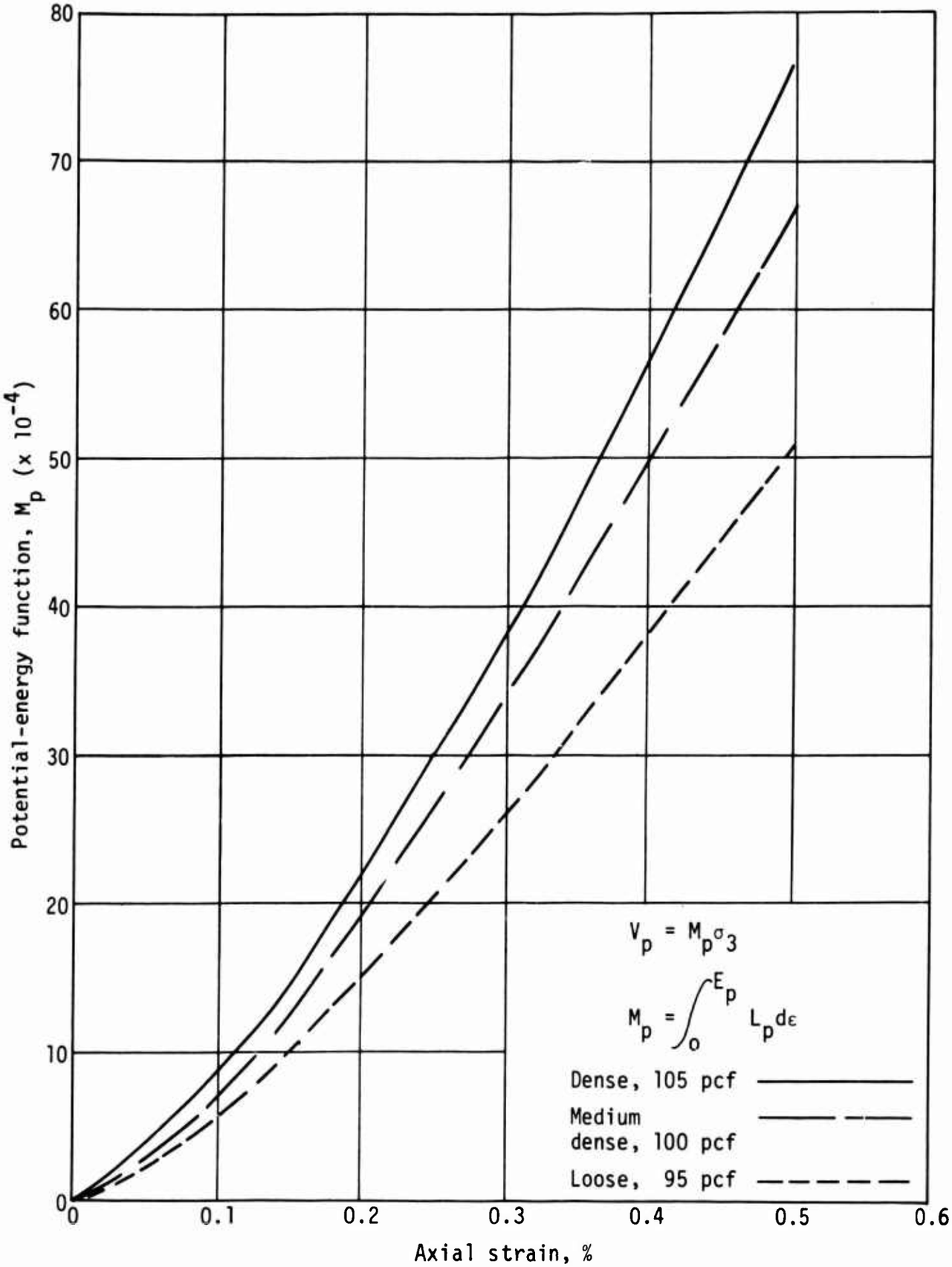

Figure 79. Potential-energy function, M_p

For example, in these experiments, L_x might include skin friction if there were relative motion between the long specimen and its foam bed, and L_x would have to include the energy consumed in flexing the little foam cantilevers even if there were no relative motion. Recognizing that the *internal* losses are included in the kinetic-energy and potential-energy expressions, and assuming that these *external* losses are small, the loss term L_x in Eq. (18) becomes zero. Thus for this case of loading only, the expression for total-energy density becomes simply

$$\xi_p = V_p + T_p \tag{50}$$

In this framework, then, one should think of the total, kinetic, and potential energies *consumed* by the event; but these energies certainly cannot be *recovered from* the event, especially for materials as hysteretic as soils.

Identifying Eqs. (47) and (49), substituting, and defining the SFC total-energy function (U_p)

$$U_p = S_p + M_p \tag{51}$$

the resulting expression for total energy is

$$\xi_p = U_p \, \sigma_3 \tag{52}$$

The total-energy functions were computed for the three material conditions in this experiment and are shown in Figure 80.

This result, Eq. (52), shows that total energy also is linearly proportional to ambient stress. It is interesting to note the empirical fact that for this sand the total-energy function is essentially a straight line at all but the lowest strains (Fig. 80).

g. Energy Partitioning in SFC Materials.

Recall that in the elastic case (Sec. II) the total energy was equally partitioned between kinetic and potential (for a free-traveling wave). It should not be expected that so simple a partitioning would result in the general plastic case; but a particularly simple result does come from the SFC case.

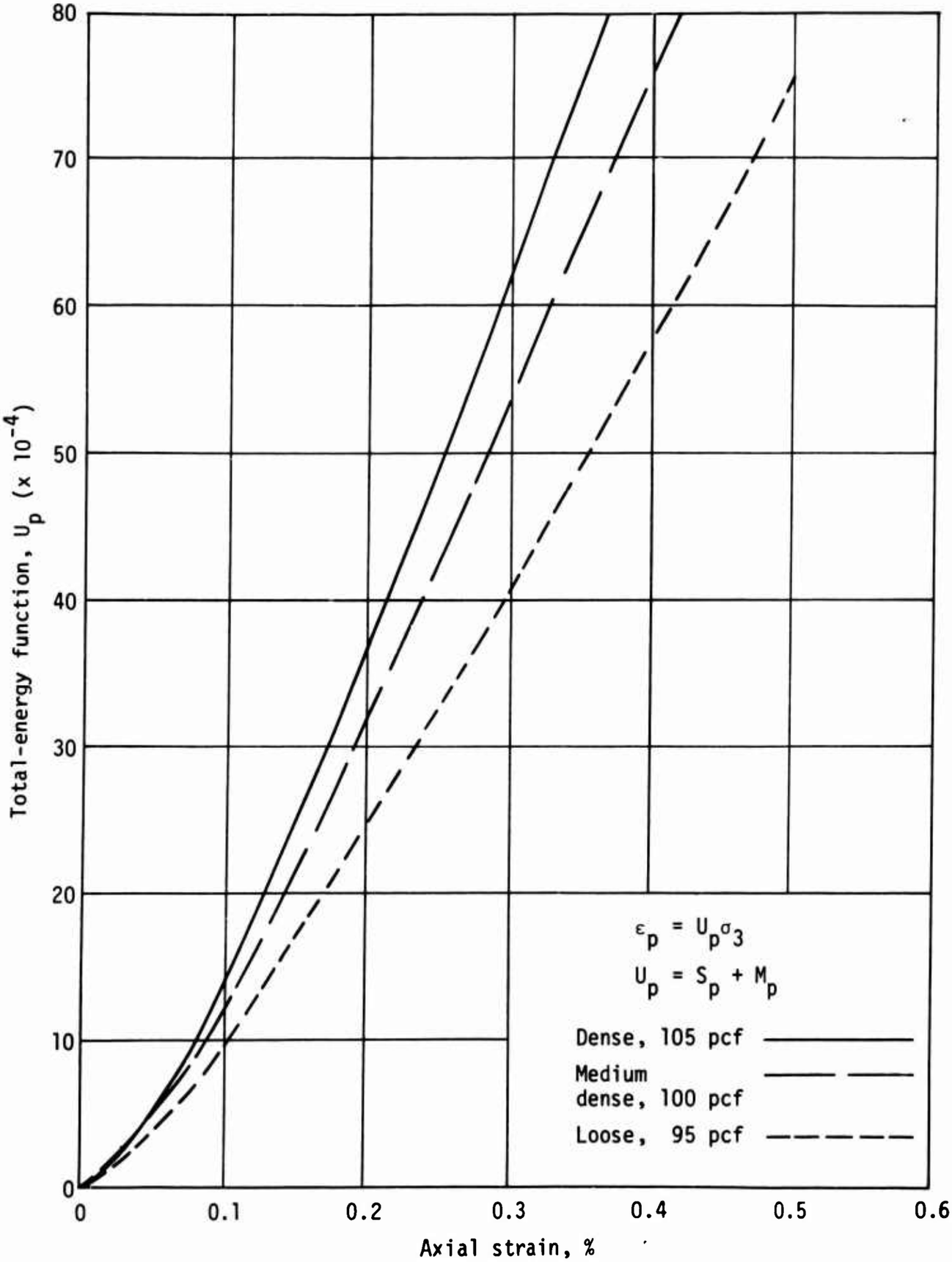

Figure 80. Total-energy function, U_p

Consider the ratio of potential to total energy

$$\frac{V_p}{\xi_p} = \frac{V_p}{V_p + T_p}$$

Now substitute from Eqs. (47) and (49) and rearrange. The resulting partitioning of potential energy is

$$\frac{V_p}{\xi_p} = \frac{1}{1 + S_p/M_p} \tag{53}$$

With only internal losses considered, the kinetic-energy partitioning is $1 - V_p/\xi_p$.

This result is particularly useful: *the partitioning of energies does not depend on the ambient stress acting.* Thus ambient stress is eliminated as a variable when energy partitioning is studied; and only material conditions need be considered for SFC materials. Figure 81 shows the potential-energy partitioning for the three material conditions in this report. It is significant to note the empirical fact that for this sand *the partitioning of energies is relatively insensitive to density.* In fact, the scatter in the curves presented can be shown to be the result of the accumulation of small errors in the several functional pickoffs and computations leading to them.

h. Reflection in SFC Materials.

For the purposes of this discussion, let the reflection factor (R_p) be defined as the ratio of the total reflected-to-incident stress

$$R_p = \frac{\sigma_{pr}}{\sigma_{pi}} \tag{54}$$

where

σ_{pi} = incident stress, and
σ_{pr} = reflected stress for SFC materials

When defined in this way, R_p is a number by which one multiplies the incident stress to obtain the total stress felt by a buried structure or gage from dynamic effects only (neglecting arching).

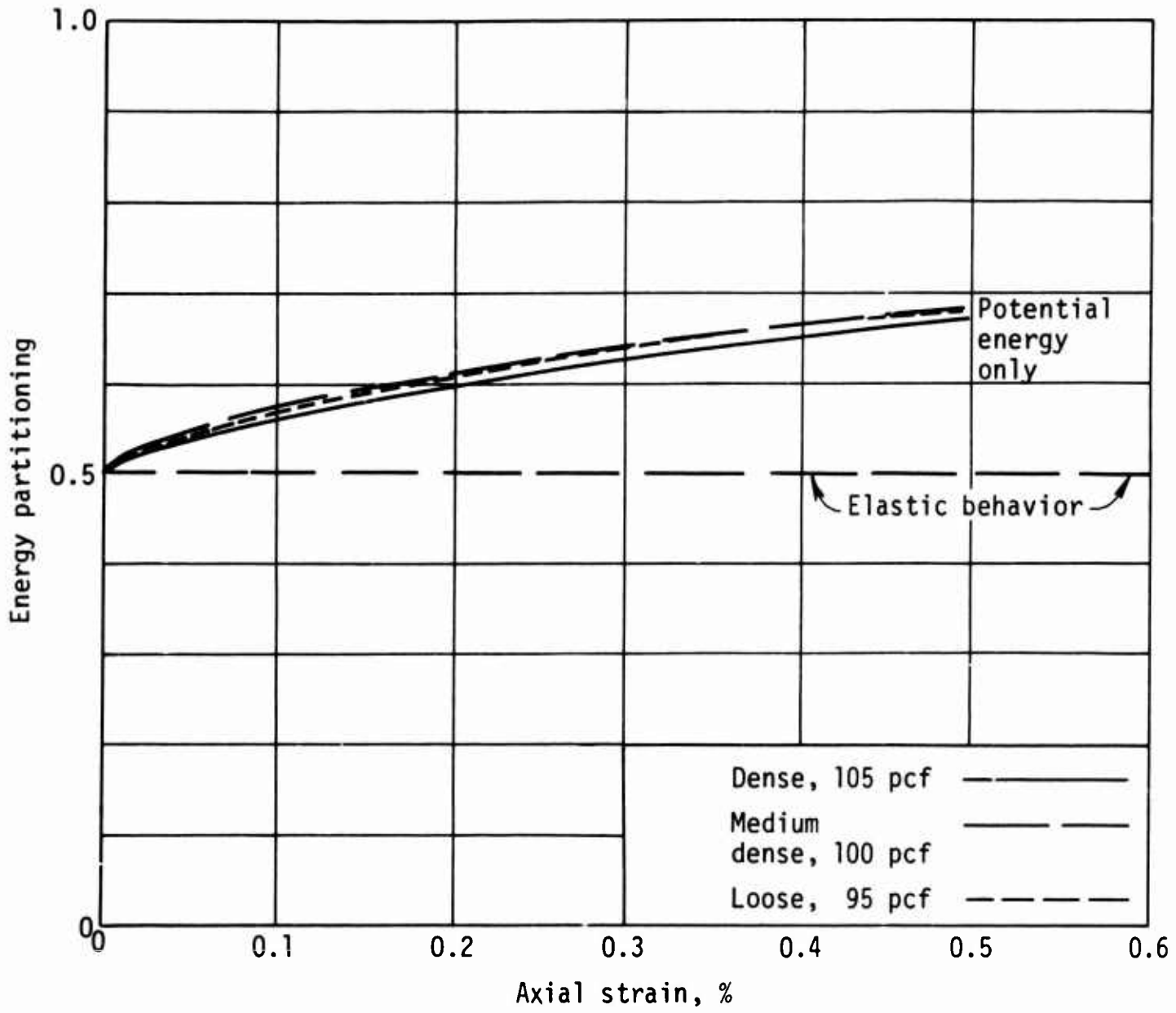

Figure 81. Energy partitioning

By recalling Eq. (35) and substituting it into Eq. (54), a more useful computational SFC form of the reflection factor results

$$R_p = \frac{L_{pr}}{L_{pi}} \tag{55}$$

where

L_{pr} = reflected stress ratio, and

L_{pi} = incident stress ratio for SFC materials

This result shows that *the reflection factor is independent of the ambient stress acting* and depends only on the soil condition. This means, for example, that stress gages buried in SFC materials will give dynamic readings proportional only to the incident pressure, quite independent of the ambient (spherical) component that the incident is creating (neglecting arching). Thus the calibration for that gage in that soil will be valid no matter what the range of incident pressures (neglecting arching). This simplification may allow closer study of dynamic arching effects because ambient stress--a variable in the incident wave--does not influence the gage reading. Similar conclusions apply for the design of subsurface structures.

It is not, in general, an easy matter to compute R_p in Eq. (55) for a reflecting boundary of arbitrary stiffness. The problem lies in determining L_{pr} for the particular conditions. If one is willing to take the limiting case of a rigid boundary, however, the computation is simple and the results are enlightening.

For the rigid-boundary case, the computations may be made solely on energy considerations, using the functions in this section. As some given strain level ε_{pi} impinges on the boundary with a unique L_{pi} (Fig. 72), its energies are partitioned according to Figure 81. When the strain ε_{pi} hits the boundary, it reflects into itself, with the result that the loading-only situation is preserved. The particle velocities, however, come to zero, with the result that the kinetic energy must go to zero. All the consumed energy, including internal losses, must, therefore, be converted to potential energy if there are no external losses. It is important to recall at this point that the energies under discussion are in fact *energy densities*. It is assumed that, as the strain reflects back into itself, halving the volume under consideration, the total-energy density

is *doubled* in the thin lamina of material directly at the boundary. In other words, the total-energy density is assumed to double and to be converted entirely to potential-energy density directly at the reflecting face

$$U_{pr} = 2U_{pi} = M_{pr} \tag{56}$$

where

U_{pr} = reflected total-energy function for SFC materials
U_{pi} = incident total-energy function for SFC materials
M_{pr} = reflected potential-energy function for SFC materials

In view of the simplicity of Eq. (56) the solution is now quite direct:

(1) for each incident strain ε_{pi}, double the total-energy versus density function in Figure 80 to obtain U_{pr};

(2) enter the potential-energy plot (Fig. 79) with the reflected-energy density U_{pr} to pick off the corresponding reflected strain ε_{pr};

(3) enter the constitutive relationship (Fig. 72), with the reflected strain ε_{pr} to pick off the reflected-stress ratio L_{pr}; and

(4) divide L_{pr} by L_{pi} according to Eq. (55) to obtain the reflection factor R_p.

The solutions for rigid-boundary reflection have been carried out for the three material conditions in this report and are given in Figure 82. It is significant to note the empirical fact that *the reflection factor is relatively insensitive to density* for this sand. That fact makes this sand particularly attractive for arching and stress-gage research. Furthermore, this type of wave-propagation test apparently leads to less density sensitivity than is found in other tests (e.g., the triaxial).

This density independence is shown by the computations given in detail in Appendix C, and summarized in Figure 83, which contains an analysis of Test H (248-0900) for which the density was 101.8 pcf. This test was chosen, although its density was different from the nominal 100 pcf intended, because it agreed well with the SFC curve at its own density of 100 pcf. The stress-time input at the front force link (Fig. 83) was converted to strains using the

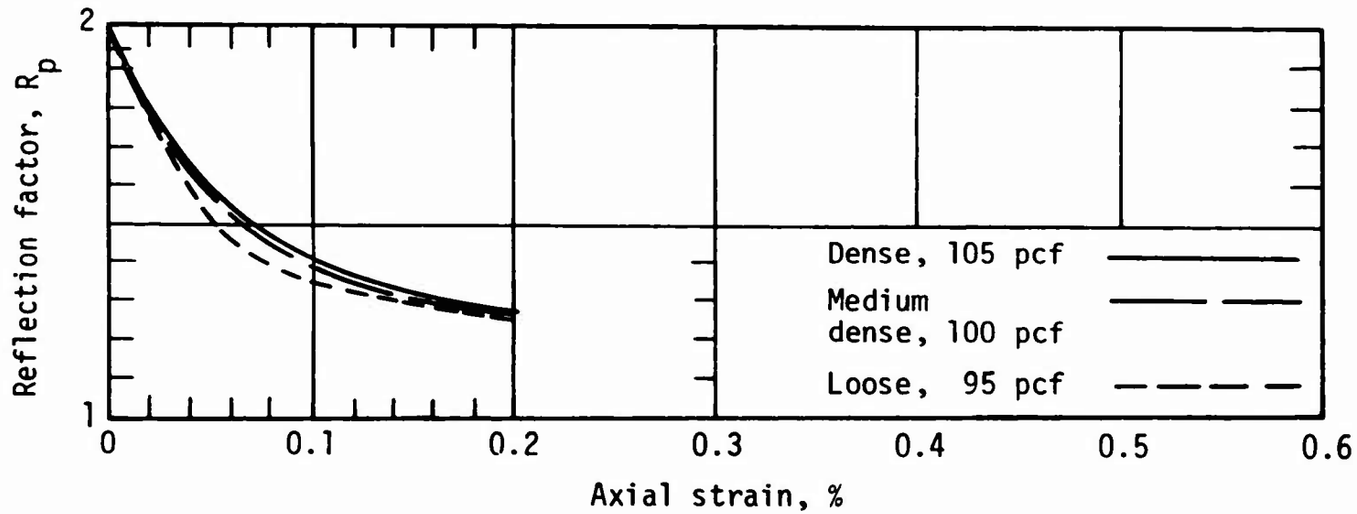

Figure 82. Reflection factor, R_p

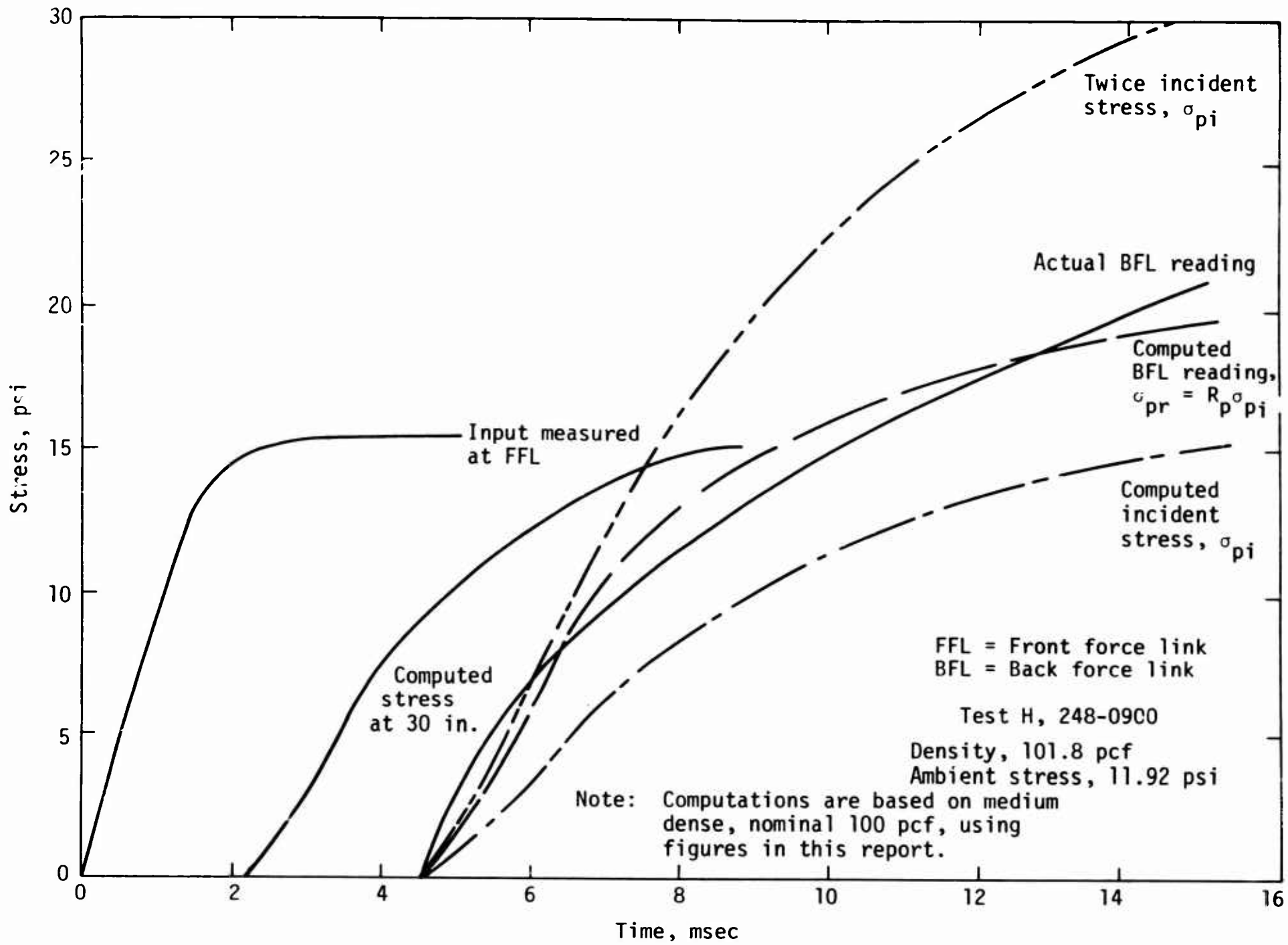

Figure 83. Reflected waveform

known ambient stress (11.92 psi), Eq. (34), and the SFC constitutive curves of Figure 72. The wave velocity of each strain was computed from the known ambient stress and the wave-velocity function of Figure 75. The time of arrival of each strain at the end of the sand rod was then computed, and the strains were reconverted to stresses. This process yielded the incident stress σ_{pi} shown in the figure. Each incident stress was then multiplied by the appropriate reflection factor at the corresponding strain (Fig. 82) to arrive at the computed back-force-link reading σ_{pr} shown in the figure. This computed result was compared with the actual back-force-link reading, shown by the heavy, dark line. Except at low stresses (strains), where both the computations and actual reading were in doubt, the agreement was within about 10 percent. This agreement tends to confirm that density differences have minor effects on the entire computation, and that the assumption of minor external losses and energy-density doubling in these experiments was valid. In evaluating the back-force-link reading, it is well to keep in mind the calibration scatter (Fig. 30) owing to eccentricities. Finally, it is interesting to note that current design manuals recommend a semi-elastic approach to this computation, leading to simply a doubling of the incident stress. The result of that computation, shown also in Figure 83, gives some feeling for the adequacy of such a procedure. The computed stress waveform at 30 inches, halfway down the rod, is also shown in Figure 83.

An alternate solution to rigid reflection can be obtained, with the result that reflected stresses can be computed directly from strains without the intermediate step of reconversion to stresses. Notice that Eq. (55) can be rewritten as $L_{pr} = R_p L_{pi}$. Also recall Eq. (35), and substitute

$$\sigma_{pr} = R_p L_{pi} \sigma_3 \tag{57}$$

Now define the SFC reflection function (W_p)

$$W_p = R_p L_{pi} \tag{58}$$

Then the reflected stress may be computed directly from

$$\sigma_{pr} = W_p \sigma_3 \tag{59}$$

and by use of Figure 84, which has the function W_p computed for the three material conditions in this report.

3. Effects of Ambient Stress on Wave-Propagation Parameters.

The effects of ambient stress on propagation at near-zero strains (seismic) have been reviewed from the literature. The conclusions to be drawn are that wave velocity varies with the 1/4 power of the ambient stress and that other seismic parameters may be estimated by elastic methods.

The effects of ambient stress on propagation at finite strains up to failure have been developed above. It has been shown that both wave and particle velocity vary with the 1/2 power of the ambient stress, that energies are linear on ambient stress, and that energy partitioning and reflection are both independent of ambient stress.

4. Effects of Density on Wave-Propagation Parameters.

Although the SFC approach above simplified the problem of the effects of ambient stress, no such simplification appears to be possible for the effects of density. The best that can be hoped for is a qualitative feeling for these effects as shown by the results of this research. In the next few paragraphs the influence of density on each variable will be systematically studied.

First, it is of some interest to note how the normal static SFC parameters L_p and ϕ_p vary with density. The variation of the stress ratio L_p is shown in Figure 85. L_p always increases with density, and the higher the strain, the greater the variation, explaining crudely why triaxial data yield such scattered results. For example, a 1-pcf error in density could yield an L_p error of 0.18 out of 1.30 at low densities and high strains. This would lead to almost 15-percent error in deviator stress, a value that would be by no means unrealistic in view of the bands of triaxial data typically obtained for sands. The effects of the stress angle ϕ_p are somewhat less drastic, as shown in Figure 86. Although there is always an increase, the rate of increase does not depend strongly on the strain level.

Recall that two functions--$f(\phi_p)$ and $d\phi_p/d\varepsilon_p$--went into the computation of the wave-velocity function. The effect of density on the inert-ϕ function $f(\phi_p)$ is very pronounced at higher strains, as shown in Figure 87. Just the opposite is true for the slope function $d\phi_p/d\varepsilon_p$ as shown in Figure 88: the variation is trivial at high strains, but is quite pronounced at low strains; and

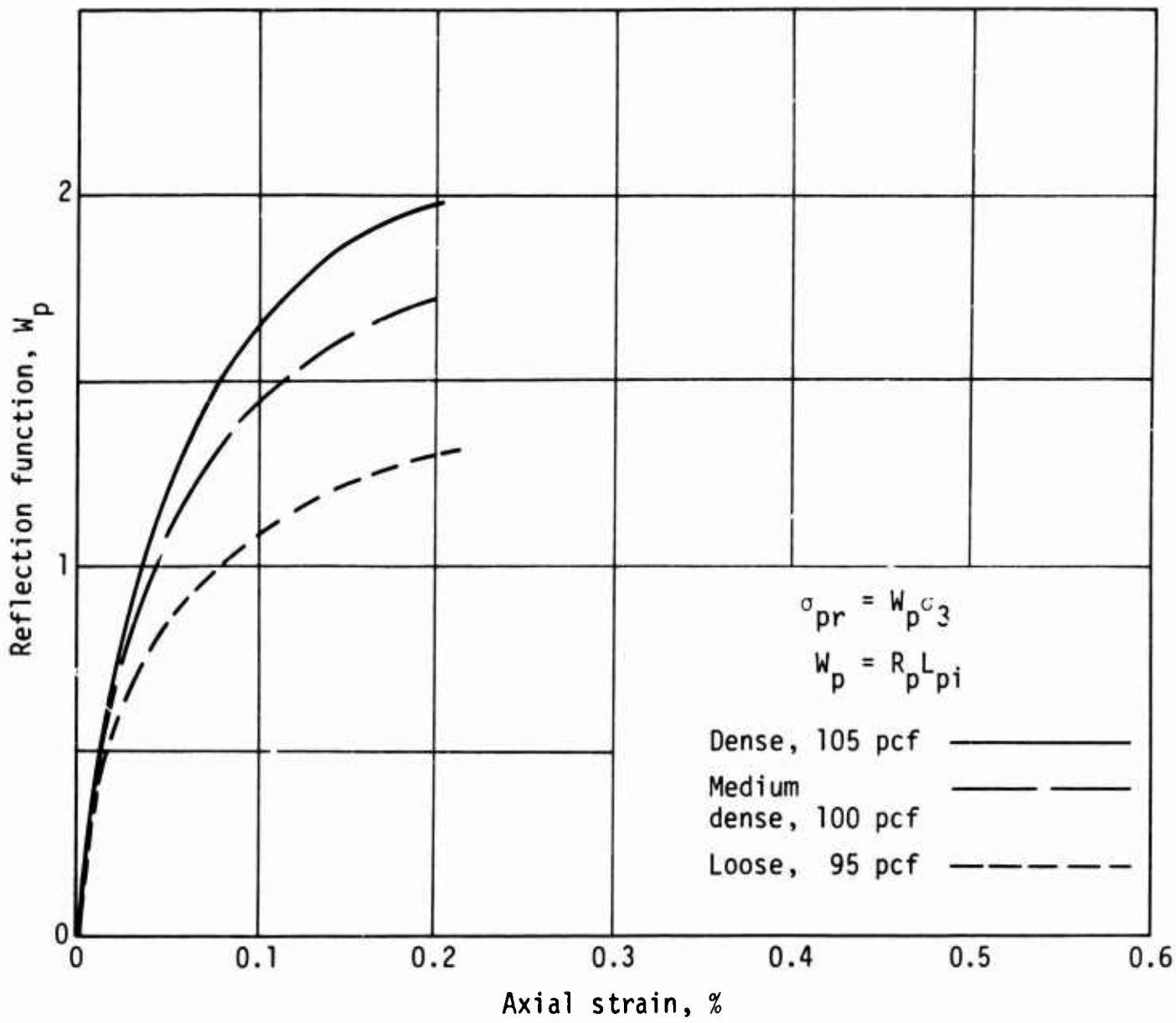

Figure 84. Reflection function, W_p

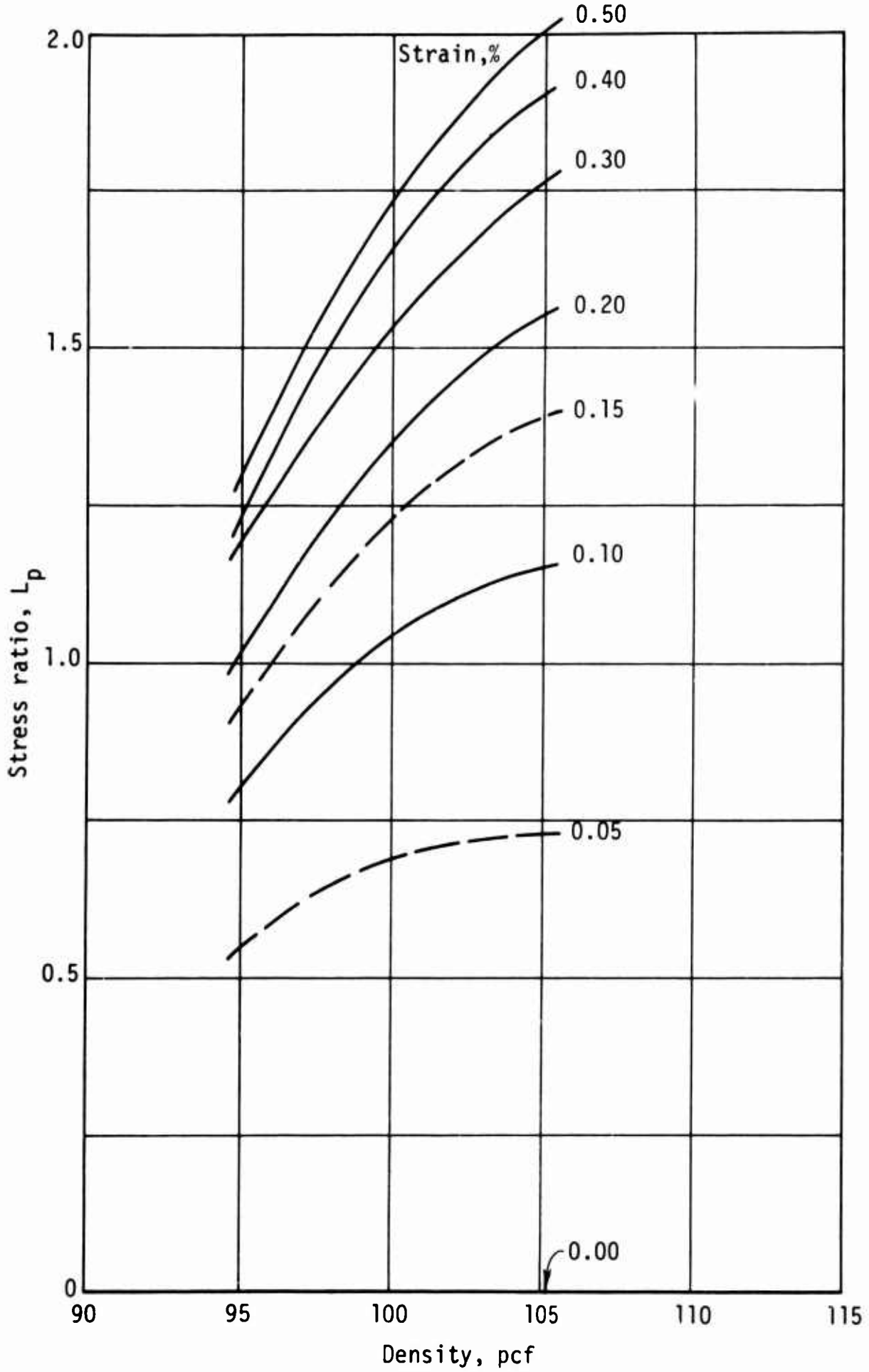

Figure 85. Effect of density on stress ratio, L_p

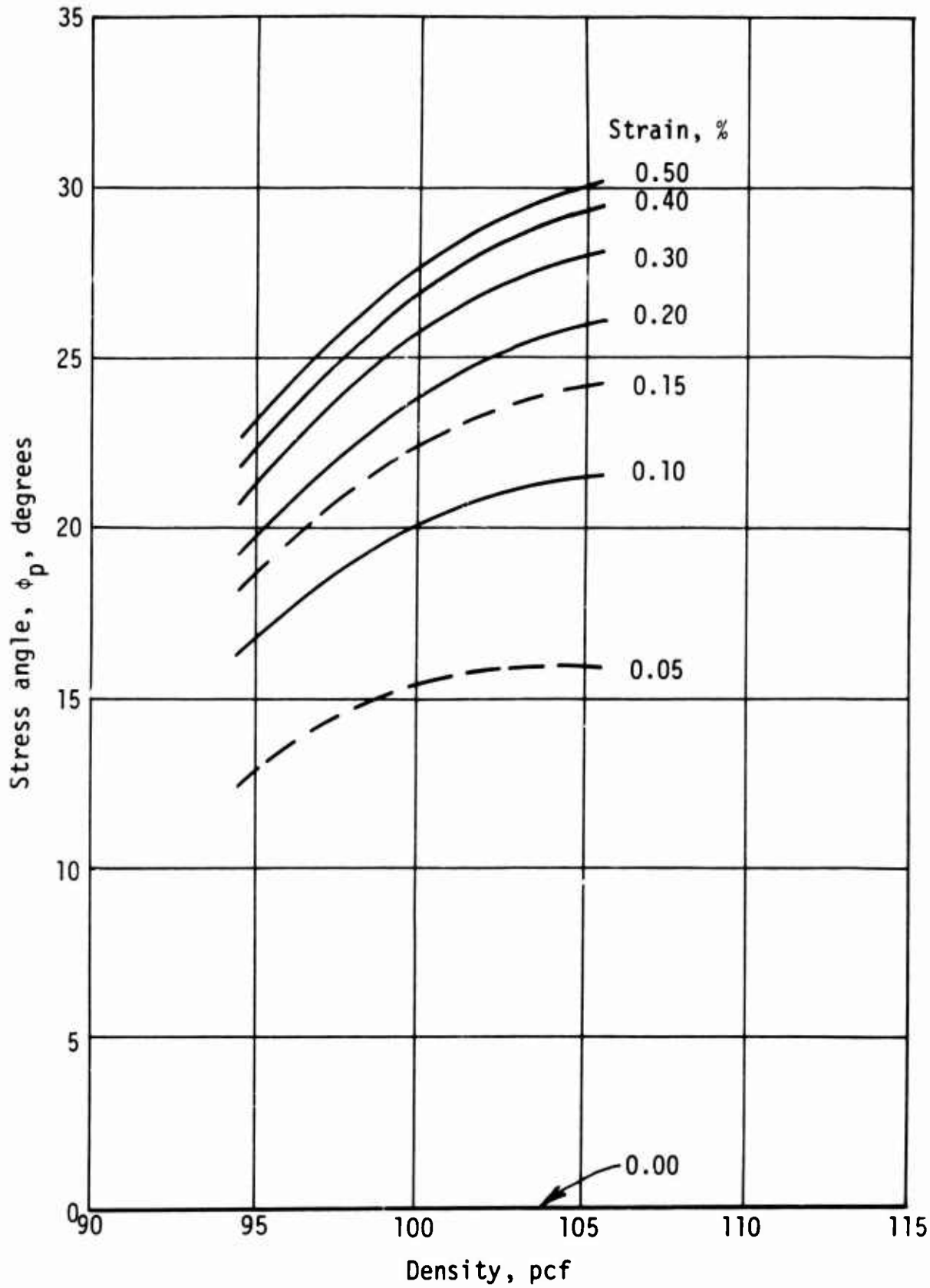

Figure 86. Effect of density on stress angle, ϕ_p

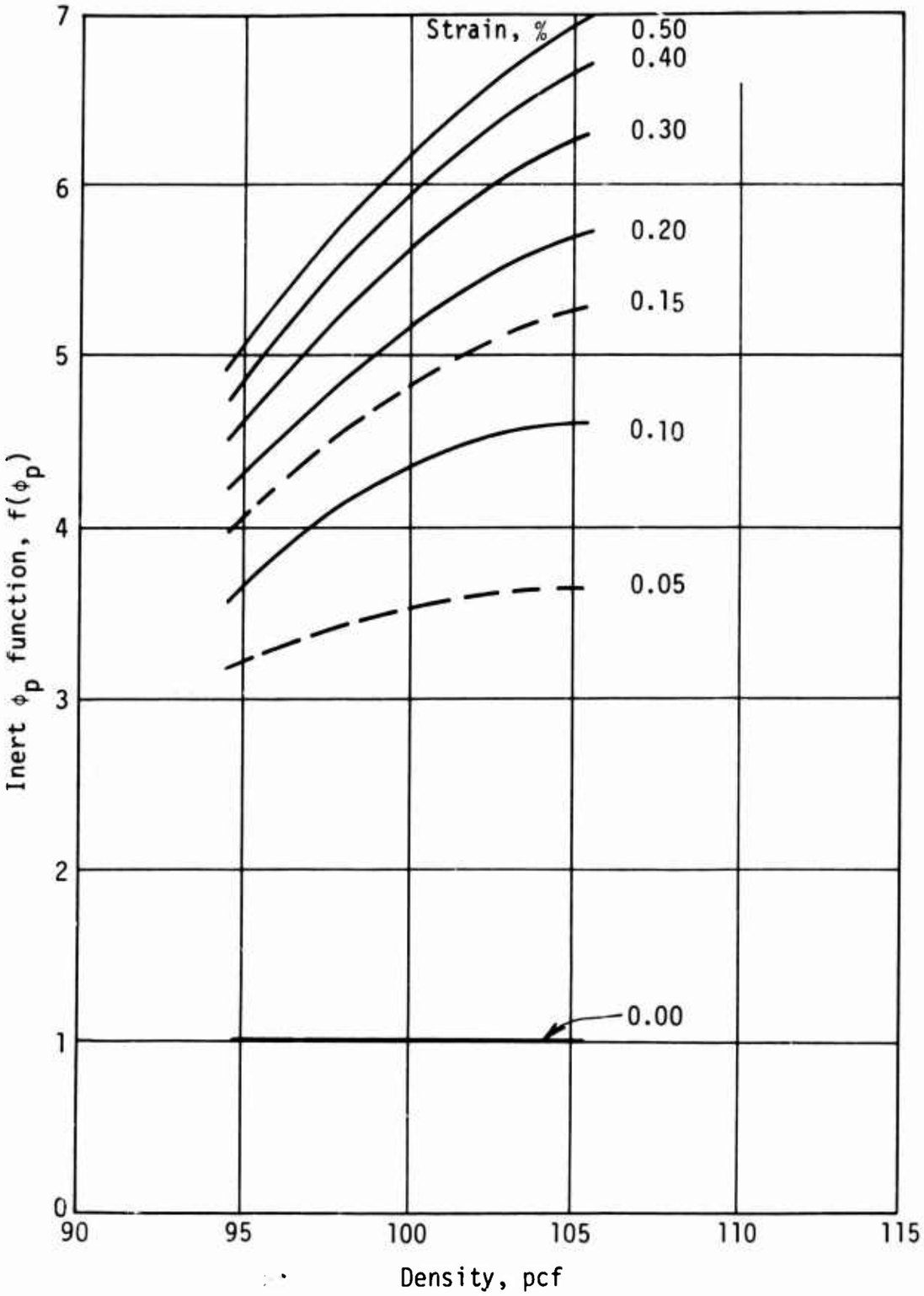

Figure 87. Effect of density on inert-ϕ_p function, $f(\phi_p)$

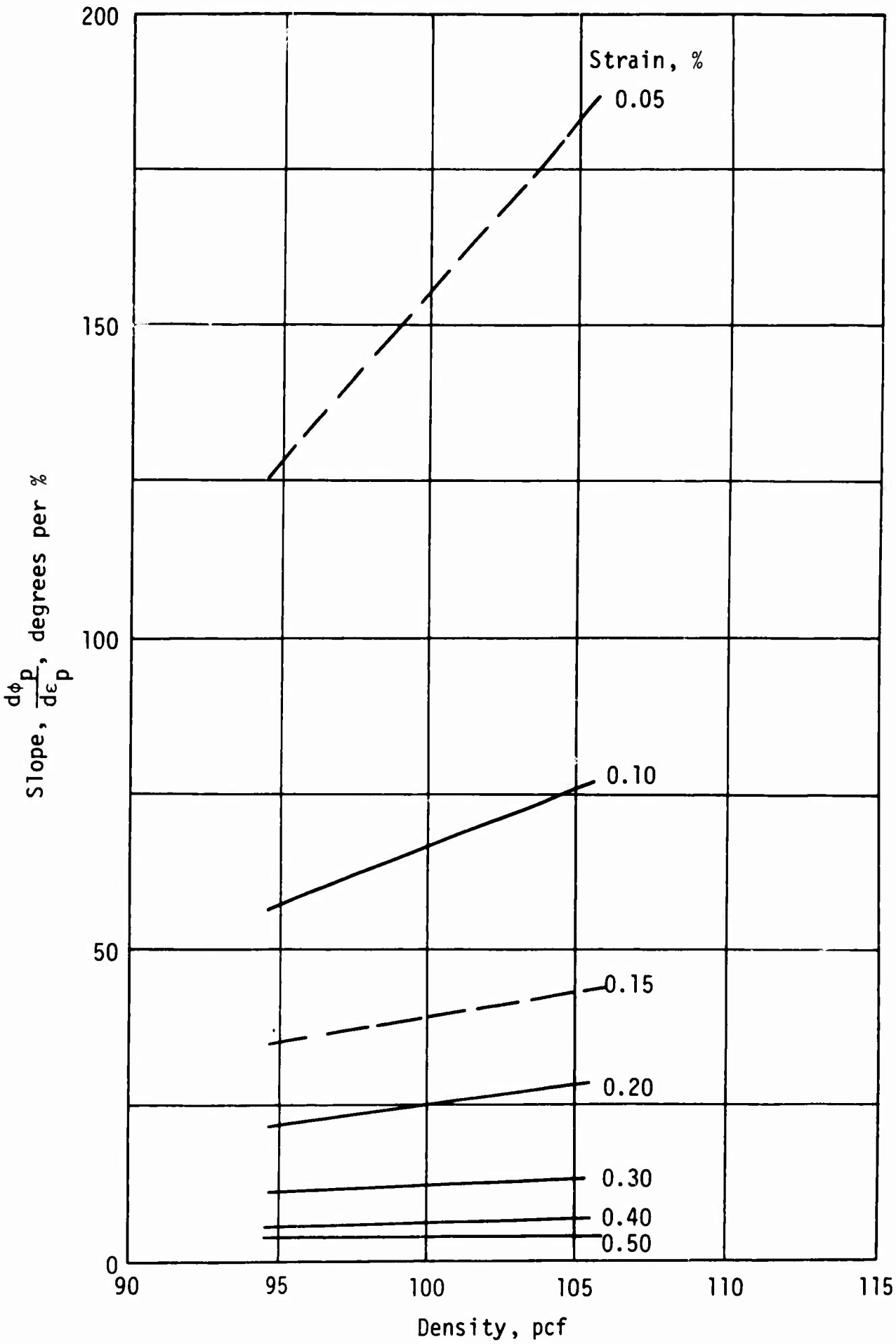

Figure 88. Effect of density on slope function, $\frac{d\phi_p}{d\varepsilon_p}$

within the accuracy of the scale chosen, the variation is linear with density for all strains. Comparison of Eqs. (36) and (41) shows that the product $f(\phi_p)$ $d\phi_p/d\varepsilon_p$ is a kind of modulus, called the *SFC propagation-modulus function.* The variation of this modulus function with density is shown in Figure 89. The overall variation appears to be controlled most strongly by the slope function. The variation is extremely sharp at low strains, but small at high strains, and is apparently linear. Because the modulus function is linear, the wave-velocity function (N_p) cannot be linear, as is illustrated by Figure 90. The curvatures are, however, quite minor; and over a restricted range of densities a linear approximation seems adequate for engineering purposes. The curvatures seem to increase for smaller strains.

This conclusion should not be emphasized, however, in view of Richart's finding of a linear relationship between seismic velocity and density, as shown in Figure 11. The relative insensitivity of this function to density is somewhat comforting: in the worst case (low density, low strain) a 1-pcf error only results in a less than 2-percent wave-velocity error; and in the best case (high density, high strain) the variation is almost trivial for practical problems. Similar qualitative conclusions can be drawn regarding the variation of the particle-velocity function (Q_p), as shown in Figure 91. Here again the curvatures are small; the variations can be linearized for engineering purposes, and the seismic values should be linear.

The effects of density are given for the kinetic-energy function in Figure 92 and for the potential-energy function in Figure 93. The variation is greater for higher strains in both cases, is essentially linear for the kinetic case, and is much higher at a given strain for the potential case. The downward concavity of the potential function forecasts possibly a more equal partitioning of energies at higher densities. Nevertheless, within the range of densities studied for this sand the effects of density on energy partitioning are negligible, as shown in Figure 81. Similarly, the effects of density on the reflection factor R_p are trivial, as previously developed and shown in Figure 92.

In summary, all wave parameters increase with increasing density. As a practical matter, all variations can be linearized over this restricted range of densities. This linearity could presumably be valid for other ranges of density. The effects of density are negligible for energy partitioning and reflection, small for velocities, but appreciable for energies.

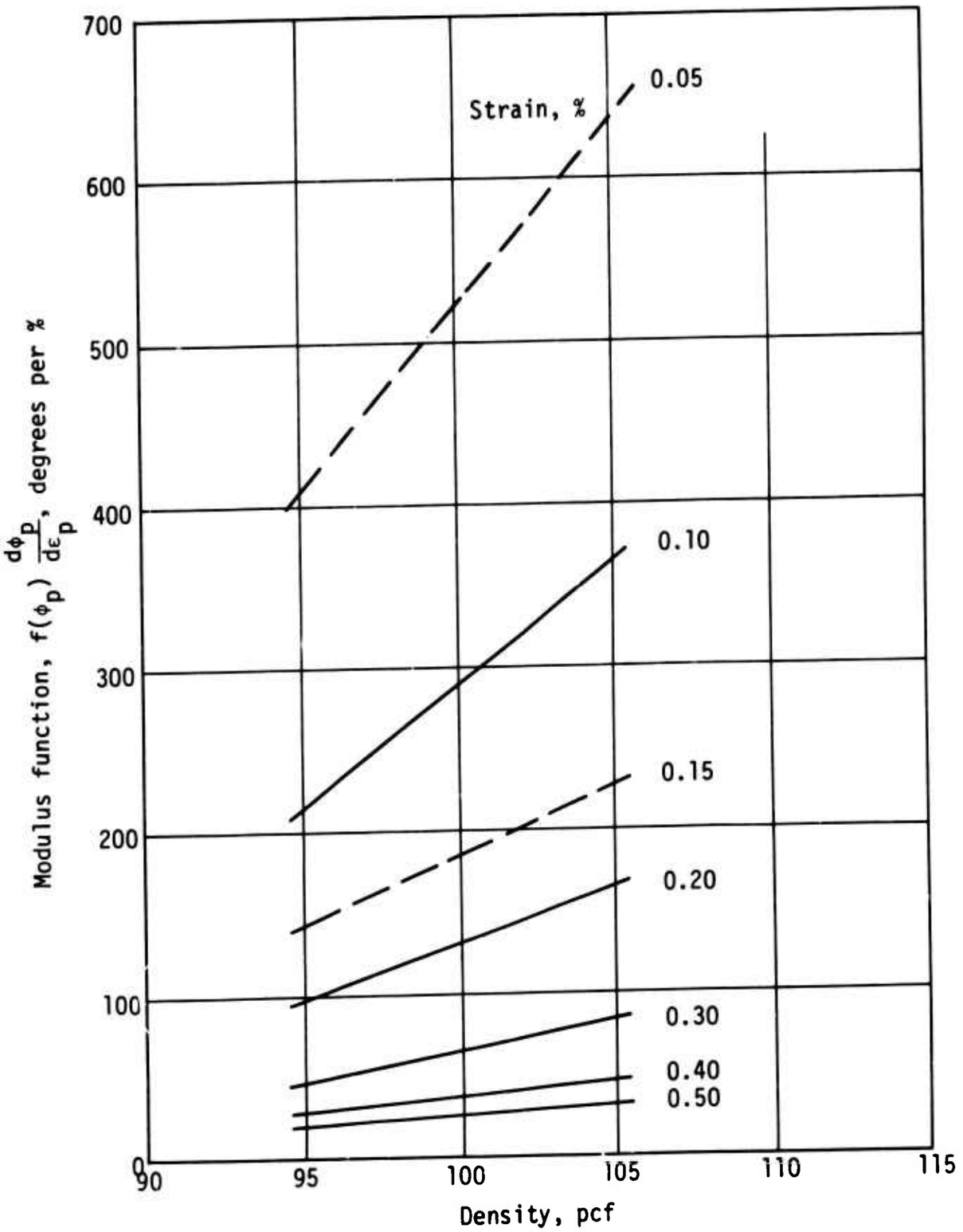

Figure 89. Effect of density on modulus function, $f(\phi_p)\frac{d\phi_p}{d\varepsilon_p}$

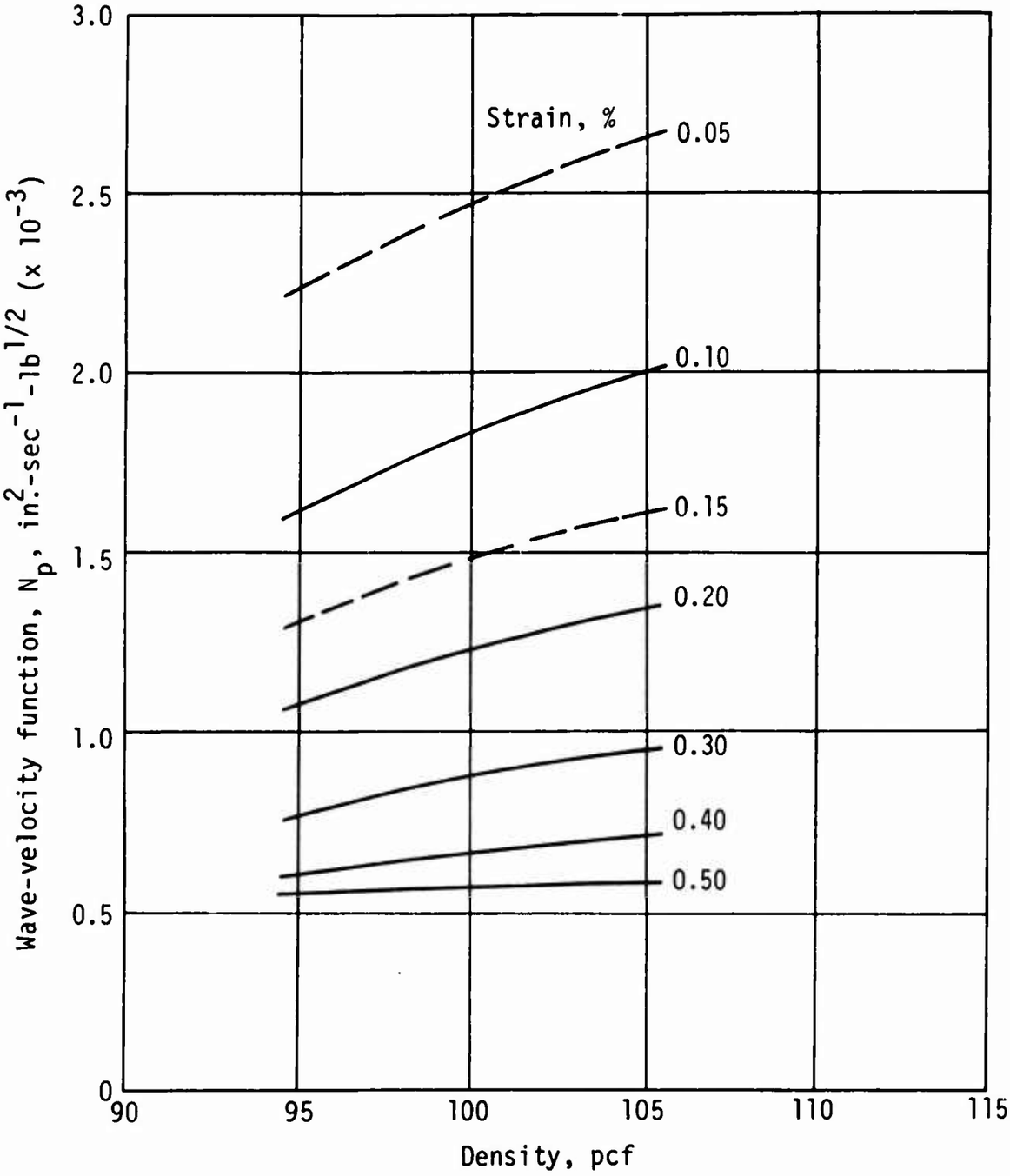

Figure 90. Effect of density on wave-velocity function, N_p

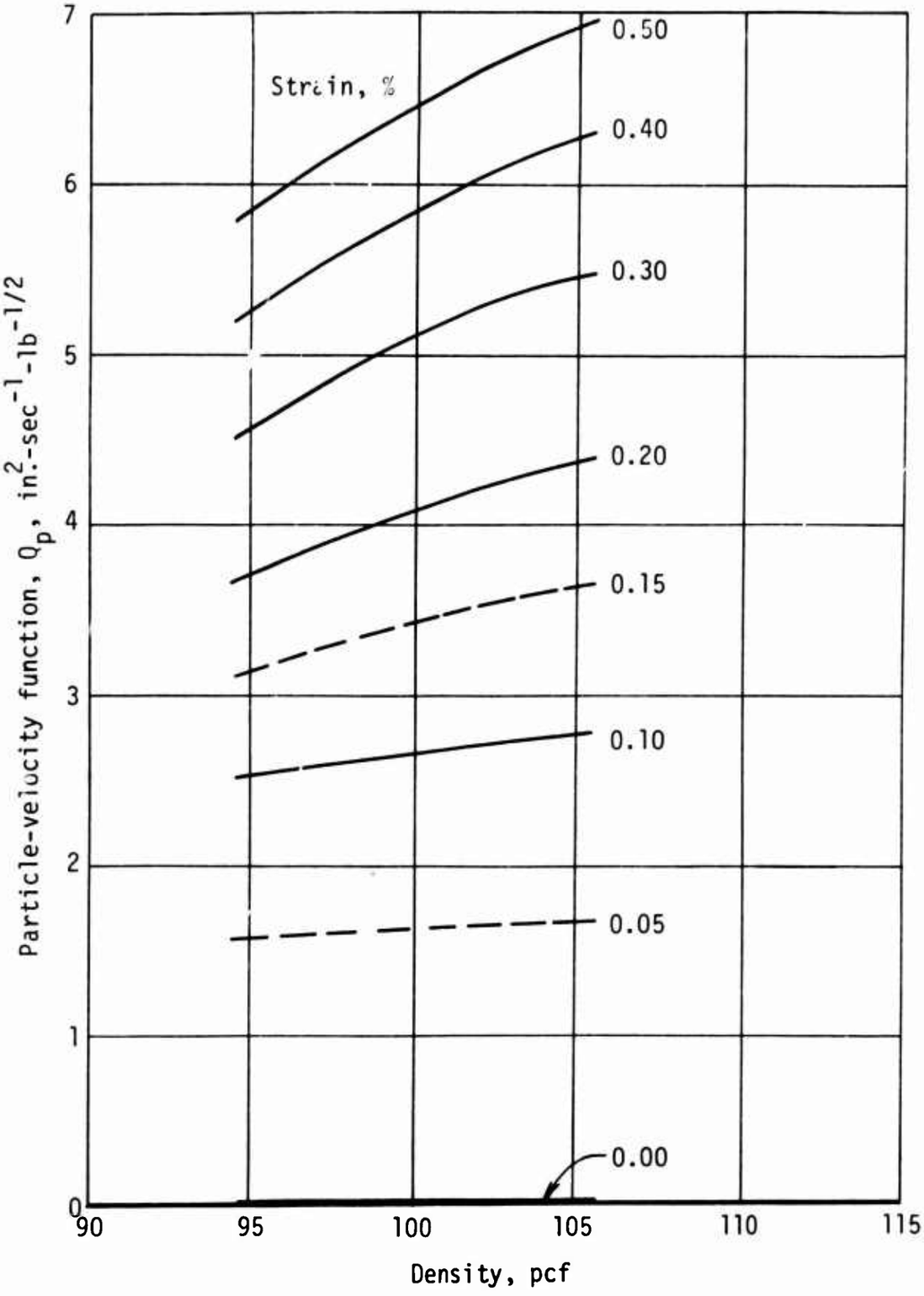

Figure 91. Effect of density on particle-velocity function, Q_p

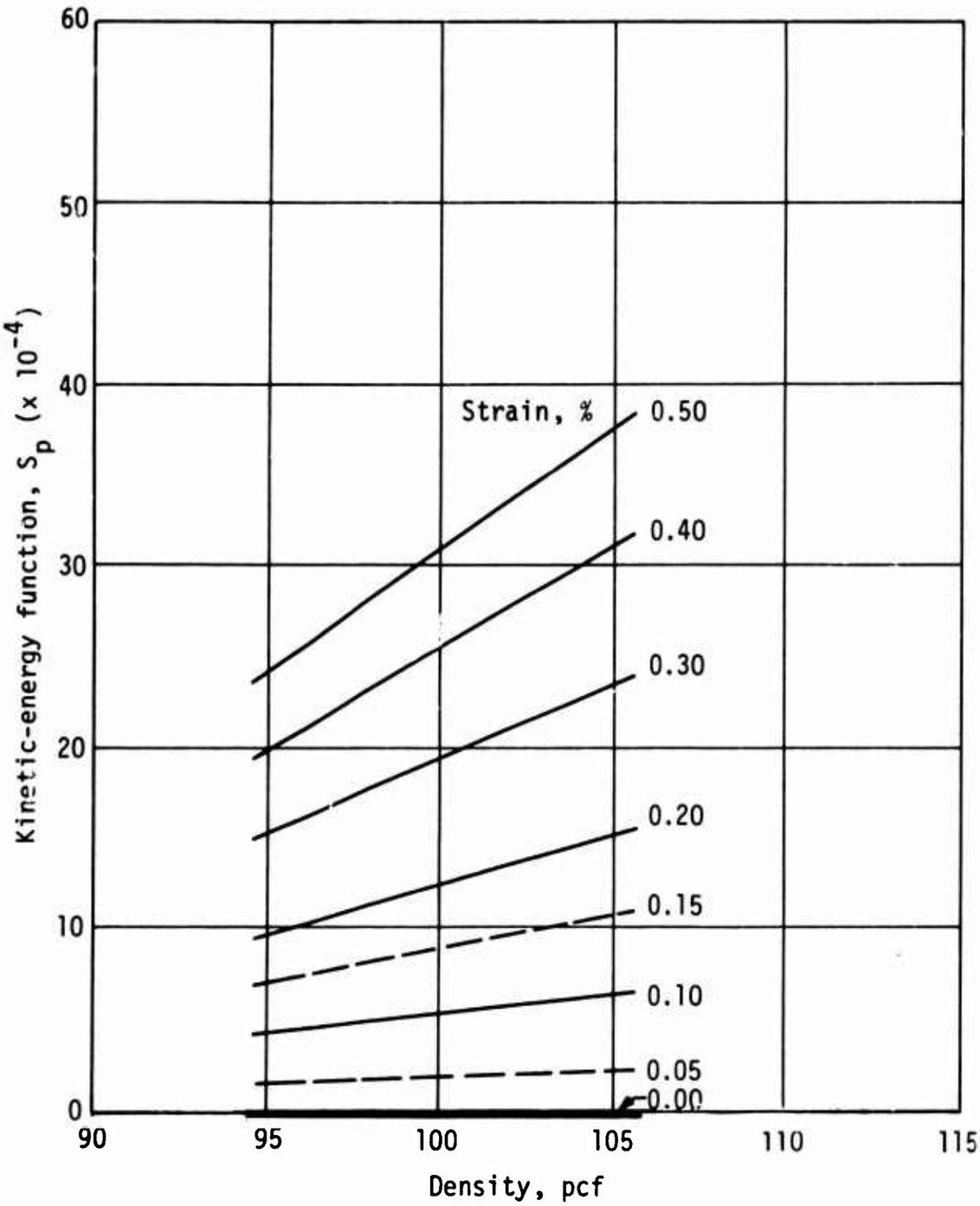

Figure 92. Effect of density on kinetic-energy function, S_p

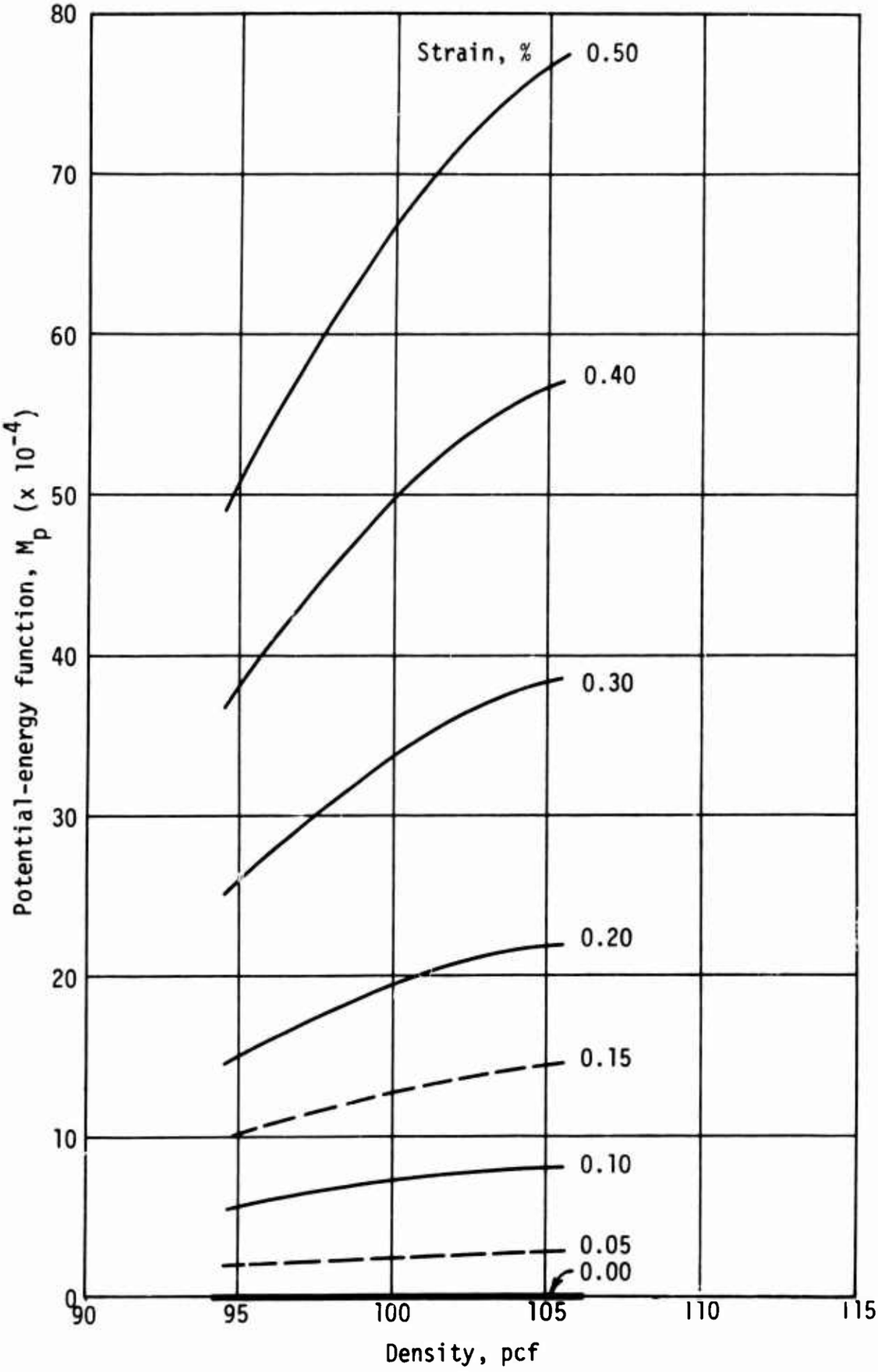

Figure 93. Effect of density on potential-energy function, M_p

5. Relationships Between Seismic Velocity and Triaxial Parameters.

There recently have been suggestions that some empirical correlation between seismic velocity and normal soil properties may exist in spite of the fact that data in the literature indicate that the dynamic and static properties of real soils do not in general show any correlation at all (Refs. 58,63,64). Nevertheless, because the seismic velocities of this sand are well known, and because the normal properties were accurately determined in these experiments, the possibilities of such a correlation have been investigated.

The strength of the sand was selected as the specific property with which to correlate seismic velocity. For this purpose strength is defined as the stress required to cause 0.5-percent strain. By this definition the variables to be correlated are reduced to four: strength, density, ambient stress, and seismic velocity. The strengths are available from the data of Figure 47; these are shown as functions of two of the variables--ambient stress and density--in Figure 94. It is interesting to note that the data in Figure 94 do not support the linear-strength versus density relationships reported elsewhere (Ref. 58). For each combination of the two static variables in Figure 94--density and ambient stress--there is a seismic velocity that can be determined from Figure 11. With these available, all four variables--strength, density, ambient stress, and seismic velocity--can now be investigated.

In general for any soil the seismic velocity is $c_o = c_o\ (\sigma_3, \gamma)$, a function of both ambient stress and condition (density for sands). For a fixed condition, Richart (Ref. 49) has shown that $c_o = c_o\ (\sigma_3$ only), and that the two are specifically related by a power function

$$c_o = h\ \sigma_3^{\ m} \tag{60}$$

and where m is on the order of 1/4 and h is a constant. Now recall that by the hypothesized SFC relationship the deviator stress is

$$\sigma_{dp} = L_p\ \sigma_3 \tag{35}$$

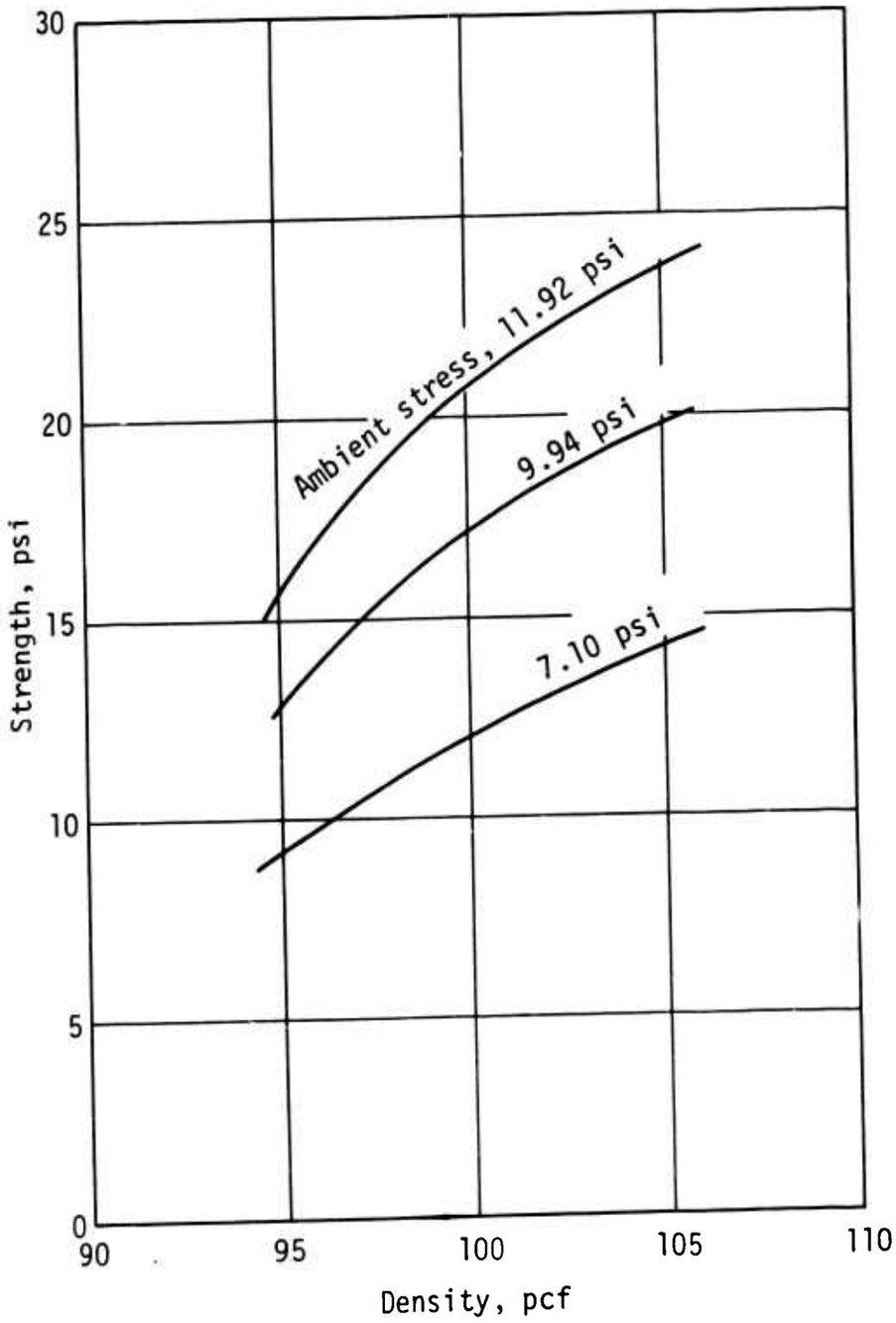

Figure 94. Strength-density relationship

This SFC relationship is probably most valid as failure impends; therefore the strengths may be written with some confidence as

$$s = L_s \sigma_3 \tag{61}$$

where

L_s = strength ratio (ratio of strength to ambient stress)

Now assume that there exists an inverse on Eq. (61)

$$\sigma_3 = \frac{1}{L_s} s \tag{62}$$

Then the strength and wave velocity can be related by

$$c_o = h \left(\frac{1}{L_s} s\right)^m \tag{63}$$

Because for a fixed condition L_s is a constant, the constants h and $(L_s)^m$ can be combined into a single constant k to write

$$c_o = ks^m \tag{64}$$

This result indicates that there should be a power-function relationship between strength and seismic velocity and that the power should be the same as for the ambient-stress versus seismic-velocity relationship, *provided the following assumptions are met:*

(1) only one condition (density) is considered;

(2) the material is coulombic;

(3) the material has a power-function relationship between ambient stress and seismic velocity.

Then, for these restricted conditions only, one may expect a correlation between strength and seismic velocity. Such a correlation for the experimental data in this report is given in Figure 95. The data are indeed essentially parallel to Richart's data, and show less scatter on density (Richart's data are a 7-pcf

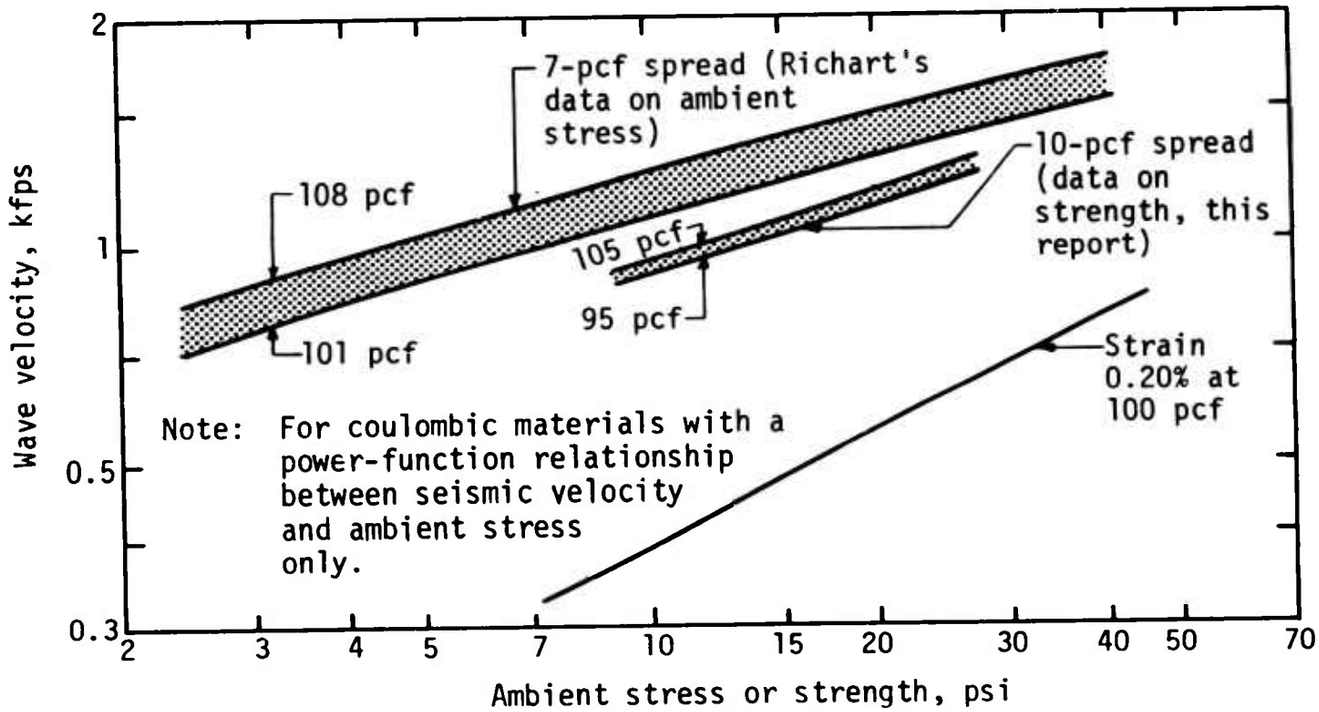

Figure 95. Seismic-velocity vs. strength relationships

spread; these data are a 10-pcf spread). For power-function comparison, the data from Figure 76 representing an intermediate strain of 0.2 percent have also been included in Figure 95.

SECTION VII

CONCLUSIONS AND RECOMMENDATIONS

The survey of the literature demonstrated that elastic theory is a valuable guide for predicting wave-propagation phenomena in soils and for setting bounds on waveform quantities. The survey also showed that at seismic-stress levels only the wave velocity is related to ambient stress by a power function, as predicted by the elastic theory for a packing of spheres. It was suggested that research is needed to determine the validity of elastic theory in more realistic clayey materials and to determine the effects of deviator stress on the resulting behavior. Finally, the survey showed that for clean dry sands the wave velocity varies linearly with the sand condition expressed as density. This important empirical fact should be studied for other soils.

The research showed that dynamic experiments can be performed using displacement (or any other kinematic quantity) measurements only. The techniques and instrumentation used in this research were a first attempt and should be improved before the research is extended. Nevertheless, it was demonstrated that dynamic experiments can be conducted and interpreted without measuring stress, with all the attendant difficulties and uncertainties. It is suggested, therefore, that the need for the development of stress gages for laboratory wave-propagation experiments is reduced, and the way for a reassessment of experimental techniques in terms of simple and reliable kinematic measurements is opened.

The survey of the literature emphasized that plastic theory requires two assumptions: (1) that wave velocity is a function only of material properties, and (2) that the material is constitutively unique. The most important implication of the first assumption is that the wave velocity does not depend on the input function. In the experiments of this report the input waveform was not a significant variable. It was not possible to find any reference to the second assumption--constitutive uniqueness--in the literature; apparently all other investigators, both theoretical and experimental, have implicitly made this same assumption. It is apparent that these two assumptions are intimately connected, since their validity depends on the insensitivity of waveform parameters to variations in the input function. It is recommended that some experimental effort be devoted to a study of the validity of these two assumptions for realistic soils: if the assumptions are found to be adequately valid, then some simple but powerful analytical methods can be brought to focus on the soil

wave-propagation problem; but if the assumptions are found to be invalid, an objective reassessment of all existing analytical approaches, both unconstrained and constrained, will be required.

The static (triaxial) results showed that this sand acts as an SFC material (one which follows Coulomb's failure law at subfailure stresses). These results were restricted in the range of ambient stress (due to the maximum vacuum) and density (due to the small diameter of the long specimen). The SFC hypothesis should be checked for this sand and for other soils utilizing a broader range of ambient stresses and conditions. These experiments need only be static in, for example, a standard triaxial cell.

The results of the research showed that plastic theory for strain-rate-insensitive materials accurately predicts the waveform parameters for this sand. The following general conclusions were drawn:

1. The sand used is for engineering purposes strain-rate insensitive.
2. The sand used is for engineering purposes an SFC material under both static and dynamic conditions.
3. Strain-rate-insensitive plastic theory adequately predicts waveform parameters.
4. Seismic arrivals from soft-fronted pulses are accurately predicted by the results of vibration tests.

On the basis of the first three conclusions, strain-rate-insensitive plastic theory was extended to a theory for wave propagation in strain-rate-insensitive SFC materials. These theoretical developments led to the following general laws for *above-seismic stresses and for a specific soil condition in a strain-rate-insensitive plastic SFC material:*

1. Wave and particle velocities are proportional to the 1/2-power of ambient stress.
2. All energy densities--kinetic, potential, and total--are linearly proportional to ambient stress.
3. Both energy partitioning and reflection factor are independent of ambient stress.

Utilizing these theoretical results, the experimental data were analyzed to assess the effects of soil density on waveform parameters *for the sand used and the limited range of densities utilized in this study.* The conclusions were the following:

1. Minor variations in density (e.g., 1 percent) lead to inordinately large variations in static parameters (e.g., 15 percent on deviator stress).

2. Minor variations in density (e.g., 1 percent) lead to tolerable variations in waveform parameters (e.g., 2 percent on velocity).
3. All waveform quantities increase in magnitude with increasing density.
4. The increase in waveform parameters with increasing density is greatest at high strains for the quantities-stress ratio, stress angle, particle velocity, and energies, but is greatest at low strains for the coulombic modulus function and wave velocity.
5. For the range of densities studied, some of the waveform parameters are specifically linear with density; and all can be taken as linear for engineering purposes over a restricted range of conditions.
6. Both energy partitioning and reflection factor are sensibly independent of density for engineering purposes over the range studied.

It was assumed that on reflection from a rigid boundary the total-energy density was doubled and entirely converted to potential energy at the reflecting face. With the use of this principle the stress at the reaction end of a dynamically loaded specimen was computed and compared with an actual gage reading. The results compared within about 10 percent except at low strains.

These conclusions apply only to this sand for the limited range of ambient stresses and densities studied. In view of the sweeping simplifications they represent, however, studies should be undertaken to determine the extent to which they can be applied to realistic soils and to the constrained geometry for engineering purposes. The experimental data and theoretical analyses showed that for SFC materials the waveform parameters are much less sensitive to random variations in condition than are the static parameters; there may be reason to believe that wave-propagation tests may be more reliable measures of dynamic soil properties than are conventional property tests. It is recommended that a study be made of the feasibility of wave-propagation tests as a standard dynamic property-testing method.

It has been shown that the seismic velocity varies as a power function of ambient stress, and for clean, dry sands varies linearly with density over restricted ranges. *For strain-rate-insensitive coulombic materials that possess a power-function relationship between seismic velocity and ambient stress,* an empirical correlation between seismic velocity and static strength can be established. This correlation has the following properties:

1. For all such materials the power of the power function relating seismic velocity and strength will be the same as that relating seismic velocity to ambient stress.
2. For the sand of this study the correlation is much less sensitive to density than is the ambient-stress versus wave-velocity relationship.

In view of its immediate applicability to engineering problems the strength of this correlation should be checked for other soils. Because the correlation depends on the material being coulombic for failure (strength) conditions, presumably such a study could be part of the SFC study suggested above.

APPENDIX A

DEVELOPMENT OF EXPERIMENTAL EQUIPMENT AND VERIFICATION TESTS

Appendix A is intended to supplement the material in Section IV. For ease of reference, Section IV and Appendix A are set up under the same topics and in the same order.

1. General Description.

   See General Description in Section IV, 1.

2. Specimen.

   a. Mold and Membrane.

      For drawings of the specimen mold, see Figure 96.

      The membranes are a surgical type (Davol-Penrose Drainage Tubing, Latex, No. 9794X), 1 inch in diameter, 3 feet long, with 0.012-inch average thickness (range 0.009 to 0.015 inch). Although these membranes are flexible (modulus 200 to 300 psi), they are extremely tough and resilient. For a membrane 5 feet long, two 3-foot sections were butt-cemented with a latex compound while stretched over a 1-inch-diameter nylon rod.

      So that the vacuum could be communicated over the entire 5-foot length of the membrane, it was necessary to place a thin layer of gauze or absorbent tissue over the single vacuum fitting and along the entire mold length. The imprint of this tissue could barely be seen by the unaided eye in the completed specimen.

   b. Soil.

      See Soil in Section IV, 2b.

3. Specimen Containment.

   a. Foam.

      The previously used sling-suspension schemes (Refs. 34,58) were studied in detail and rejected because: the specimen would have to span between slings, and the effects of this bending could not be assessed with any accuracy. From the previous work it was clear that at least three and preferably four slings would be required at each support point, but the practical problems associated with the exact alignment and tension balance of each sling set proved

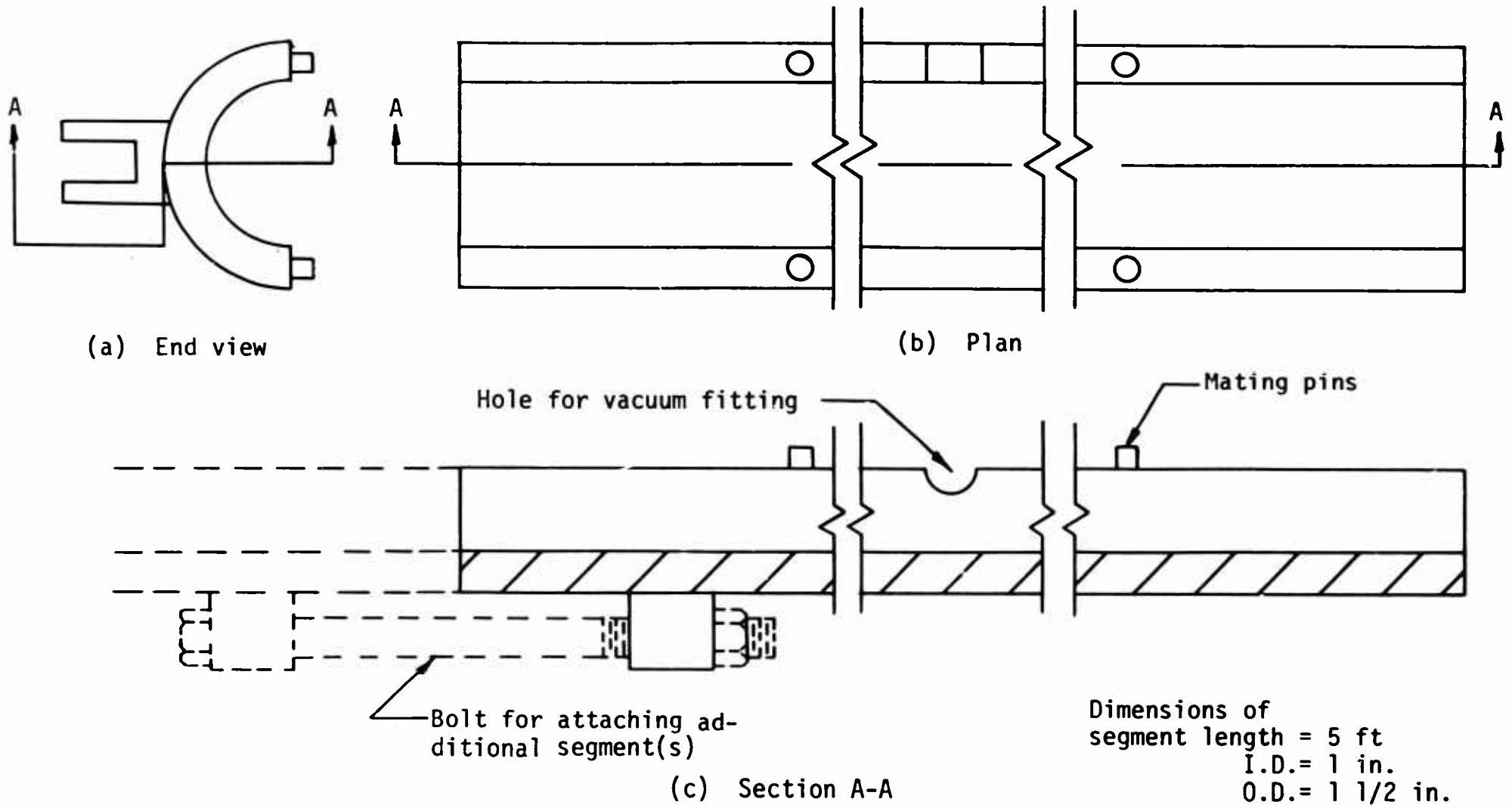

Figure 96. Drawing of specimen mold (each segment has two halves, identical except for mating pins or holes)

to be inordinately time consuming; and for reasonable motions at the loaded end, a three- or four-point sling system could generate appreciable axial force on the specimen.

A heavy-liquid floating scheme was considered but rejected for two reasons: (1) buckling could still occur, so that antibuckling provisions would have had to be made; and (2) waves coupled into the liquid at the loading end could have arrived at distant stations before the arrival of the wave through the soil.

Consideration of these preliminary studies brought the problem into sharper focus. The containment scheme had to meet three criteria: (1) negligible axial resistance; (2) adequate lateral resistance to minimize buckling; and (3) negligible coupling and transmission of waves.

On first assessment it seemed that a foam-rubber bed might meet all three criteria. Samples of several commercial foam rubbers were obtained to test. Only minimal tests were performed because of the practical difficulties of making an adequate foam bed. Attempts were made to cut a round bed in the foam. These schemes all depended on saturating and freezing the foam so that it could be cut with some precision. The efforts proved fruitless because the material thawed from the heat of the cutting operation, and even when refrozen during cutting (e.g., with a CO_2 bottle), the resulting cuts were jagged and rough and were not the proper size after thawing. Furthermore, tests showed that for reasonable deformations the axial resistance could become a substantial proportion of the loads anticipated in the wave-propagation tests. Although it was recognized that the cutting of frozen foams is a developed technique and that consultative assistance might have overcome the practical cutting difficulties, further studies of commercial foams were abandoned because of the unfavorable axial-resistance results. The experience did, however, show that the foam bed would have merit if the shaping and axial-resistance problems could be overcome.

The shaping problem was overcome by forming the foam directly in a mold of the proper shape. Several two-component foaming compounds were tried. It was found that extremely clean shapes could be obtained by careful mold shaping and forming techniques, and the consistency of the foams could in many cases be varied simply by varying the relative proportions of the two components. After many tests it was found that a silicon (Dow-Corning, Silastic S5370 R.T.V.)

mixed in the ratios recommended by the manufacturer met all the requirements satisfactorily. Further testing of other foams was therefore terminated.

The excessive axial resistance was felt to result principally because the foam was required to act as a deep shear beam. If this were so, the axial resistance should show a significant decrease if the bending moment of inertia could be reduced so that the beam would act in usual moment bending. This was accomplished by molding the foam with transverse cuts, as shown in Figure 20.

In the experiments the cantilevers were cocked slightly forward; i.e., they were bent about 1/8-inch (125 mils) toward the front of the specimen. In this way the subsequent specimen motions were resisted by a slight tension decreasing to zero and possibly passing into slight compression. These motions and resistances tended crudely to average, and were small in any case, as shown by the data from an axial-load test on the foam with the use of a nylon rod (Fig. 97). The data in Figure 97 overemphasize the problem: the motions are larger than those of the experiments; and the nylon rod, being unsupported at its end, does not strain appreciably. The results in Figure 97 should be compared with the results from a load of from 10 to 15 pounds used in these experiments.

It is not possible to derive a meaningful number, such as a subgrade coefficient, for the lateral resistance of the foam: a compression test on one of the supporting members would be meaningless because continuity in the experiment would prevent the instability that would occur in such a test; and a full-length compression test would not be meaningful because an actual soil specimen would tend to buckle over only a few of the members. In an attempt, however, to obtain at least a feeling for the lateral resistance, the following test was performed: a nylon rod was bedded in one of the sections and loaded laterally to compress the foam. The results are given in Figure 98.

Although each cantilever leaf weighs about 35 gm, the possibility of coupling from the soil into the cantilevers was felt to be small because only a fraction of the cantilever was in effective motion, and the accelerations were small. Computations of the dynamic reading on the back force link (see page 67) showed disagreements of only 10 percent, indicating negligible loss.

b. Cradle and Frame.

The specimen cradle is sketched in Figure 99.

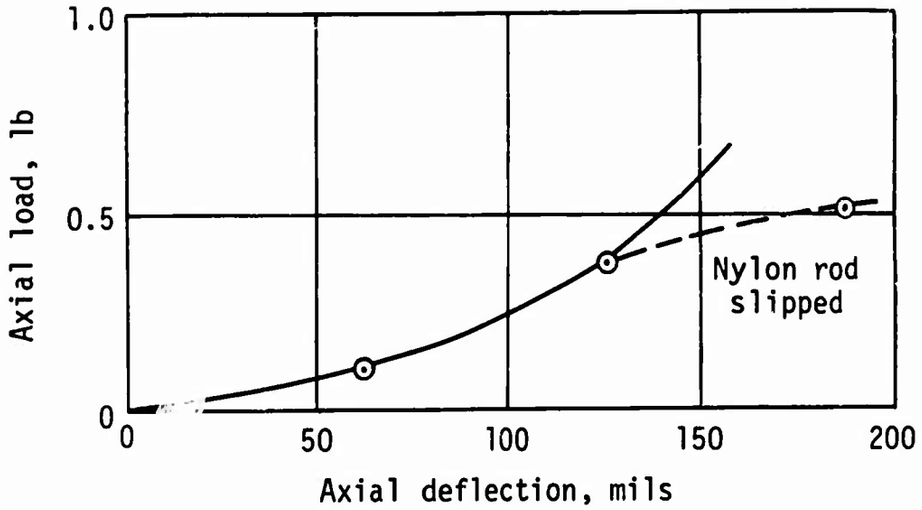

Figure 97. Axial-load test on foam bed

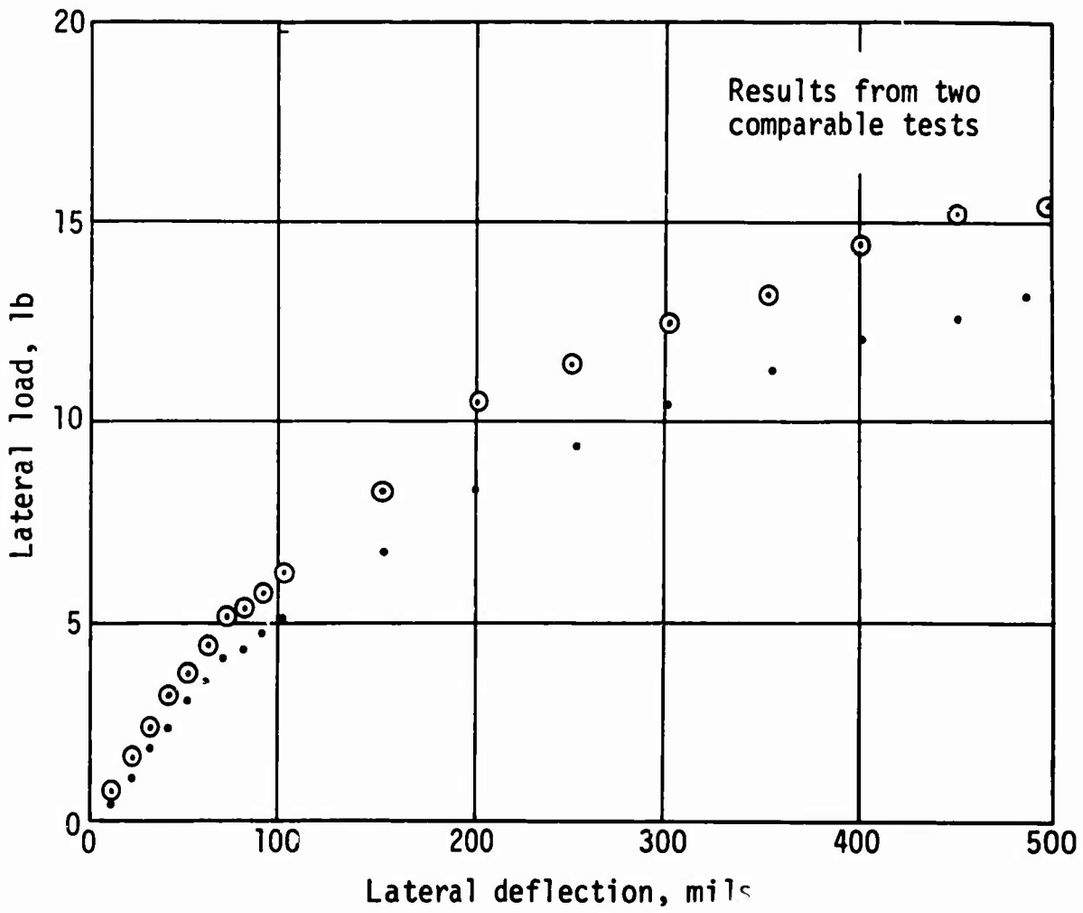

Figure 98. Lateral resistance of foam beds

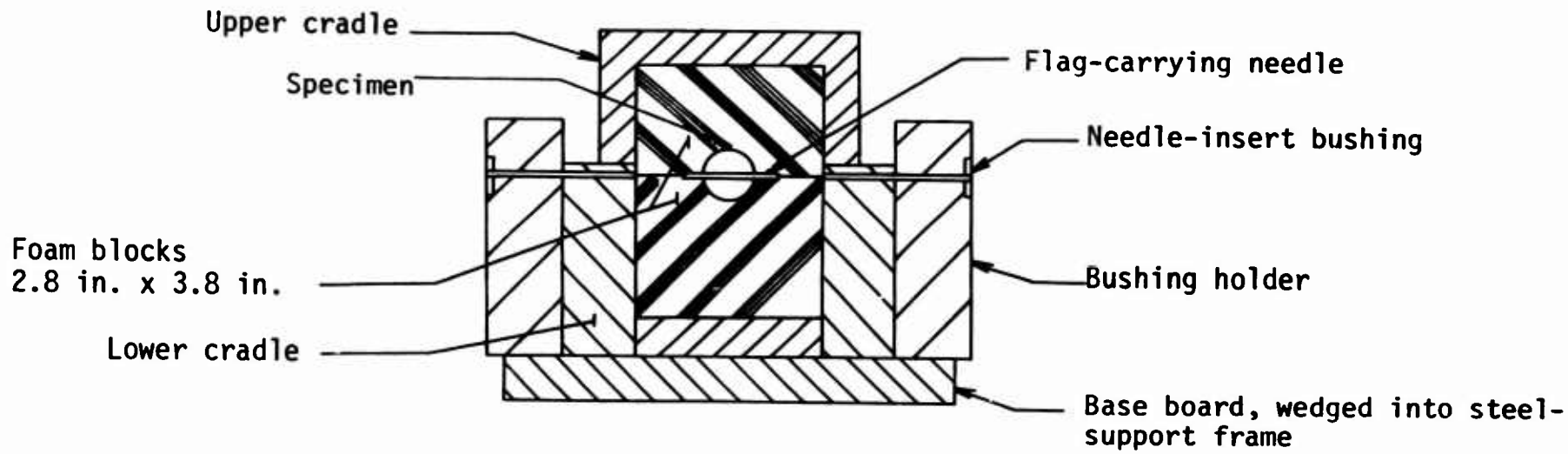

(a) Section A-A

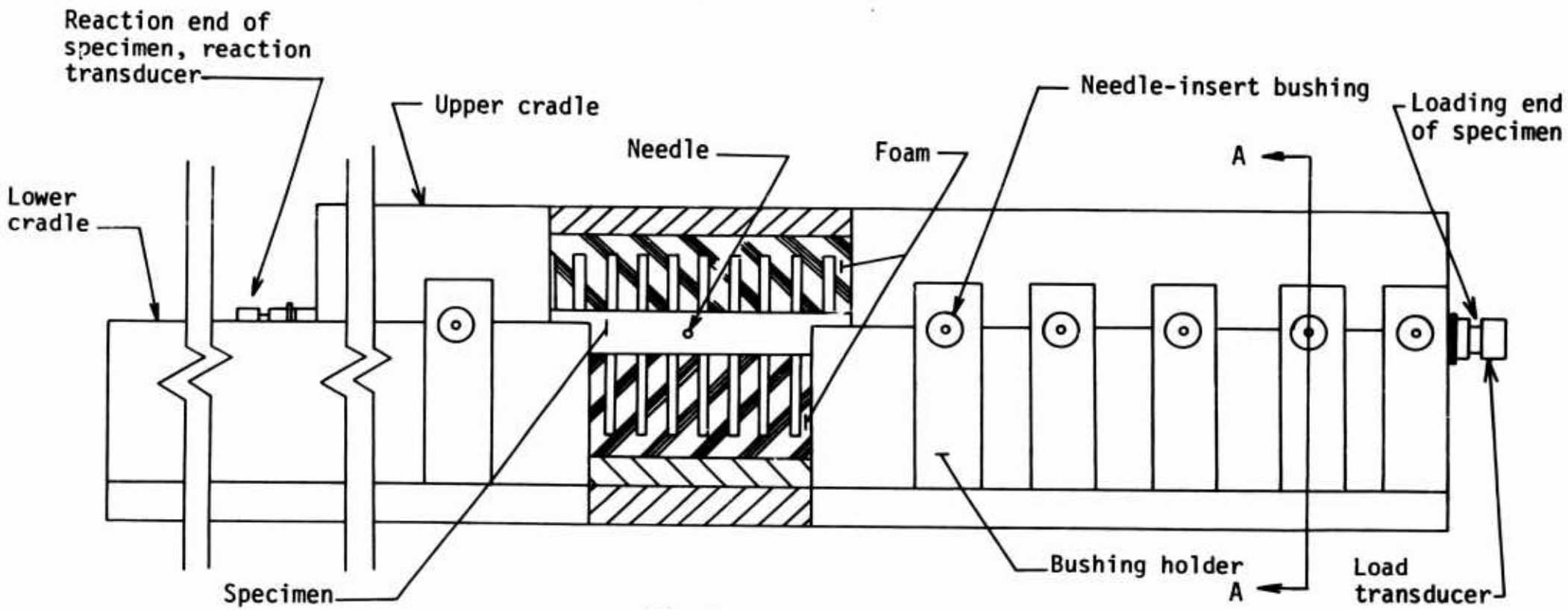

(b) Side elevation

Figure 99. Drawing of specimen cradle

4. Loading Device.

The key to the loading device is the expansion chamber, shown in Figure 100, and the keys to the efficacy of the expansion chamber are its short length, which prevents clean-shock formation, and the selection of the diaphragm. It was found by experimentation that the pulse shape could be controlled either (1) by using selected diaphragm materials such as plastic, celluloid, rubber sheeting, and cemented combinations of these; or (2) by placing a metering plate (a sheet of thick celluloid drilled with holes of certain sizes and in certain patterns) on the high-pressure side of the diaphragm and using the thinnest convenient diaphragm. Of the two schemes, the metering plate was by far the most reproducible and dependable, and it was used for most of the experiments described.

5. Displacement Measurements.

a. Light System.

For convenience three standard flag sizes were made: 0.375, 0.750, and 1.250 inches; these are the dimensions used to denote each flag in the discussion to follow. The triangular cutouts were made in different ways, depending on the size of the flag: by overcutting for the 0.375-inch flags, using razor blades to form the sides of the triangle; by a stamp-and-die cutter for the 0.750-inch flags; and by hand cutting to the finished product for the 1.250-inch flags. Each flag was tested for linearity, as described below. The precise trimming of a flag to linearity was an extremely tedious procedure, resulting in perhaps one acceptable flag from every five or ten made.

As shown in Figure 26, the light cell was fixed in place, but the photodiode crystal had two degrees of freedom in the horizontal plane, normal to the light rays. Before the system was either used or calibrated, the illumination center of the light-diode system was found by moving the diode about in the horizontal plane until maximum output with no flag present was obtained. In practice, because the collimating slit was made so that the incident light beam was larger than the crystal, the allowance in adjustment for illumination center was rather generous. For this reason guidelines, which were scribed on the first setup of a system, were adequate for subsequent positioning of the crystal from test to test.

b. Sensitivity Calibration.

See Sensitivity Calibration in Section IV, 5b.

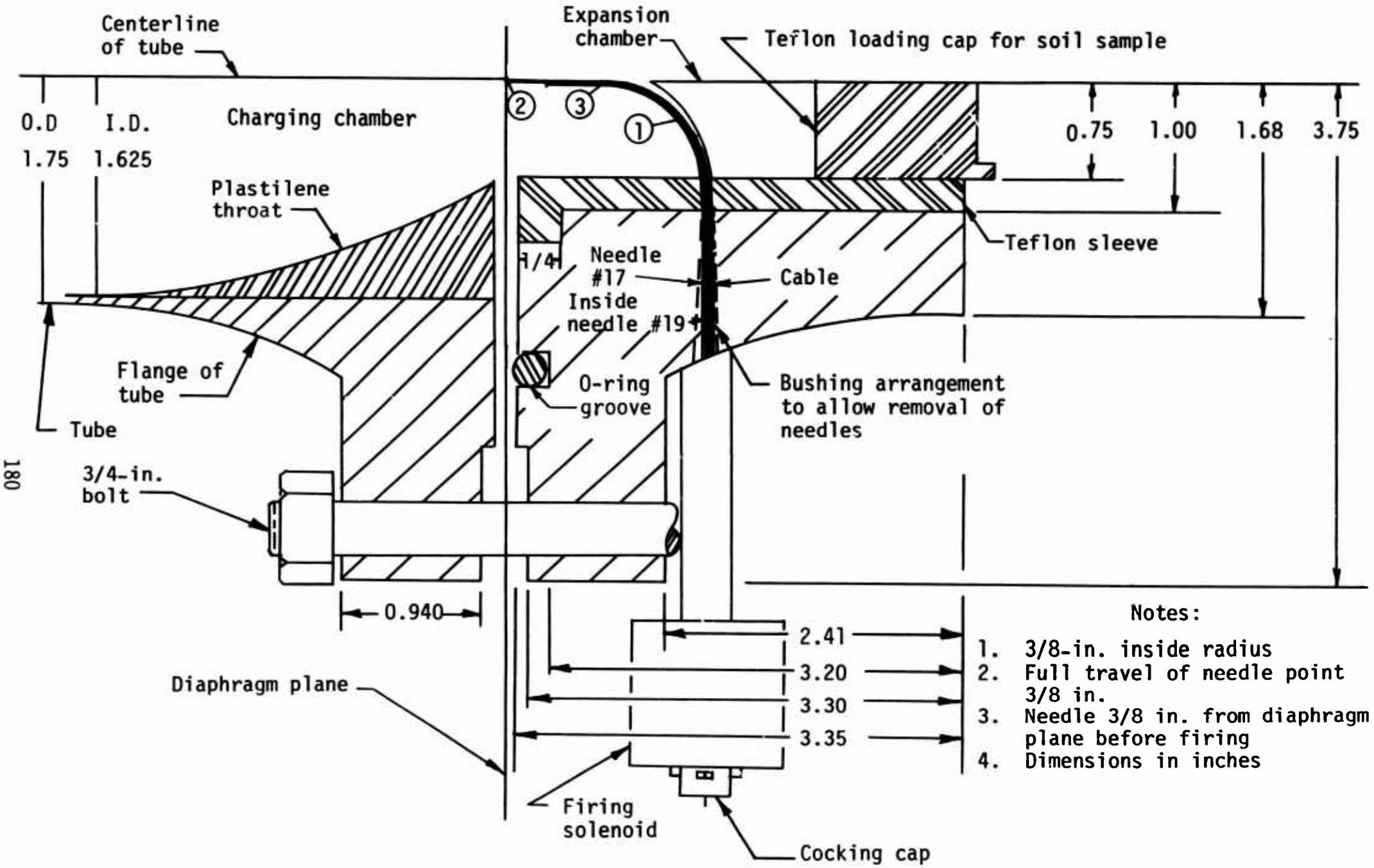

Figure 100. Drawing of expansion chamber

c. Placement.

See Placement in Section IV, 5c.

d. In-Place Calibration.

See In-Place Calibration in Section IV, 5d.

e. Verification Tests.

Five possible experimental errors are (1) temperature effects; (2) light-source and photodiode stability over short times; (3) stability of the power to the lights; (4) errors in flag-to-crystal spacing as a result of the flag-placement procedure; and (5) errors in transverse flag positioning. The tests to be described have been performed to evaluate these errors. The errors are presented in millivolt (mv) output from the crystal, to be compared with a typical full-scale output on the order of 25 mv.

In the test for temperature effects an ordinary laboratory thermometer was placed in silicone grease next to the crystal and the temperature was raised over a reasonable ambient range of 70° F. to 80° F. This range was considered reasonable because it provided the same temperature increase that would have occurred from a light source in any wave-propagation experiment. The results are shown in Figure 101a. Over this temperature excursion the output from the crystal changed by slightly more than 1 mv, with most of the change occurring in the first few minutes after the light was turned on. In practice, the lights were left on for at least 15 to 20 minutes before a test so that the temperatures would sensibly stabilize. In this range (78° F. to 80° F.), the errors are in the submillivolt range and may accumulate to fractions of a percent of full scale.

The short-term stability of the light source and photodiode system was determined by subjecting the system to the conditions of an experiment, consisting of a 20-minute warmup, an output reading, and a cooloff period. The system was exercised in this way ten times. The results are shown in Figure 101b. Because no consistent trend was noted, the test was terminated. The actual readings, as well as the confidence band, are shown. The results show a good degree of stability, but they also show that misreadings of perhaps 0.5 mv can occur from cycle to cycle. This is equivalent to about 4 percent of full scale. It has not been possible to find the source of these readings, and this error is presently accepted as one limitation of the experiment. These results were taken to imply that, within the error noted, a single calibrate would be valid for

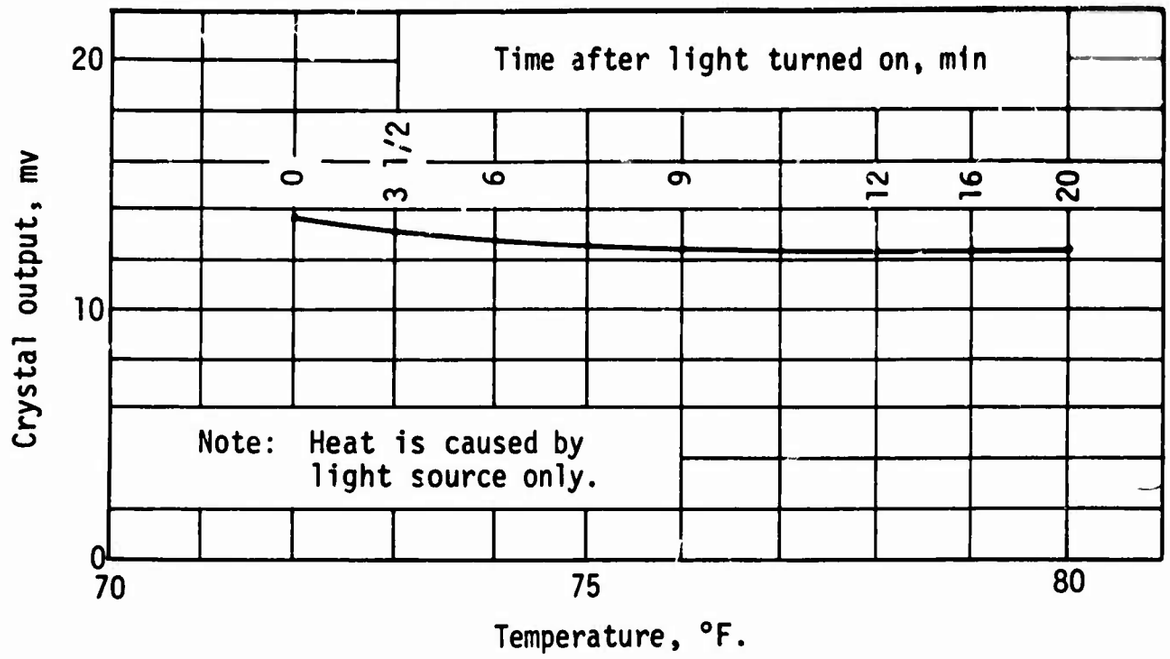

(a) Temperature effects

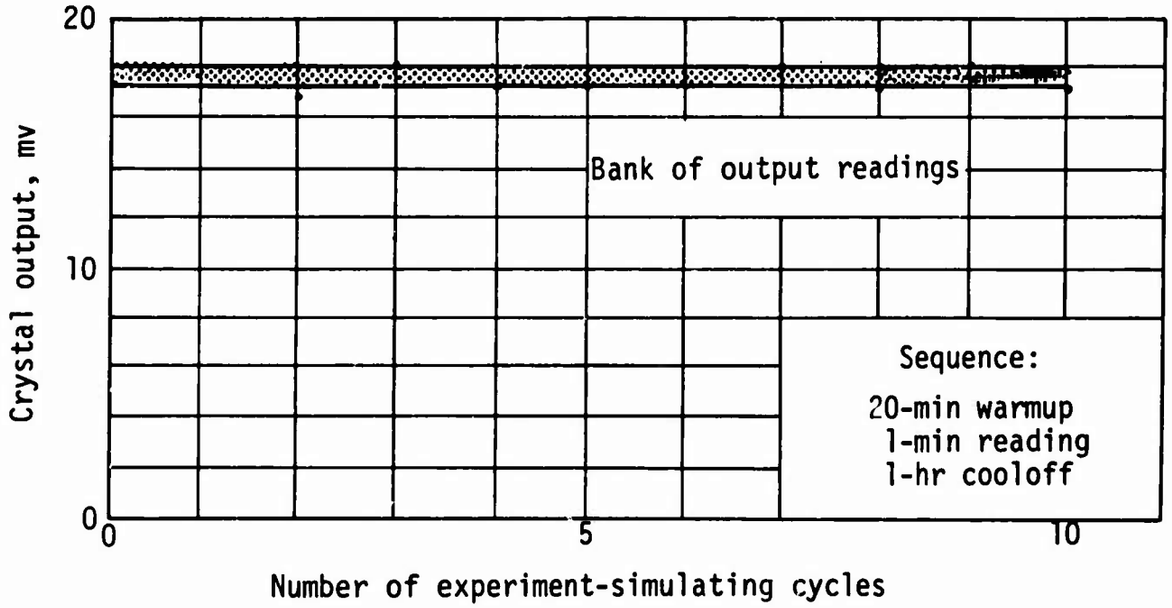

(b) Stability effects

Figure 101. Crystal temperature and stability effects

a 3- or 4-shot day's series of tests. The true long-term degenerative effects of the lights and the crystals were measured by the output-displacement calibration which was performed always before and usually after a day's series of tests.

The stability of the power to the lights was fairly well assured by the design of the regulated power supply. Occasional checks on a digital voltmeter were made to verify stability. The regulated power supply caused a crystal-output ripple of about 8 microvolts (μv) which could not even be sensed when normal readout was taken. In order to assess the possibility of an error due to this ripple, the voltage sensitivity of the light-crystal system was determined. The results for three flag positions are shown in Figure 102. Even for the maximum output (butt position) the ripple effect would lead to negligible crystal-output reading errors.

As has been described, the flag-carrying needles were placed in the specimen through rigid guide bushings. Careful measurements showed, nevertheless, that the final flag position could vary from the desired flag-to-crystal spacing of 0.250 inch by perhaps as much as 0.05 inch. For this reason a series of tests was conducted to determine the errors that could be induced by incorrect flag-to-crystal spacings. To get readable differences in output and to make sure that the maximum errors were measured, a very large flag-to-crystal mispositioning was selected for the verification test: ± 1/4 inch, over twice the observed mispositioning. Thus for each of the three flag sizes (0.375, 0.750, and 1.250 inches) three flag-to-crystal spacings were used in the test, 3/8, 1/4, and 1/8 inch. At these spacings the flags were calibrated for output-displacement, as described above. The results are shown in Figure 103.

The results from the 1.250-inch flag are felt to be most representative of the errors involved: the lack of output difference from the 0.750-inch flag leads to the conclusion that perhaps a fortuitous flag selection was made; and the 0.375-inch flag had razor-blade edges from which, it was later found, spurious reflections could occur (these edges were later sprayed with flat black paint to reduce the reflections). For these gross mispositionings, the readout error could be about 0.5 mv and would be perhaps half this value for the known possible errors involved in positioning the flags for the experiment; therefore the reasonable error due to this effect would be less than 2 percent.

The possible errors due to transverse flag mispositioning were evaluated by moving the flag transversely and measuring the output. This was

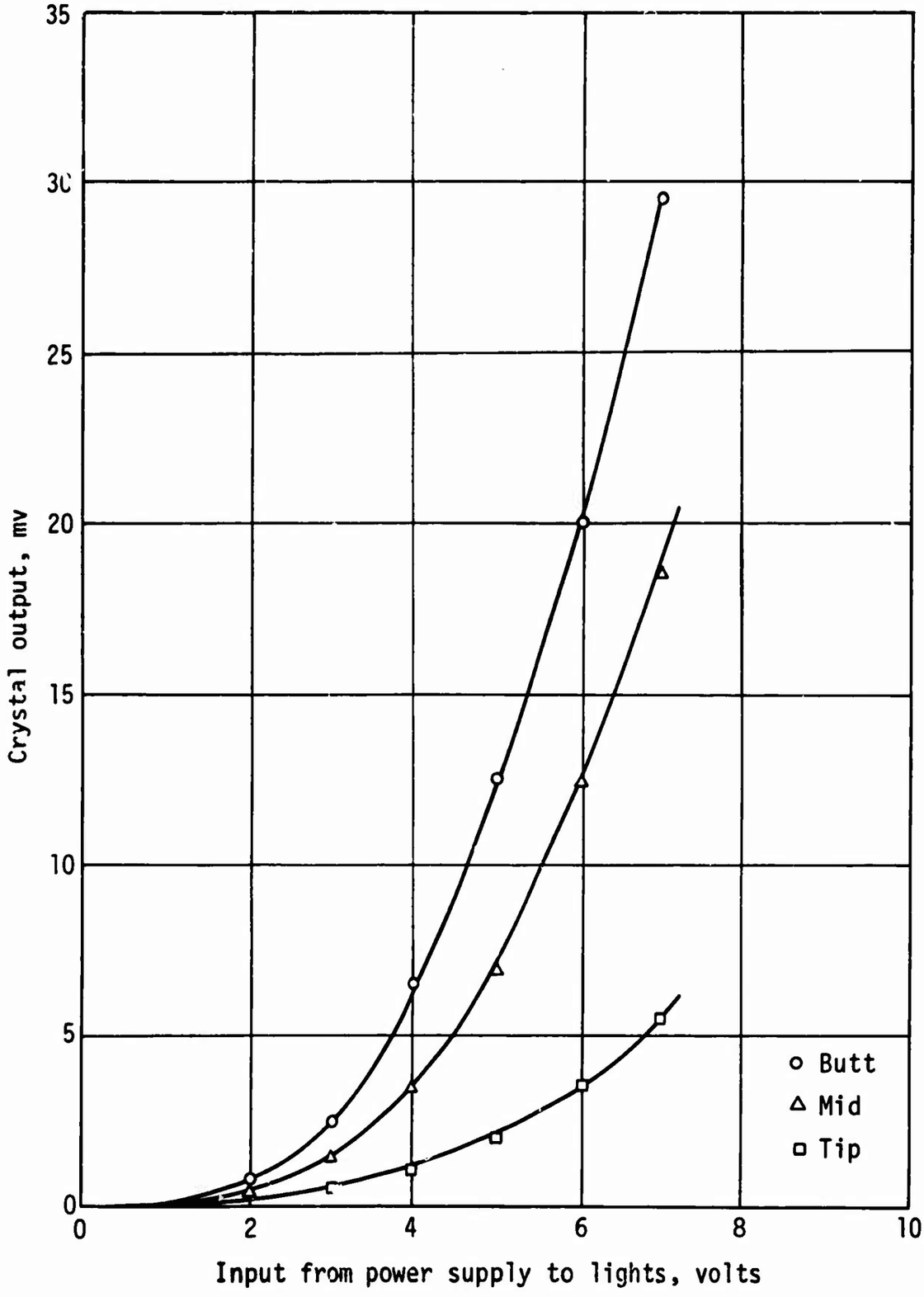

Figure 102. Input-voltage sensitivity

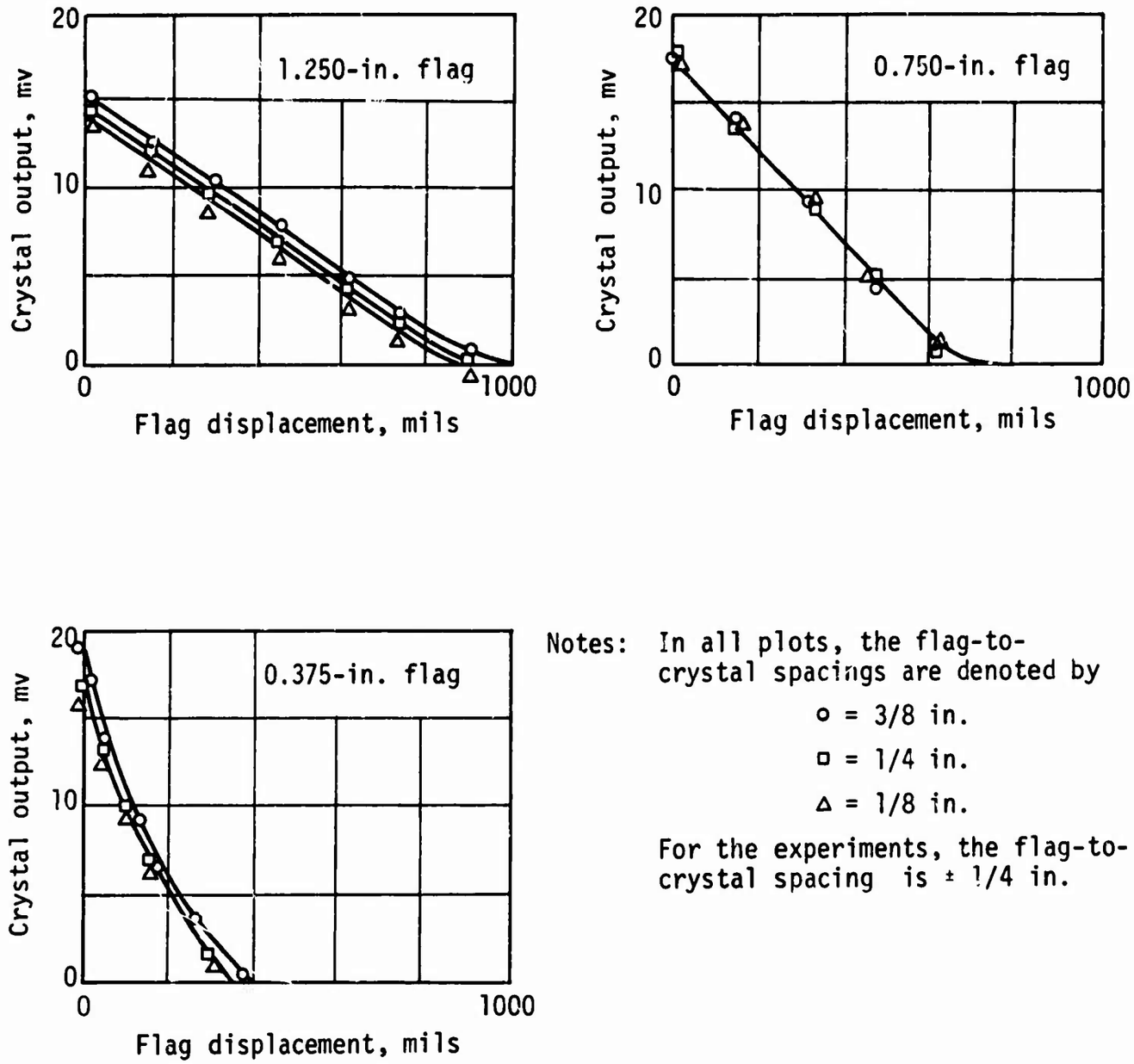

Notes: In all plots, the flag-to-crystal spacings are denoted by

o = 3/8 in.

□ = 1/4 in.

Δ = 1/8 in.

For the experiments, the flag-to-crystal spacing is ± 1/4 in.

Figure 103. Possible errors due to flag-to-crystal misposition

done for each of the three glag sizes (0.375, 0.750, and 1.250 inches), and for completeness, for the three flag-to-crystal spacings used in the tests described above. In addition, because the errors would depend on that portion of the flag actually in the field, three flag settings--butt, mid, and tip--were also used. The results of these tests are given in Figures 104 and 105.

Figure 104 is an expanded and detailed plot of the typical result for the 0.375-inch flag with all conditions included; Figure 105 shows only the results of the 1/4-inch flag-to-crystal spacing for all three flag sizes and settings. These results show that the butt-positioning procedure was fairly critical (top graph of Fig. 104), but that the system was relatively insensitive to transverse motions for the mid and tip flag settings. Assuming transverse-positioning errors of ± 0.050 inch, readout errors could be as large as 0.7 mv at the butt setting, 0.2 mv at the mid setting, and less than 0.2 mv at the tip setting. These represent errors of about 3 percent at the butt, some 2 percent at the mid, and perhaps 4 percent at the tip (which was never used). These results were useful from three standpoints: (1) they showed the overall transverse-mispositioning errors to be small; (2) they showed a sharp nadir in the butt position, making the positioning operation easier; and (3) they showed the measuring system to be relatively insensitive to vagrant minor transverse motions of the specimen during tests.

Another item to be verified was that the response time of the crystal was shorter than the response time required to measure the displacements. Assuming that the particle velocities of the soil specimen could approach 50 feet per second (fps), the time required for a point on the flag to transverse the crystal (width approximately 0.16 inch) would be about 270 microseconds (μs). The manufacturer of the crystal quotes a response time of 20 μs or less, depending on the load resistance.

This value was checked crudely in the following manner. The crystal was taped to the face of a dual-beam oscilloscope (Tektronix 555), and the bottom beam of the scope was set for high intensity and positioned in the middle of the crystal. The upper beam of the scope was connected to the output of the crystal. The scope was then triggered, with the result shown in Figure 106. The crystal output rose to its maximum value in about 14 μs and then decayed more slowly, owing to the persistence of the phosphorous screen. The variables involved in this response-time test were the rise time of the oscilloscope amplifiers, the luminescent time of the phosphorous screen, and the desired response time of the

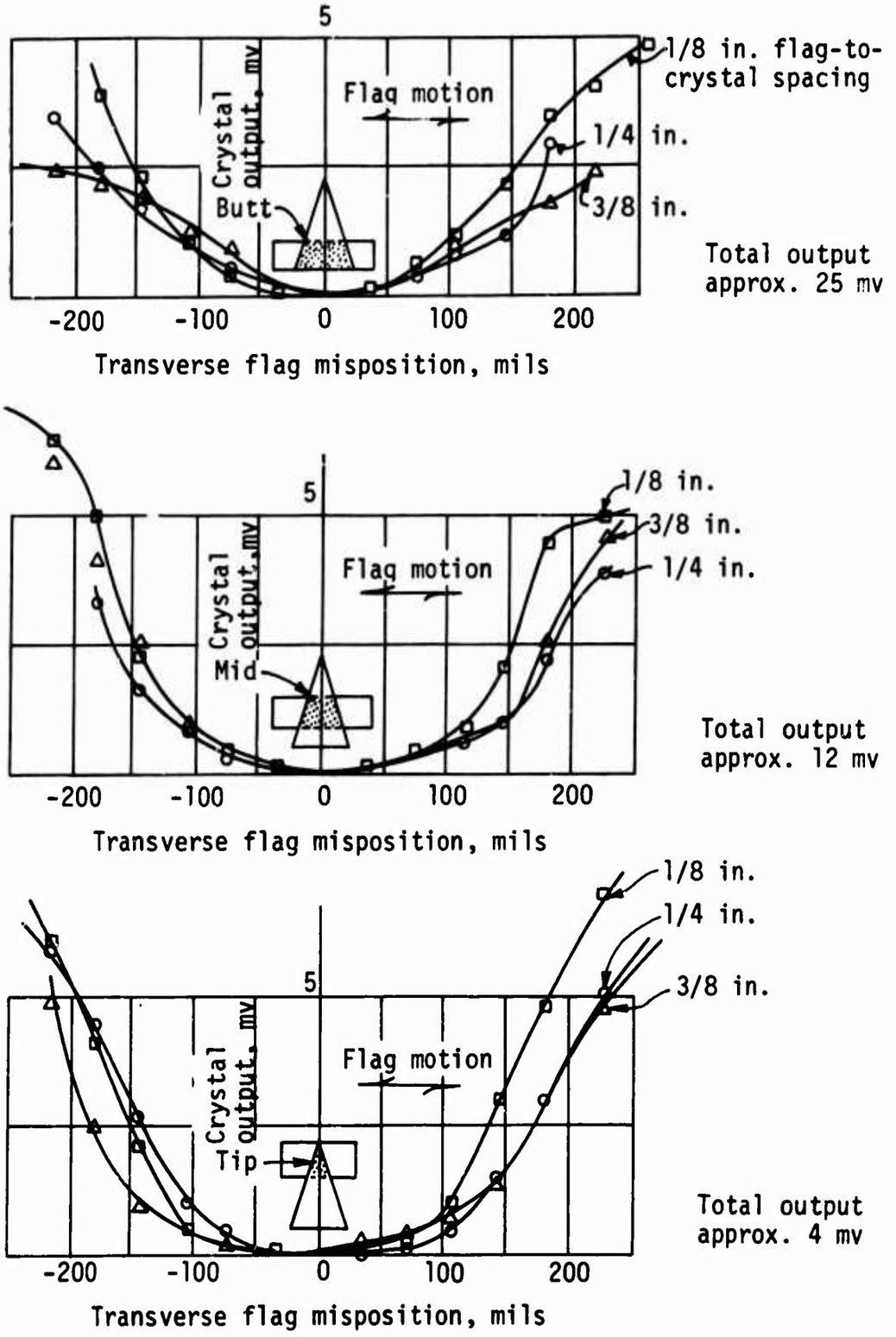

Note: For experiments the probable positioning error is less than 50 mils.

Figure 104. Details of transverse positioning errors (0.375-in. flag only)

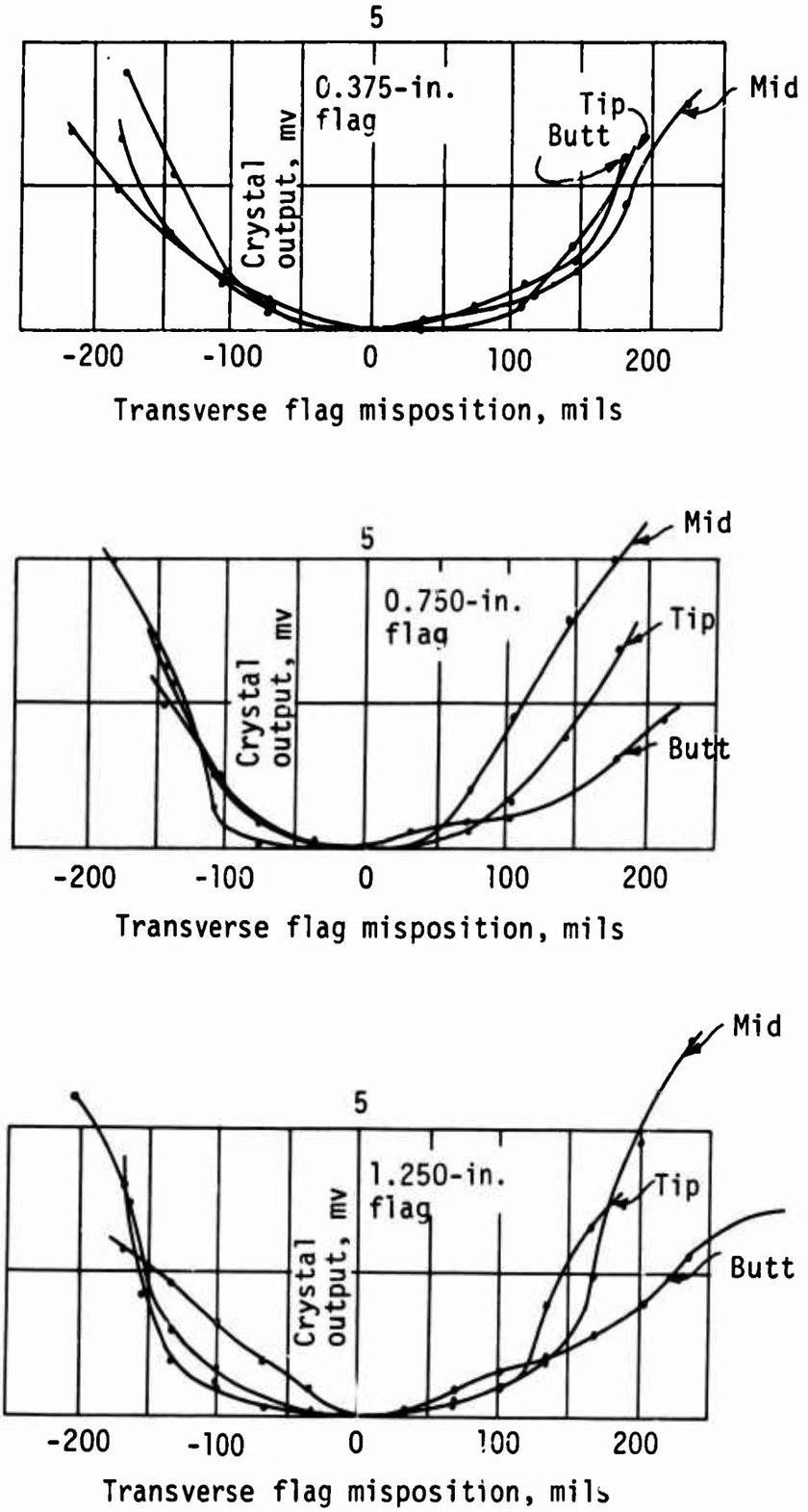

Note: Total outputs approximately 25 mv a
at butt, 12 mv at mid, 4 mv at tip.

Figure 105. Transverse positioning errors (all for 1/4-in. flag-to-crystal spacing)

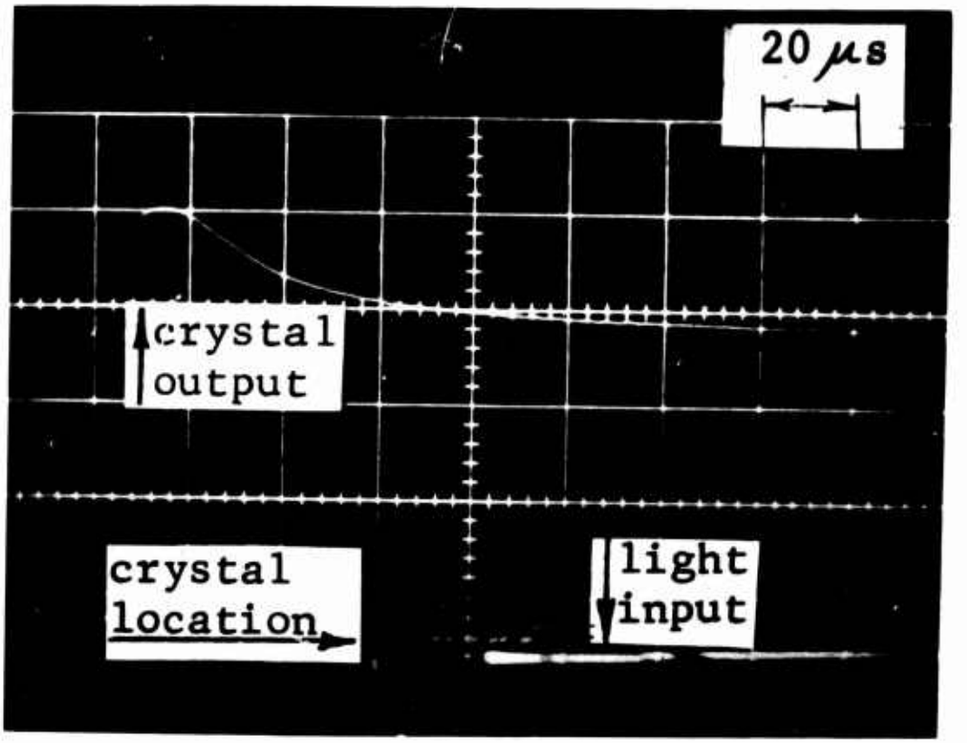

Figure 106. Crystal rise time test

crystal. Because the first two variables are finite (and can be combined to add as much as 10 μs), the value of 14 μs was taken as the absolute upper limit for the crystal response time from full dark to intense light.

If on the basis of this crude test the crystal response time were taken to be perhaps 10 μs, then a physical particle velocity of 50 fps would be interpreted to be as small as 48.5 fps for an error of 3 percent. Because all worst conditions were assumed in this test and in the calculations, the 3-percent error was taken to be an upper limit, and the response time of the crystal was considered adequate for the experiments.

6. Force Measurements.

   See Force Measurements in Section IV, 6.

7. Fabrication and Placement of Specimen.

   See Fabrication and Placement of Specimen in Section IV, 7.

8. Remote-Recording System.

   See Remote-Recording System in Section IV, 8.

9. Triaxial Tests.

The technique for the triaxial tests is described in Section IV, 9; only the membrane-effect tests are described here.

For a crude check on the stiffness of the surgical membrane, a specimen was tested in it with no ambient stress. The result is shown by the curve at the bottom of Figure 34. No such test could be performed with the prophylactic membranes because the 1-inch specimen would immediately collapse in the 1.4-inch membrane when removed from the mold. If a 1-inch prophylactic membrane were commercially available and were tested, some sort of similar effect would certainly be observed. The effect noted did not explain the observed differences; therefore study was continued.

It was thought that the prophylactic membranes might be leaking air, making the true ambient stress less than that recorded by the manometer. The additional vacuum gage was mobilized to check this. Although some leakage was noted, it could not be attributed with certainty to the membrane. To eliminate the uncertainty, the membrane was generously coated with vacuum grease and covered with another membrane. The leakage could then be traced to a series of minute leaks in the vacuum fittings, which were eliminated by generous application of vacuum grease and by constant monitoring of the vacuum at both ends of the specimen in all subsequent tests.

It was then felt that if the modulus of the surgical rubber were sufficiently high compared with the modulus of the soil, it might carry significant axial load on its small area since it was restrained from buckling by the ambient stress. Computations showed that the rubber would need a modulus of 6,000 psi at least for any effect of significance. In addition, the circumferential stiffness of the membrane could cause additional ambient stress on the specimen. Taking the case of a Poisson's ratio equal to 0.5, the modulus would have to be more than 3,000 psi for significant effect. Finally, it was possible that the rubber could be a pressure-hardening material, exhibiting more stiffness when under ambient stress.

The modulus of the rubber was, therefore, experimentally determined under the following conditions: An axial-tension test was performed on a 22-inch-long tube of the rubber. The specimen was linear to about 10-percent strain, with a modulus of about 250 psi. To test the possibility of pressure hardening, a strip of gauze was placed inside the tube, and tests were performed under

vacuums (ambient stresses) of 0.00, 4.26, 7.10, 9.94, and 11.92 psi. The results were the same in all cases (E = 250 psi), showing that the rubber is not a pressure-hardening material. It was then suggested that the rubber might have different characteristics in tension and compression. To check this, a series of disks, 0.65 inch in diameter, were stamped out of the membrane with a cork cutter. These were stacked to a height of about 0.6 inch, preloaded to extrude all air, and tested in compression. The resulting modulus was about 230 psi. On the basis of these calculations and tests it was concluded that the surgical rubber was not contributing either axial or radial stiffening.

At this point it was noted that the mold actually had a 1.045-inch I.D. Since the I.D. of the unstretched surgical membrane was 1.000 inch when in the evacuated mold, it was prestretched to an I.D. of about 1.020 inches. To check the effect of this small prestretch, a double membrane was used for molding, and the outer membrane was stripped away before testing; therefore the single-test membrane was unstretched. The results of this test were the same (i.e., less than 5 percent maximum difference) as the results of a companion test using the normal procedure. It was concluded that the small prestretch had no effect; but it should be noted that the mold used in the long-specimen tests had an I.D. of 1.000 inch; therefore the effect could not exist there anyway.

Previous observations had shown that the 1.4-inch prophylactic membrane would wrinkle badly in the 1-inch mold, and that there were usually continuous wrinkles up to 0.1-inch deep running the length of the specimen. On the chance that these wrinkles might be inducing stress concentrations, a 1-inch prophylactic membrane was fabricated by pulling the 1.4-inch membrane snugly around a 1-inch-diameter nylon rod, folding over the excess and cementing it with a latex compound. A specimen was then fabricated and tested, with the same results as for a 1.4-inch wrinkled membrane. It was concluded that the wrinkles were not concentrating stresses to any significant degree.

A survey of test conditions indicated that when the mold was removed, the end caps on many of the prophylactic membranes would tilt visibly, some so badly that the specimen had to be remade. In consideration of the condition and the work to verify the insignificance of the surgical-membrane effect, the prophylactic membrane was then considered the adverse member of the study. To check this conclusion, a series of vacuum triaxial tests was run at the true 1.4-inch-diameter of the prophylactic membranes. These tests agreed with the results of the 1.0-inch-diameter surgical-membrane tests (Fig. 34). Because of this agreement

it was concluded that some unknown end effect was occurring when the 1.4-inch membrane was used to confine a 1.0-inch specimen, and that the tests of surgical membranes 1.0 inch in diameter were as valid as the tests of the more normal prophylactic membranes 1.4 inches in diameter; therefore, the surgical membranes were used for the series of triaxial tests reported.

APPENDIX B

DISCUSSION OF STATIC LONG-SPECIMEN TESTS

1. Recorded Data and Analysis.

The method of performing the static long-specimen tests and of recording the data has already been described in detail in Section IV: the specimen was loaded by air pressure slowly built up in the shock tube, and the load was recorded with a proving ring. Each time the proving-ring dial traversed 0.0010 inch (equivalent to 1.07 psi on the specimen), an electrical pip was manually placed on the remote-record tapes. Typical photographic readout is shown in Figure 107. The upper trace is the manually induced pulses indicating the proving-ring reading; the lower trace is the reading from a typical gage (C-1). So that the data could be studied in detail, the traces were progressively expanded in amplitude and time as shown on the sequence of four photographs of the same trace in Figure 107. (The leading pulse on the upper trace is always the first pulse, here representing zero load at the start of the event.)

This type of photographic readout is extremely tedious to reduce and is not entirely satisfactory for accuracy. For this reason, the data were processed by the computer, with the typical results shown in Figures 108 and 109. The full-event reduction was obtained to view the entire event and to check the value of the calibration pulse (which is the step pulse between 0 and 1.6 seconds). The expanded readout was taken for the detailed data study. Each gage was individually plotted by the computer, as shown in the figures. Data values were picked from these plots and were replotted by hand according to gage pairs. For example, Figure 110 shows such a plot for gages C-1 and C-2 for Test C (244-0800). The readings from each gage pair were averaged to obtain the displacement history of that gaging station. In Figure 110 the gage readings in mils (0.001 inch) are plotted against the pip number, which is in fact stress on the specimen. The trends evident in Figure 110 are fairly typical: each gage in the pair agreed reasonably well at low displacements; but at high loads, particularly when buckling was occurring, the displacements could disagree substantially. For this reason the average was used for data analysis on the assumption that minor bendings in a horizontal plane (at least) would be canceled; but less weight was attached to displacement data at high readings, when substantial disagreements sometimes occurred.

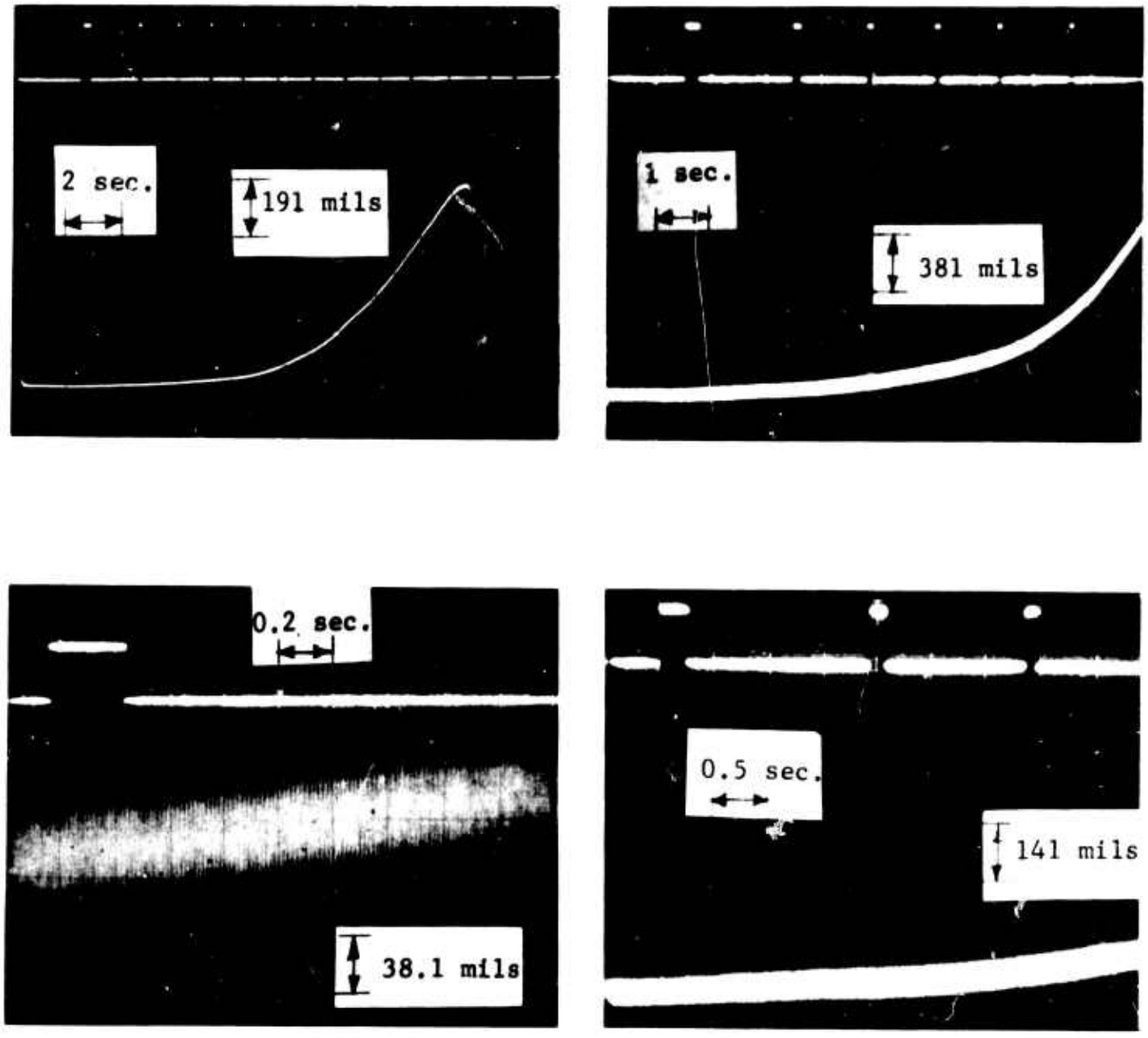

Figure 107. Static tests: typical raw data

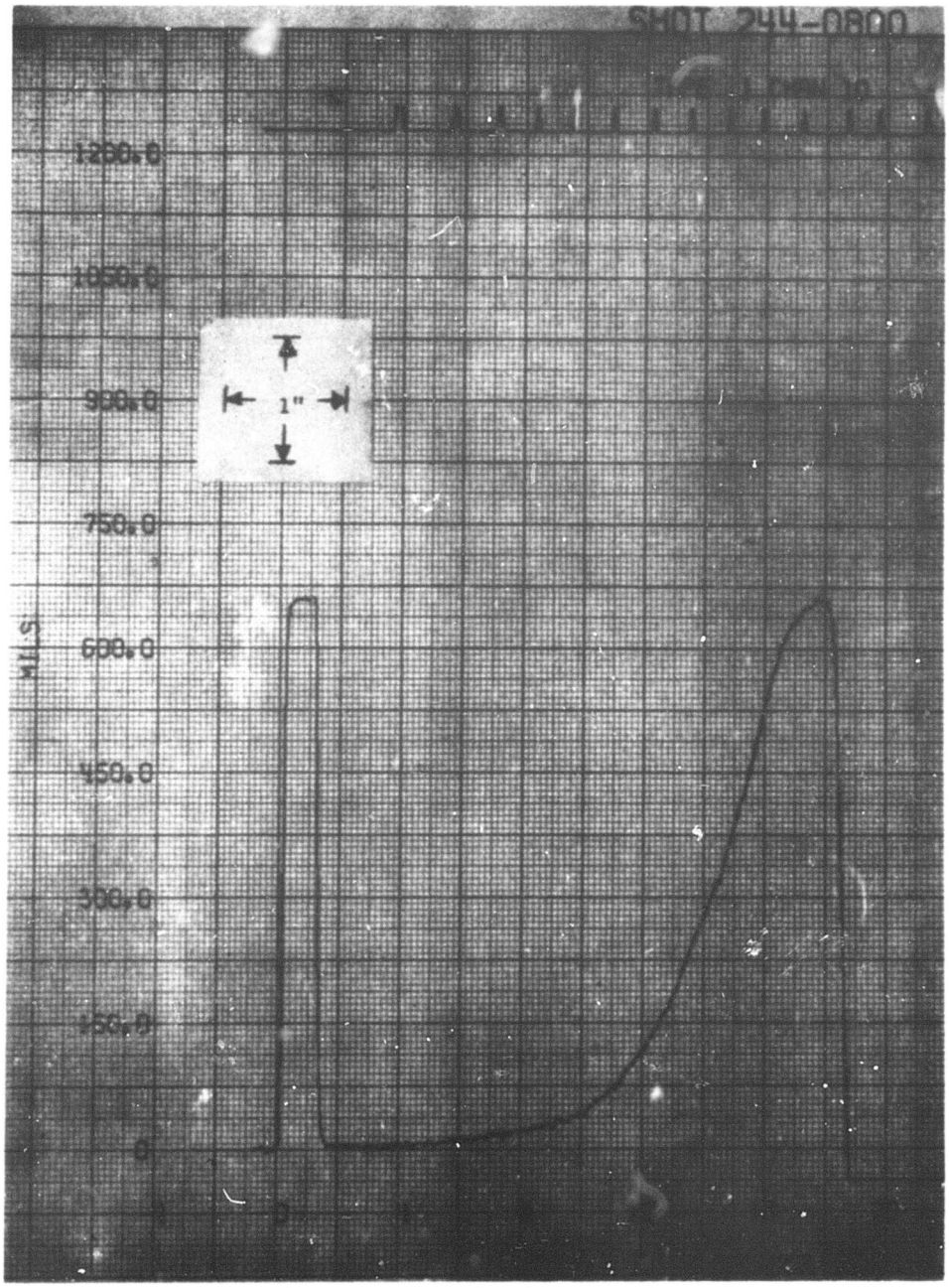

Figure 108. Static tests: typical full-event computer reduction

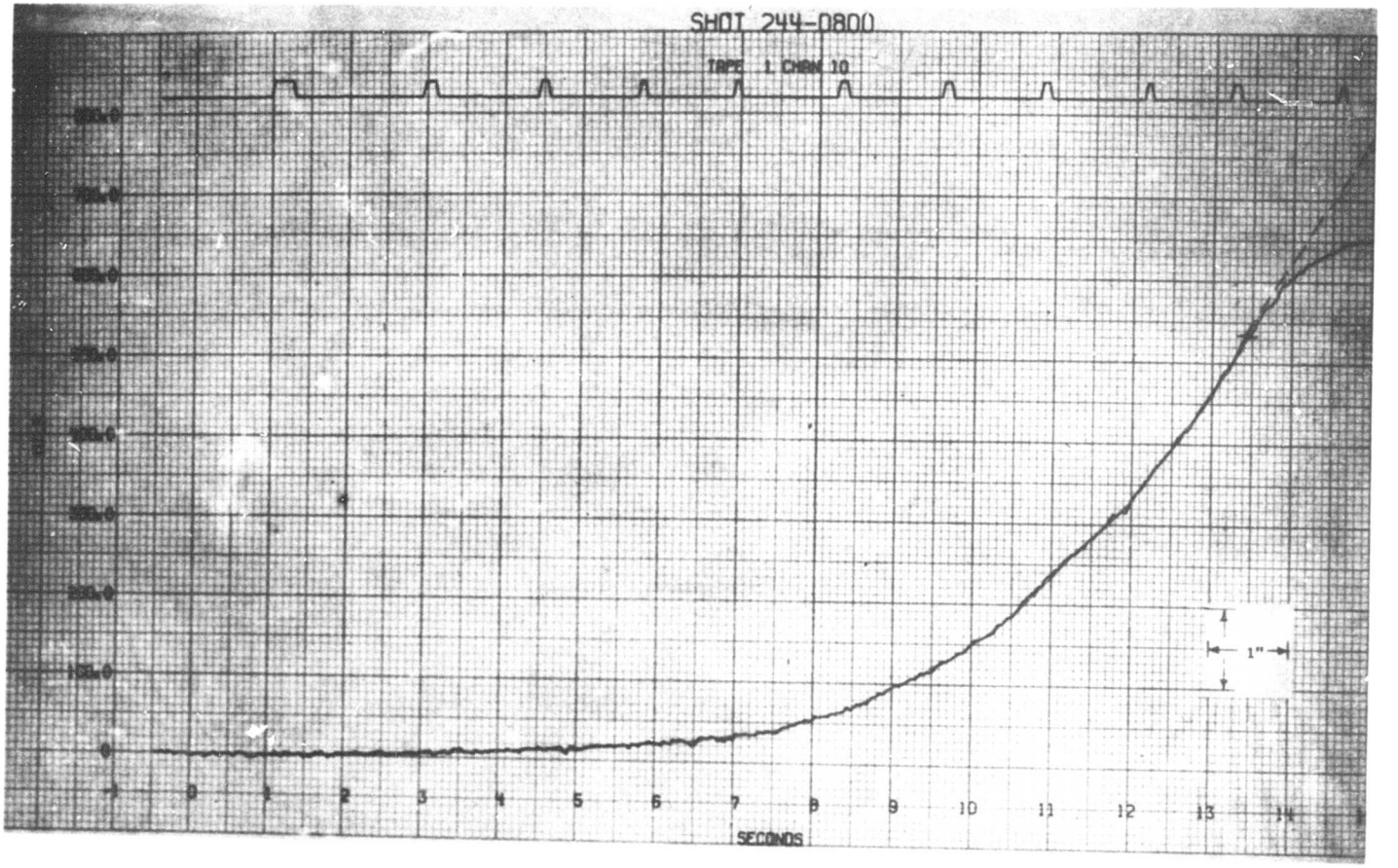

Figure 109. Static tests: typical expanded computer reduction

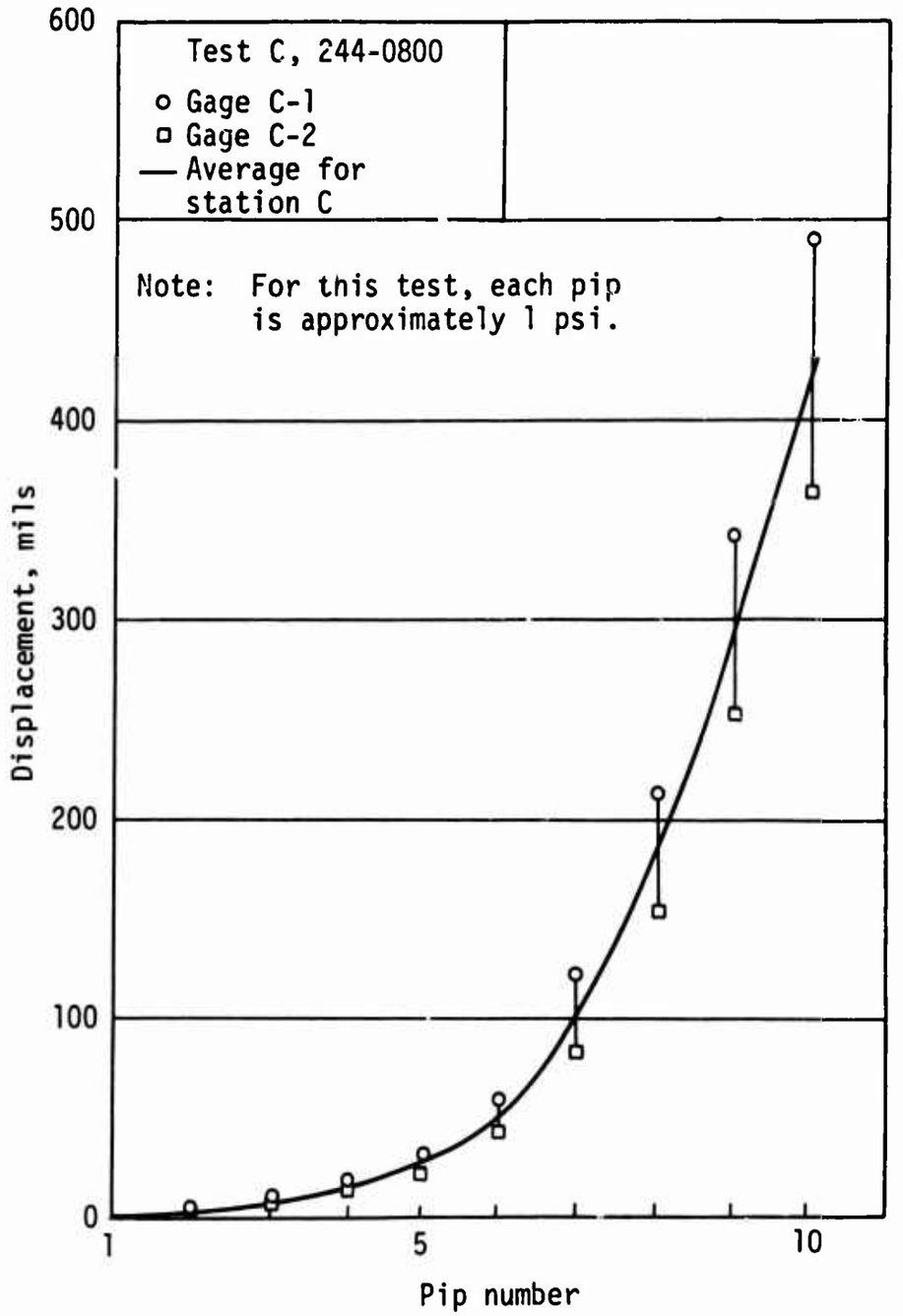

Figure 110. Static tests: typical actual and averaged data

When all the data were reduced and in the form shown in Figure 110, the displacement readings for each pulse were plotted as a function of gage-station position in the specimen. Figure 111 shows the data for Test C (244-0800) for the sixth pip, for example. When plotted in this way, the slope of a line joining the points is in fact the strain. On the assumption of uniform strain, the line should be straight. Advantage was taken of this fact to draw a best-fit straight line to the data points, as shown in Figure 111. In all cases the readings at station A were given little weight because any blow-by around the loading cap or seating errors would unduly affect the flags at this station, which was only 1/4 inch from the end of the specimen. When gages at stations B and C began to read higher than a best-fit straight line to the readings at the other stations, they were discounted on the assumption that buckling had started.

For example, the data in Figure 111 show this trend, indicated by the dashed line. The result shown in Figure 111 is rather discouraging: it indicates that buckling was occurring by the sixth pip, which represents about 6 psi on a specimen with a strength of 20 to 25 psi. This in fact was true, due to the extra cutouts in the foam bed made for the more closely spaced gaging stations, A through E. Because the data could not be reduced quickly enough, the situation was not noted until about half of the tests were completed (Tests C-H, J in Series 244 and 248, Tables I and II), after which reinforced foam beds were used. The data could, however, be extended approximately, even though buckling had commenced. This was done by applying the uniform-strain technique of Figure 111, giving increasing weight to the back gages. For example, Figure 112 shows the extended uniform-strain lines for Test C. The inaccuracies of this extension are discussed below.

2. Results of Static Long-Specimen Tests.

The vertical intercept in Figure 112 is the displacement for a 60-inch specimen which, when divided by that length, yields the average or uniform strain. Each pulse number represents a certain stress in the specimen, from the known area and the load calibration of the proving ring. From these results a stress-strain curve follows directly. Because of the extended uniform-strain technique used (Fig. 112), some disagreement should be expected between the static long-specimen and the triaxial tests. Specifically, the long-specimen results should lie *below* the triaxial results because some, though minor, weight was given to leading-gage readings, even though buckling might have commenced. Thus for a given pulse (stress) the computed strain would be higher than the real strain if no buckling

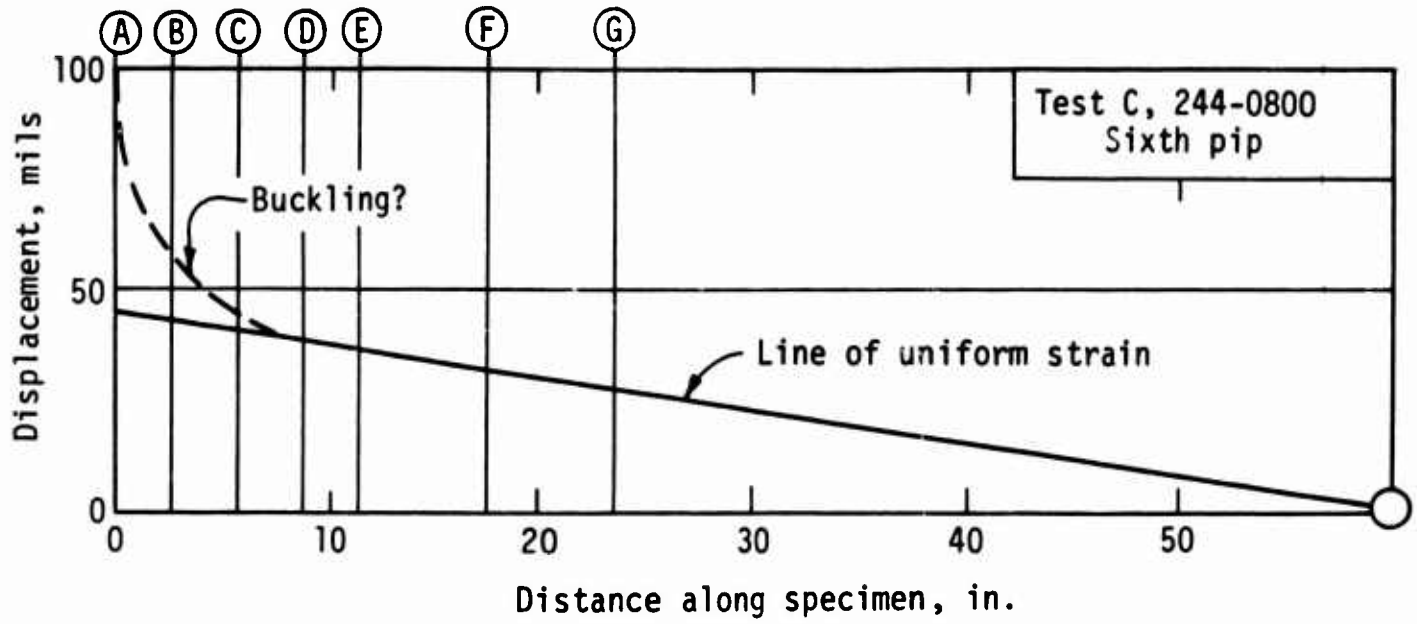

Figure 111. Static tests: typical uniform-strain analysis

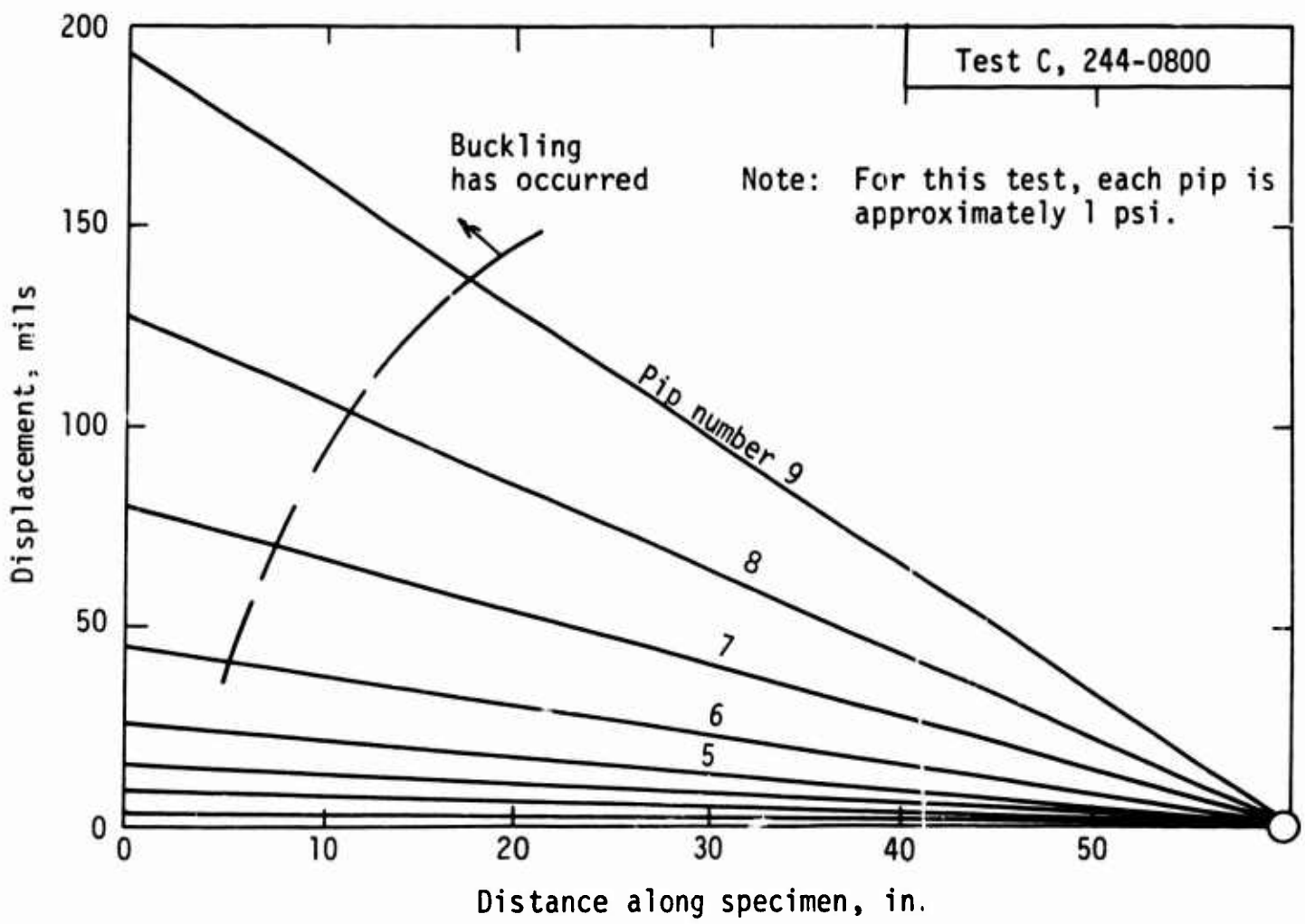

Figure 112. Static tests: typical extended uniform-strain analysis

had occurred. Thus the data are expected to agree reasonably well with the triaxial data for stresses below the observed buckling stresses (perhaps up to 10 psi), and then to agree with or be slightly below the triaxial curves above these stresses, depending upon whether buckling had occurred or not.

The foregoing comments apply only to data taken before the foam was reinforced. For those later tests (Series 252 and 253, Tables III and IV), reasonable agreement was expected, except that at large displacements the static-test results might lie above the triaxial because the slight extra stiffness of the foam bed might require slightly greater stress to cause a given strain.

These expectations are borne out by the data, given in Figures 113 through 119. For example, the results for Tests C and D (which were amazingly coincident) are given in Figure 113. At the specimen densities (104.7 and 104.9 pcf the results are compared to the SFC-smoothed curve and to the triaxial band at the nominal density of 105 pcf. Up to about 8 or 9 psi the results are indistinguishable on the plot. Above this value the static-test results are lower, passing a 10-percent difference at about 13 psi.

The specimens in Tests E and F, being placed more carefully as the personnel had gained experience, apparently did not buckle seriously. The results of Test E (Fig. 119) followed very closely the SFC-smoothed curve and lie above the envelope of triaxial data, which came (Fig. 42) from specimens at densities *lower* than the nominal 95 pcf. The results of Test F (Fig. 116) show excellent agreement with the SFC curve and the triaxial envelope, but tend more closely toward the triaxial envelope. (Note that the triaxial data of the envelope in Figure 39 and of Test F are both less than the nominal density of 100 pcf.) A curious excursion should be noted for Test F: at about 11 psi there is a distinct discontinuity in the static stress-strain curve. It is believed, from events noted during the test, that the needles at station A bound in the foam owing to a buckle, thus restraining the displacement.

The results of tests taken after the foam was reinforced similarly bear out the expectations described above. For example, Test L (Fig. 114) agrees closely with the SFC curve and the triaxial envelope. Test P (Fig. 115) appears substantially stiffer at low strains, but soon joins the SFC curve. Close study of the data from the test verify this result; most of the displacement gages in Test P simply did not start responding appreciably until substantial load was indicated by the proving ring. The exception is station D, which showed a sensible response commencing at the first load, and which, if used as the only data

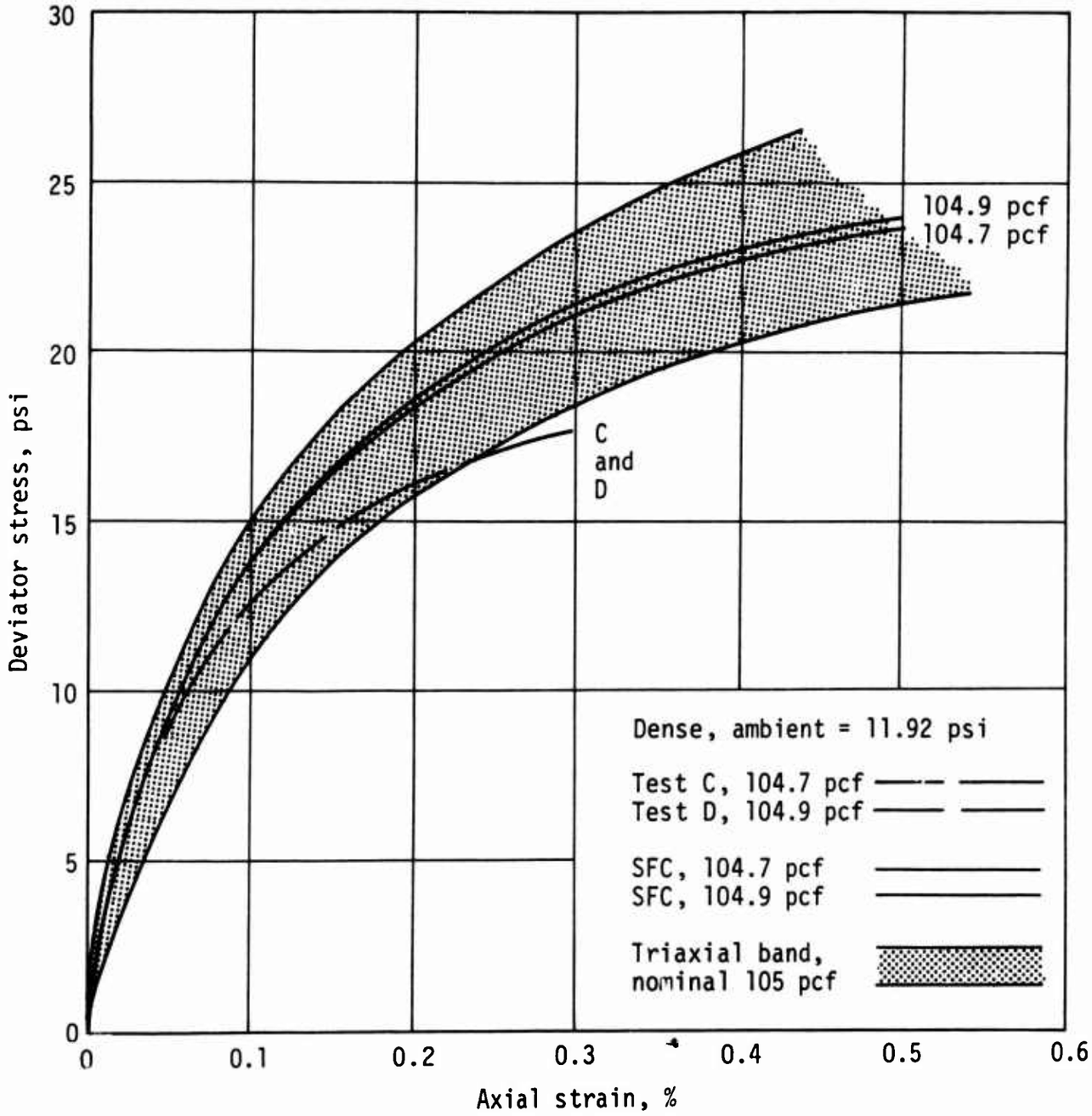

Figure 113. Static comparison: dense, high-ambient stress

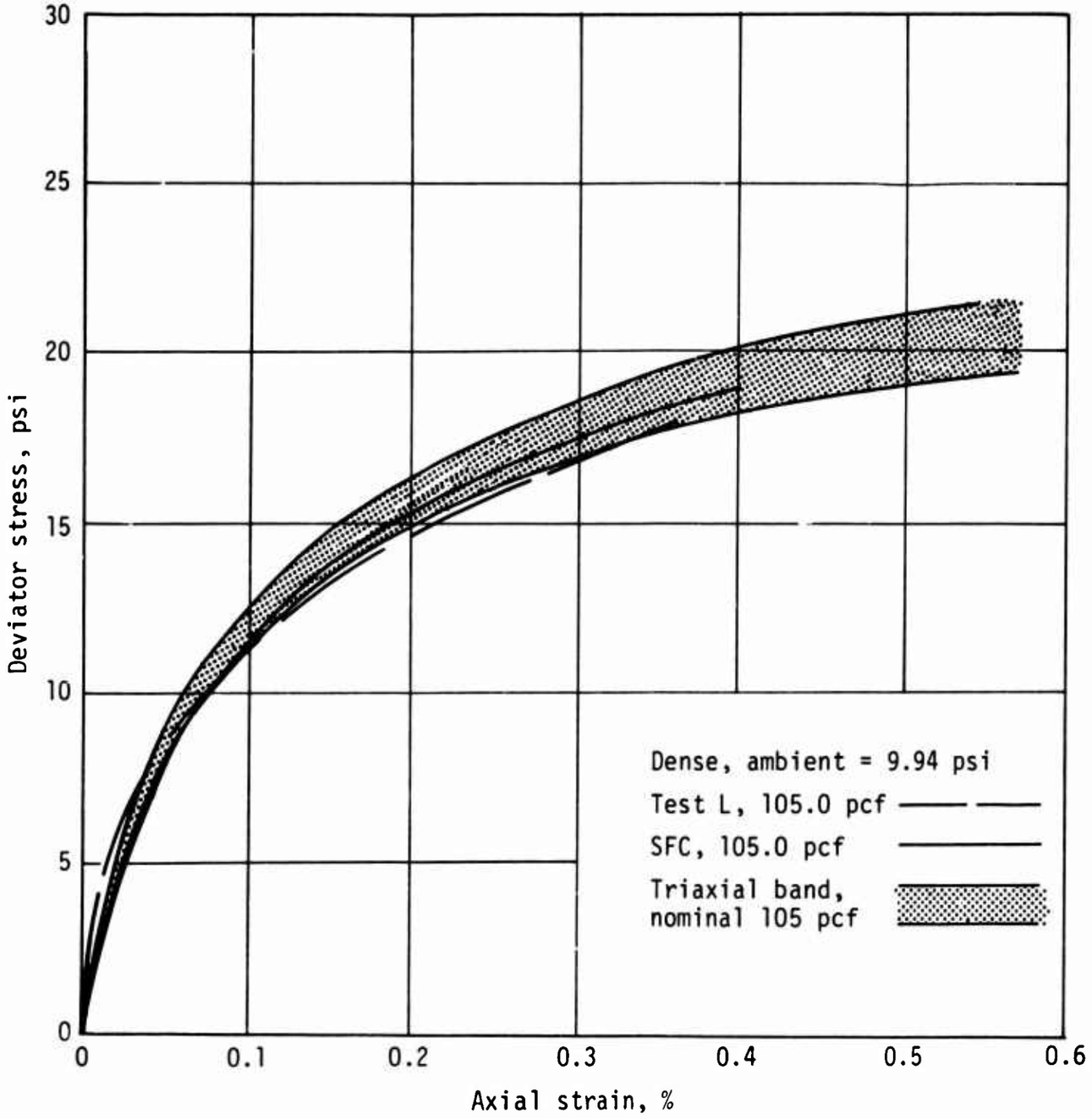

Figure 114. Static comparison: dense, middle-ambient stress

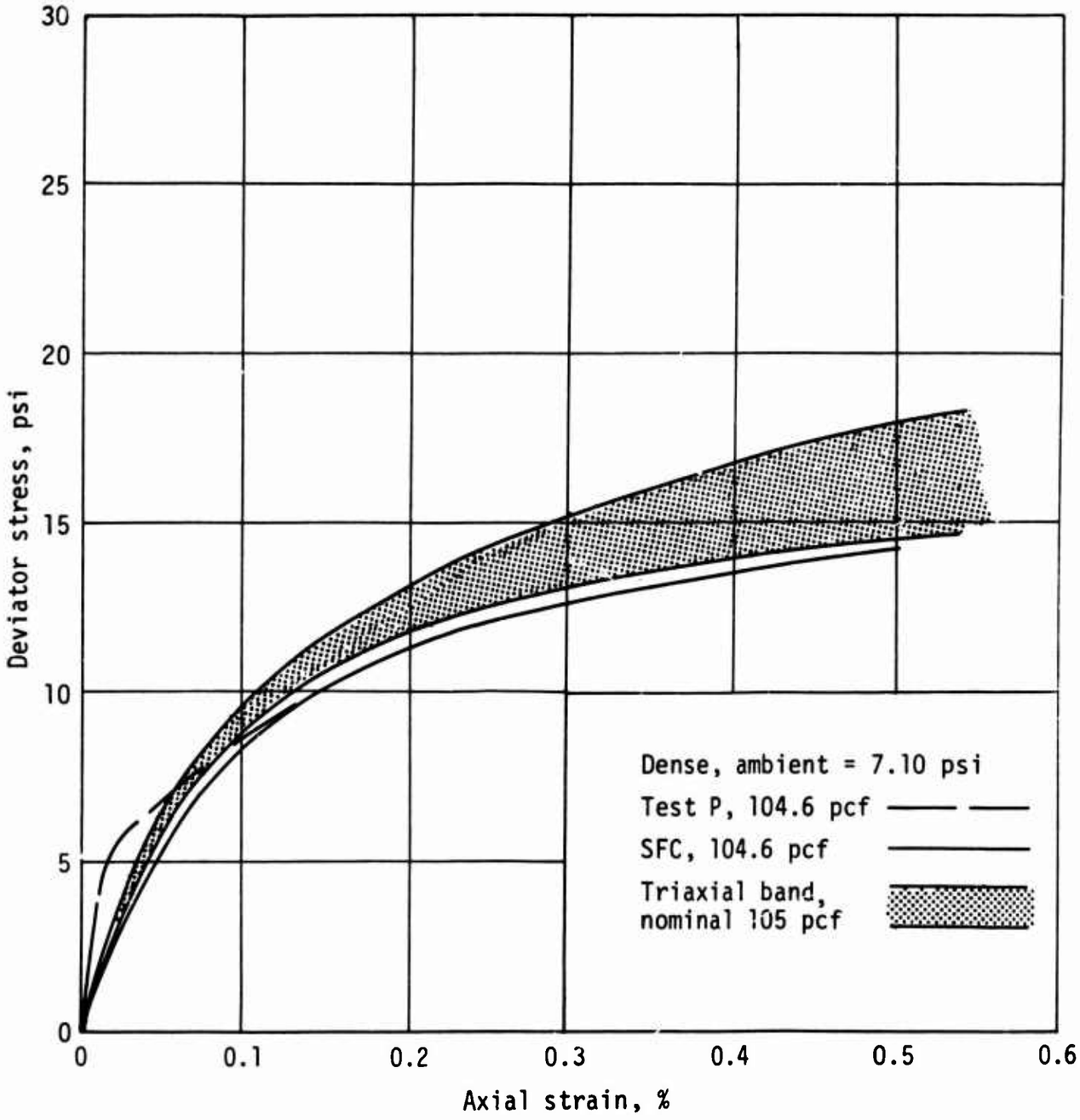

Figure 115. Static comparison: dense, low-ambient stress

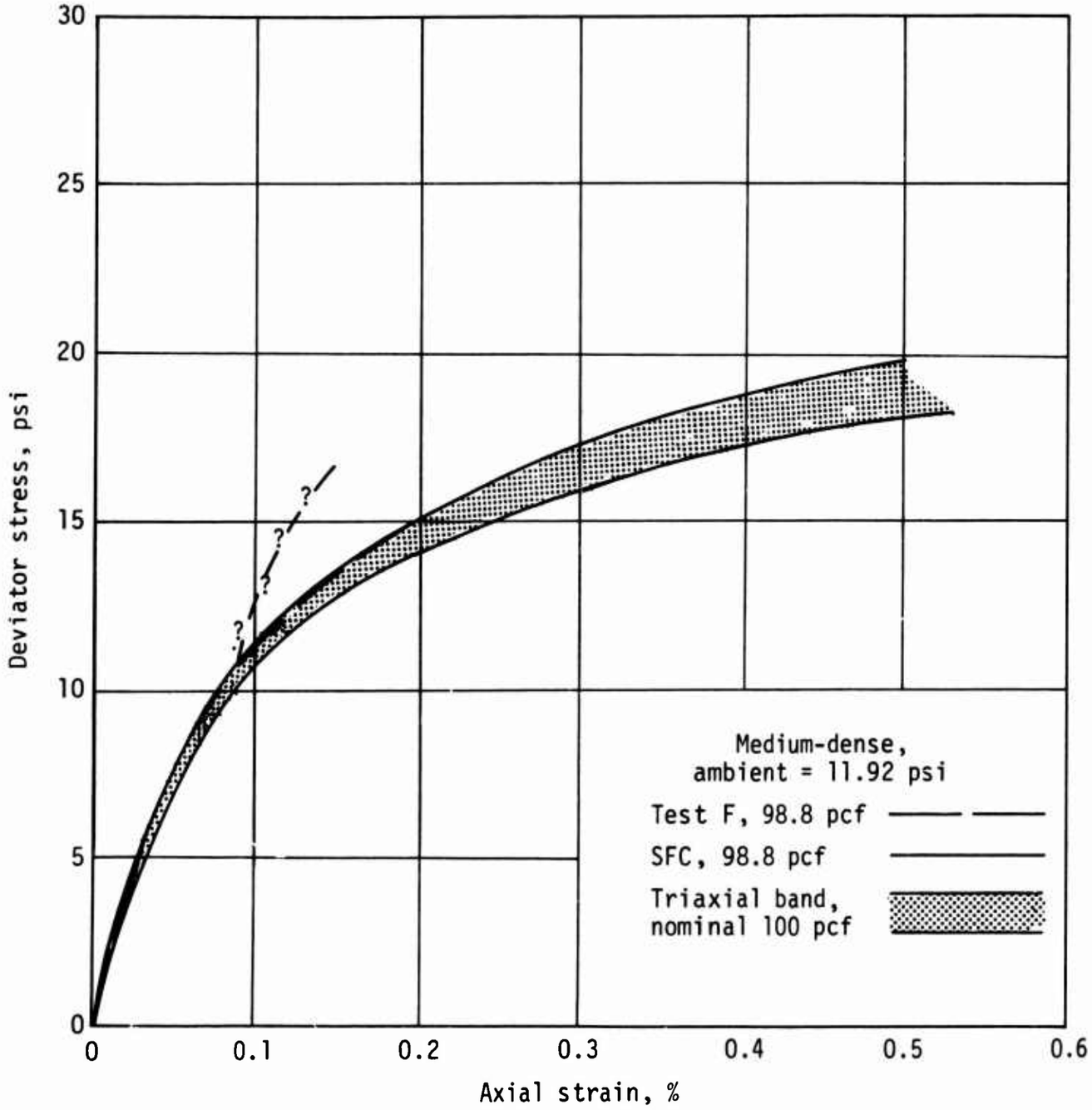

Figure 116. Static comparison: medium-dense, high-ambient stress

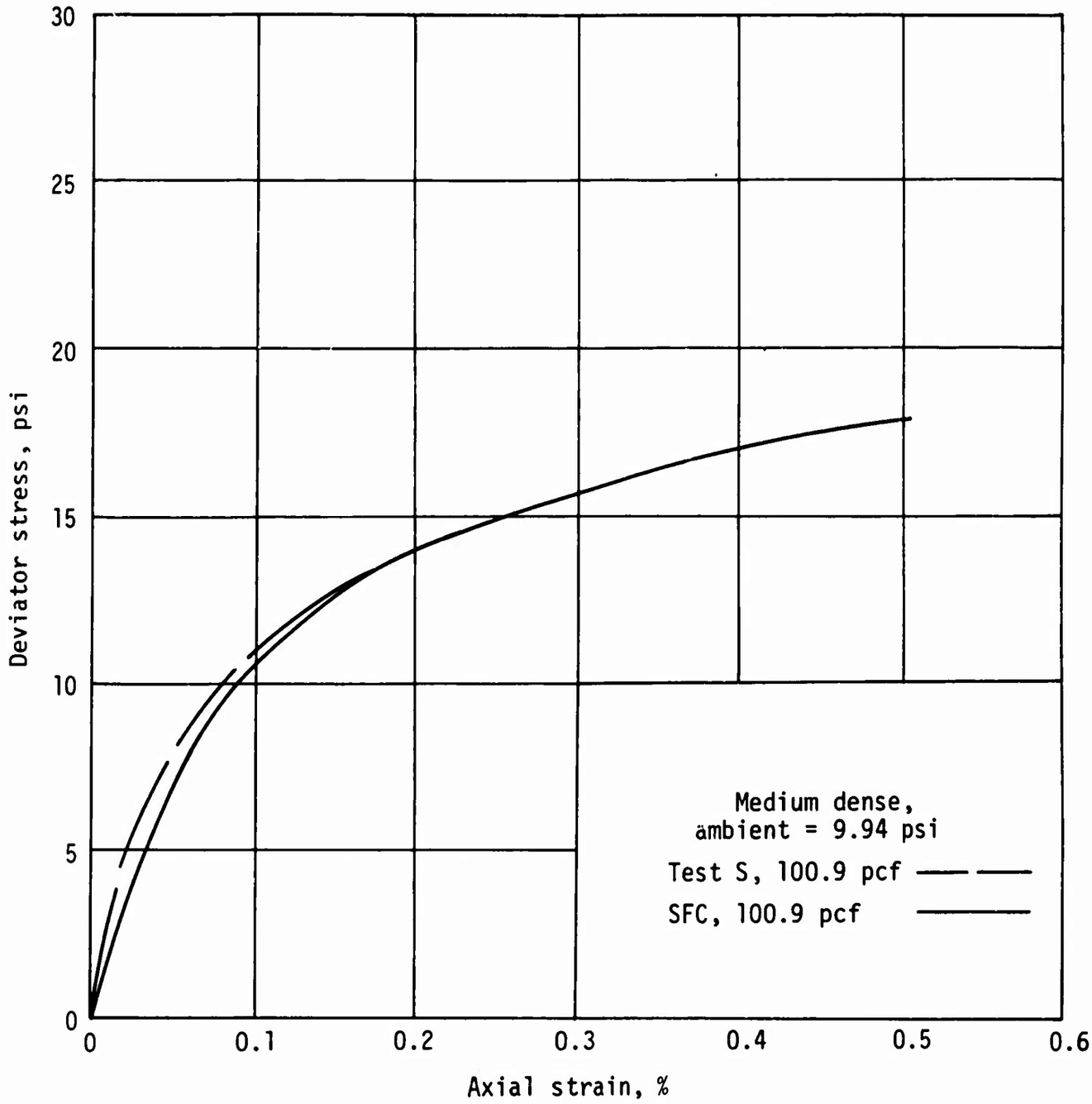

Figure 117. Static comparison: medium-dense, middle-ambient stress

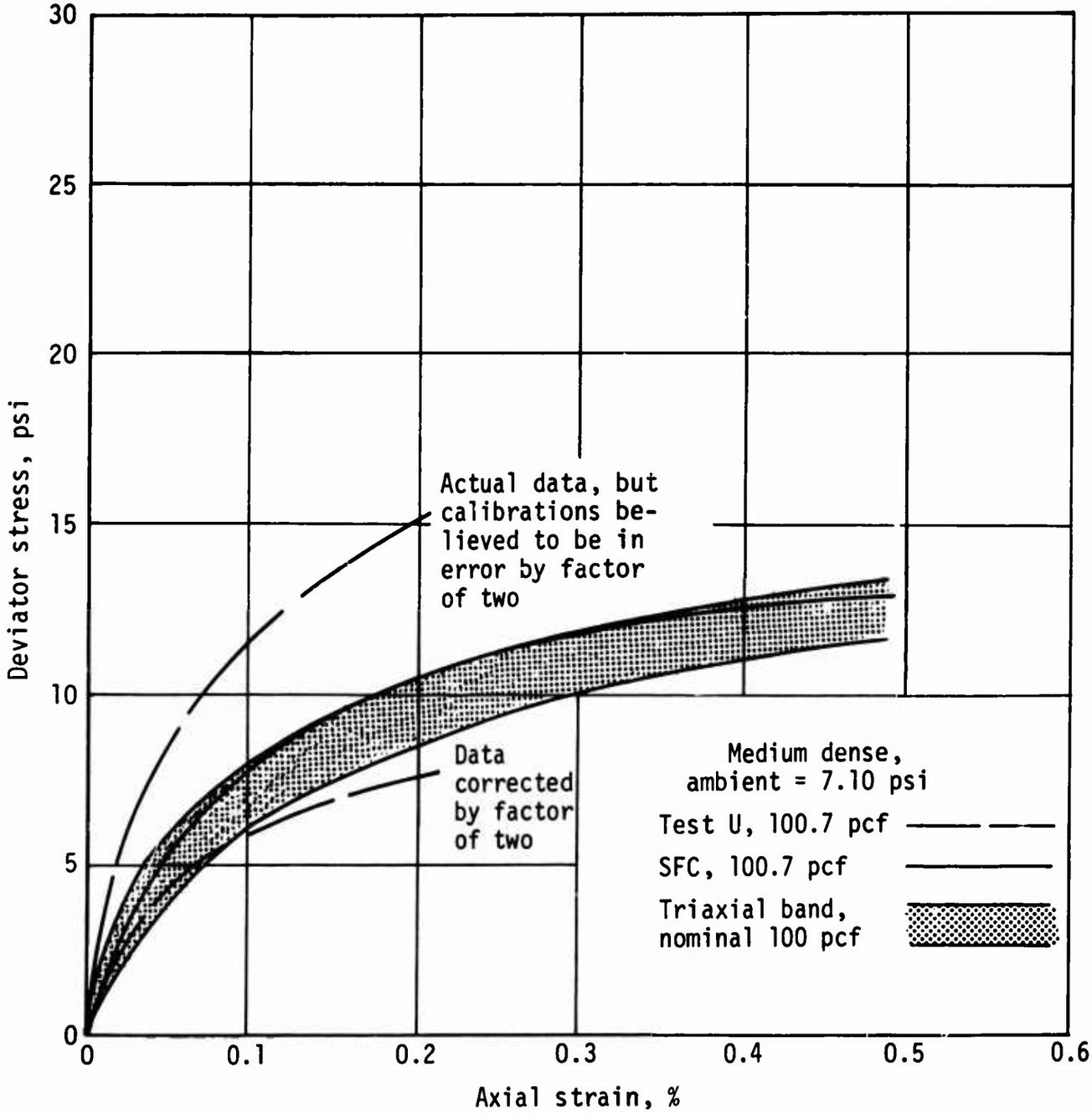

Figure 118. Static comparison: medium-dense, low-ambient stress

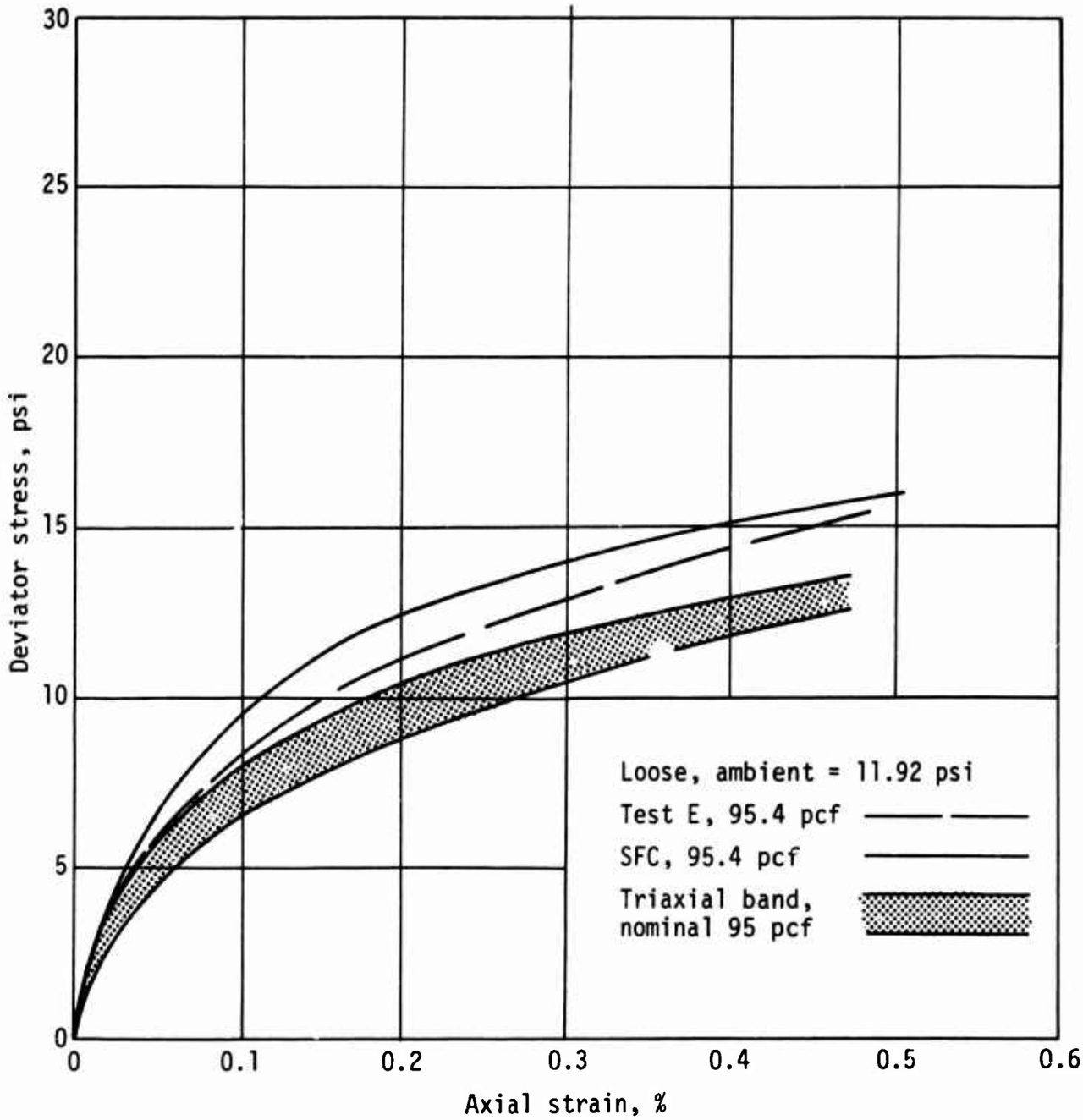

Figure 119. Static comparison: loose, high-ambient stress

point, would yield a sensible stress-strain curve. To conform to consistent data-analysis procedures, however, the data were analyzed as for the other long-specimen tests. Similar seemingly anomalous results were occasionally noted in triaxial tests. Note, for example, triaxial Test E1 (Fig. 36), which contributed substantially to the low-strain spread in the envelope for that condition. The results of Test U (Fig. 118) are questionable. The curve for the data as reduced is much stiffer than both the SFC curve and the triaxial envelope. There is reason to believe that the calibrations in this test could have been off by a factor of two. However, when the reduced data are divided by two, as shown in Figure 118, the resulting curve agrees to a stress of perhaps 3 psi and then indicates a buckling behavior. Since buckling is an unstable phenomenon, this could have happened; and since post-test inspection of the static specimens always showed buckling because the tests were carried to complete failure, it was not possible to determine definitely if early buckling had occurred. In view of the uncertainties connected with Test U, the results are ignored as anomalous to the pattern established by the other tests.

Test S (Fig. 117) agreed very well with the SFC curve.

3. Discussion of Results.

In the preceding comparisons of triaxial with long-specimen data, exact agreements were not expected. The discrepancies in testing sands are attributed to the difficulty of determining the density of a long, slender specimen, the possibilities of nonuniformities in the long specimen, and the unknown validity of the SFC method for small strains. Even within these recognized limitations the agreement was generally quite good.

The results of the static long-specimen tests presented a consistent pattern which, except for explainable deviations, was sensibly coincident with the conventional triaxial results. These static long-specimen tests were performed to verify the long-specimen setup and to provide the static stress-strain data for comparison with the dynamic results. The triaxial tests were performed later to indicate the data scatter to be expected under even ideal conditions, and, hopefully, to augment the few static long-specimen tests that could be performed. The data presented justify this hope: the static data agree with the triaxial within the ranges of data scatter to be expected in sands. For this reason, the triaxial data were taken as a basis for comparison with the dynamic tests; and in order that the basis for comparison would be uniform and subject to

minimal effects of data scatter, the SFC-smoothed curve for each specimen at its own density was used for comparison.

Close study of the static data leads to a conclusion to be kept in mind when studying the dynamic data: the agreements are best at low strains up to 0.2 percent and fall below the triaxial data for Series 244 and 248 or above it for 252 and 253 at higher strains, for reasons developed above.

Finally, it should be noted that the normal data scatter is generally more than the maximum strain-rate sensitivity of 20 percent, as has been pointed out in the literature (Refs. 34,58).

APPENDIX C

EXAMPLE OF COMPUTATIONS

This appendix contains an example of how, given the SFC constitutive relationship, one can compute the stress-time history at a specified point in space and time. The results of this example are given in Section VI, 2h. Table V summarizes the computations. The data are from Test H (248-0900), which was nominally medium dense (nominal density 100 pcf) and which was tested at an ambient stress of 11.92 psi.

The problem may be stated as follows: given the stress-time input and the constitutive relationship, predict the stress-time history to be recorded at the reaction end of a specimen 60 inches long.

In Table V columns 1 and 2 show the input stress-time history recorded at the front force link (FFL). Knowing that the ambient stress is 11.92 psi and by using Eq. (34), the stress ratio L_p can be computed. The results are given in column 3. Then from the constitutive relationship for this material in a 100-pcf condition (Fig. 72) the strain is obtained (col. 4, Table V). By using the strain, the value of the wave-velocity function (in col. 5) is found from Figure 75. The wave velocities are then computed by multiplying the value of the wave-velocity function by the square root of the ambient stress according to Eq. (42), with the results in column 6. The amount of time required for the particular stress level to travel the 60 inches to the back force link (BFL) is found by dividing 60 inches by the wave velocity, column 7. As explained in Section III, 2a, the time at which the wave arrives is this travel time plus the time lag of the input for that particular stress level, as shown in column 8. By utilizing Figure 82 and the given strains, the reflection factors R_p (in col. 9) can be found. These factors, when multiplied by the input stresses from column 2, yield the values of the reflected stresses in column 10. Columns 8 and 10 are the desired stress-time history prediction at the rigidly supported BFL. Column 11 is a duplication of the stress-time computations for the midpoint of the rod (30 inches from the end).

The computed results are compared with the measured results in Figure 83.

Table V

SUMMARY OF COMPUTATIONS

(1) Input time, Δt_w (msec)	(2) FFL stress, σ_{pi} (psi)	(3) Stress ratio, L_p	(4) Strain, ε_p (%)	(5) Wave-velocity function, N_p	(6) Wave velocity, c_p (in./msec)	(7) Wave-traverse time (msec)	(8) Arrival at BFL, t_a (msec)	(9) Reflection factor, R_p	(10) Stress at BFL, σ_{pr} (psi)	(11) Midpoint arrival, time (msec)
0	0	--	0	--	13.32*	4.50	4.50	2.00†	0†	2.25
0.2	2.10	0.176	0.011	3240	11.19	5.36	5.56	1.88	3.95	2.88
0.4	4.20	0.352	0.025	2900	10.02	5.99	6.39	1.76	7.39	3.38
0.6	6.25	0.524	0.034	2740	9.46	6.32	6.92	1.69	10.55	3.77
0.8	8.10	0.679	0.050	2455	8.48	7.07	7.87	1.58	12.79	4.34
1.0	9.82	0.824	0.066	2220	7.66	7.83	8.83	1.43	14.04	4.92
1.2	11.46	0.961	0.091	1930	6.66	9.00	10.20	1.39	15.91	5.71
1.4	12.70	1.076	0.107	1790	6.18	9.70	11.10	1.37	17.39	6.25
1.6	13.58	1.140	0.124	1650	5.70	10.52	12.12	1.33	18.06	6.86
1.8	14.20	1.192	0.137	1560	5.38	11.14	12.94	1.32	18.74	7.38
2.0	14.65	1.229	0.150	1485	5.13	11.69	13.69	1.31	19.18	7.85
2.2	14.95	1.254	0.159	1440	4.97	12.06	14.26	1.31	19.50	8.24
2.4	15.10	1.267	0.162	1410	4.87	12.31	14.71	1.30	19.61	8.56
2.6	15.15	1.272	0.164	1395	4.82	12.44	15.04	1.30	19.66	8.82

*From Reference 49

†Estimated only to the third significant number

REFERENCES

Abbreviations:

ASCE	American Society of Civil Engineers
ASTM	American Society for Testing Materials
HRB	Highway Research Board, National Research Council
ICE	Institution of Civil Engineers (Great Britain)
ICSM&FE	International Conference on Soil Mechanics and Foundation Engineering
JAM	*Journal of Applied Mechanics*, in the *Transactions of the American Society of Mechanical Engineers*
JASA	*Journal of the Acoustical Society of America*
JSM&FE	*Journal of the Soil Mechanics and Foundations Division of the American Society of Civil Engineers*
MIT	Massachusetts Institute of Technology
Phys. Rev.	*Physics Review*
Proc.	Proceedings
RAND	The RAND Corporation
SESA	Society for Experimental Stress Analysis
STP	Special Technical Publication
Trans.	Transactions
WES	Waterways Experiment Station, U.S. Army Corps of Engineers

1. Timoshenko, S., and Goodier, J. N., *Theory of Elasticity*, McGraw-Hill, N.Y., 1951.

2. Hoffman, O., and Sachs, G., *Theory of Plasticity*, McGraw-Hill, 1953.

3. Kolsky, H., *Stress Waves in Solids*, Clarendon Press, Oxford, England, 1953 (reprint by Dover Press, N.Y., 1964).

4. de Vault, G. P., and Curtis, C. W., "Elastic Cylinder with Free Lateral Surface and Mixed Time-Dependent End Conditions," *JASA, 34*, No. 4, April 1962.

5. Redwood, M., *Mechanical Waveguides*, Pergamon Press, N.Y., 1960.

6. Love, A. E. H., *Mathematical Theory of Elasticity*, Cambridge University Press, Cambridge, England (reprint by Dover Press, N.Y., 1927).

7. Bancroft, D., "The Velocity of Longitudinal Waves in Cylindrical Bars," *Phys. Rev.*, *59*, April 1941.

8. Donnell, L. H., "Longitudinal Wave Transmission and Impact," *JAM*, *52*, 1930.

9. Plass, H. J., Jr., and Ripperger, E. A., "Current Research on Plastic Wave Propagation," *Plasticity, Proc. Second Symposium on Naval Struct. Mech.*, Pergamon Press, 1960.

10. Bullen, K. E., *Theory of Seismology*, Cambridge University Press, Cambridge, England, 1959.

11. Ewing, W. M., Jardetsky, W. S., and Press, F., *Elastic Waves in Layered Media*, McGraw-Hill, N.Y., 1957.

12. Jeffries, H., *The Earth*, Cambridge University Press, Cambridge, England, 1962.

13. Leet, L. D., *Earth Waves*, Harvard University Press, Cambridge, Mass., 1950.

14. Leet, L. D., *Vibrations from Blasting Rock*, Harvard University Press, Cambridge, Mass., 1960.

15. Wilson, S. D., and Sibley, E. A., "Ground Displacements Resulting from Air-Blast Loading," *JSM&FE*, Paper 3346, December 1962.

16. ASCE, *Design of Structures to Resist Nuclear Weapons Effects*, Manual 42, N.Y., 1961.

17. Sung, T. Y., "Vibrations in Semi-Infinite Solids due to Periodic Surface Loading," *ASTM*, STP156, 1953.

18. Richart, F. E., Jr., "Foundation Vibrations," *Trans. ASCE, Part 1, 127*, 1962.

19. Hsieh, T. K., "Foundation Vibrations," *Proc. ICE*, No. 6571, London, 1962.

20. Barkan, D. D., *Dynamics of Bases and Foundations*, McGraw-Hill, N.Y., 1962.

21. Major, A., *Vibration Analysis and Design of Foundations for Machines and Turbines*, Collet's Holdings, Ltd., London, 1962.

22. Lorenz, H., *Grundbau-Dynamik*, Springer Verlag, Berlin, 1960.

23. U.S. Army Corps of Engineers, *Effect of Antenna Operation on Structure and Foundation Behavior, TTR Tower, White Sands Missile Range, New Mexico*, WES, MP4-580, 1963.

24. U.S. Army Corps of Engineers, *Development and Evaluation of Soil Bearing Capacity Foundations of Structures*, WES, TR-3-632, 1963.

25. Jones, R., "In-Situ Measurement of the Dynamic Properties of Soil by Vibration Methods," *Geotechnique*, London, March 1958.

26. Heukelom, W., and Foster, C. R., "Dynamic Testing of Pavements," *Trans. ASCE, Part I, 127*, 1962.

27. Heukelom, W., "Analysis of Dynamic Deflexions of Soils and Pavements," *Geotechnique*, London, September 1961.

28. U.S. Army Corps of Engineers, *A Procedure for Determining Elastic Moduli of Soils by Field Vibratory Techniques*, WES, MP4-577, 1963.

29. U.S. Army Corps of Engineers, *Nondestructive Dynamic Testing of Proposed Radar Sets, White Sands Missile Range, New Mexico*, WES, MP4-584, 1963.

30. Glasstone, S. (ed.), *The Effects of Nuclear Weapons*, U.S. Atomic Energy Commission, U.S. Government Printing Office, Washington, D.C., 1962.

31. Casagrande, A., and Shannon, W. L., "Strength of Soils Under Dynamic Loads," *Trans., ASCE, 114*, 1949.

32. Taylor, D. W., and Whitman, R. V., *The Behavior of Soils Under Dynamic Loadings - I*, AFSWP-116, MIT, Cambridge, Mass., August 1952.

33. Taylor, D. W., and Whitman, R. Y., *The Behavior of Soils Under Dynamic Loadings - II*, (ASTIA AD-28-650), MIT, Cambridge, Mass., July 1953.

34. Whitman, R. V., *The Behavior of Soils Under Dynamic Loadings - III*, (ASTIA AD-64032), MIT, Cambridge, Mass., August 1954.

35. Whitman, R. V., and Healy, K. A., *Shearing Resistance of Sands Under Rapid Loadings*, MIT Publication 114, Cambridge, Mass., October 1961.

36. Whitman, R. V., and Healy, K. A., *Shearing Resistance of Sands During Rapid Loadings*, MIT Publication 115, Cambridge, Mass., May 1962.

37. Whitman, R. V., and Healy, K. A., "Shear Strength of Sands During Rapid Loadings," *Trans., ASCE, Part II, 128*, 1963.

38. Whitman, R. V., *Testing Soils With Transient Loads*, ASTM, STP232, 1957.

39. Healy, K. A., *Pore Pressure Measurements During Transient Loading*, MIT Publication 107, Cambridge, Mass., November 1960.

40. Peters, J. D., "A Gage for Measuring Pore Water Pressures in Soils Under Dynamic Loads," Ph.D. Thesis, University of Illinois, Urbana, Ill., 1963.

41. Seed, H. B., and Lundgren, R., "Investigation of the Effect of Transient Loading on the Strength and Deformation Characteristics of Saturated Sands," *ASTM Proc., 54*, 1954.

42. Healy, K. A., *Triaxial Tests Upon Saturated Fine Silty Sand*, MIT Publication 128, Cambridge, Mass., September 1962.

43. Healy, K. A., *The Dependence of Dilation in Sand on Rate of Shear Strain,* MIT Publication 139, Cambridge, Mass., February 1963.

44. Healy, K. A., *Undrained Strength of Saturated Clayey Silt,* MIT Publication 141, Cambridge, Mass., March 1963.

45. Jacobsen, L. S., and Ayre, R. S., *Engineering Vibrations,* McGraw-Hill, N.Y., 1958.

46. Wilson, S. D., and Dietrich, R. J., "Effect of Consolidation Pressure on Elastic and Strength Properties of Clay," *Proc., ASCE Conf. on Str. of Soils,* Boulder, Colo., 1961.

47. Shannon, W. L., Yamane, G., and Dietrich, R. J., "Dynamic Triaxial Tests on Sand," *Proc. First Pan-American Conf. on Soil Mech., I,* Mexico City, 1960.

48. Richart, F. E., Jr., Hall, J. R., and Lysmer, J., *Study of the Propagation and Dissipation of Elastic Wave Energy in Granular Soils,* WES Contract DA-22-079-eng-314, September 1962.

49. Hardin, B. O., and Richart, F. E., Jr., "Elastic Wave Velocities in Granular Soils," *JSM&FE*, Paper 3407, February 1963.

50. Duffy, J., and Mindlin, R. D., "Stress-Strain Relations and Vibrations of a Granular Medium," *JAM, 24*, 1957.

51. Lawrence, F. V., Jr., *Laboratory Measurement of Dilatational Wave Propagation Velocity,* MIT Publication 113, Cambridge, Mass., July 1961.

52. Lawrence, F. V., Jr., *Propagation Velocity of Ultrasonic Waves Through Sand,* MIT Publication 140, Cambridge, Mass., March 1963.

53. Smith, R. H., and Newmark, N. M., *Numerical Integration of One-Dimensional Stress Waves,* Department of Civil Engineering, University of Illinois, Urbana, Ill., August 1958.

54. Parkin, B. R., *Impact Wave Propagation in Columns of Sand*, RAND, RM-2486, November 1959.

55. Parkin, B. R., "Impact Waves in Sand: Theory Compared with Experiments on Sand Columns," *Trans., ASCE, Part I, 127,* 1962.

56. Parkin, B. R., "Impact Waves in Sand: Implications of an Elementary Theory," *Trans., ASCE, Part I, 127*, 1962.

57. Malvern, L. E., "The Propagation of Longitudinal Waves of Plastic Deformation in a Bar of Material Exhibiting a Strain-Rate Effect," *JAM, 18,* 1951.

58. Selig, E. T., "Shock Induced Stress Wave Propagation in Sand," Ph.D. dissertation, Illinois Institute of Technology, Chicago, Ill., 1964.

59. Heierli, W., "Inelastic Wave Propagation in Soil Columns," *Trans. ASCE, Part I, 128,* 1963.

60. Chen, L. S., "An Investigation of Stress-Strain and Strength Characteristics of Cohesionless Soils by Triaxial Compression Tests," *Proc., Second ICSM&FE, 5,* 1948.

61. Campbell, W. R., "Determination of Dynamic Stress-Strain Curves from Strain Waves in Long Bars," *Proc., SESA, X,* No. 1, 1952.

62. Dove, R. C., and Adams, P. H., *Experimental Stress Analysis and Motion Measurement,* Charles E. Merrill Books, Inc., Columbus, Ohio, 1964.

63. Terzaghi, K., *Theoretical Soil Mechanics,* John Wiley and Sons, Inc., N.Y., 1943.

64. Seed, H. B., and McNeill, R. L., *A Comparative Study of Soil Deformations in Normal Compression and Repeated Load Tests,* HRB, Bull. 141, 1956.

Unclassified

Security Classification

DOCUMENT CONTROL DATA - R&D

(Security classification of title, body of abstract and indexing annotation must be entered when the overall report is classified)

1. ORIGINATING ACTIVITY *(Corporate author)* The Eric H. Wang Civil Engineering Research Facility University of New Mexico Albuquerque, New Mexico	2a. REPORT SECURITY CLASSIFICATION Unclassified 2b. GROUP

3. REPORT TITLE

A STUDY OF THE PROPAGATION OF STRESS WAVES IN SAND

4. DESCRIPTIVE NOTES *(Type of report and inclusive dates)*

January 1964 to May 1965

5. AUTHOR(S) *(Last name, first name, initial)*

McNeill, Robert L.

6. REPORT DATE March 1966	7a. TOTAL NO. OF PAGES 244	7b. NO. OF REFS 64
8a. CONTRACT OR GRANT NO. AF29(601)-6002 b. PROJECT NO. 5710 c. Subtask No. 13.144 d.	9a. ORIGINATOR'S REPORT NUMBER(S) AFWL-TR-65-180 9b. OTHER REPORT NO(S) *(Any other numbers that may be assigned this report)*	

10. AVAILABILITY/LIMITATION NOTICES

Distribution of this document is unlimited.

11. SUPPLEMENTARY NOTES	12. SPONSORING MILITARY ACTIVITY Air Force Weapons Laboratory (WLDC) Kirtland AFB, New Mexico 87117

13. ABSTRACT

The propagation of near-failure, soft-fronted stress waves in 5-foot-long, 1-inch-diameter, unconstrained rods of dry 20-30 Ottawa sand is studied. The input is created by a shock tube, modified to yield soft-fronted, long-duration, air-pressure loadings. Primary data are displacement-time histories from seven stations along the rod, read by light-sensing gages designed for negligible inertia and friction; secondary data are stress-time histories at the input and the rigidly held reaction ends. Static, dynamic, and additional static triaxial data are given Variables are applied ambient stress and sand density. From findings that the material is strain-rate insensitive and follows Coulomb's failure law at subfailure stresses, the following observations of wave-propagation parameters for above-seismic stresses and a specific material condition have been made: (1) wave and particle velocities depend on the one-half power of ambient stress; (2) all energy densities depend on the first power of ambient stress; and (3) energy partitioning and reflection are independent of ambient stress. Effects of density on wave-propagation parameters for the sand and the variables studied are that (1) all increase with increasing density, (2) some are specifically linear on density, and all can be taken as such for engineering purposes, and (3) waveform parameters are much less sensitive to small errors in density than are static parameters. Also shown: (1) reflections of stress from rigid boundaries can be estimated for non-linear materials; and (2) correlation between seismic velocity and triaxial strength exists, provided there is a power-function relationship between seismic velocity and ambient stress and the material follows Coulomb's law.

DD FORM 1 JAN 64 1473

Unclassified

Security Classification

Unclassified

Security Classification

14. KEY WORDS	LINK A ROLE	LINK A WT	LINK B ROLE	LINK B WT	LINK C ROLE	LINK C WT
Wave propagation in soil columns						
Shock tubes						
Dynamic properties of sands						

INSTRUCTIONS

1. ORIGINATING ACTIVITY: Enter the name and address of the contractor, subcontractor, grantee, Department of Defense activity or other organization *(corporate author)* issuing the report.

2a. REPORT SECURITY CLASSIFICATION: Enter the overall security classification of the report. Indicate whether "Restricted Data" is included. Marking is to be in accordance with appropriate security regulations.

2b. GROUP: Automatic downgrading is specified in DoD Directive 5200.10 and Armed Forces Industrial Manual. Enter the group number. Also, when applicable, show that optional markings have been used for Group 3 and Group 4 as authorized.

3. REPORT TITLE: Enter the complete report title in all capital letters. Titles in all cases should be unclassified. If a meaningful title cannot be selected without classification, show title classification in all capitals in parenthesis immediately following the title.

4. DESCRIPTIVE NOTES: If appropriate, enter the type of report, e.g., interim, progress, summary, annual, or final. Give the inclusive dates when a specific reporting period is covered.

5. AUTHOR(S): Enter the name(s) of author(s) as shown on or in the report. Enter last name, first name, middle initial. If military, show rank and branch of service. The name of the principal author is an absolute minimum requirement.

6. REPORT DATE: Enter the date of the report as day, month, year; or month, year. If more than one date appears on the report, use date of publication.

7a. TOTAL NUMBER OF PAGES: The total page count should follow normal pagination procedures, i.e., enter the number of pages containing information.

7b. NUMBER OF REFERENCES: Enter the total number of references cited in the report.

8a. CONTRACT OR GRANT NUMBER: If appropriate, enter the applicable number of the contract or grant under which the report was written.

8b, 8c, & 8d. PROJECT NUMBER: Enter the appropriate military department identification, such as project number, subproject number, system numbers, task number, etc.

9a. ORIGINATOR'S REPORT NUMBER(S): Enter the official report number by which the document will be identified and controlled by the originating activity. This number must be unique to this report.

9b. OTHER REPORT NUMBER(S): If the report has been assigned any other report numbers *(either by the originator or by the sponsor)*, also enter this number(s).

10. AVAILABILITY/LIMITATION NOTICES: Enter any limitations on further dissemination of the report, other than those imposed by security classification, using standard statements such as:

(1) "Qualified requesters may obtain copies of this report from DDC."

(2) "Foreign announcement and dissemination of this report by DDC is not authorized."

(3) "U. S. Government agencies may obtain copies of this report directly from DDC. Other qualified DDC users shall request through _____."

(4) "U. S. military agencies may obtain copies of this report directly from DDC. Other qualified users shall request through _____."

(5) "All distribution of this report is controlled. Qualified DDC users shall request through _____."

If the report has been furnished to the Office of Technical Services, Department of Commerce, for sale to the public, indicate this fact and enter the price, if known.

11. SUPPLEMENTARY NOTES: Use for additional explanatory notes.

12. SPONSORING MILITARY ACTIVITY: Enter the name of the departmental project office or laboratory sponsoring *(paying for)* the research and development. Include address.

13. ABSTRACT: Enter an abstract giving a brief and factual summary of the document indicative of the report, even though it may also appear elsewhere in the body of the technical report. If additional space is required, a continuation sheet shall be attached.

It is highly desirable that the abstract of classified reports be unclassified. Each paragraph of the abstract shall end with an indication of the military security classification of the information in the paragraph, represented as *(TS)*, *(S)*, *(C)*, or *(U)*.

There is no limitation on the length of the abstract. However, the suggested length is from 150 to 225 words.

14. KEY WORDS: Key words are technically meaningful terms or short phrases that characterize a report and may be used as index entries for cataloging the report. Key words must be selected so that no security classification is required. Identifiers, such as equipment model designation, trade name, military project code name, geographic location, may be used as key words but will be followed by an indication of technical context. The assignment of links, rules, and weights is optional.

GPO 886-551

Unclassified

Security Classification